



Max-Planck-Institut
für Polymerforschung

Max Planck Institute
for Polymer Research



Conjugated Porous Polymers for Visible-Light Photocatalysis

Dissertation

zur Erlangung des Grades

"Doktor der Naturwissenschaften"

im Promotionsfach Chemie

am Fachbereich Chemie, Pharmazie und Geowissenschaften

der Johannes Gutenberg-Universität Mainz

Saman Ghasimi

geboren in Mahabad/Iran

Mainz, 2016

Erklärung:

Ich versichere, dass ich die vorliegende Arbeit selbständig verfasst und keine anderen als die angegebenen Quellen und Hilfsmittel benutzt habe.

Mainz, 25.10.2016

Dekan:

1. Gutachter:

2. Gutachter:

Tag der mündlichen Prüfung:

Table of Contents

Einführung	1
Abstract	3
1. Introduction	4
2. Aim of the Work	6
3. Theoretical Background	7
3.1 Catalysis.....	7
3.1.1 Photocatalysis.....	8
3.1.2 Design strategies for enhanced photoredox processes via energy band position alignment of conjugated organic semiconductors.....	13
3.2 Classification of porous materials.....	17
3.3 Synthesis of conjugated microporous polymers (CMPs).....	18
3.4 Applications of Conjugated Microporous Polymers (CMPs).....	20
3.4.1 Gas adsorption, storage, separation.....	20
3.4.2 Heterogeneous Catalysis.....	20
3.4.3 Heterogeneous Photocatalysis.....	21
3.4.4 Pollutant absorption and removal.....	21
3.5 Strategies to water-compatible conjugated porous polymers (WCPP).....	22
3.6 Conjugated Polyelectrolytes (CPEs).....	24
3.6.1 Cross-linked conjugated Polyelectrolytes (CPEs).....	26
3.7 Applications of Conjugated Polyelectrolytes (CPEs).....	28
3.7.1 Cell Imaging.....	28
3.7.2 Analysis of Cellular Processes and Fluorescence Assays.....	28
3.7.3 Cell Damage.....	29
3.8 Green Chemistry.....	29
4. Characterization Techniques	30
4.1.1 UV-Vis spectroscopy (UV-Vis).....	30

4.1.2 UV-Vis Diffuse Reflectance Spectroscopy (UV-Vis DRS)	31
4.2 Fast Fourier Infrared Spectroscopy (FT-IR)	32
4.3.1 Nuclear Magnetic Resonance Spectroscopy (NMR)	33
4.3.2 Solid State Nuclear Magnetic Resonance (Solid State NMR).....	34
4.4 Electron Paramagnetic Resonance Spectroscopy (EPR).....	35
4.5 Cyclic Voltammetry (CV).....	36
4.6 Brunnauer-Emmet-Teller Isotherm Method (BET)	37
4.7 Scanning Electron Microscopy (SEM)	38
4.8 Transmission Electron Microscopy (TEM).....	38
5. Results and Discussion	39
5.1 Water compatible conjugated microporous poly-azulene networks as visible light photocatalysts in aqueous medium.....	39
5.1.1 Introduction.....	40
5.1.2 Synthesis and Characterization	40
5.1.3 Photoreduction and photoredox cascade-reactions of metals in water	53
5.1.4 Conclusion	57
5.2 Heterophase photocatalyst from water-soluble conjugated polyelectrolytes: a self-initiation example under visible light.....	58
5.2.1 Introduction.....	58
5.2.2 Synthesis and Characterization	59
5.2.3 Photocatalytic activity for self-initiated cross-linking and Characterization.....	62
5.2.4 Photocatalytic Dye Degradation, Photoreduction of Cr(VI), Photopolymerization of Methyl Methacrylate (MMA)	70
5.2.5 Conclusion	74
5.3 Photocatalytic Stille-type coupling reactions using conjugated organic catalysts with visible light.....	75
5.3.1 Introduction.....	75
5.3.2 Synthesis and Characterization	77

5.3.3 Photocatalytic Applications and Investigation of Reaction Mechanism	84
5.3.4 Conclusion	95
6. Experimental Part	96
6.1 Materials and Instruments	96
6.2 Water compatible conjugated microporous poly-azulene networks as visible light photocatalysts in aqueous medium.....	100
6.2.1 Synthesis of azulene CMP: P-Az-1.....	100
6.2.2 Synthesis of azulene CMP: P-Az-2.....	100
6.2.3 Protonation of the poly-azulene networks	101
6.2.4 Synthesis of 1,3-dibromoazulene.....	101
6.2.5 Synthesis of 1,3-Bis(phenylethynyl)azulene (Az-Ph ₂)	103
6.2.6 Photocatalytic reduction of Cr(VI) to Cr(III) using poly-azulene networks.....	105
6.2.7 Photocatalytic reduction of Cr(VI) to Cr(III) using protonated Az-Ph ₂	106
6.2.8 Photoreduction of Cr(VI) to Cr(III) using poly-azulene networks and additional metal cations as co-catalysts in a cascade cycle	107
6.2.9 Photoreduction of Cr(VI) to Cr(III) using poly-azulene networks and formic acid as extra electron donor	108
6.2.10 Determination of Fe(II) in the cascade catalytic cycle	108
6.2.11 Repeating experiments.....	108
6.2.12 Apparent Quantum Yield Measurements.....	109
6.3 Heterophase photocatalyst from water-soluble conjugated polyelectrolytes: a self-initiation example under visible light.....	110
6.3.1 Synthesis of P-FL-BT-1	110
6.3.2 Synthesis of P-FL-BT-2	111
6.3.3 Synthesis of P-FL-BT-3 as nanoparticles	112
6.3.4 Synthesis of P-FL-BT-3 as porous monolith	112
6.3.5 Synthesis of poly(9,9-bis(6-bromohexyl)-fluorene) P1	113
6.3.6 Synthesis of P2Br.....	114

6.3.7 Synthesis of P3Br.....	115
6.3.8 Synthesis of P3X (X = BF ₄ , PF ₆ or TFSI)	115
6.3.9 Synthesis of PMMA using P-FL-BT-1 as photoinitiator	115
6.3.10 Photodegradation of rhodamine B and methylene blue	115
6.3.11 Photoreduction of Cr(VI) to Cr(III)	117
6.3.12 Scavenger study of rhodamine B degradation using P-FL-BT-3 as photocatalyst	117
6.4 Photocatalytic Stille-type coupling reactions using conjugated organic catalysts with visible light	118
6.4.1 Synthesis of P-Az-B.....	118
6.4.2 Synthesis of L-Az-B	119
6.4.3 Synthesis of 1,3-bis(phenyl)azulene (Az-Ph ₂).....	120
6.4.4 Bromination of azulene.....	121
6.4.5 Photocatalytic destannylation reaction of aryl stannanes using P-Az-B as photocatalyst	121
6.4.6 Radical trapping experiment with N-tert-butyl- α -phenylnitrone (PBN)	121
6.4.7 General procedure for the photocatalytic Stille-type coupling of aromatic iodides with stannanes	122
6.4.8 Repeating experiments of the photocatalytic Still-type coupling of 4-iodonitrobenzene with 2-(tributylstannyl)furan	122
6.4.9 Apparent Quantum Yield Measurements.....	122
6.4.10 ¹ H-NMR spectra of coupling products	123
6.4.11 ¹³ C-NMR spectra of coupling products	129
7. Overall Conclusion and Outlook	135
8. List of Abbreviations.....	137
9. Literature	140
10. Scientific Contributions	150

Einführung

Diese Arbeit befasst sich mit neuen Konzepten für die Entwicklung von konjugierten polymerbasierten heterogenen Photokatalysatoren sowohl für die Anwendung im wässrigen als auch in nicht-wässrigen Lösungsmitteln. Es werden unterschiedliche Designstrategien für die Herstellung wasserkompatibler poröser Polymere vorgestellt. Darüber hinaus werden die unterschiedlichen mechanistischen Aspekte von photokatalytischen Reaktionen an Hand einer C-C Knüpfungsreaktion beschrieben. Die hier vorgestellten Designstrategien lassen sich als allgemeine Konzepte ansehen und sind auf andere vernetzbare Polymersysteme übertragbar.

Zunächst wurden hydrophobe Polymere durch eine gezielte Funktionalisierung für die Photokatalyse in Wasser modifiziert. Zwei unterschiedliche molekulare Designstrategien für die Realisierung von hydrophilen heterogenen Photokatalysatoren auf Basis von vernetzten konjugierten Polymeren wurden umgesetzt. Das photoaktive Element dieser Photokatalysatoren besteht aus konjugierten Donor-Akzeptor Polymerketten, welche durch kovalente Vernetzung und Porenbildung neben einer signifikanten Stabilitätszunahme auch einen mehrfach synergetischen Effekt mit sich bringen. Anschließend wurde an Hand von vernetzten konjugierten Polymeren die effiziente metallfreie Photokatalyse von organischen Reaktionen demonstriert, und der photokatalytische Reaktionsmechanismus wurde aufgeklärt.

Das erste Beispiel handelt von Azulen basierten konjugierten mikroporöse Polymere (CMPs). Die Azulen-CMPs zeichnen sich dadurch aus, dass durch einen einfachen Protonierungsschritt die Tropylium-Kationen der Azulen-Einheiten entstehen und dauerhaft stabilisiert werden. Durch dieses Konzept des kontrollierten Wechsels von hydrophoben zu hydrophilen Netzwerken konnte gezeigt werden, dass hochfunktionelle CMPs für eine Vielfalt von Lösungsmitteln einsetzbar sind. Die Auswirkungen der Postmodifikation auf die Porosität, die Morphologie und die optoelektronischen Eigenschaften wurden analysiert. Die photokatalytische Effizienz in Wasser wurde durch die Reduktion von Chrom (VI) zu Chrom(III)-Ionen demonstriert, wobei die Effizienz mit der der bisherigen anorganischen heterogenen Photokatalysatoren vergleichbar war.

Im zweiten Beispiel werden photoaktive konjugierte Donor-Akzeptor-Polymere mit vernetzbaren ionischen Seitengruppen zu einem konjugierten Polyelektrolyten (CPE) kombiniert. Dieses Konzept vereint mehrere Materialeigenschaften. 1.) Die Bestrahlung mit sichtbarem Licht führt zu einer Selbstinitiierung und Vernetzung. 2.) Die amphiphile Eigenschaft ermöglicht es, dass das Polymer als Stabilisator für Kolloide und Emulsionen auftritt. 3.) Die stabilen Polymeraggregate lassen sich durch die Bestrahlung mit sichtbarem Licht dauerhaft vernetzen. Damit lassen sich stabile heterogene Photokatalysatoren mit definierter Makrostruktur herstellen. Die Materialeigenschaften vor der Vernetzung, die Morphologie und die optoelektronischen Eigenschaften wurden analysiert. Schließlich wurde die photokatalytische Leistungsfähigkeit an Hand bekannter Reaktionen wie Photoabbau von organischen Farbstoffen oder die Photoreduktion von Metallionen demonstriert.

Im dritten Beispiel werden hydrophobe Azulen-basierte konjugierte Polymere als wiederverwendbare Photokatalysatoren in einer übergangsmetallfreien Stille Kupplungsreaktion eingesetzt. Das Anwendungsspektrum der Photokatalysatoren auf die C-C-Kupplungsreaktion wurde mit verschiedenen substituierten aromatischen Halogeniden und aromatischen Stannanen demonstriert. Die zugrundeliegenden Reaktionsmechanismen der photokatalytischen Stille-Reaktion wurden durch spezifische Modellreaktionen untersucht.

Die Aufklärung der Mechanismen erfolgte sowohl mit elektrochemischen Methoden, als auch indirekt mit chemischen Methoden sowie durch Abfangen und Detektieren reaktiver Spezies.

Abstract

In this thesis, two different aspects of porous conjugated polymers as visible-light-active and heterogenous photocatalysts have been discussed: 1.) Synthesis strategies for control of hydrophilicity 2.) Metal-free photoredox mediated reaction design as replacement for traditional transition metal-catalyzed carbon-carbon bond formation reactions.

The pristine hydrophobic polymers were modified by a specific functionalization in order to conduct photocatalysis in water. Two different molecular design strategies for modification of cross-linked conjugated polymers are presented. Moreover, the photocatalysts were applied to aqueous and non-aqueous reactions. The photocatalytic reaction mechanisms were elucidated by various methods.

The first design strategy of the hydrophilicity control was demonstrated via a simple protonation step of a series of azulene-based conjugated microporous polymers (CMPs). Here, the protonation of the azulene units led to the formation and permanently stabilization of tropylium cations. This concept of the controlled change from hydrophobic to hydrophilic networks showed that highly functional CMPs can be used in both organic and aqueous solvent systems. After post-modification, the change on porosity, morphology, and optical-electronical properties were analyzed. The photocatalytic efficiency of the modified polymers in water were demonstrated by the reduction of chromium(VI) to chromium(III), whereas the efficiency was comparable to established inorganic heterogeneous photocatalysts.

The second example of hydrophilicity control was demonstrated by the combination of photoactive conjugated donor-acceptor polymers with cross-linkable ionic side groups, which led to the formation of a series of highly porous conjugated polyelectrolytes (CPEs). This concept merged multiple material properties: 1.) The irradiation with visible light led to a self-initiation and cross-linkage process of the polymers; 2.) The amphiphilic properties allowed one to use the polymer as stabilization agent for colloids and emulsions; 3.) The irradiation with visible light of those aggregates leads to permanent cross-linkage, and therefore the formation of stable heterogeneous photocatalysts with defined macrostructure inside the materials. The material properties, the morphology, and the optical-electronical properties of the materials were analyzed. Finally, the photocatalytic performance by means of known reactions such as photodegradation of organic dyes or the photoreduction of metal-ions were demonstrated.

The third example deals with the photocatalytic Stille-type C-C coupling reaction, which was demonstrated by the employment of azulene based conjugated polymers. In order to determine the range of C-C coupling reactions, a series of aromatic halides and aromatic stannanes were tested. The photoredox mediated reaction mechanism was investigated and the key steps have been identified.

In addition, the elucidation of the photocatalytic reaction mechanism was conducted via electrochemical methods as well as indirect chemical methods or trapping and detection of reactive species.

1. Introduction

The main challenge of the 21st century is to establish a global solution for the increasing demand for energy and the production of pollution. Since the industrial revolution the economy has become increasingly dependent on exhaustible energy resources such as fossil fuels with constantly growing population.^[1-3] However, the tremendous consumption of traditional fossil energy leads to large risks in the environmental and health issue, caused by uncontrolled emission.^[4] The other important issue is the limitation of the current traditional energy carriers on earth. Therefore a long-term solution of environmentally friendly and renewable energy sources is highly needed.^[5] Moreover, a paradigm shift in setting goals from high yield productions to waste elimination at source is required. Catalysis, in particular, was recognized as a central tool for efficient industrial processes by reducing waste, reaction energy and facilitating purification procedures.^[6] Among other catalysis procedures, photocatalysis provides the combination of energy efficiency with sustainability in an outstanding way.

In this view, the utilization of sunlight as a clean and inexhaustible source of renewable energy inspired materials scientists to harvest, convert, store and utilize solar energy.^[7]

More than 100 years ago, Giacomo Ciamician presented his revolutionary idea on using solar energy to drive chemical processes: *“Man had to understand nature’s ability to make chemistry only with solar energy. To utilize the photosynthesis in plants not only for storing solar energy into chemical bonds as in starch, but also to build up secondary materials and other chemicals”*.^[8-9]

In the past years, a vast number of different photocatalyst classes have been developed. Among them, metal oxides, which usually absorb in the high energetic UV range, transition metal complexes such as ruthenium or iridium based materials, which can be activated in the visible range, have been intensely studied in the last two decades.^[10-12] Organic dyes, as metal-free alternative, have also shown applications in organic synthesis.^[10] Nevertheless, there are still drawbacks associated with those molecular catalytic systems such as high costs, limited availability and toxicity or stability problems such as photobleaching effect or photocorrosion, which largely affect the catalyst recovery and long-term usage. There is therefore a strong need to develop a more sustainable, pure organic, stable and metal-free class of new photocatalysts. Recently, graphitic carbon nitrides showed excellent properties as stable, metal-free and heterogeneous photocatalysts, and have been used for a number of photocatalytic reactions under visible light irradiation such as hydrogen evolution.^[13-14]

Conjugated porous polymers have been emerged recently as stable and highly reusable photocatalysts with activity in the visible light range.^[15-20] The main advantages of conjugated polymer systems are that their optical and electronic properties can be controlled via a rational structural design on the molecular level.^[21] In addition, the solubility and hydrophilicity can be controlled by side chain modifications in order to adjust intermolecular interactions.^[22]

Beside the material design aspect for novel catalytic systems, one of the main objectives still remains the catalysis media. Organic solvents, in which most of the chemical processes are conducted, are mostly inflammable, toxic, hazardous and volatile. Therefore, a more sustainable and environmentally friendly alternative for the common organic solvents is indeed strongly needed. Water, in particular, is considered as non-toxic, non-hazardous, non-inflammable, cheap and most readily available green solvent.^[23]

It is therefore an urgent need for organic and materials chemist to further develop a new class of new visible light active, heterogeneous and stable photocatalyst, combined with a promising water-compatibility.

The main target of this thesis is set on the molecular design strategy and hydrophilicity control of the polymer-based photocatalytic systems. For this purpose, two different methods have proved to be successful by modification and functionalization of highly cross-linked conjugated polymers as the active materials. (1) Hydrophilicity control via simple protonation on pristine conjugated microporous polymers, and (2) construction of highly porous conjugated polyelectrolytes.

The material properties of the designed polymers such as porosity, morphology and electronic band structures, and their influence on the photocatalytic activity were investigated. A series of photocatalytic reactions in aqueous medium were conducted to demonstrate the feasibility of the design strategy.

Furthermore, the underlying photoredox processes as the driving force in photocatalytic reaction mechanisms were investigated in detail for reactions in aqueous and organic medium.

2. Aim of the Work

The main objective of this work was to develop highly porous and heterogeneous photocatalysts based on conjugated donor-acceptor-containing polymers for aqueous and non-aqueous applications. Different molecular design strategies for water-compatible polymers (Figure 2.1) as well as the development of reaction strategies for photoredox mediated reactions have been pursued. 1.) The formation of water-compatible conjugated microporous polymers (CMPs) via a post-protonation strategy of hydrophobic azulene-based polymer networks.

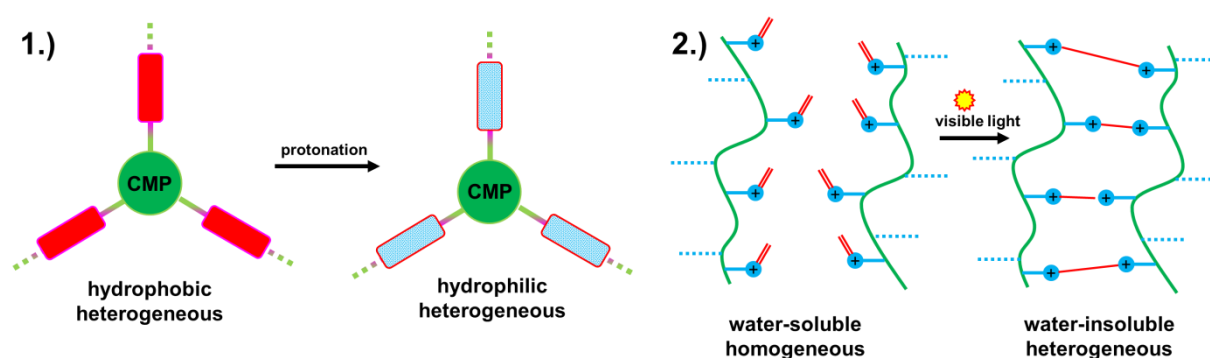


Figure 2.1: Project drafts in this work.

2.) The introduction of hydrophilic 1-vinyl-imidazolium side groups into the photoactive and conjugated polymer backbone, leading to the formation of amphiphilic conjugated polyelectrolytes (CPE) with cross-linkable sidechains.

This new molecular design strategy offers the formation of a multifunctional polymer with interesting properties such as an amphiphilic nature and therefore the surfactant-like ability, combined with its high photocatalytic activity under visible light.

In order to demonstrate the photocatalytic performance, different photocatalytic reactions such as degradation of organic dyes, reduction of chromium (VI) to chromium (III), and free radical polymerization of methyl methacrylate (MMA) have been conducted under visible light irradiation as model reactions.

3.) The utilization of photoredox processes as the driving force for the Stille-type C-C coupling reaction of a series of aromatic halides with aromatic stannanes. The visible light mediated photocatalytic reaction mechanism comprises other reaction steps than in the traditional transition metal mediated Stille coupling reaction.

Beside the structural design, important parameters such as surface morphology of the porous conjugated polymers has also been studied with various analytical methods, in order to enhance the catalytic performance of the materials. Moreover, to understand the new photocatalytic reaction mechanism, photophysical and electrochemical methods have been also applied.

3. Theoretical Background

3.1 Catalysis

Since the beginning of the 19th century, the systematic exploration of new catalysts for industrial production started to be an ongoing process. Today, catalysis is the driving power in industrial productions and almost 85 to 90% of all processes are based on catalytic procedures.^[24]

The term catalysis was introduced for the first time in 1836 by the Swedish chemist J.J. Berzelius. It means to untie or loosen up (derived from Greek). A more modern and practical definition is that, catalysts are involved in reactions, but they are not consumed.^[24] Catalysis offers an alternative reaction path, which is energetically favored compared to non-catalyzed pathways. The activation barrier is much lower than for conventional non catalyzed reactions. Catalysis speeds up reactions via changing the kinetics of a reaction, but it has no effect on the thermodynamic equilibrium position of the reaction.^[24-25]

Figure 3.1 shows, from the kinetic perspective, the distinct difference between homogeneous and heterogeneous reaction. The required activation energy E_{hom} for a certain homogeneous reaction is much higher than E_{het} for a heterogeneous reaction. The reduced energy barrier for heterogeneous reactions is derived from adsorbed molecules at the surfaces and the interaction between those molecules and surface atoms. Additionally, the selective adsorption strength of molecules has to be considered in terms of reaction rates. However, prior to reaction the energy barrier for adsorption has to be provided as well as the energy for overcoming the desorption after product formation. Nevertheless, the potential energy for the reaction partners and products remains unchanged if either it is homogeneous or heterogeneous reaction.^[26] Many reactions are known for their harsh reaction conditions. Without catalysis, the technical feasibility of these reactions is impossible.

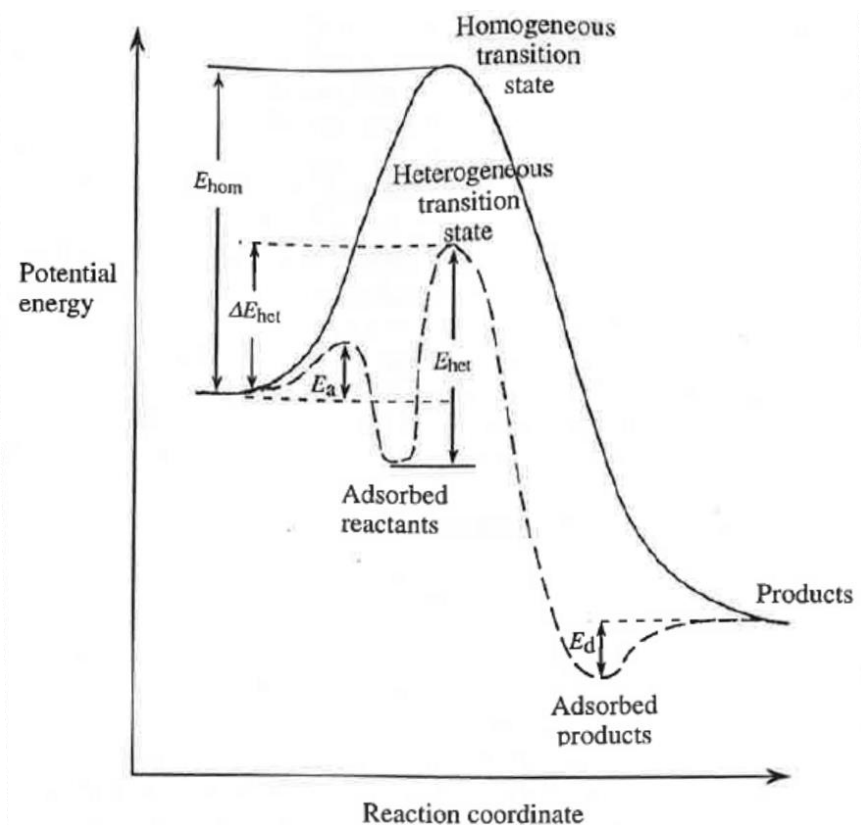


Figure 3.1: Potential energy diagram of homogeneous and heterogeneous reactions (p. 125, *Surface Chemistry*, E. M. McCash, By Permission of Oxford University Press).^[26]

3.1.1 Photocatalysis

The development of photocatalysis emerged for the first time at the beginning of the 20th century.^[27] In recent years, homogeneous and heterogeneous photocatalysts have been applied to a large number of chemical transformations. In comparison to conventional catalysts driven by heat, photocatalytic processes are activated by light.

The sun light emission (1353 W/m^2) provides much more energy than the total energy consumed and needed by mankind.^[28] Considering the energy perspective, the distribution of sun light can be divided in about 3% in high energetic UV range, 44 % in visible light range, and 53% in low energetic infrared irradiation (Figure 3.2).^[11] Compared to the highly energetic UV light, which often leads to bond fission of molecules, the visible light range shows a lot of advantages such as broad irradiation area and sufficient energetic level for photocatalytic reactions. It is worth to note that in the nature photosynthesis process, the plants mainly absorb light in the visible range.

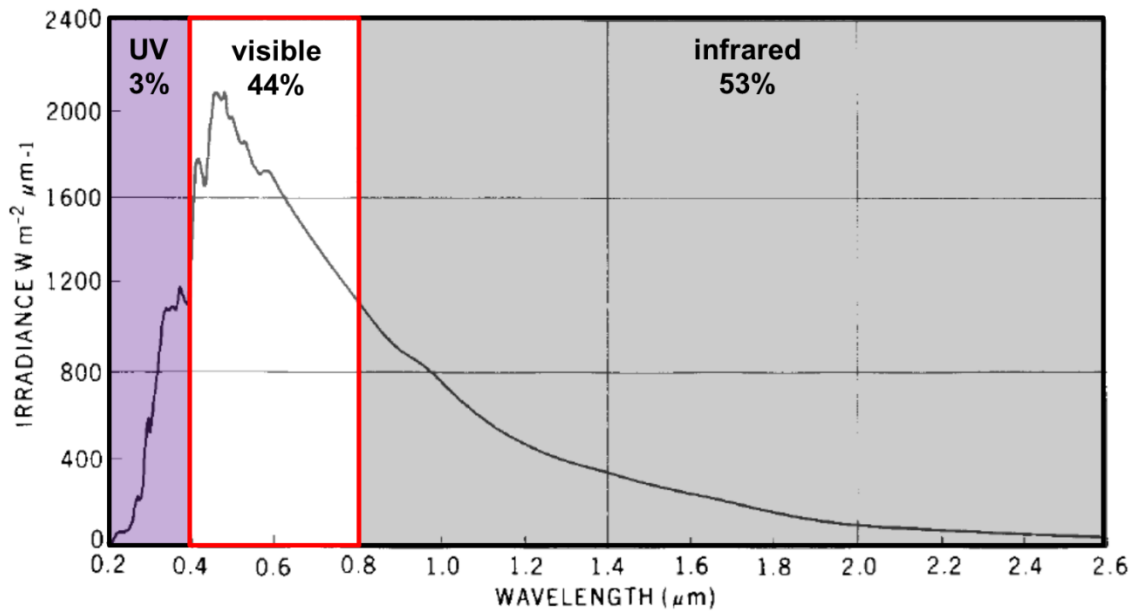


Figure 3.2: Solar spectral irradiance and wavelength distribution.^[28]

In the photocatalytic process, the absorption of light leads to the excitation of an electron from the ground state to an energetic higher state of the photocatalyst, which will be left by usually two different pathways: 1.) Interaction with the substrates via electron transfer, which results in chemical reactions; or, 2.) Energy transfer processes directly from the photocatalyst into its environment such as radiative recombination of the excited state (luminescence) or non-radiative departure (heat and molecular vibrations). The first case involving electron transfer onto the substrate can be called as “quenching process” (Figure 3.3). Depending on the electron transfer direction, either from the photocatalyst to the substrate, or the opposite direction, the quenching process can be described as oxidative or reductive quenching.

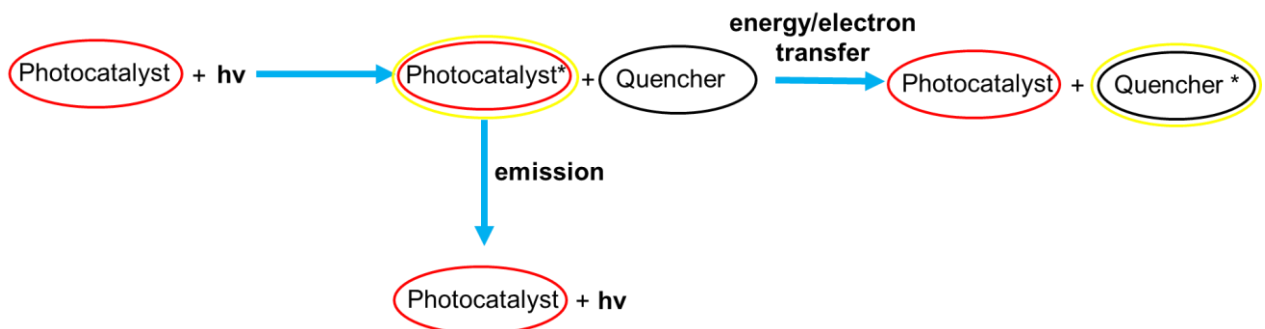


Figure 3.3: The possible reactions of excited photocatalyst.

The equation below describes the Gibbs energy of the photoinduced electron transfer between an electron-donor and acceptor.^[29]

$$\Delta_{\text{ET}}G = (E_{\text{ox}}^{\circ} - E_{\text{red}}^{\circ}) - E_{0,0} - \Delta E_{\text{coulombic}}$$

Here, E_{ox}° refers to the standard electrode potential at which the oxidation occurs, E_{red}° to the standard electrode potential at which the reduction occurs, $E_{0,0}$ is the excitation energy for the S_0 - S_1 transition. Negative Gibbs values indicate a favored photoinduced electron transfer from a donor to an acceptor.

Figure 3.4 shows a popular transition metal organic complex ruthenium polypyridine, which has been widely used for photocatalytic redox reactions under light irradiation. By absorbing one photon, one electron from the metal center is delocalized on the pyridine ligand. This process is known as metal-to-ligand charge-transfer (MLCT) process. On this basis, the location of excess electrons on the ligand leads to the formation of both oxidation or reduction centers in the metal complex molecule. The modification of redox levels and redox strength can be adjusted via metal center or ligand variations.

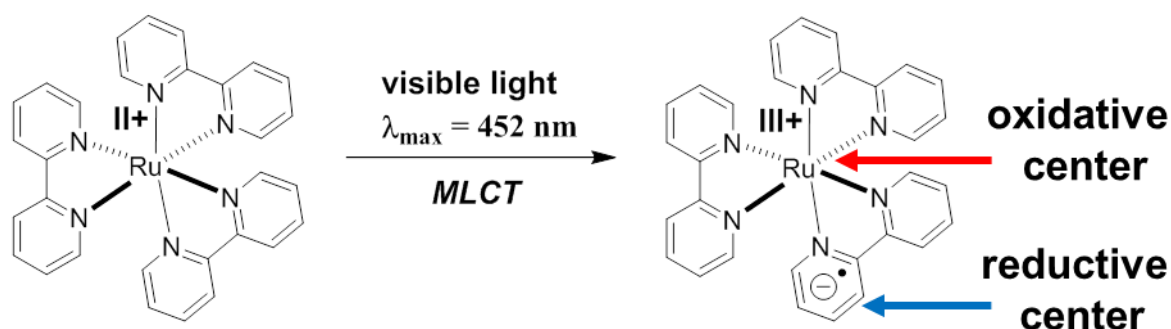


Figure 3.4: $Ru(bpy)_3Cl_2$ metal complex upon visible-light irradiation.^[30]

Figure 3.5 shows a simplified overview of involved photooxidation and reduction steps employing $Ru(bpy)_3Cl_2$ in photocatalysis. In general, the feasibility of a reaction step depends on both the redox levels of the metal complex and the reaction partner. According to the equation for the Gibbs energy of a photoinduced electron transfer, the evaluation of the probability for the single reaction steps is possible.

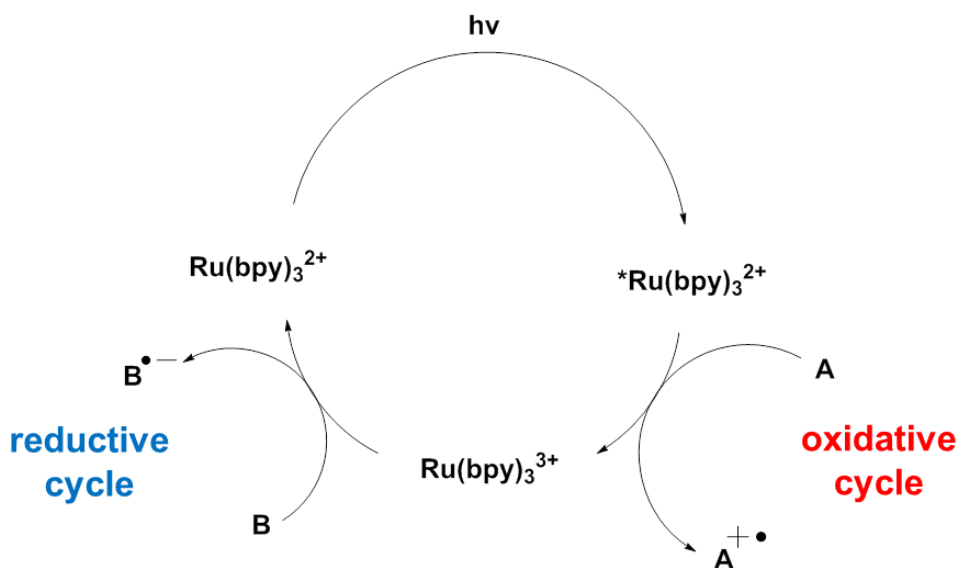


Figure 3.5: Photoredox cycles of $Ru(bpy)_3Cl_2$ complex.

A different reaction mechanism is presented by using semiconductors as photocatalysts. The electronic properties of semiconductors are determined by the underlying band structure. Basically with increasing number of atoms their energetic coupling and interaction increases and leads to the formation of band structures. Bonding (highest occupied molecular orbitals, HOMO) and antibonding (lowest unoccupied molecular orbital, LUMO) atomic energy levels overlap and merge to continuous bands where electrons are shared between atoms, as shown in Figure 3.6.

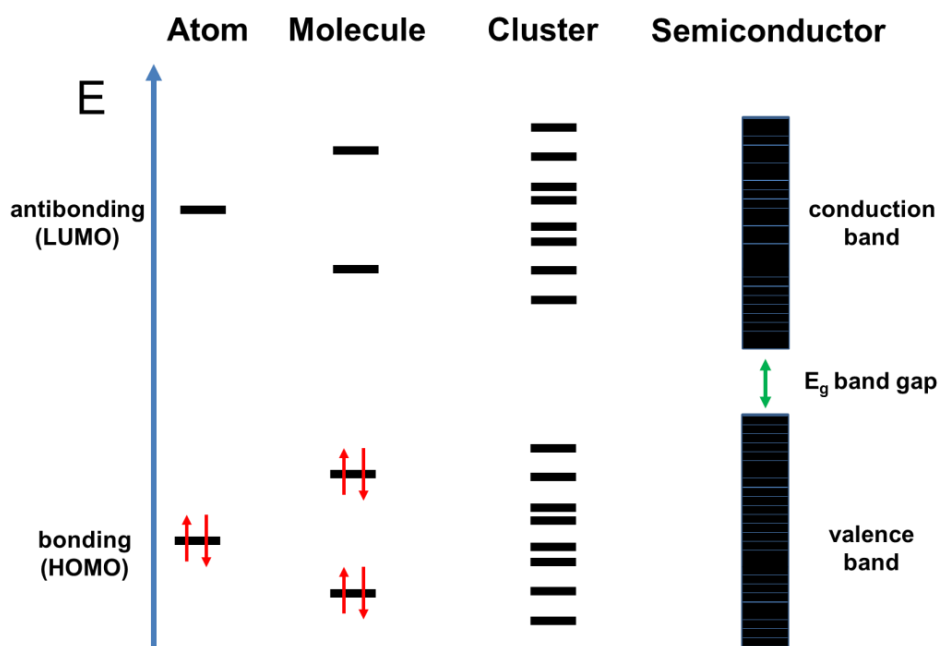


Figure 3.6: The band formation of N molecular orbitals via merging different energetic levels.

In conjugated polymers, the band structure formation occurs by overlapping of π -orbitals and delocalization of electrons. This effect correlates with the conjugation chain length, increasing chain length leading to band growth and gap narrowing, whereas the band position is influenced by combining various electron withdrawing (acceptor) or electron pushing (donor) groups (-/+inductive, -/+mesomerism effects) attached to the conjugated system. Therefore electronic properties of conjugated polymers are mainly affected by the choice of an appropriate donor-acceptor systems, as displayed in Figure 3.7.

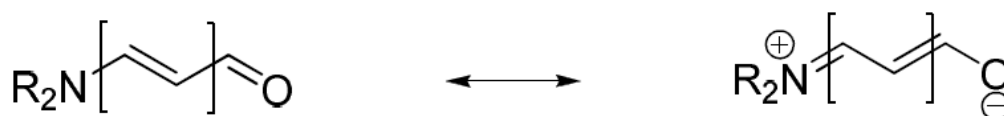


Figure 3.7: Electron resonance structure of a conjugated polymer bearing donor-acceptor groups.

Photophysical properties such as absorption wavelength are directly coupled with the band gap energy, as well as the strength of the oxidation center and reduction center mentioned earlier.

As displayed in Figure 3.8, the mechanism using semiconductor as photocatalyst is described. The absorption of light leads to the separation of an electron located on the conduction band, and a hole on valence band. Both species are highly active. Indeed, they are the driving force for photocatalytic reactions. In general, the valence band acts in photooxidations of substrates as the oxidation center. The conduction band acts in photoreductions of substrates as the reduction center. Both type of reactions are coupled in photoredox cycles, mostly one substrate is utilized as sacrificial agent in order to complete a cycle.^[31]

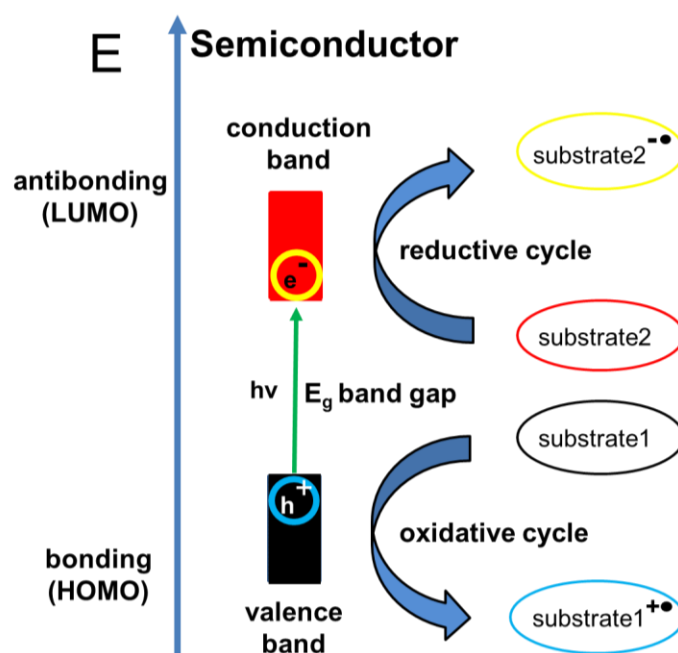


Figure 3.8: Mechanistic overview of semiconductive photoredox reaction steps.

3.1.2 Design strategies for enhanced photoredox processes via energy band position alignment of conjugated organic semiconductors

The reaction design of feasible photocatalytic transformation depends largely on the understanding and adjustment of photoredox processes. Basically, the oxidation and reduction potentials of the photocatalyst are fundamental parameters which determine the successful activation and therefore consecutive reaction steps of certain substrate molecules. As depicted in Figure 3.9, photooxidation of substrate is achieved only if the oxidation potential of photocatalyst is more positive. On the other hand, photoreduction of substrate is achieved if the reduction potential of photocatalyst is more negative.^[31]

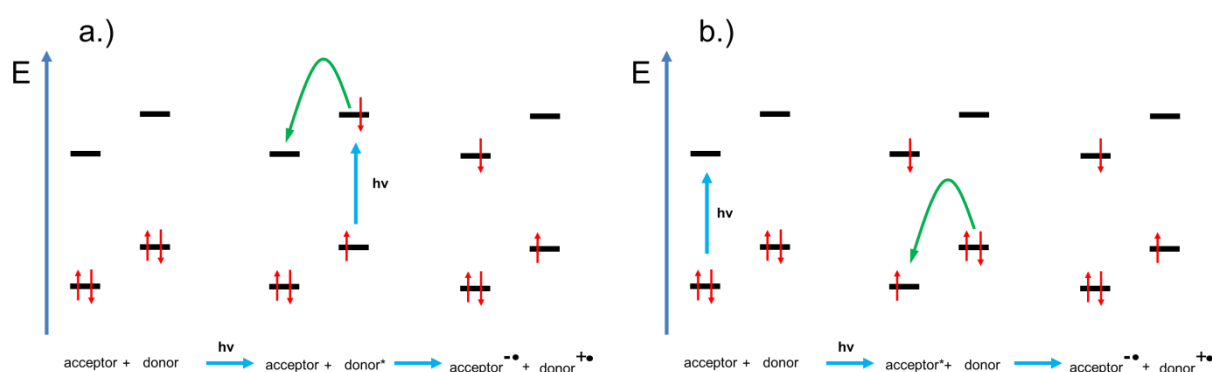


Figure 3.9: Photoinduced electron transfer (PET) from excited donor to acceptor (a – photoreductive-) and from excited acceptor to donor (b –photooxidative-).

From the perspective of conjugated organic photocatalyst the tuning of donor-acceptor properties is directly coupled to the photoredox parameters and position of HOMO/LUMO levels. The introduction of chromophores with either electron withdrawing or releasing groups (positive or negative inductive/mesomeric effects) into the conjugated system is the main tool to control the photoredox properties and reaction patterns of the photocatalyst. Figure 3.10 lists typical donor-acceptor chromophores in conjugated polymers.^[21]

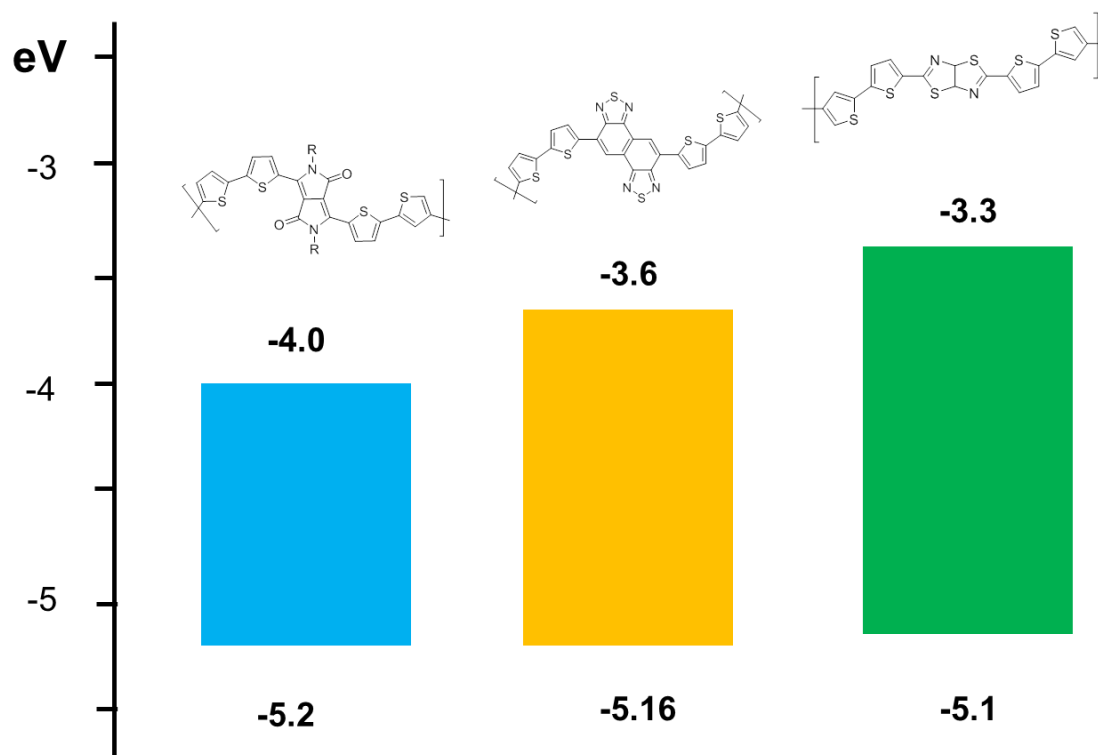


Figure 3.10: The incorporation of different acceptor monomers in conjugated polymers and the changes on oxidation potentials.

In order to modify the chemical selectivity of photocatalytic dehalogenation of multiple halogenated aromatic compounds, the photoreduction potential of 10-phenylphenothiazine (PHT) was shifted from -2.1 to -1.5 V via incorporation of electron withdrawing groups (Figure 3.11). According to the lower photoreduction potential a more selective dehalogenation was achieved.^[32]

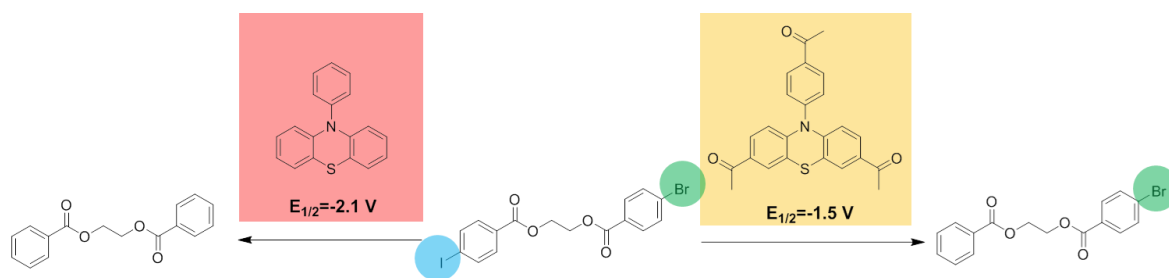


Figure 3.11: Structure modification of reduction potentials of PHT and changes on selective dehalogenation.

As mentioned above, redox potentials of substrate molecules must fit the redox potentials of photocatalyst in order to form active intermediates. In general electron withdrawing or releasing groups lead to structural stabilization of charged active intermediates which highly

determines successful product formation. Figure 3.12 shows the reaction of an electron poor A with an electron rich B reactant to the coupling product C. Both reactants are capable of stabilizing the charged intermediate state via structural configuration. Here, the radical anion intermediate A is stabilized by an electron withdrawal group (EWG), the radical cation intermediate B is stabilized by an electron donating groups. ^[33]

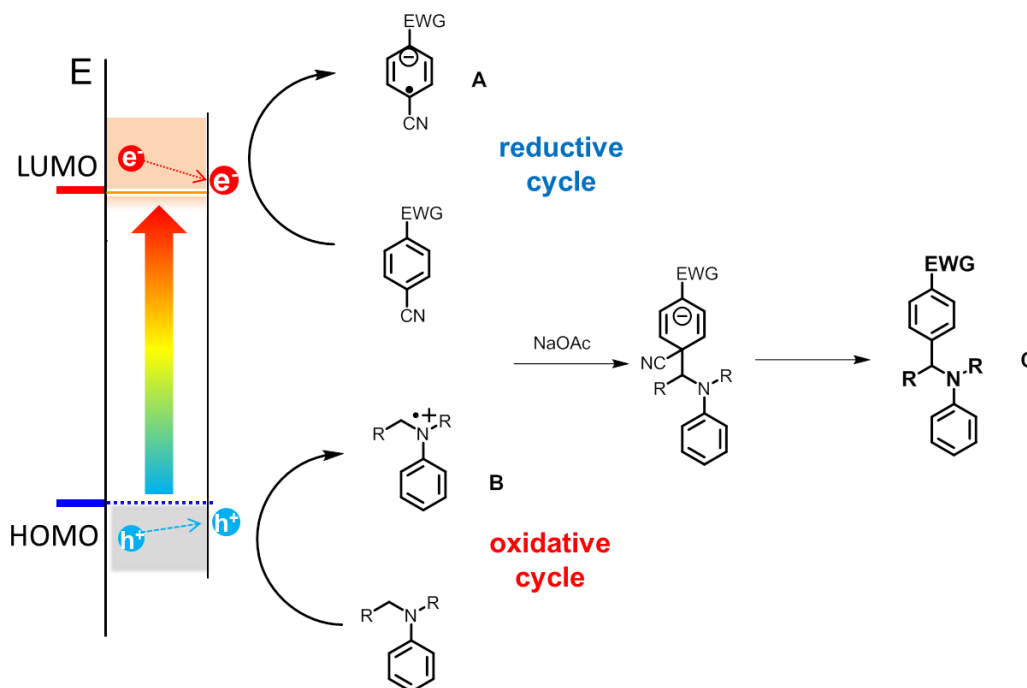


Figure 3.12: *Stabilizing ability of substrate molecules in photoredox processes.*

Moreover, resonance structures as present in quinoid or conjugated structures are capable of driving the reactions towards certain product structures. The effects of molecular orbitals on transition states play an important role in stabilization of reaction pathways. As shown in Figure 3.13, the dehalogenation of 1,2-dibromo-1,2-diphenylethane leading to fully conjugated molecule stilbene. The reduction is favored and leads to the formation of the extended conjugated chain length. ^[34]

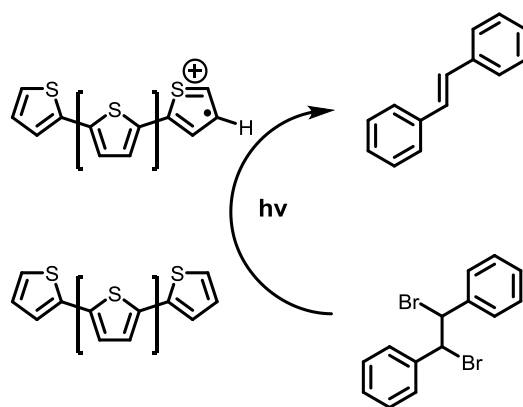


Figure 3.13: Photoreductive dehalogenation of 1,2-dibromo-1,2-diphenylethane.

These examples reveal that photoredox processes depend on structure modifications. It is known that electron donating or accepting orbitals stabilize transition states. Therefore, orbital interaction plays crucial role in the reactivity of substrate molecules. Figure 3.14 shows the stabilizing effect of electron donor alkoxy groups adjacent to photooxidized center.^[35]

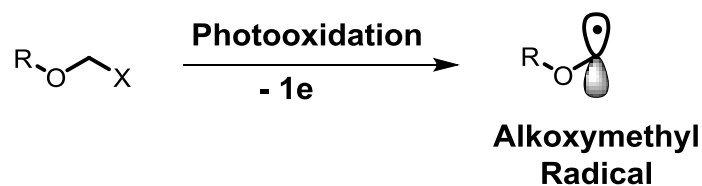


Figure 3.14: Alkoxy acting as electron donor and stabilizers for electron deficient transition processes.

Apart of the structural properties, general strategies such as side product trapping, or using sacrificial agents are decisive for high yields and successful outcome. According to the type of intermediate which have been formed, the solvent polarity can either enhance or quench reaction processes.^[36]

3.2 Classification of porous materials

The classification of porous materials can be undertaken by describing the structural properties which cause continuous pore formation in the material. Basically, two different types of structures are distinguished. Textured porous materials describe randomly distributed and packed particles leading to remaining cavities with low mechanical stability. Structured porous materials describe the porosity of highly ordered crystalline structures such as zeolites or disordered amorphous structures such as interconnected polymer gels. This work deals primarily with structured porous materials. According to the International Union of Pure and Applied Chemistry (IUPAC), structured porous materials are classified in three categories as described in Table 3.1: (1) microporous materials with a pore diameter smaller than 2 nm, (2) mesoporous with a pore diameter between 2 and 50 nm, and (3) macroporous materials with a pore diameter larger than 50 nm.^[37]

Table 3.1: *Classification of porous materials according to IUPAC.*

	Microporous	Mesoporous	Macroporous
Pore diameter	< 2 nm	2 – 50 nm	> 50 nm
Crystalline examples	Zeolite, MOF, COF, activated charcoal	Templated materials, Carbon materials, ceramics	Templated materials, Colloidal structured monolith
Amorphous examples	CMP, HCP	Aerogel, Xerogel	Foam, polyHIPE, gel, cross-linked polyelectrolytes

The pore size is substantial for various applications and determines the surface area as well as the adsorption capacity. Small pore sizes limit the mass transport and allow only certain molecules with defined shapes and sizes to pass the pores. On the contrary, the efficient catalytic processes depend on unrestricted mass transport processes in the pores. Microporous materials are known for high surface areas and mostly contribute to high adsorption capacities. Well known examples of microporous materials such as activated charcoal, zeolites, or recently intensely studied metal organic frameworks (MOFs) showed extremely high surface areas up to 7140 m²/g.^[38] Especially, microporous materials with narrow pore size distribution are also used for the shape selective pores and molecular sieve applications. Mesoporous materials have the advantage for hosting guest molecules within the cavities. This special property leads to enhanced mass transfer on microscopic scales. The large pore size of macroporous materials contributes also to better mass transport of macromolecular materials.

In this view, considering chemical reactions at the surface of porous catalytic materials, the performance of heterogeneous catalysis depends on efficient diffusion and adsorption processes. Therefore, high surface areas and open pore structures contribute to high reaction rates.^[39]

3.3 Synthesis of conjugated microporous polymers (CMPs)

In general, conjugated microporous polymers (CMPs) are synthesized via the connection of a bifunctional (bridge) to a multifunctional monomeric unit (cross-linker), as displayed in Figure 3.15. The main feature of CMPs is that they combine permanent microporosity and fully conjugated polymer backbones. In this sense, CMPs merge all advantages of linear conjugated polymers combined with high mechanical and chemical stability.

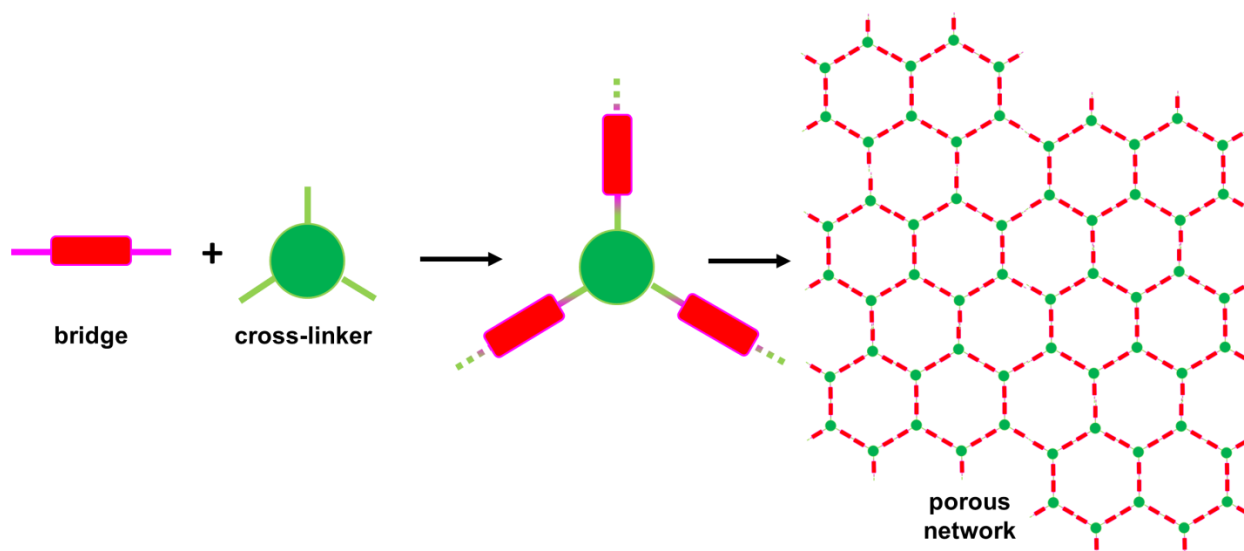


Figure 3.15: Simplified cross-linking procedure between bridging unit and trifunctional cross-linker.

The first examples of CMPs were reported in 2007 by Cooper et al. via the Sonogashira–Hagihara cross-coupling of 1,3,5-triethynylbenzene type cross-linkers with 1,4-iodobenzene type monomers, shown in Figure 3.16.^[15]

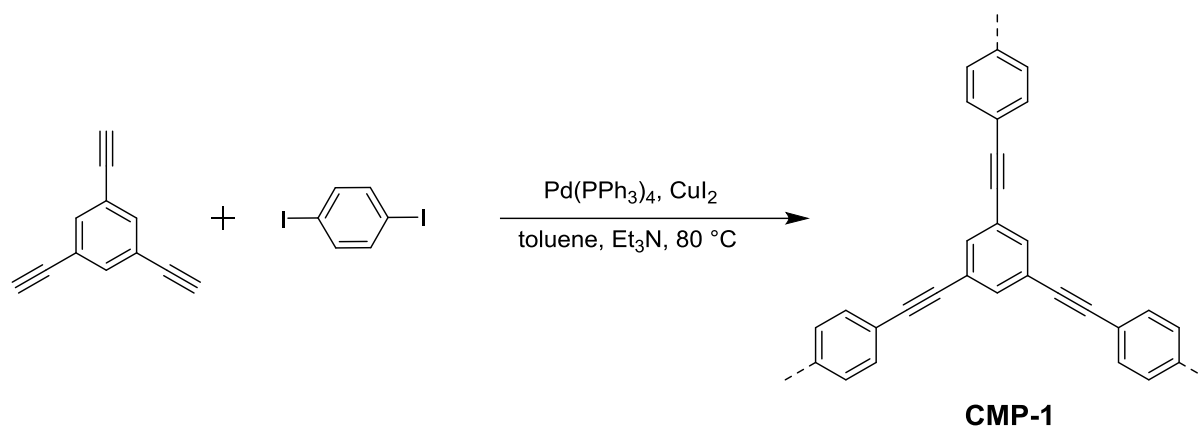


Figure 3.16: The first reported CMP synthesized via Sonogashira–Hagihara cross-coupling reaction.^[15]

In the following years a vast number of cross-linking reactions for the synthesis of CMPs were reported, for example via the metal-catalyzed Suzuki coupling^[40], Heck coupling^[41], Yamamoto coupling^[42], Buchwald-Hartwig coupling^[43], and alkyne-alkyne homocoupling^[42] etc.. Other approaches such as “azide-alkyne-click” chemistry^[42], Knoevenagel condensation^[44], FeCl₃ oxidation^[45] and electrochemical polymerization^[46] have been also conducted.

In general the cross-linking reaction step is governed by kinetic processes. Taking the example above, Sonogashira–Hagihara cross-coupling leads to random cross-linking of trifunctional cross-linkers with bifunctional bridge units by continuous non-reversible bonding steps which overweighs the thermodynamic driving forces leading usually to structure formation. The kinetic forces drive the reaction towards amorphous structures by random structure organization.^[15, 47] A similar modular structuring known from highly crystalline metal organic frameworks (MOFs) cannot easily be adapted to CMPs and high crystallinity usually cannot be achieved inside the CMPs.^[15]

It was shown that different lengths of the bifunctional bridging agents could affect the pore size as well as surface area of the CMPs. For instance, an increasing length of bridging units led to higher pore sizes but lower surface areas.^[47] Additionally, it was found that the functionality of the cross-linker such as fourfold functional tetrahedral monomer could enhance the surface area by decreasing pore size. A similar effect was observed while employing the trifunctional cross-linker in stoichiometric excess.^[47-48] Moreover, it was shown that the choice of solvent is crucial for the polymerization reaction rate and improves the porosity towards higher surface areas in the following order: DMF > dioxan > THF > toluene.^[49]

The main feature of CMPs is the combination of the photophysical properties of a semiconductive conjugated polymer backbone and a highly stable microporous solid structure. It was shown that the Suzuki-Miyaura polycondensation of bifunctional benzene and tetrafunctional pyrene monomers allow the emission wavelength adjustment of CMPs

from blue to red via simple stoichiometric variations of comonomers. Furthermore, by using this method it was possible to control the optical band gap in the range 1.94 to 2.95 eV.^[50] A similar approach was developed by the introduction of small amount of acceptor-type comonomer as dopants into a polyphenylene network. This method allows to fine tune the optical band gap and emission wavelength.^[51] Another structural design strategy is the core-shell synthesis of CMPs. Here, the electrical properties of the core are different from the shell, the results are similar to those of donor-acceptor variations of linear conjugated polymers. The core unit is extended via a second cross-linking step in order to build up the shell unit. The successful continuous conjugated architecture of these core-shell CMPs allows one to adjust the emission of the CMPs in the full visible-range.^[52]

3.4 Applications of Conjugated Microporous Polymers (CMPs)

3.4.1 Gas adsorption, storage, separation

Owing to the high surface area of conjugated microporous polymers, gas adsorption and gas storage are among the first known applications of these materials. Especially, hydrogen storage is challenging due to its low boiling point (20 K). A low density ($0.08988 \text{ kg m}^{-3}$) and very high pressures around 450 bar are required in order to achieve high storage capacities.^[53] Therefore, chemical storage strategies in solids are attractive ways to reduce costly procedures. A non-functionalized CMP with a surface area about $842 \text{ m}^2/\text{g}$ show reversible H_2 adsorption around 131 ml/g (at 77K and 1.13 bar).^[54] Moreover, it was found that the adsorption of H_2 is more sensitive to the monomer structure than to the pore size in CMPs.^[55] Additionally, it was shown that doping with metal-ions enhances the gas storage selectivity and capacity of CMPs to 6.1 wt% (US Department of Energy aims 5.5 wt% for 2017 for mobile fuel devices).^[56] However, selective gas adsorption and storage abilities of conjugated microporous polymers have been employed to separate gas mixtures. The selective gas uptake of CO_2 in CO_2/CH_4 and CO_2/N_2 at room temperature were successfully demonstrated.^[57] Among other porous systems such as MOF, activated carbon, porous organic polymers, and microporous polycarbazole has a one of the highest CO_2 uptake values about 21.2 wt% (1.0 bar and 273 K) as required for successful gas separation application.^[58]

3.4.2 Heterogeneous Catalysis

According to the application needed, various functionalities can be integrated into the stable network scaffolds. The first known example of a heterogeneously catalyzed Knoevenagel condensation via the application of conjugated porous polymers is dated back to 2008. The cross-linked poly(benzimidazole) acted as a heterogeneous base for the reaction between various aldehydes and malonic derivatives. The reactions were conducted at room or elevated

temperatures with quantitative yields. The catalyst was reused for several reactions prior to the recovery of basicity.^[59] Conjugated porous polymers based on permanent functionalization with incorporated iridium complex units proved to be a successful design for the heterogeneous catalysis of the reductive amination between various ketones and amines. The reaction was conducted with high yields (>90%).^[60] The incorporation of metalloporphyrin into conjugated porous polymers led to a highly selective heterogeneous catalyst for the ambient oxidation of sulfides to sulfoxides in quantitative yields.^[61]

3.4.3 Heterogeneous Photocatalysis

Conjugated microporous polymers (CMPs) combine photoactive conjugated polymers backbone with 3-dimensional geometry. Owing to the high stability and the large surface areas, CMPs have been successfully introduced as reusable heterogeneous photocatalysts, enabling sustainable applications under light irradiation of the range of visible light. The first known photocatalytic reaction with a conjugated porous polymer was the photosensitized oxygen addition to alpha-terpinene. The reaction was conducted in a continuous flow fashion with almost quantitative yields.^[62] The incorporation of Rose Bengal into CMP scaffolds led to quantitative yields in the aza-Henry reactions. The reaction was repeated ten times while the conversion dropped to less than 10%.^[63] Later, it was shown that by incorporating Ru(bpy)₃ chromophores into the CMP backbone, the life time of the Ru-based catalysts strongly depended on the CMP backbone scaffold variations. It was found that the lifetime increases with widely spaced chromophores due to low interactions of the adjacent chromophores.^[64] Based on an iron(III)porphyrin CMP, the selective visible light mediated dye degradation of Congo Red was achieved within 120 s.^[65] Moreover, the photocatalytic hydrogen evolution from aqueous solution have been achieved via visible light irradiation of conjugated porous polymers in several examples.^[50, 66] The manifold photocatalytic applications of CMPs was shown by carbazole based conjugated porous polymers. The carbazole CMPs were applied with a 14 W fluorescent light bulb to the quantitative reductive dehalogenation of phenacyl bromide, the oxidative hydroxylation of arylboronic acids with yields ranging from 65 – 94%, and the α -alkylation of aldehydes with yields ranging from 68 to 92%.^[67] Other photocatalytic reactions using conjugated porous polymers are the photocatalytic oxidative conversion of amines into imines^[68], photoinitiated free radical and cationic polymerizations of vinyl monomers^[69], the photocatalytic degradation of dyes^[70], and the photocatalytic oxidation of thioanisole to methylphenyl sulfoxide^[71].

3.4.4 Pollutant absorption and removal

Hydrophobic conjugated porous polymers could act as efficient absorbers and are promising candidates for the removal of organic pollutants and heavy metals. The open pore structures with hydrophobic surfaces enable selective absorption of toxic organic pollutants from aqueous solutions. For instance, only 7 mg (1 cm³) of porous sponge were capable of

removing 3300 wt% of nitrobenzene.^[72] Perfluoro-conjugated microporous polymers showed the highest absorption capability of porous materials for organic dyes, here Congo Red (1376.7 mg/g) and Methylene Blue (629.1 mg/g) have been completely absorbed within 3 h. The same CMP was applied to an aqueous solution with Pb(II) and As(V) cations. The capture capacity for these metal ions was 826.1 mg/g Pb(II) and 303.2 mg/g As(V). Moreover, the absorption of organic oils (~3000 wt%) and solvents (~2000 wt%) by this CMP surpassed the absorption capabilities of an active carbon up to 4 times. Interestingly, the simultaneous removal of dyes, metal-ions, and solvents/oils from aqueous mixtures was easily achieved with perfluoro-conjugated microporous polymers.^[73]

3.5 Strategies to water-compatible conjugated porous polymers (WCPP)

The majority of conjugated porous polymers are highly hydrophobic due to their fully conjugated polymer backbones. In order to obtain water-compatibility, different strategies were reported previously by our group and other researchers (Figure 3.17).

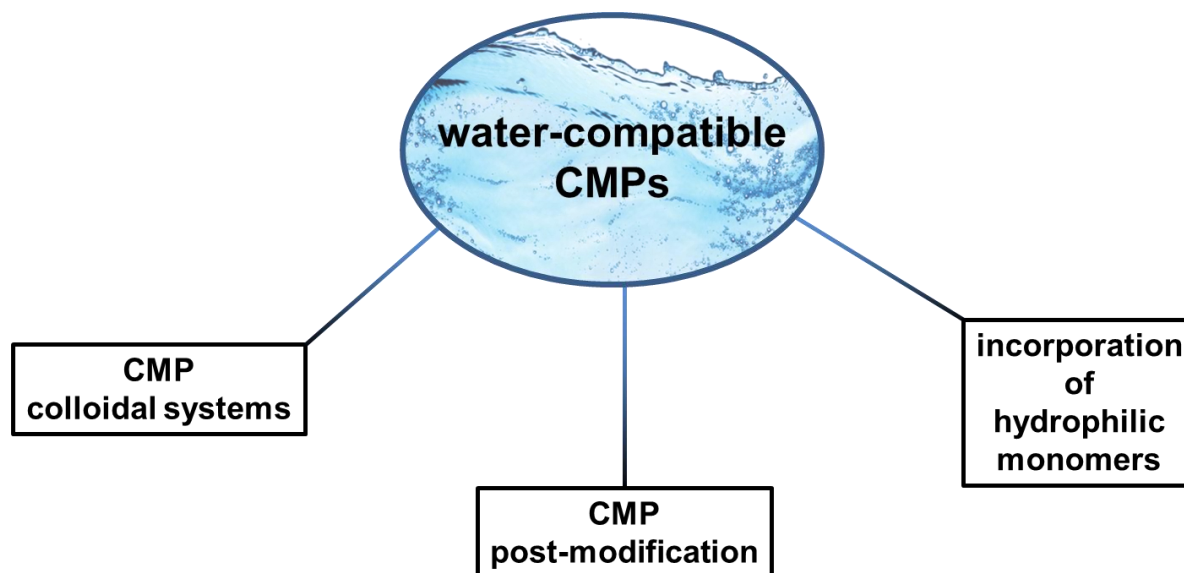


Figure 3.17: Overview for possible strategies to develop water-compatible CMPs.

The formation of nano particulate conjugated porous polymers, led to high water dispersibility, while the electronic properties remain unchanged as that in the bulk material.^[74-75] As shown in Figure 3.18 the highly dispersible conjugated nanoporous polymer colloids (CNPCs) were synthesized via surfactant assisted Sonogashira-Hagihara coupling reaction.

The highly confined reaction environment led to spherical, fully cross-linked, and porous nanoparticles with a narrow size distribution. However, the CNPCs were dispersible in water as well in common organic solvents.

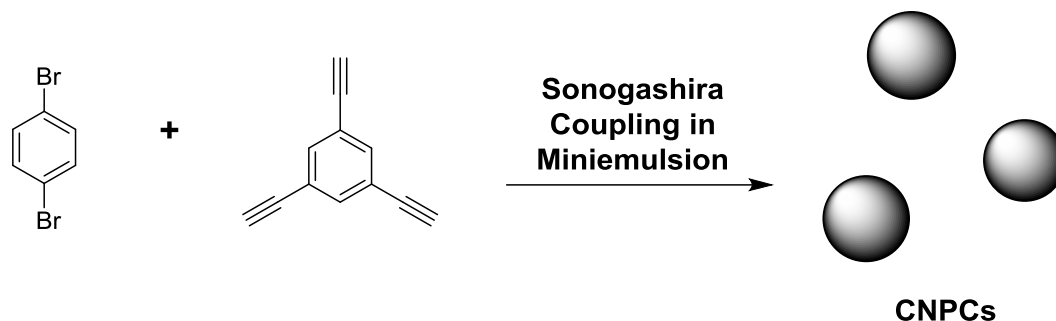


Figure 3.18: Miniemulsion templated synthesis of conjugated nanoporous polymer colloids (CNPCs).

The introduction of monomers with side groups bearing hydrophilic functionalities such as carboxylic acid, hydroxyl, amine, acetate, or alkoxide groups during the polymer synthesis lead to water-compatible CMPs (WCMPs).^[76] The post-modification of conjugated porous polymers via thiol-yne addition reaction lead to water-compatible CMPs. In Figure 3.19 the insoluble conjugated microporous benzothiadiazole polymer was modified by a treatment with 3-mercaptopropionic acid. The water-compatibility was achieved after the incorporation of 0.1 equivalents of 3-mercaptopropionic acid.

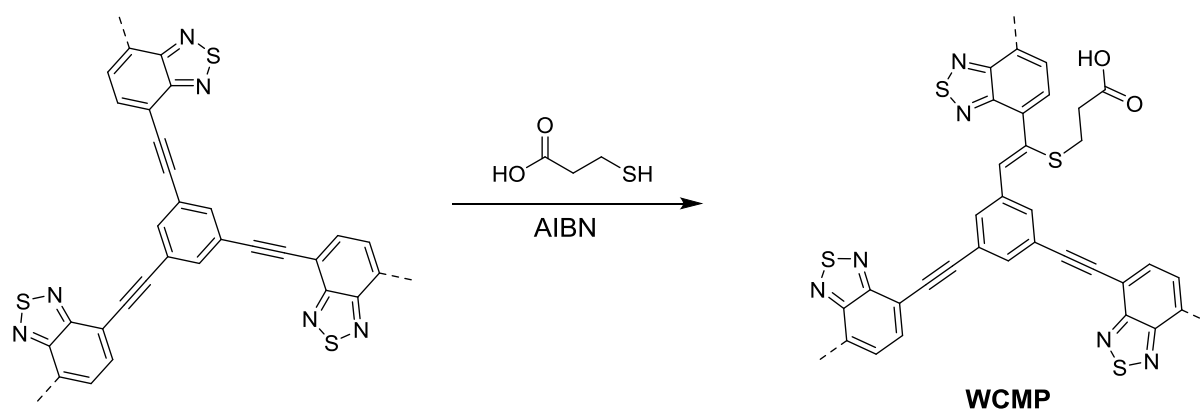


Figure 3.19: Thiol-yne modification of CMPs.

However, the modified WCMPs showed excellent water-compatibility but less stability during photocatalytic application.^[77] In both examples of WCMPs, the presence of hydrophilic groups was a necessary condition for effective applications in aqueous media.

3.6 Conjugated Polyelectrolytes (CPEs)

Conjugated polyelectrolytes (CPEs) consist usually of a conjugated polymer main chain and ionic side groups. In recent years, they have been used in the fields of optoelectronic devices, bioassays, photodynamic therapy, and reactive oxygen generation for cell damage.^[78] The combination of unique properties such as π -delocalized semiconductive backbones and ionic side chains enable applications in an aqueous environment.^[79]

The linear conjugated main chain of the CPEs is usually synthesized by means of a transition metal catalyzed coupling reaction, a Knoevenagel condensation, a Wittig-Horner reaction,^[80] or oxidation polymerizations^[81] of suitable conjugated monomers with at least one monomer bearing periphery functionalities. A subsequent modification enables the introduction of ionic groups onto the hydrophobic polymer main chain.

According to the type of the attached ionic side chain, CPEs are classified in cationic or anionic polyelectrolytes. Typical anionic side groups are sulfonate, carboxylate, and phosphonate. Cationic CPEs are attached with quaternary ammonium, imidazolium, and pyridinium groups. Figure 3.20 shows a few examples of different possible anionic and cationic CPEs.

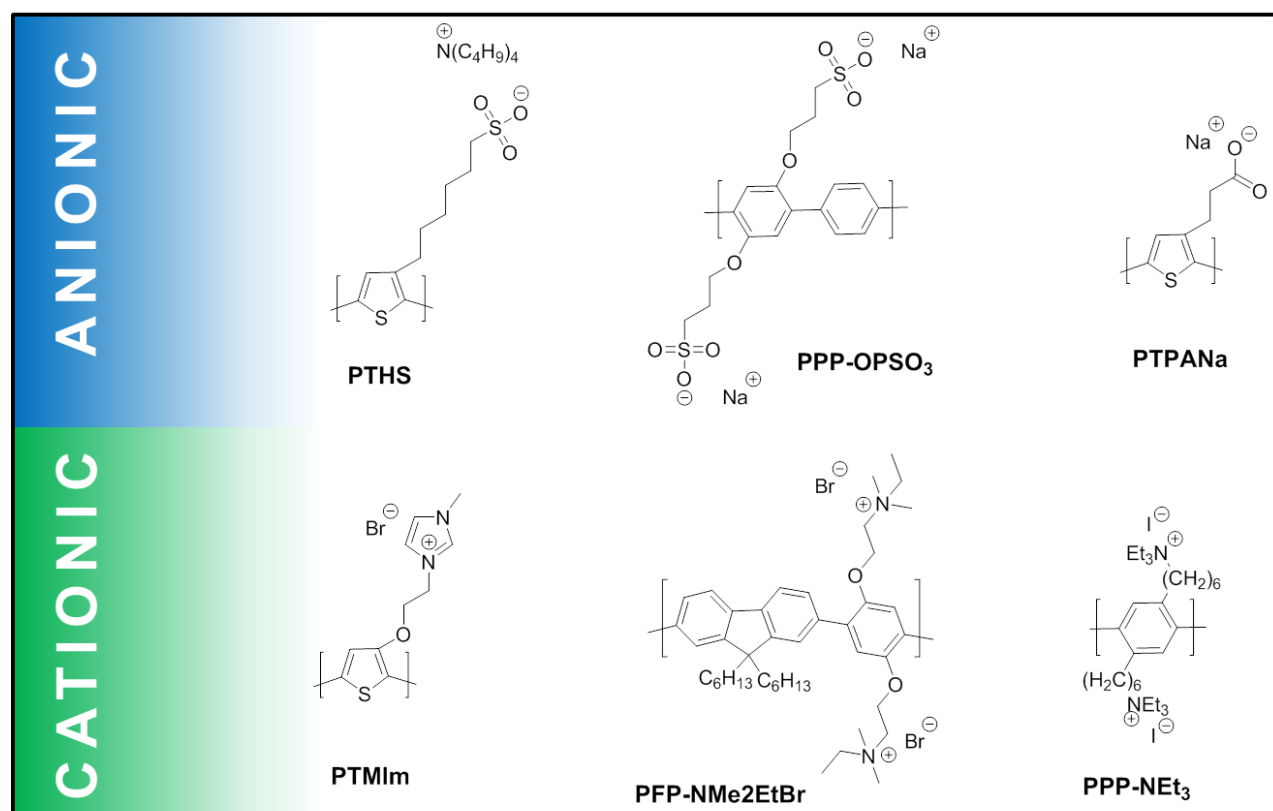


Figure 3.20: Examples of conjugated polyelectrolytes attached with anionic and cationic side groups.^[81-86]

Owing to the hydrophobic backbone with ionic side groups, CPEs are amphiphilic, which lead to distinct self-assembly behaviors as depicted by examples in Figure 3.21.^[87]

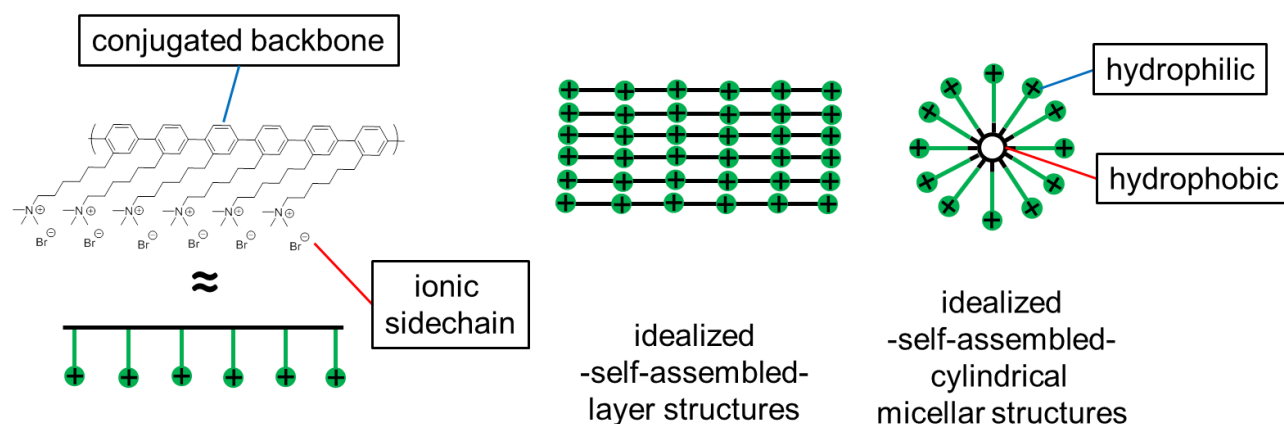


Figure 3.21: Schematic description of self-assembly and possible alignments of cationic conjugated polyelectrolyte.

However, the solvent interaction and self-assembly behavior depends not solely on the ionic side group functionality. In fact, the type of the counter ion also plays a substantial role. It was shown that for anionic PTPANa (Figure 3.20), the size of the counter ions affects the superstructure formation and absorption range in a tremendous way. Small counter ions lead to efficient self-assembly and therefore larger wavelength absorption, while bulky counter ions disrupt the self-assembled structure and the absorption wavelength was shifted about 100 nm towards shorter wavelengths.^[84]

Apart from the self-assembly, the full planarization of conjugated backbones of the CPEs depends indirectly on the solvent polarity and the efficient solvation of side chains. It was shown that photophysical properties such as fluorescence, quantum yield but also process ability of anionic PBS-PFP depends on solvent polarity effects, as displayed in Figure 3.22 for different ratios of dioxane-water mixtures.^[88]

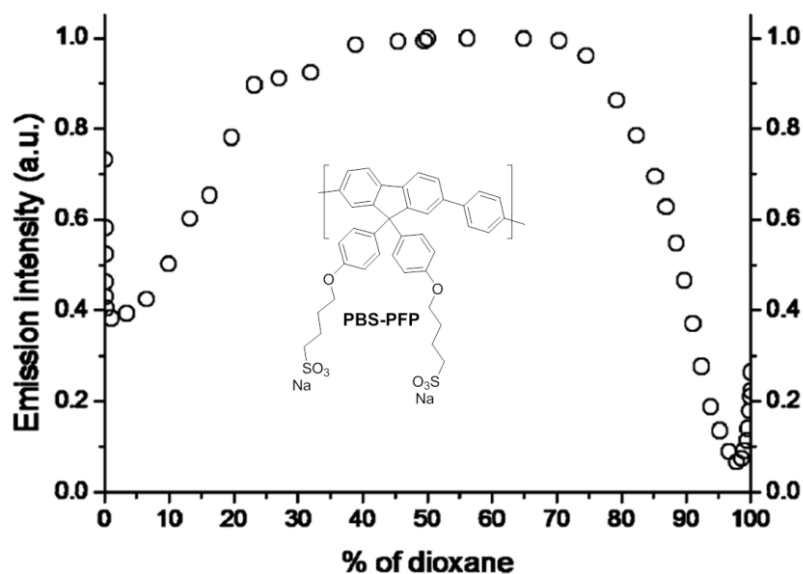


Figure 3.22: Fluorescence intensity as a function of dioxane-water ratio.^[88]

In general, the control of solubility of CPEs in different solvents is achieved via counter ion exchange. It was shown that for cationic CPEs, a complete reversal of the solubility is possible by moving from smaller to bulkier counter anions, as displayed in Figure 3.23.^[89-90]

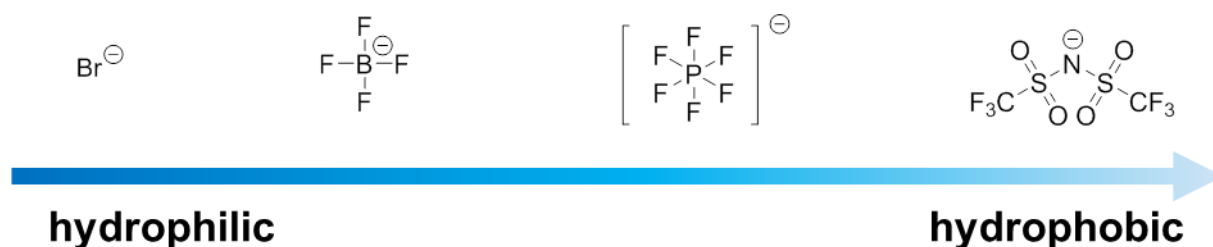


Figure 3.23: Control of hydrophilicity via counter anion exchange of conjugated polyelectrolytes.

3.6.1 Cross-linked conjugated Polyelectrolytes (CPEs)

Since the discovery of synthetic polyelectrolytes within the 1950s, several reports on structure modifications such as methods for cross-linked polyelectrolytes emerged.^[91] However, due to the young field of CPEs, cross-linked conjugated polyelectrolytes have not been investigated so far, in comparison to the non-conjugated cross-linked polyelectrolytes (PEs). Therefore, the objective of this work is to present the first example on cross-linked CPEs for applications in water. Most properties of cross-linked PE primarily correlate with the ionic functionalities and the behavior of network superstructures. In this view, apart from π -conjugated donor-acceptor polymer chains, the structure patterns of cross-linked CPEs are similar.

In Table 3.2 a general overview of non-cross-linked PEs and cross-linked PEs is given.

Table 3.2: *Properties of non-cross-linked PE and cross-linked PE.*

	Polyelectrolyte	Cross-linked Polyelectrolyte
Solubility	soluble	insoluble
Type of Superstructure	Self-assembled structures; micelles, layers	Random covalently interconnected chains (network)
Effects of Ion Exchange	Control of solubility, complexation with oppositely charged molecules	Control of swelling and shrinking, control of dispersibility

In principle, any functional side group capable of a covalent bond formation fulfills the requirements for synthesis of cross-linked PEs. Basically, the cross-linking of soluble PEs leads to phase separation and increased glass transition temperature T_g , while the oxidative, chemical, mechanical, and the overall long-term stability improve.^[92-94]

So far known, different cross-linking protocols for non-conjugated PEs have been reported in the past: cross-linking via benzophenone or other photoinitiators^[95-97], sulfonated cross-linkers^[92], cross-linking via formation of amide bonds^[98], cross-linking via the reaction between amine and acetoacetate groups^[93], cross-linking via nucleophilic substitution between amine and bromide^[94]. Moreover, it was demonstrated that anion exchange led to increased hydrophobicity and reversible pore formation in cross-linked PE gels. After the porous polymer was immersed in organic solvents, the pores closed and the gel could be recovered.^[90, 99] The shrinkage and swelling of colloidal silica crystal templated cross-linked PEs was used in another example for the naked-eye anion detection via photonic crystals.^[100]

In general, the solvent polarity reversibly affects the network structure. The stimuli responsiveness such as shrinking and swelling of cross-linked PEs could be tuned by counter ion exchange. It depends on the balance of electrostatic forces and translational entropy leading to the formation of ion pairs (ionomer regime) and free ion movements (polyelectrolyte regime) as displayed in Figure 3.24. Free ion movements maintain high osmotic pressures and swelling, whereas a lowered osmotic pressure lead to shrinking of pores.^[101-102]

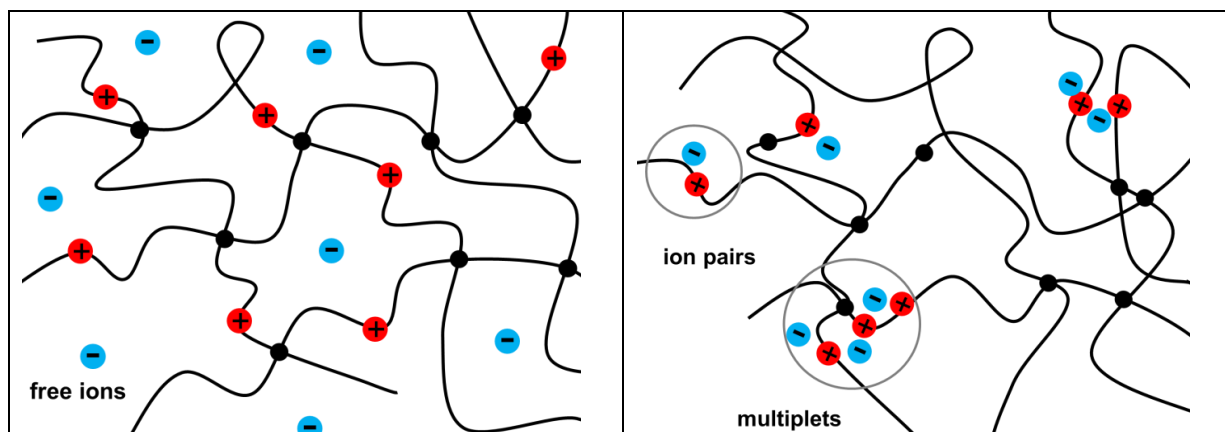


Figure 3.24: *Polyelectrolyte type structure adjustment with free ion movements(left), ionomer type structure adjustment with ion pairs and multiplet formation (right).*^[101]

3.7 Applications of Conjugated Polyelectrolytes (CPEs)

A vast number of biological applications of linear CPEs were reported in recent years. In the following, a few examples are listed.

3.7.1 Cell Imaging

CPEs containing thiophene derivatives were reported as labeling agents for monoclonal antibodies or immunostaining of cells.^[103] Different poly(p-phenyleneethynylene) derivatives (PPEs) with red and green emission colors have been coupled to different antibodies. This procedure did not impair the selectivity and was utilized for cross-selective quantitative cell imaging of B- and T-cells.^[104]

3.7.2 Analysis of Cellular Processes and Fluorescence Assays

The change of emission behavior of CPEs could illustrate their interaction with products of cellular processes. In this view, it is important for the system being able to discriminate and display the different interaction partners. It was shown that the blend of two different cationic CPEs enable rapid and label free detection of pathogens. Based on the fluorescence resonance energy transfer (FRET) principle and different adsorption behaviors to the cell membranes, it was possible to achieve different FRET results and visually discriminate bacteria and fungi.^[105] Moreover, a cationic CPE based on a poly(p-phenylenevinylene) derivative selectively binds to cells. The discrimination of apoptosis cells from normal cells was achieved by exploiting released anionic phosphatidylserine on apoptotic cell membranes.^[106]

The polyfluoren-benzothiadiazole backbone was used as cationic and anionic CPE derivatives for binding oppositely charged substrates such as adenosine triphosphate (anionic) and polyarginine peptide (cationic). The charge interaction caused a fluorescence shift from blue to green. After exposure and cleavage of substrates by enzymes the resulting weak interaction of fragments with the CPE was the main reason for recovering blue emission.^[107]

3.7.3 Cell Damage

It was shown that cationic amine quaternized chitosan CPEs interact with the negative membrane of gram positive and negative bacteria, and fungi. The chitosan CPE act as an anion sponge and inhibited by > 99% the activity by disrupting the membrane structure. Furthermore, the chitosan based systems proved to be *in vitro* and *in vivo* compatible.^[108] Moreover, it was shown that cell surfaces of bacteria and spores which were coated by poly(p-phenyleneethynylene) CPEs lead to cell damage upon visible light irradiation. The light mediated interfacial generation of reactive singlet oxygen destroyed the cell structure.^[109]

3.8 Green Chemistry

There are a few aspects towards the reaction condition optimization, for example the use and further development of catalysts to enhance the reaction efficiency, or the employment of so-called clean and sustainable energy resources such as light instead of heat for a more environmentally friendly reaction condition as the aim of this thesis.

Another important aspect beside the materials design for the before-mentioned purpose lies on the reaction media. Traditionally, mainly organic solvents are used in the chemical processes, which lead to the production of a tremendously huge amount of organic waste in the chemical industries. In Table 3.3, an overview of the annual waste production in the world is given.

Table 3.3: Typical amounts of produced waste/kg product and annual production sums.^[6]

Industry segment	Product tonnage	Waste kg/kg product
Oil refining	10^6 - 10^8	<0.1
Bulk chemicals	10^4 - 10^6	<1-5
Fine chemicals	10^2 - 10^4	5-50
Pharmaceuticals	10 - 10^3	25-100

Therefore, the use of the so-called “green solvents” has been introduced lately in order to eliminate organic waste and avoid toxic and hazardous reagents or solvents from chemical manufactories by means of energy efficient and highly atom efficient procedures.^[6]

Water can be seen as a cleaner and sustainable solvent compared to organic solvent, and fulfills the criteria as being “green”. The advantages of using water as reaction medium in chemical processes are apparently the low costs, high availability, safety, non-volatility, non-toxicity and non-carcinogenicity.

The objective of this thesis is to develop new heterogeneous photocatalysts which offer environment friendly solutions such as: 1.) reduction of energy by exploitation of visible light instead of heat; 2.) reduction of waste by recovery of the photocatalyst and facilitation of work-up processes; 3.) employment of green solvents such as water.

4. Characterization Techniques

4.1.1 UV-Vis spectroscopy (UV-Vis)

UV-Vis spectroscopy allows fast and easy optical analysis of liquid samples in the ultraviolet and visible range. In principle any sample which consists of a chromophoric system such as π -conjugated systems in combination with auxochrome systems such as donor/acceptor functionalities is suited for analysis. The measurement process is conducted by placing a quartz cuvette filled with the diluted sample into the measurement chamber. The absorption of distinct wavelengths by the chromophore is displayed as a function of transmission. The absorption process is based on the excitation of valence electrons (highest occupied molecular orbital, HOMO) to higher energy level (lowest unoccupied molecular orbital, LUMO) by the interaction with light. The required energy for the HOMO-LUMO gap transition is located at the onset of the absorption spectra and the band gap energy is calculated by the equation which describes the relation between energy and wavelength:

$$E = \frac{h \cdot c}{\lambda} = \frac{1240 \text{ (eV} \cdot \text{nm)}}{\lambda(\text{nm})}$$

The electron transitions are measured in absorption intensity as a function of wavelength. Furthermore, absorption intensities are described by the Lambert-Beer Law, an empirical law:

$$A = \log \frac{I_0}{I} = \varepsilon \cdot c \cdot d$$

It describes the intensities of the incident light before I_0 and after I passing the measurement cell. The relation takes the extinction coefficient ε , a specific material constant, the concentration c (mol/L), as well as the measurement cell thickness d into consideration.^[110]

In this work UV-Vis spectroscopy have been used to detect reaction progress by colorimetric methods, and to determine the optical band gap energy.

4.1.2 UV-Vis Diffuse Reflectance Spectroscopy (UV-Vis DRS)

For insoluble solid samples, standard liquid UV-Vis spectroscopy is not sufficient. An indirect measurement method to determine the absorption properties of insoluble solid samples is UV-Vis diffuse reflectance spectroscopy (DRS). Here, the absorption is measured by reflectance. A typical measurement setup consists of a thin film of the solid sample within an integrating sphere. The possible physical light-matter interactions beside absorption are (a) specular reflection, which is comparable to the reflection of an incident light beam in the mirror; (b) internal reflection, which describes the mirror-reflection at all non-oriented reflecting surfaces within the sample; (c) diffuse reflection. All types of reflections are observed to occur and exist beside each other, as well as multiple scattering effects.^[111] In order to collect the diffuse light during a measurement process, the integration sphere is employed as a light collector/reflector setup for common UV-Vis spectrometers or as stand-alone devices (Figure 4.1). Its main feature is based on the efficient reflection of light by a non-absorptive background, usually white BaSO₄ coating.

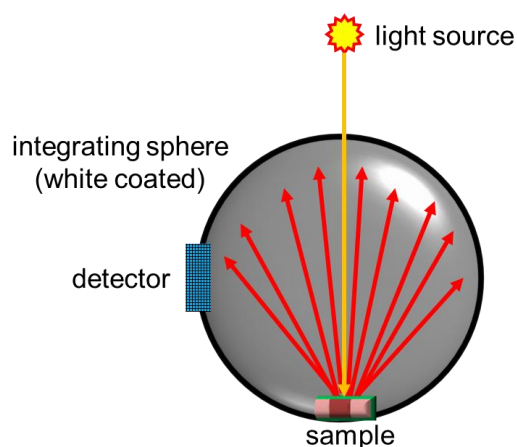


Figure 4.1: *Function and design of an integration sphere.*

The reflection spectrum is influenced factors such as particle size of the solid materials, packing density, shape, refractive power. For instance decreasing particle size is indicated by lower light penetration depth and higher scattering effects. Increasing particle size increases light penetration depth and reduces scattering.^[112]

In this work, UV-Vis DRS measurements have been conducted to characterize the optical properties of cross-linked polymers.

4.2 Fast Fourier Infrared Spectroscopy (FT-IR)

FT-IR spectroscopy is based on the interaction of a molecule with electromagnetic irradiation in the wavenumber range 4000 to 200 cm^{-1} . The provided wavenumber range is derived from an interferometric setup. An IR measurement is conducted by placing the sample (solid or liquid) into the IR beam chamber or a sample holder equipped with a ATR-crystal (attenuated total reflectance). In general, transmission spectra as a function of absorption are displayed. The absorption of infrared irradiation causes oscillation of molecular bonds, which is based on a time dependent change of the dipole moment. Among the possible vibrations, asymmetric and symmetric valence vibrations, as well as the so-called in- plane and out-of-plane deformation vibrations can be determined. The valence vibrations occur above 1400 cm^{-1} , whereas deformation vibrations are detected in the finger print range between 1400 and 400 cm^{-1} . Mostly the sum of absorption bands in the finger print range are used for analysis, in order to avoid ambiguous assignments caused by overlap with molecule fragment vibrations. In Table 4.1 according to the absorption ranges, different functional molecule groups are listed.^[113] In this work FT-IR spectroscopy has been employed for characterizing of porous polymers and modifications of those.

Table 4.1: Range of absorption of different functional molecule groups.^[113]

Wavenumber cm ⁻¹	3500-2500	2500-1800	1800-1400	fingerprint
Absorbing group	O-H, N-H, C-H	C≡C C≡N X=Y=Z	C=C C=O C=N	Other valence, deformation, and combination vibrations

4.3.1 Nuclear Magnetic Resonance Spectroscopy (NMR)

NMR spectroscopy is used for analysis and determination of molecular structures and molecular dynamics. Basically NMR measurements can be conducted with all kind of isotopes, nuclei that possess a nucleus spin (I), caused by uneven nucleus protons and neutron numbers. Within organic chemistry, the most vital nuclei are ¹H and ¹³C, whereas the natural occurrence (¹H 99.9% and ¹³C 1.08%) determines the signal intensities. ¹H and ¹³C have spin quantum numbers I=1/2 and will align in 2I+1 different orientations. A NMR spectroscopy consists of an external magnet, a radio frequency transmitter, a receiver, and a processing unit. By the introduction of an external magnetic field the nucleus magnets align in an energetically low (α) and high spin (β) state. The energy difference between α and β state is described by:

$$\Delta E = \frac{h\gamma B_0}{2\pi}$$

B_0 refers to the external magnet field, h is the Planck constant, γ is the gyromagnetic constant of proportionality of a specific core. The spin distributions are governed by the Boltzmann law of distribution. Radio frequencies in the range of the nucleus resonance frequency ω , the nucleus spin flips from low to high energy state, where the number of nucleus in a higher state is accumulated:

$$\omega = \frac{\gamma \cdot B_0}{2\pi}$$

The nucleus resonance frequency ω is determined by the external magnet field strength. NMR spectrometers operate between 60 to 1000 MHz. By applying radio frequencies in the range of the resonance frequency, an oscillating magnet field B_1 rectangular to B_0 is created. This acts like a disturbance field on the nucleus spin ensemble. Finally, after removal of the additional disturbance field, the emitted relaxation frequencies are received and processed. In general, deuterated solvents are used in liquid NMR measurements. Furthermore, the signals are referred to an internal standard signal, mostly trimethylsilane (TMS). In this work, NMR was used for the structure elucidation of compounds dissolved in deuterated solvents.

4.3.2 Solid State Nuclear Magnetic Resonance (Solid State NMR)

The NMR spectrum of solid samples is different from solution NMR spectra, due to several effects causing anisotropic behavior of the powder sample. The effects of nuclear spin interaction which depend on the crystallite orientation are chemical shielding, dipole-dipole coupling, and quadrupole coupling. However, the average field of these effects is achieved by the magic angle spinning (MAS) technique (Figure 4.2).

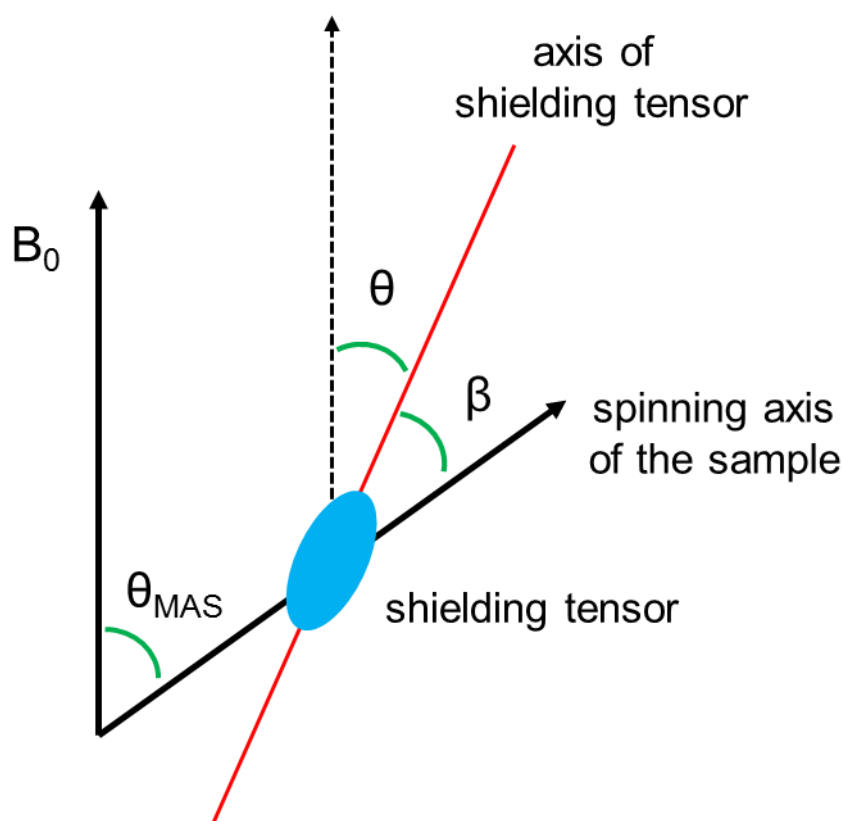


Figure 4.2: Principle of Magic Angle Spinning (MAS) sample alignment.

However, the orientation dependence of nuclear spin interaction leads to the formation of a shielding tensor aligned with the angle θ to the applied magnetic field B_0 and with β to the spinning axis of the sample. The average of orientation dependence interactions can be described as following and equals zero if $\theta_{MAS} = 54.74^\circ$:

$$\langle 3\cos^2\theta - 1 \rangle = \frac{1}{2} (3\cos^2\theta_{MAS} - 1)(3\cos^2\beta - 1)$$

The anisotropic and asymmetric nuclear interactions cause sidebands which depend on the spinning frequency. Only at high spinning rates the anisotropy is averaged and can be removed. In order to remove all sidebands and to obtain the unchanged isotropic line of the chemical shift, the spinning has to be conducted at very high frequencies, usually kHz frequencies up to 50 kHz are applied. The high spinning frequencies are also needed to reduce fast effects of homonuclear dipolar couplings leading to line broadening. Basically low abundant nuclei lead to a poor signal to noise ratio, but show long relaxation times. In order to enhance the magnetization of these diluted nuclei, abundant nuclei of the same spin are exploited. After coupling both nuclei by sending a short contact pulse, the abundant nucleus is decoupled while the relaxation of low abundant nucleus is recorded.^[14] In this work, solid-state NMR was used for the structure elucidation of solid samples.

4.4 Electron Paramagnetic Resonance Spectroscopy (EPR)

The EPR spectroscopy enables the analysis of unpaired electrons and allows structural insights into their interactions with adjacent atoms. It is usually used for the analysis of radicals. In combination with spin-trapping agents, EPR allows one to reveal the formation and mechanism of highly reactive intermediates of reaction processes. Similar to NMR spectroscopy, the electron spin levels are divided by the Zeeman effect into low and high energy states. Most electrons populate in the low state according to the Boltzmann distribution. An EPR spectroscope consists of an external magnet, a microwave generator, a detector, and a resonator with sample holder. The absorption of microwave usually in the frequency range of 9 GHz lifts the unpaired electron to a high energy state. EPR spectra are converted to the first derivative of absorbance. The energy difference of both spin states is described by:

$$\Delta E = g \cdot \beta \cdot B$$

where g is a constant of proportionality, β is the Bohr magneton, and B the magnetic field.^[115] In this work, the EPR spectroscopy was used for the characterization of radicals and reactive species such as intermediates. Moreover, by means of trapping agents further information about the type of reactive species was obtained.

4.5 Cyclic Voltammetry (CV)

Cyclic voltammetry is a potential-controlled electrochemical method with current response. The current is a function of the cyclic potential change by predetermined sweep times (Figure 4.3). CV enables insights into electrochemical reduction/oxidation steps as well as changes in the structure upon electron transfer processes. The typical CV experimental configuration consists of a measurement cell with three electrodes (working electrode, counter electrode, reference electrode) and a certain electrolyte in organic solvents or aqueous solution. The electrolytes are employed in order to reduce the charge migration and to enhance conductivity. For instance, a frequently used electrolyte is tetrabutylammonium tetrafluoroborate in acetonitrile solution, which allows measurements in the potential range +3.4 to -2.9 V (vs. SCE) without influencing the electrochemical process.

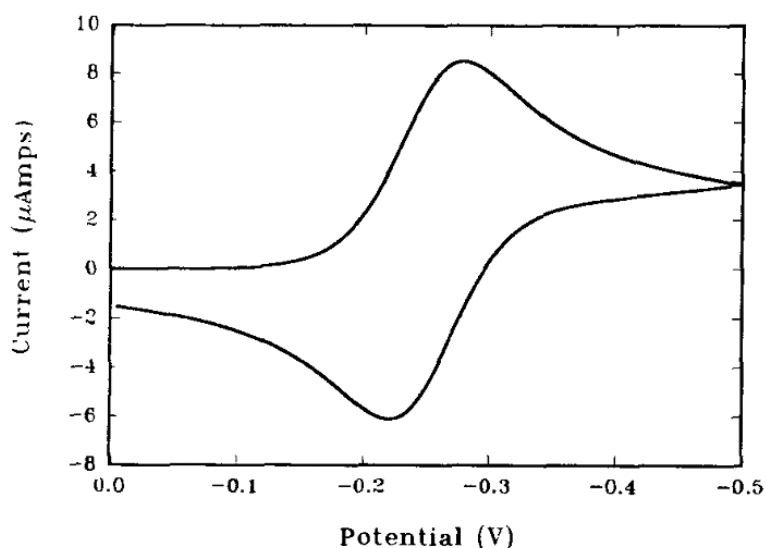


Figure 4.3: Typical cyclic voltammogram showing the oxidation and reduction cycle.

Commonly used electrodes are glassy carbon or gold electrodes as working electrode, platinum wires as counter electrode, and standard calomel electrode (SCE) or Ag/AgCl as

reference electrode. From the obtained redox potentials of the samples, their HOMO and LUMO levels can be derived.^[116]

In this work, CV was used to determine the electrochemical HOMO/LUMO levels.

4.6 Brunauer-Emmet-Teller Isotherm Method (BET)

In this work, the gas sorption measurement is the main analysis tool to obtain insights into the porous structure of conjugated porous polymers. The obtained information is based on the adsorption and desorption behavior of an adsorbate, mostly nitrogen gas molecules on the surface of an adsorbent. Among the different theories in the literature, the Brunauer-Emmet Teller (BET) theory suggests a multilayer adsorption process, whereas the Langmuir theory is only based on a monolayer adsorption. The BET method is based on three pre-assumptions: 1) each layer coverage (Langmuir monolayer) must be completed before the next layer can begin; 2) the heat of adsorption of the first step is governed by adsorbate-adsorbent interaction, and; 3) the heat of adsorption of next following layers is governed by adsorbent-adsorbent interactions and leads to heat of condensation. However, according to the IUPAC definition, the gas sorption isotherms are classified in 6 types (Figure 4.4):^[117]

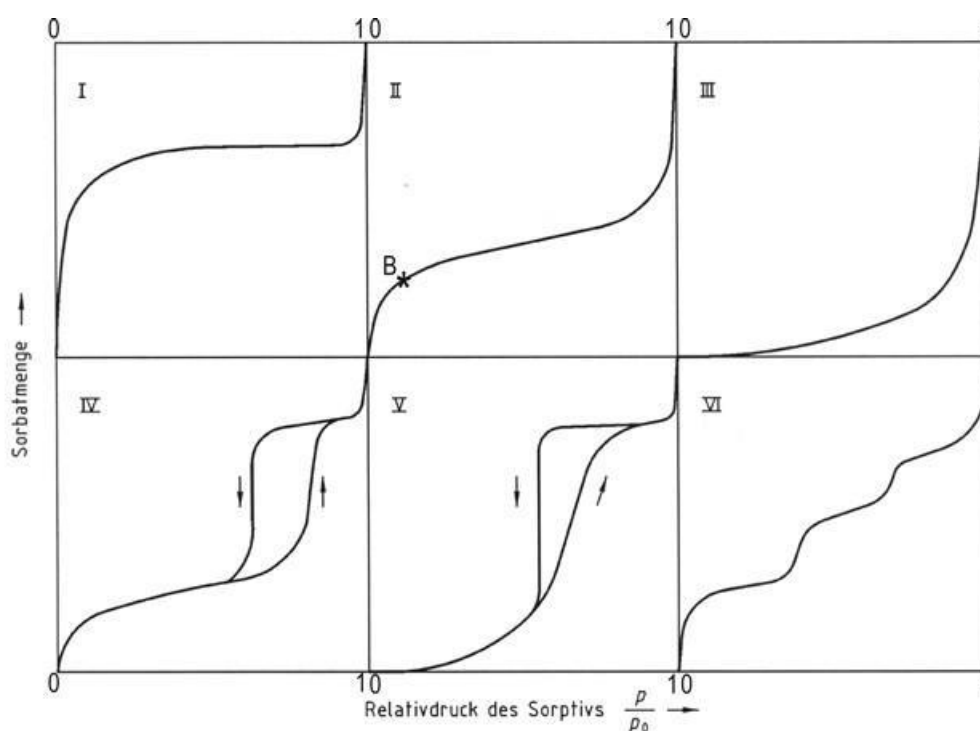


Figure 4.4: *Different BET isotherms.*

Type I isotherm reflects micro-pore filling at low pressures and surface coverage via adsorbate monolayer. After reaching higher pressures and surpassing the monolayer level, additional layers start to build as in type II. Low adsorbate-adsorbent interactions as described by the onset of type III isotherms, show multilayer formation. In general, hysteresis formation as in type IV and V isotherms occurs with large pores, whereas the desorption shifts to lower pressure values are caused by a condensation phenomenon. The shape of the curve can display additional information about the pore size and pores shape. In this work, the BET method was used to determine important porosity parameters such as surface area, pore size, and pore size distribution.

4.7 Scanning Electron Microscopy (SEM)

SEM is an efficient method for the imaging of surface structures with an up to 100 000 fold magnification. In this work the porous surface structures of highly porous polymers were analyzed via scanning electron microscope. Usually, the electron microscope operates with a tungsten wire or lanthanum hexaboride electron beam source, the so-called Wehnelt cylinder. The electron beam is pulled by the opposite charged anode. The acceleration voltage is defined by the potential difference between the electron gun and the anode, and determines the interaction with the sample and the final image resolution. The condenser lens concentrates the electron beam towards the sample. Moreover, the magnet controller within the objective lens is responsible for the scanning ability of the electron beam. The impact of the electrons on the sample surface causes secondary electrons which are collected and detected by a positively charged detector. Different surface locations scatter different secondary electron numbers, which indicate raised or dropped positions. Furthermore, among the collected electrons, the inelastic scattered electrons are the surface information bearing electrons in SEM.^[118] In this work, SEM was used for displaying the surface morphology of the photocatalysts.

4.8 Transmission Electron Microscopy (TEM)

TEM enables the imaging of internal structures of samples. The device setup of the transmission electron microscope is similar to scanning electrode microscope, with the difference that the electrons pass through the sample. The mean magnification of TEM is 500 000 fold with a maximum resolution of 0.2 nm. According to the de Broglie equation the wavelength decreases with increasing velocity:

$$\lambda = \frac{h}{m \cdot v}$$

Here, h is the Planck constant, m is the electron mass, and v is the velocity. In general acceleration voltages between 20 to 1000 kV are possible.

The passing of electrons through the sample allows the imaging of internal structures by interaction of electrons with the sample. The electron beam is produced by the electron gun, which will be controlled and focused at the condenser lens. The apertures help to avoid aberrations and enable round homogenous spots. Apertures ensure a contrast enhancement and removal of scattering electrons. The complex objective lens setup bears at the same time the sample holder. Here, the electron beam passes the sample. In order to improve the magnification on the fluorescence screen or the camera, the beam passes the diffraction lens, the auxiliary lens, and the projection lens.^[118] In this work, the transmission electron microscope was used for displaying internal structures of the conjugated microporous polymers and nanostructures.

5. Results and Discussion

The following chapter is divided in three main sections, which are based on three previously published articles and one unpublished article about 1.) water-compatible conjugated microporous polymers and 2.) porous, cross-linked conjugated polyelectrolytes and 3.) conjugated microporous polymers employed in photocatalytic Stille-type coupling reactions. The main purpose of this chapter is to demonstrate the synthesis and characterization of highly porous conjugated polymer-based materials as visible-light photocatalysts for any kind of solvents. Additionally, the photocatalytic reaction mechanisms will be discussed in detail.

5.1 Water compatible conjugated microporous poly-azulene networks as visible light photocatalysts in aqueous medium

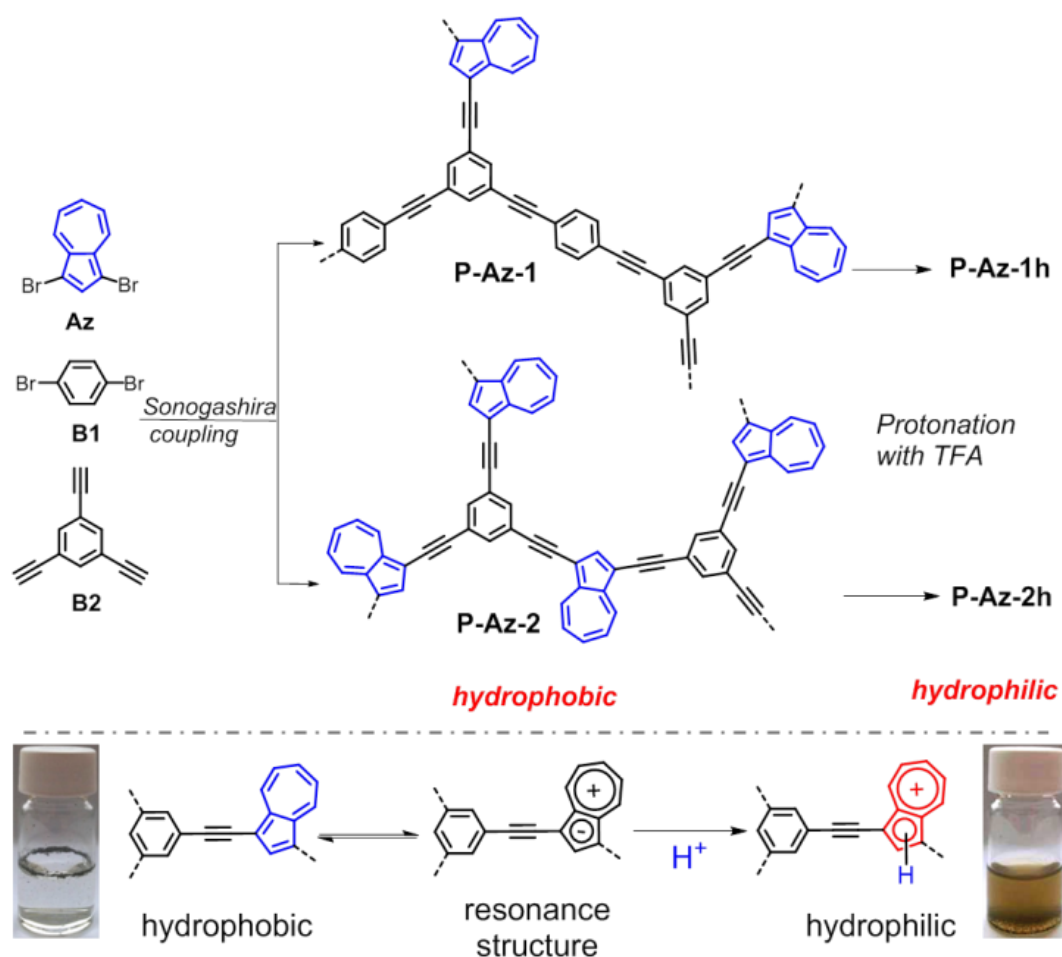
This section is based on the publication “Water compatible conjugated microporous poly-azulene networks as visible light photocatalysts in aqueous medium”, **ChemCatChem**, 2016, 8, 694 – 698 (DOI: 10.1002/cctc.201501102) with copyright (2016) from Wiley VCH (Weinheim).

5.1.1 Introduction

This section deals with the hydrophilicity control of hydrophobic Azulen-CMPs by a simple modification strategy via protonation of azulene units within the network. Additionally, the morphology and electronic properties were investigated before and after modifications. To evaluate the photocatalytic performance of the modified azulene-CMPs, the photoreduction reaction of heavy metal ions was chosen as the model reaction.

5.1.2 Synthesis and Characterization

In Scheme 5.1, the structures and the modification method to obtain water-compatible polymer networks based on poly-azulene are illustrated. Two conjugated microporous polymers P-Az-1 and P-Az-2 were synthesized via Sonogashira cross-coupling of 1,3-dibromoazulene, 1,4-dibromobenzene and 1,3,5-triethynylbenzene as cross-linker.



Scheme 5.1: Synthetic pathway and modification method for hydrophilic, conjugated microporous poly-azulene networks.

In order to elucidate the influence of the azulene content on the material properties, different azulene moieties were incorporated into the networks. In particular, the stoichiometric ratios of the 1,3-dibromoazulene moiety and the comonomer 1,4-dibromobenzene with respect to the cross-linker 1,3,5-triethynylbenzene in P-Az-1 was 0.5/0.5/1.5, while the ratios in P-Az-2 was 0.5/0/1.5, where no comonomer was used. It has been reported that exposure of azulene-containing materials to an acidic environment leads to protonation of the electron-rich cyclopentadiene ring of azulene, forming a stable aromatic six- π -electron tropylium cation.^[119-122] Taking advantage of the ease of the resonance structure formation as illustrated in Scheme 5.1, the two as-synthesized, hydrophobic polymers P-Az-1 and P-Az-2 were subsequently protonated by adding trifluoroacetic acid (TFA) and thus forming the hydrophilic polymers P-Az-1h and P-Az-2h, which were well dispersible in water. In comparison, the pristine polymers P-Az-1 and P-Az-2 were highly hydrophobic and could not be dispersed in water. The experimental details and polymer characterization data are described in the following section. The solid-state ^{13}C CP MAS NMR spectra of P-Az-1 and P-Az-2 showed characteristic signals between 110 and 155 ppm. The peak at ca. 90 ppm was typical for alkyne groups (Figure 5.1 and 5.2).

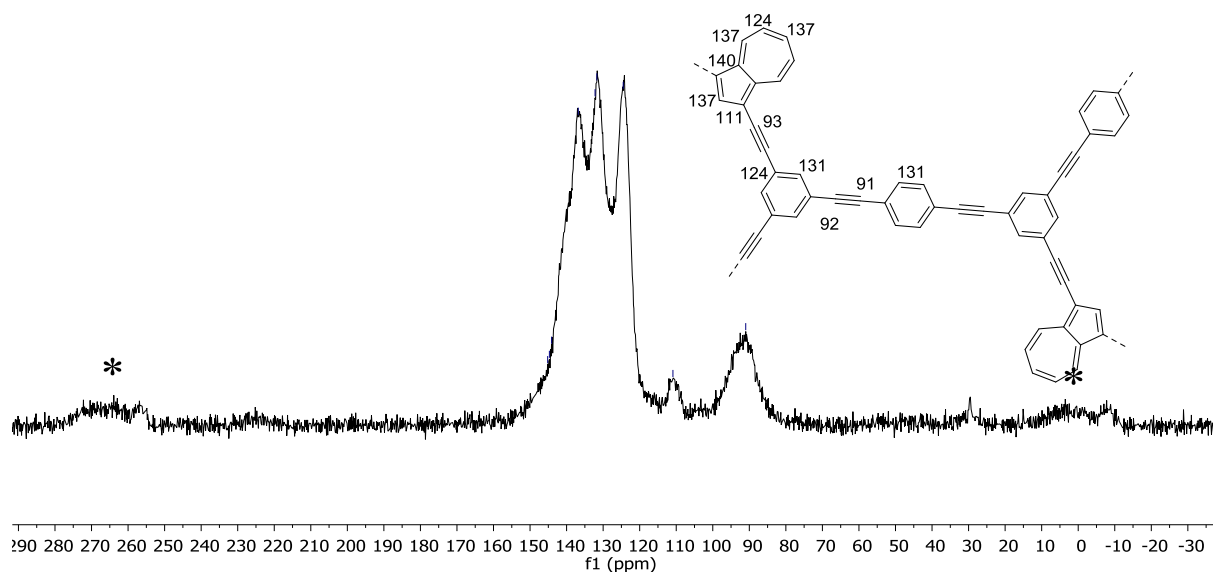


Figure 5.1: ^{13}C -NMR CP-MAS solid-state NMR spectrum of P-Az-1 (* sidebands).

After protonation, a slight change of the signals was observed. Especially the peak at ca. 45 ppm could be assigned to the protonated 5-membered ring of the azulene units (Figure 5.2).

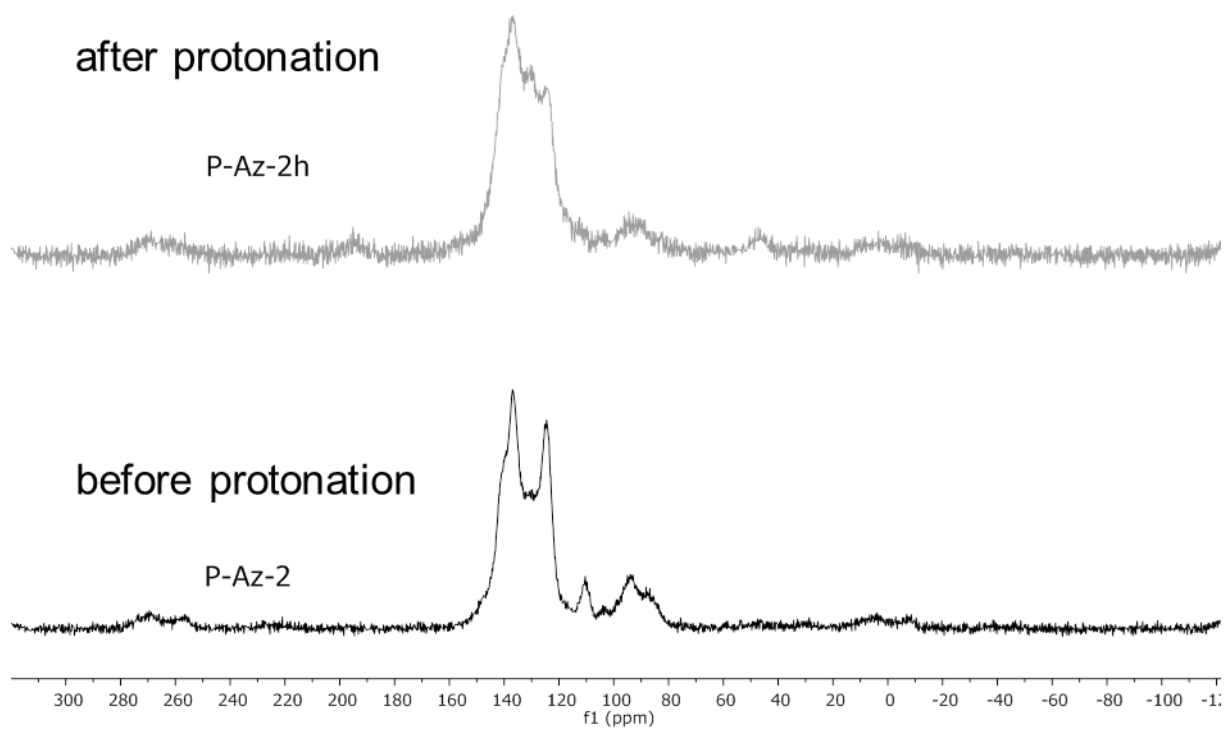


Figure 5.2: ^{13}C -NMR CP-MAS solid-state NMR spectrum of P-Az-2 and P-Az-2h (before and after protonation).

The Brunauer-Emmett-Teller (BET) surface areas of P-Az-1 and P-Az-2 were determined to be $514\text{ m}^2/\text{g}$ and $418\text{ m}^2/\text{g}$, with pore volumes of $0.660\text{ cm}^3/\text{g}$ and $0.744\text{ cm}^3/\text{g}$, respectively.

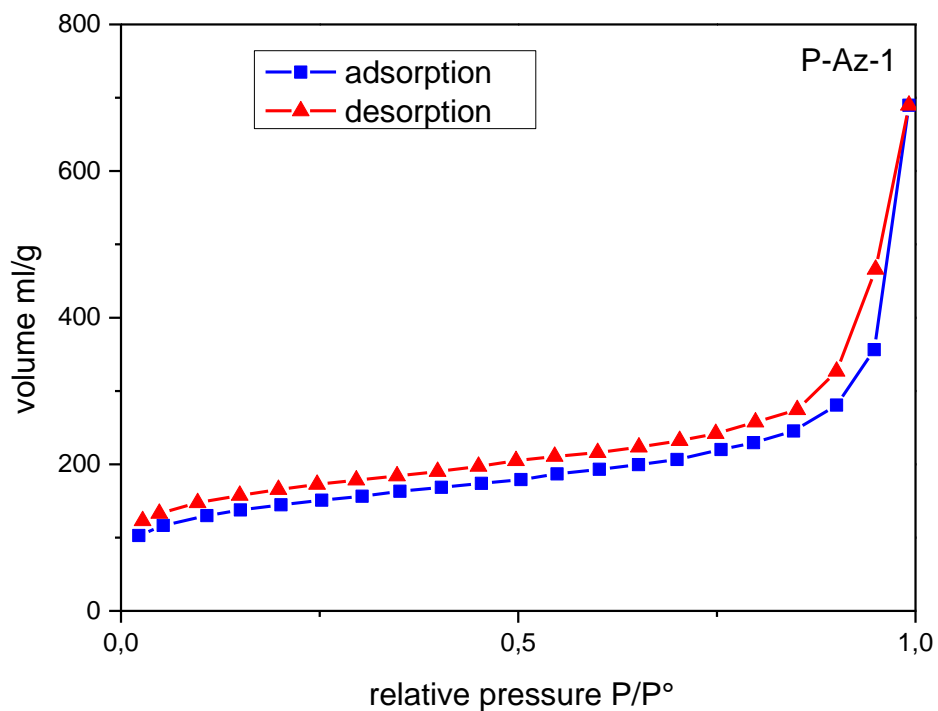


Figure 5.4: Gas sorption isotherms of P-Az-1.

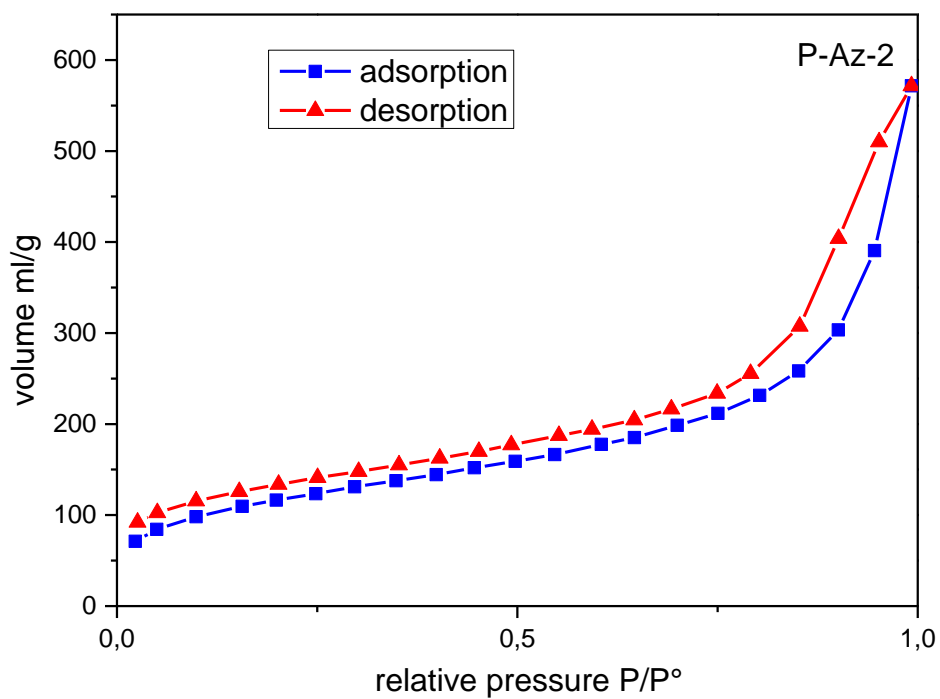


Figure 5.5: Gas sorption isotherms of P-Az-2.

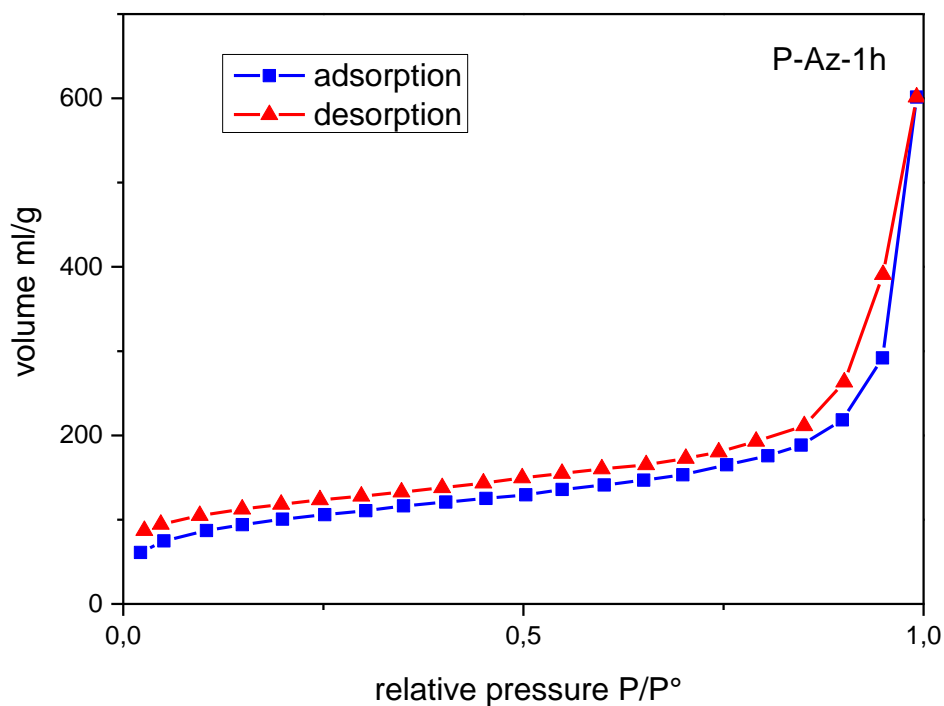


Figure 5.6: Gas sorption isotherms of P-Az-1h.

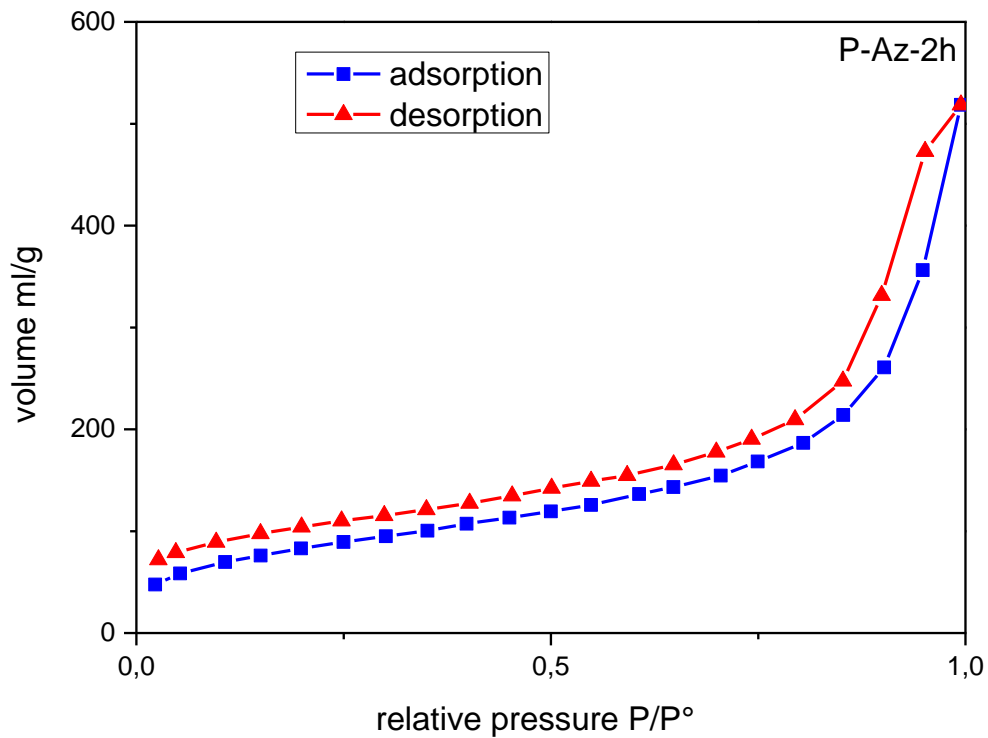


Figure 5.7: Gas sorption isotherms of P-Az-2h.

After protonation, the obtained hydrophilic polymers P-Az-1h and P-Az-2h showed decreased BET surface areas of 364 m²/g and 303 m²/g and as well as reduced pore volumes of 0.556 cm³/g and 0.686 cm³/g, respectively.

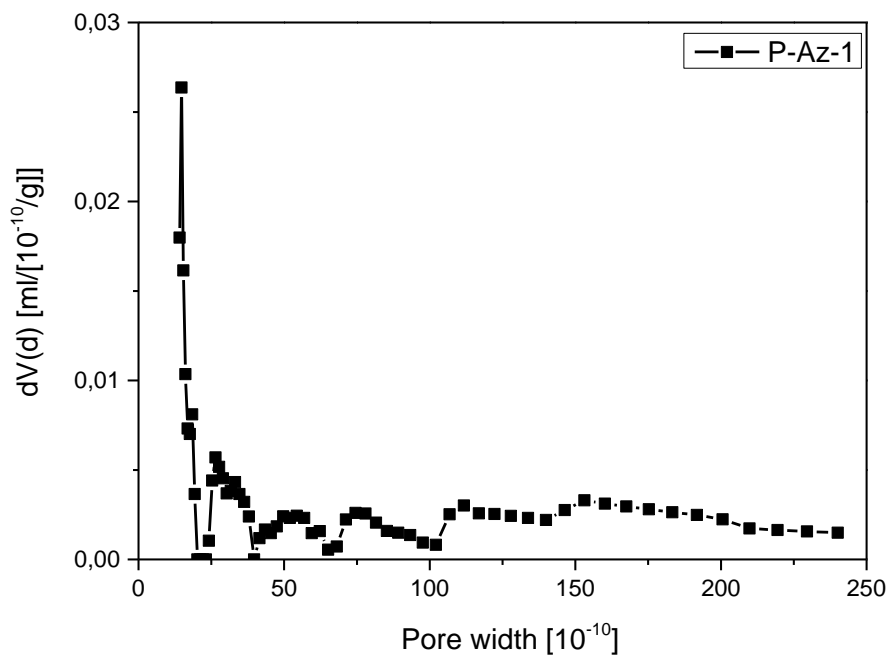


Figure 5.8: Pore size distributions of P-Az-1.

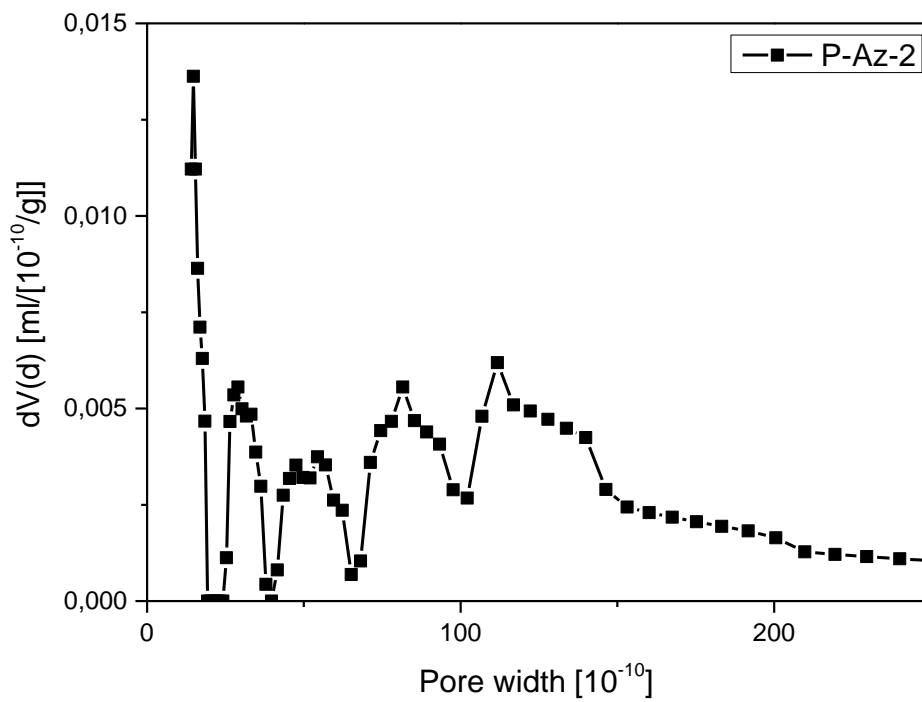


Figure 5.9: Pore size distributions of P-Az-2.

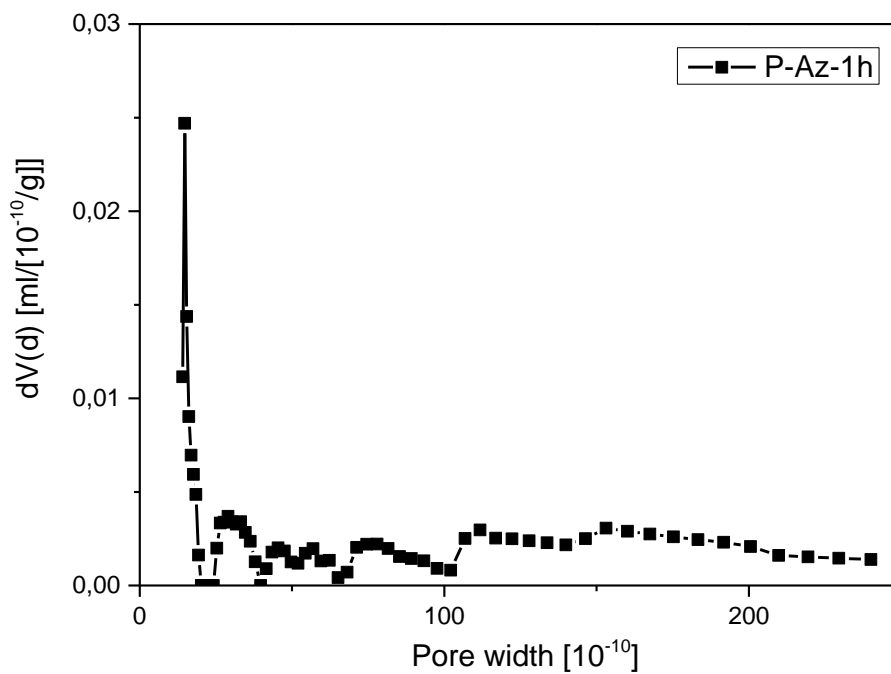


Figure 5.10: Pore size distributions of P-Az-1h.

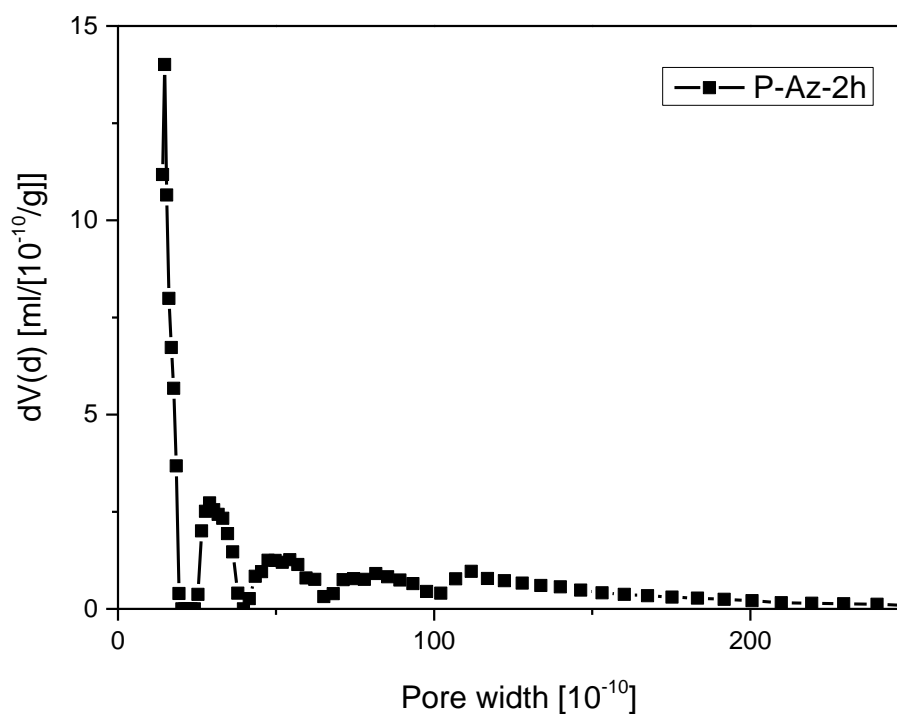


Figure 5.11: Pore size distributions of P-Az-2h.

The reason of the decreased porosity after protonation could be caused by the fact that the trifluoroacetic acid as counter ions were largely incorporated within the network for the balance of the tropylium cations. This might result in the filling of the micropore channels to some extent, leading to a decreased pore volume and BET surface area. For all four polymers, similar pore diameters of round 1.5 nm were determined (Table 5.1, Figure 5.4-5.11).

Table 5.1: Porosity data of the polymers.

Polymer	S_{BET} (m^2/g)	Pore Volume (cm^3/g)	Pore Size (nm)
P-Az-1	514	0.660	1.5
P-Az-2	418	0.744	1.5
P-Az-1h	364	0.556	1.5
P-Az-2h	303	0.686	1.5

Thermal gravimetric analysis (TGA) measurements showed that the polymers P-Az-1 and P-Az-2 remained intact up to 300 °C under nitrogen, while the protonated polymers P-Az-1h and P-Az-2h became less thermally stable (up to 120 °C) (Figure 5.12).

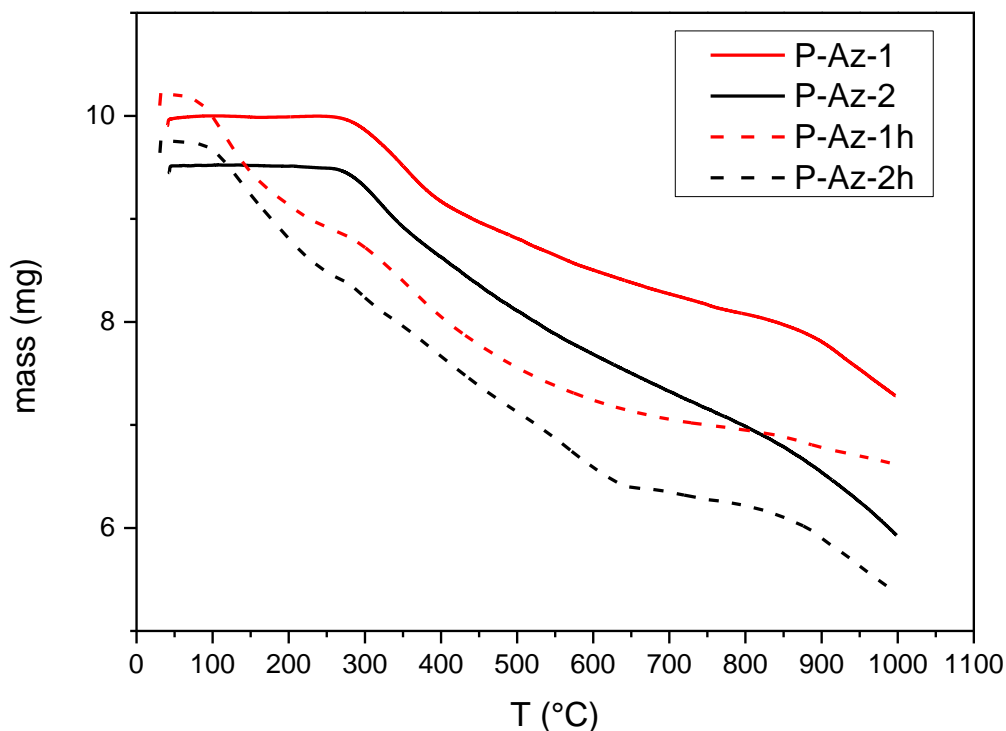


Figure 5.12: TGA analysis of P-Az-1 and P-Az-2 before and after protonation.

The reason of the lower stability of the protonated polymer networks could be due to the decreased stabilizing effect of the trifluoroacetic acid anions on the tropylium cations inside the polymer network. By increasing temperature, the higher mobility of the trifluoroacetic acid anions could lead to their less efficient stabilizing effect and therefore the low stability of the polymer networks.

The SEM images of the polymer are displayed in Figure 5.13. After protonation, the polymers P-Az-1h and P-Az-2h showed a rougher morphology than P-Az-1 and P-Az-2, indicating the more polymeric salt-like nature of both protonated polymers.

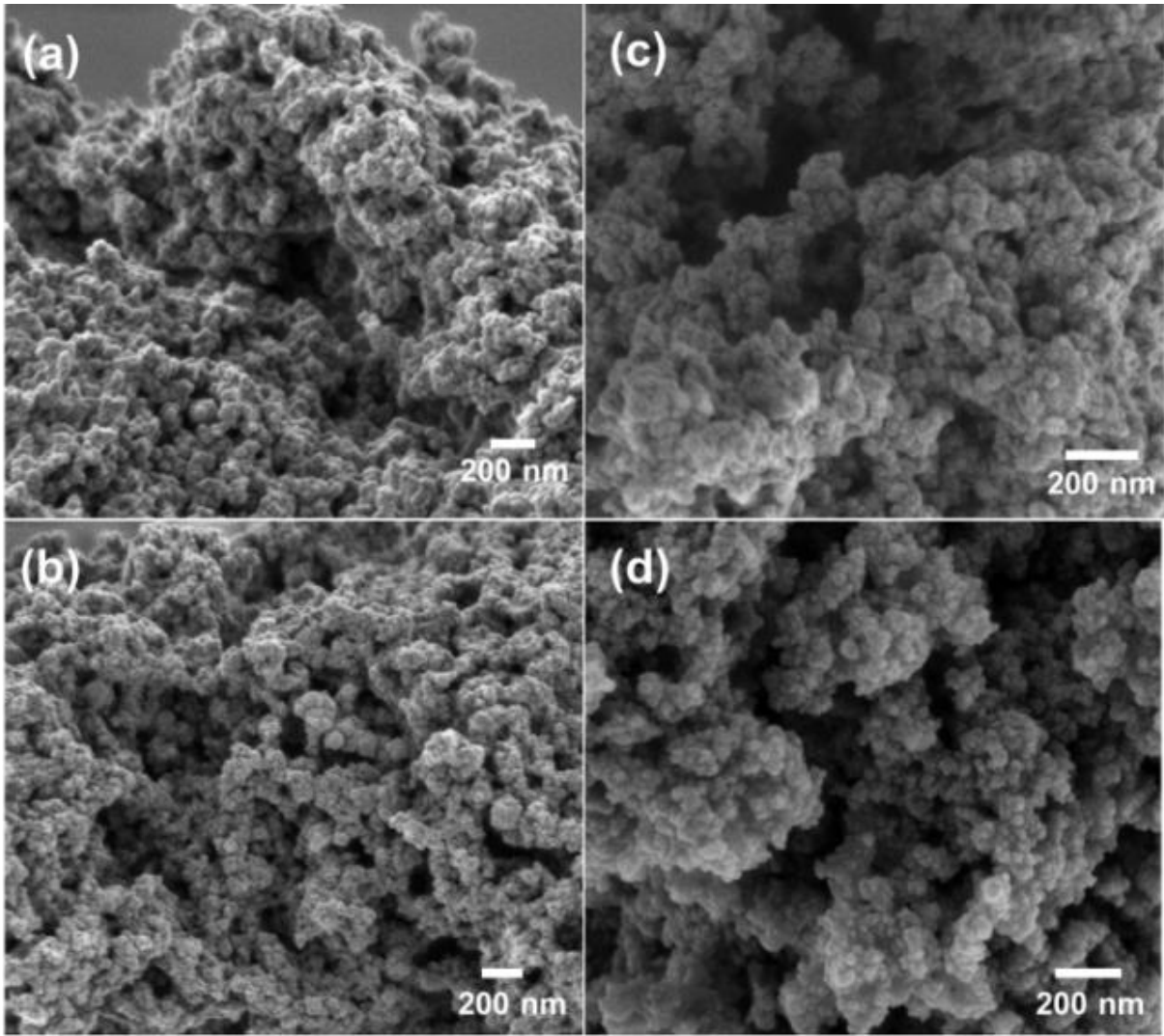


Figure 5.13: SEM images of (a) *P-Az-1* and (b) *P-Az-2*, and their protonated forms (c) *P-Az-1h* and (d) *P-Az-2h*.

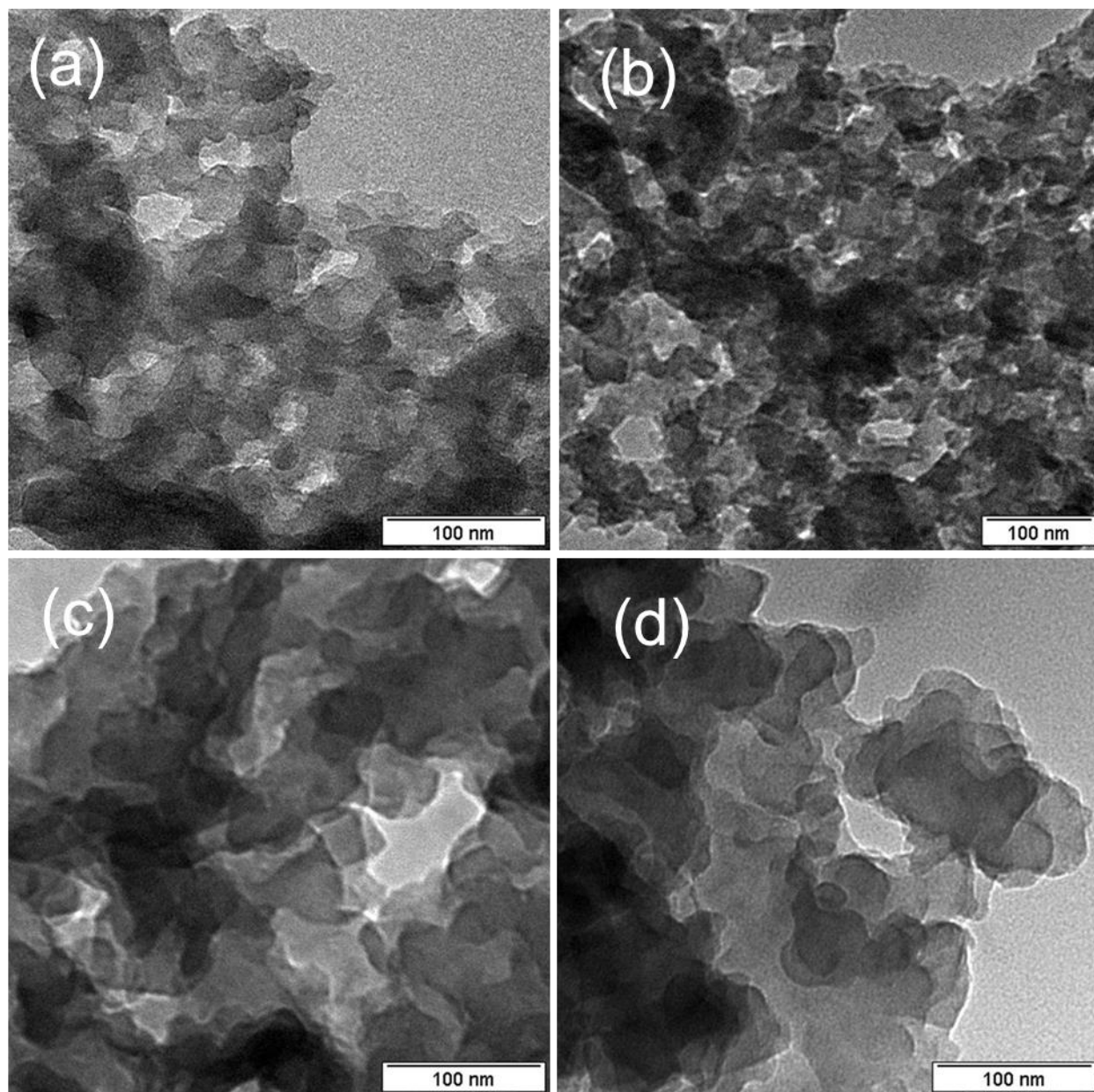


Figure 5.14: TEM image of a.) *P-Az-1*, b.) *P-Az-2*, c.) *P-Az-1h*, d.) *P-Az-2h*.

Nevertheless, the TEM images did not show a clear morphology change after protonation of the polymers (Figure 5.14). The FT-IR spectra of the polymers showed a significant signal change after protonation (Figure 5.15).

New stretching modes appeared between at about 1170 and 1690 cm^{-1} can be assigned to the asymmetric and symmetric valence stretching of the trifluoroacetic anion. The enhanced signal at ca. 1570 cm^{-1} can be assigned to the -C=C- stretching mode of the protonated azulene unit after protonation.

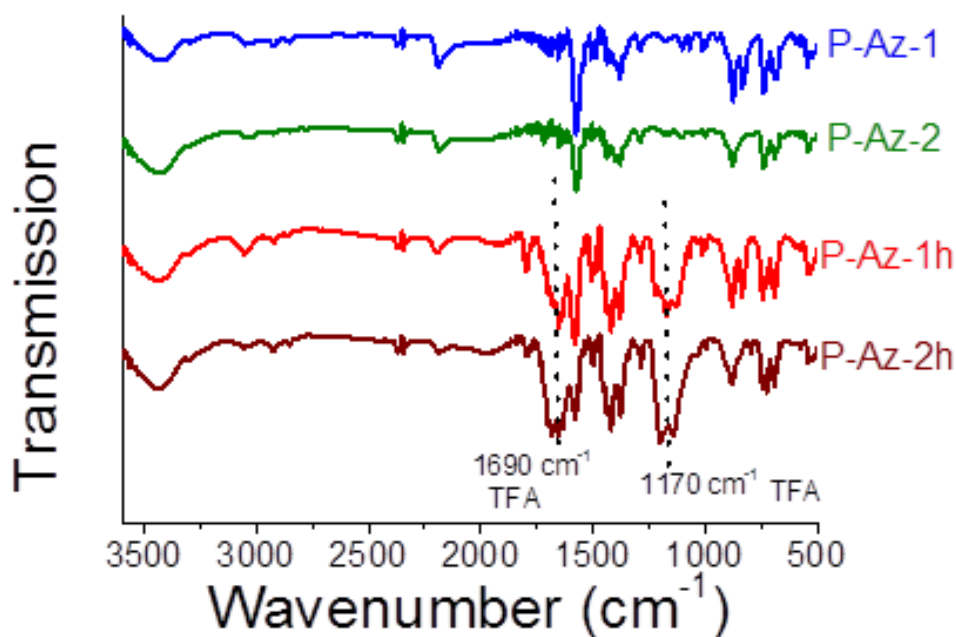


Figure 5.15: FT-IR of the poly-azulenes and their protonated forms.

The UV/Vis diffuse reflectance spectra (DRS) of the polymer are displayed in Figure 5.16. P-Az-1 and P-Az-2 showed both a broad absorption range with shoulders until over 800 nm. After protonation, the absorption spectra of both polymers became even broader ranging up to the infrared region (>1000 nm).

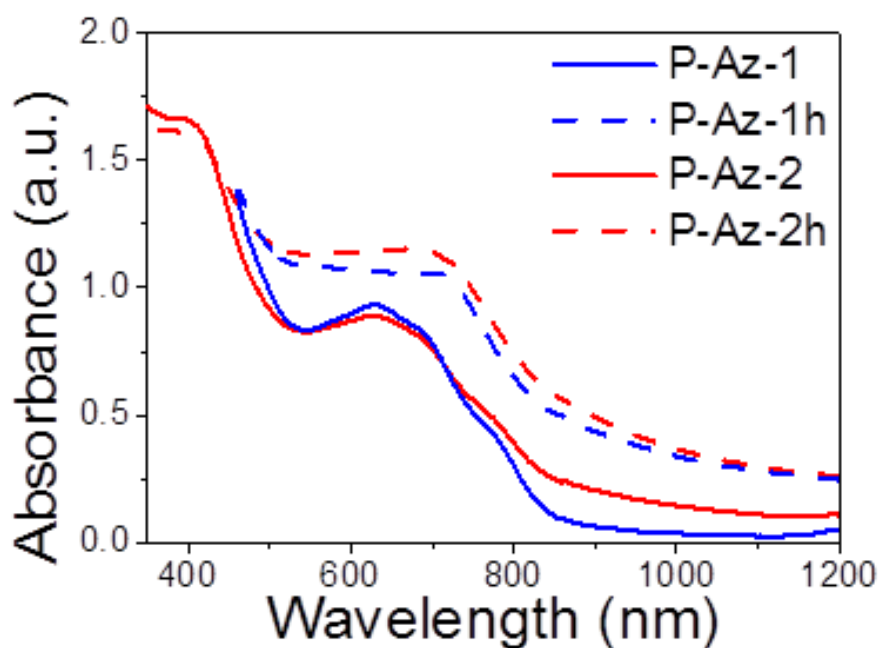


Figure 5.16: UV/vis DR spectra of the poly-azulenes and their protonated forms.

This explains the more intense colors of both protonated polymers P-Az-1h (dark green) and P-Az-2h (black) compared to P-Az-1 (green) and P-Az-2 (dark green) as displayed in Figure 5.17.

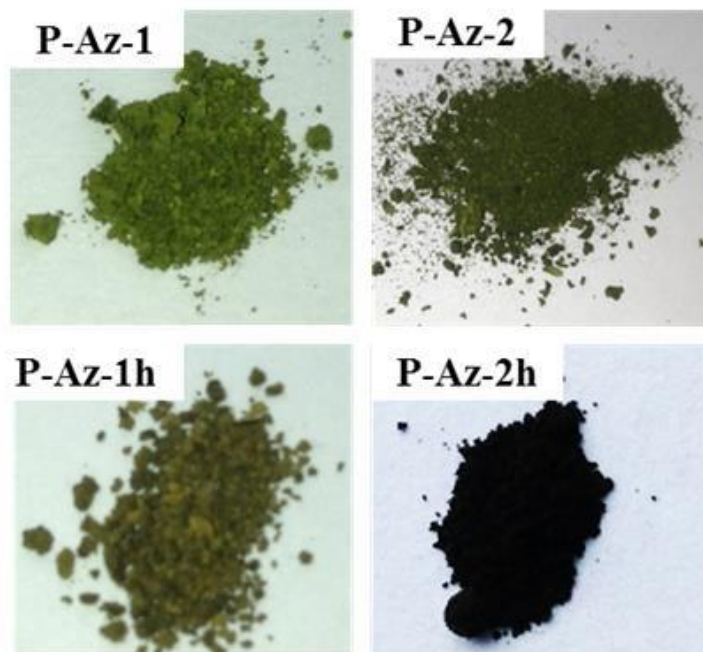


Figure 5.17: Different poly-azulene modifications before (*P-Az-1*, *P-Az-2*) and after (*P-Az-2*, *P-Az-2h*) protonation.

The electron paramagnetic resonance (EPR) spectra showed a clear increase in signal intensity for the protonated polymers P-Az-1h and P-Az-2h compared to P-Az-1 and P-Az-2.

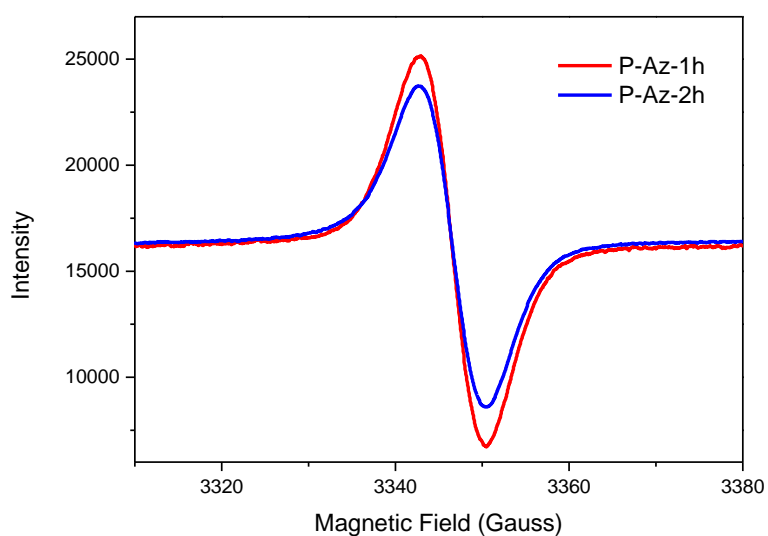


Figure 5.18: EPR spectra of *P-Az-1h* and *P-Az-2h* under light irradiation.

This is likely due to the protonated form of the polymers, where the positively charged 7-membered ring of the azulene unit acts as an artificial “hole”. This could be reason of the large signal increase. Under light irradiation, P-Az-1h exhibited a more enhanced signal compared to P-Az-2h, indicating that longer living electron-hole pairs could be generated in P-Az-1h under light irradiation than in P-Az-2h (Figure 5.18).

For photocatalytic systems, the valence band (VB) and conduction band (CB) positions represent their light-promoted redox potentials and therefore influence the catalytic efficiency. Cyclic voltammetry (CV) measurements revealed different oxidation and reduction onset potentials of the polymers, implying various VB and CB positions for the polymers. The VB and CB of P-Az-1 lay at 1.14 and -0.81 V vs SCE. P-Az-2 possessed a narrower band gap with VB and CB lying at 0.79 and -0.73 V vs SCE. After protonation, the band positions of both polymer slightly changed, with the VB and CB of P-Az-1h and P-Az-2h being 1.22 and -0.84 V, and 0.92 V and -0.54 V vs SCE, respectively (Figure 5.19).

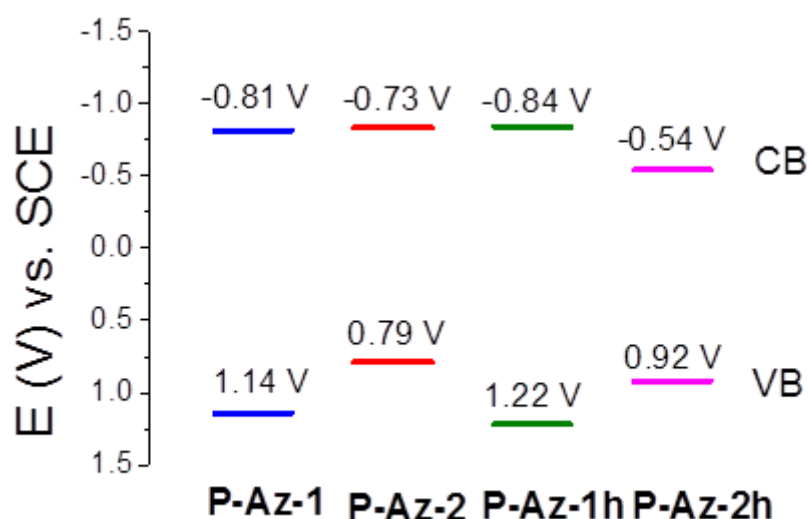


Figure 5.19: Valence band (VB) and conduction band (CB) positions of the polymers.

It is worth to note that the VB and CB positions of P-Az-1 and P-Az-1h are comparable to the redox potentials of well-established organometallic photocatalysts such as $[\text{Ru}(\text{bpy})_3]^{3+}$ (+1.29 V vs SCE) and $[\text{Ru}(\text{bpy})_3]^{2+}$ (-0.81 V vs SCE), or organic molecular photocatalysts such as Eosin (+0.83 and -1.06 V vs SCE).^[123]

5.1.3 Photoreduction and photoredox cascade-reactions of metals in water

The feasibility of the water-compatible polymers P-Az-1h and P-Az-2h as promising heterogeneous photocatalysts in aqueous medium was investigated. The photocatalytic reduction of aqueous Cr(VI) was carried out under visible light irradiation as a real-life-relevant model reaction due to the fact that heavy metals, especially the highly toxic and carcinogenic chromium compounds are well-known pollutants in industrial waste water.^[124] It is worth to point out that a 23 W household energy saving light bulb was used as light source, which demonstrated a clean and cost-effective solution of the application.

As displayed in Figure 5.20, both polymers, P-Az-1h and P-Az-2h, were able to catalyze the reduction of the highly toxic Cr(VI) to much less toxic Cr(III)^[125] quantitatively after 60 min, with P-Az-2h being slightly more efficient than P-Az-1h. The apparent quantum yield was determined for a monochromatic light source at 460+/-30 nm to be 0.0012%.

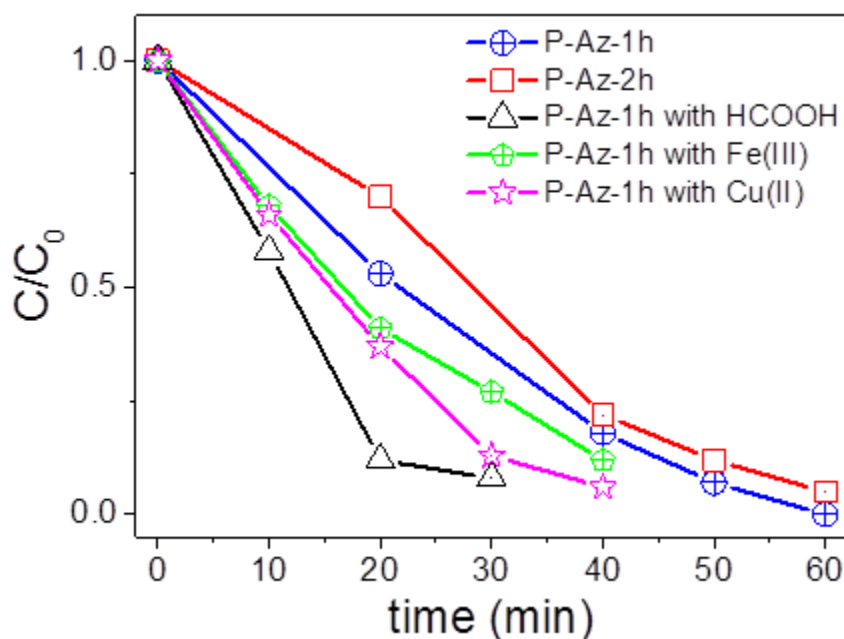


Figure 5.20: Photocatalytic reduction of Cr(VI) to Cr(III) using P-Az-1h and P-Az-2h, Fe(III) or Cu(II) as co-catalyst in a cascade catalytic cycle, and formic acid (HCOOH) as extra electron donor in water under irradiation of a 23 W household energy saving light bulb.

The potential required for the reduction reaction from Cr(VI) to Cr(III) is 1.57 V (vs. SCE).^[126] P-Az-1h has a band gap of 2.06 eV and the conduction band lies at -0.84 V (vs. SCE, Table 5.2) in the excited state, which is sufficient enough for the reduction of Cr(VI) to Cr(III). In comparison, the CB of P-Az-2h lays at -0.54 V, which explains its slightly lower photocatalytic activity during the reduction reaction of Cr(VI).

Table 5.2. Electrochemical properties of the polymers. (The HOMO/LUMO levels are calculated according to the equations: $E_{HOMO} = -(4.4 + E_{ox-onset})$ eV and $E_{LUMO} = -(4.4 + E_{red-onset})$ eV^[127]).

	$E_{Ox-Onset}$ [V vs. SCE]	$E_{red-Onset}$ [V vs. SCE]	HOMO [eV]	LUMO [eV]	Band gap [eV]
P-Az-1	1.14	-0.81	-5.54	-3.59	1.95
P-Az-1h	1.22	-0.84	-5.62	-3.56	2.06
P-Az-2	0.79	-0.73	-5.19	-3.67	1.52
P-Az-2h	0.92	-0.54	-5.32	-3.86	1.46

To understand the electron transfer from the polymer P-Az-1h to Cr(VI) during the photoreduction process, we then conducted a control experiment using formic acid as extra electron donor. An enhanced reduction rate of Cr(VI) to Cr(III) could be observed (Figure 5.20). Additional metal cations with lower reduction potentials than Cr(VI) were introduced to facilitate the electron transfer process in a cascade catalytic cycle.^[128] It could be shown that by using Fe(III) with a reduction potential of ca. +1.01 V (vs. SCE) or Cu(II) with a reduction potential of +0.40 V (vs. SCE), the reduction rate of Cr(VI) increased significantly (Figure 5.20). Based on the observations of the control experiments, we propose a possible reaction mechanism as displayed in Figure 5.21.

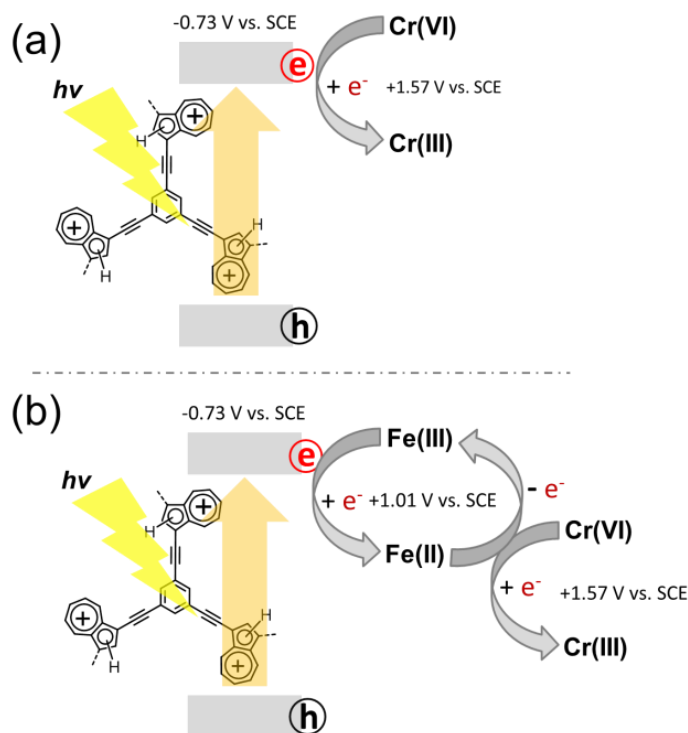


Figure 5.21: (a) Proposed mechanism of the photocatalytic reduction of Cr(VI) to Cr(III) only using the water-compatible polymers P-Az-1h. (b) Photoreduction of Cr(VI) to Cr(III) using P-Az-1h and Fe(III) as co-catalyst in a cascade cycle.

By only using the water-compatible polymer P-Az-1h, the photogenerated electrons from the CB could directly reduce Cr(VI) to Cr(III) under visible light irradiation. By using additional metal cations, a cascade catalytic cycle was obtained. The photogenerated electrons from the CB of P-Az-1h could first reduced either Fe(III) or Cu(II) to Fe(II) or Cu(I), respectively, followed by the further reduction of Cr(VI) by the reduced metal cations, forming Cr(III) and the pristine Fe(III) and Cu(II) cations (Figure 5.21). This cascade-type step could be determined by visualizing of the color change of the yellowish Fe(III) complex potassium ferricyanide ($K_3[Fe(CN)_6]$) via reduction to the bluish complex containing Fe(II) catalyzed by P-Az-1h (Figure 7.22).

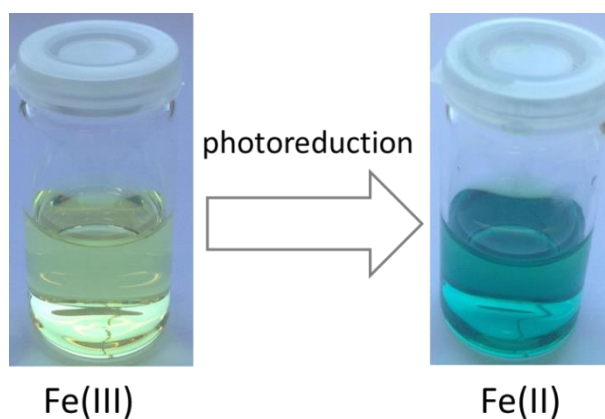


Figure 5.22: Determination of the cascade species Fe(II) generated by photoreduction of Fe(III) using P-Az-1h. The Fe(III) cation in the yellowish potassium ferricyanide ($K_3[Fe(CN)_6]$) was reduced to Fe(II), followed by the color change of the complex to blue.

To demonstrate the stability and reusability of P-Az-1h as heterogeneous photocatalyst, we then conducted the same reduction reaction of Cr(VI) for 5 extra repeating cycles (Figure 5.23).

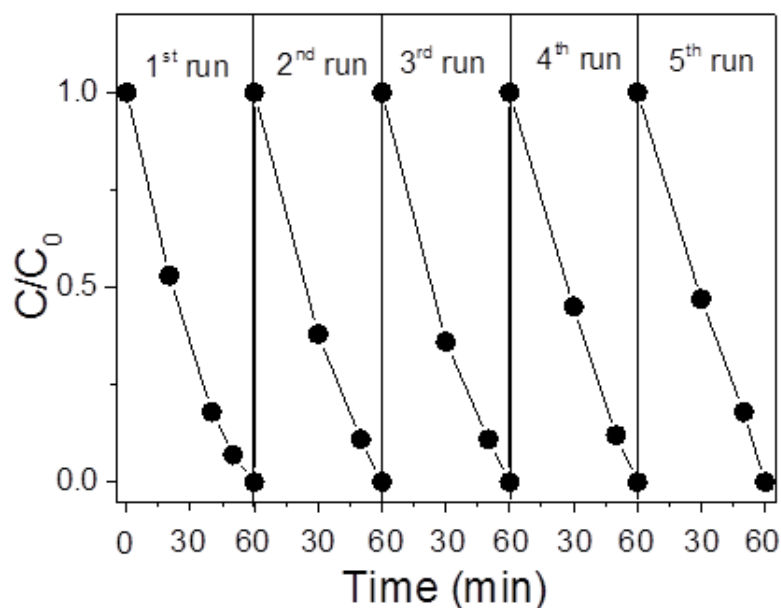


Figure 5.23: Repeating cycles of the photocatalytic reduction of Cr(VI) using P-Az-1h as catalyst. C is the initial concentration of Cr(VI), and C_0 is the initial concentration after research reaching adsorption/desorption equilibrium in dark.

Cr(VI) was reduced almost quantitatively in each run. The FTIR spectrum of the reused P-Az-1h showed slightly enhanced signal intensity of the TFA mode at 1690 cm^{-1} and 1170 cm^{-1} , and the -C=C- stretching mode at 1570 cm^{-1} and 1420 cm^{-1} compared to the unused one (Figure 5.24).

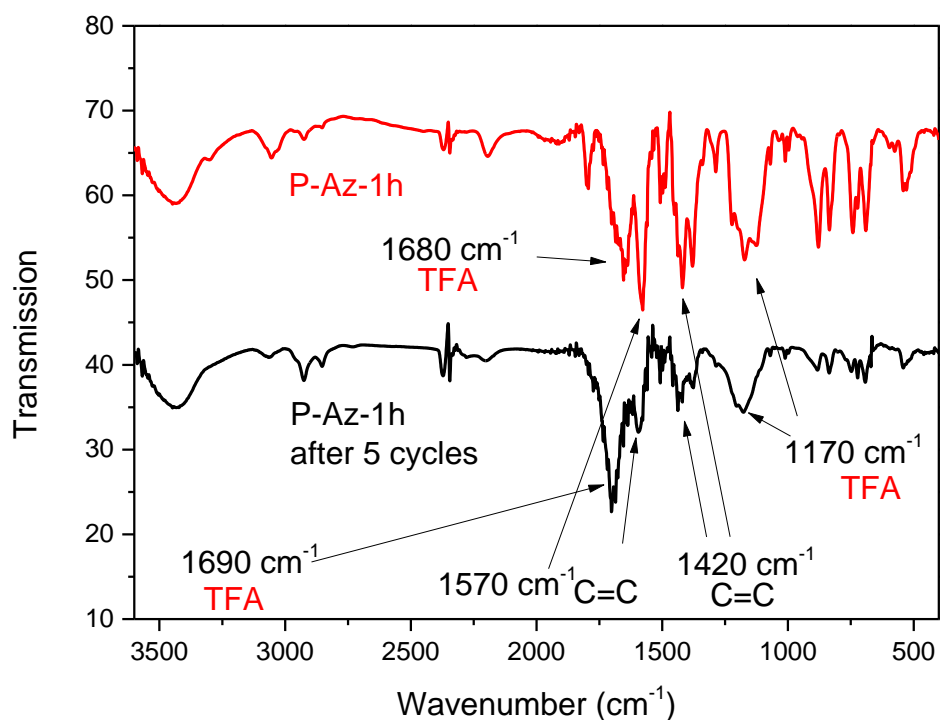


Figure 5.24: FT-IR spectra of P-Az-1h before and after 5 photocatalytic cycles of Cr(VI) to Cr(III) in water.

A similar morphology of P-Az-1h was observed by the SEM image (Figure 5.25).

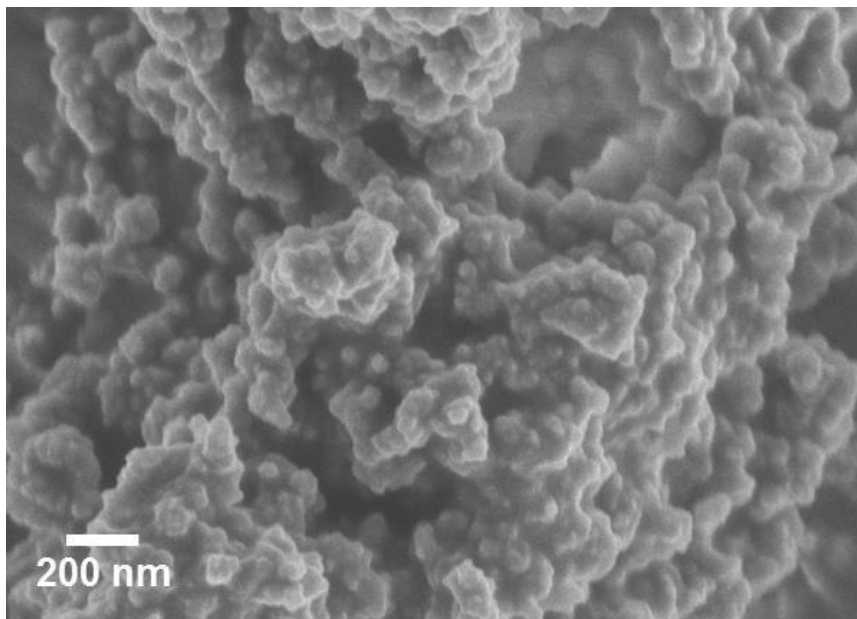


Figure 5.25: SEM image of P-Az-1h after 5 photoreduction cycles of Cr(VI) to Cr(III) in water.

The result demonstrates that the polymer can be used as highly effective and stable water-compatible photocatalyst. And in the absence of P-Az-1h, the photoreduction reaction did not occur under the same reaction conditions.

5.1.4 Conclusion

In conclusion, the incorporation of post-modifiable monomers into conjugated microporous polymers enabled highly functional materials allowing efficient control of hydrophilicity. This strategy holds the potential to transform any hydrophobic cross-linked polymer into water-compatible systems. We demonstrated a synthetic and modification method to obtain water-compatible, stable, visible light-active and heterogeneous photocatalysts via simple protonation of the pristine, highly hydrophobic conjugated microporous polymer networks. The obtained water-compatible polymers can serve as efficient and recyclable photocatalyst under visible light in water, i.e. real daily life conditions to reduce heavy metal ions such as Cr(VI) to Cr(III) under irradiation of a 23 W household energy saving light bulb. A cascade catalytic cycle could also be created by using additional metal cations as co-catalysts.

5.2 Heterophase photocatalyst from water-soluble conjugated polyelectrolytes: a self-initiation example under visible light

This chapter is based on the publication “Heterophase photocatalyst from water-soluble conjugated polyelectrolytes: a self-initiation example under visible light”, *Angew. Chem. Int. Ed.*, **2015**, 54, 14549–14553 (DOI: 10.1002/anie.201505325) and “Polyfluorene polyelectrolyte nanoparticles: synthesis of innovative stabilizers for heterophase polymerization”, *Macromol. Rapid Commun.*, **2014**, 35, 1925–1930 (DOI: 10.1002/marc.201400440) with copyright (2016) from Wiley VCH (Weinheim). In the previous chapter 5.1 the post modification method of hydrophobic porous polymers led to water-compatible photocatalysts. The control of hydrophilicity was achieved via a simple protonation step. In this chapter, the water-compatible porous polymers are obtained via cross-linking of hydrophilic conjugated polyelectrolyte chains.

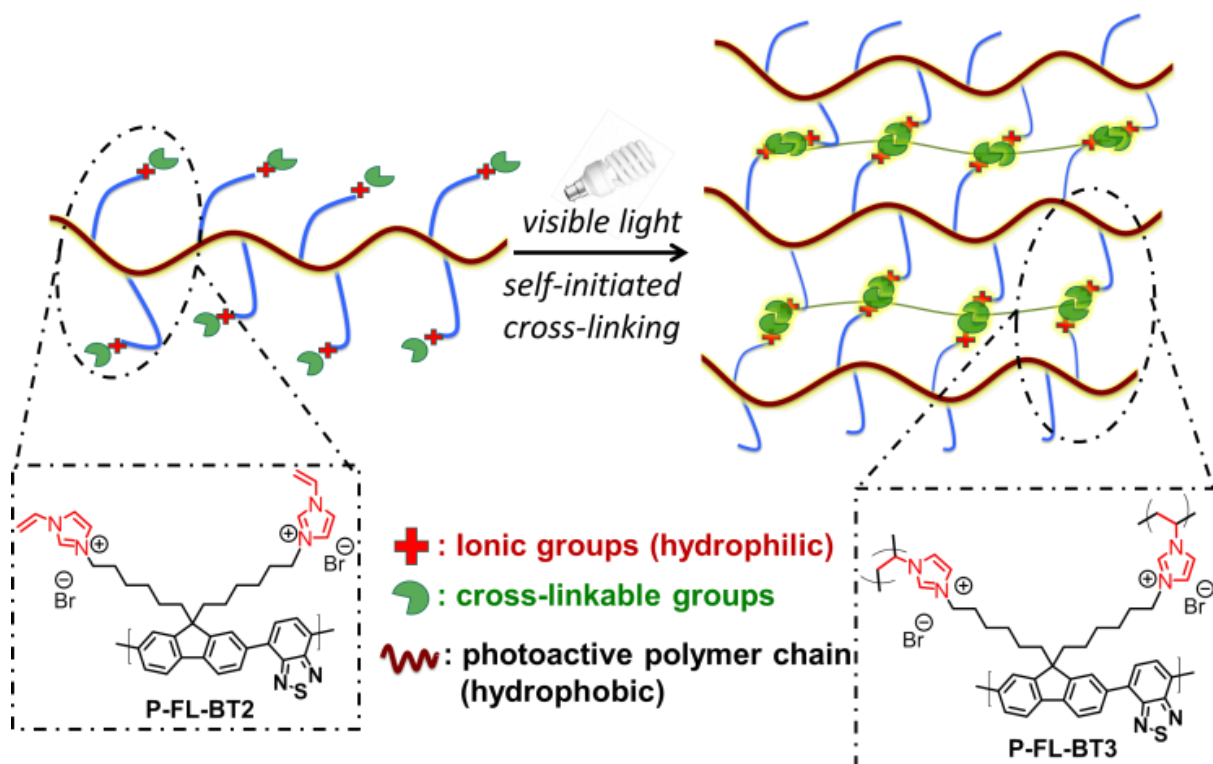
5.2.1 Introduction

From the view of heterogeneous catalyst design, two heterophase models are of high importance, the nanoparticulate system and the porous polymer. Nanoparticles are characterized by a high surface-to-volume ratio and porous materials by a large surface area.

In this section, the design and synthesis of water-compatible conjugated nanoparticulate and porous polymer bearing imidazolium-based ionic liquid units^[90, 97, 129-135] as highly efficient metal-free visible light photocatalyst in an aqueous environment is reported. Via incorporation of cross-linkable vinylimidazolium side chains onto the conjugated poly(benzothiadiazole/fluorene) backbone, both nanoparticles and porous monoliths, depending on the polymer concentration, were produced via a unique self-initiated intramolecularly radical cross-linking process under visible light irradiation. High photocatalytic activity of the as-synthesized polymer in aqueous medium was demonstrated in the degradation of rhodamine B and methylene blue dyes and photoreduction of Cr(VI) into Cr(III) under white light irradiation.

5.2.2 Synthesis and Characterization

The synthetic principle of targeted conjugated polymers is illustrated in Scheme 5.2. The water-soluble conjugated polymer P-FL-BT-2 bearing cross-linkable vinylimidazolium side groups was obtained by functionalization of the hydrophobic conjugated polymer P-FL-BT-1 bearing bis(6-bromohexyl)-fluorene units with N-vinylimidazole as shown in Figure 5.26.



Scheme 5.2: Illustration of the side product-free synthesis via visible light-promoted self-initiated cross-linking of a photoactive conjugated polymer bearing cross-linkable imidazolium-based ionic liquid units.

To note, a stepwise heating program from 60 to 100 °C is important to achieve a high quaternization degree without occurrence of dehydrobromination side reactions. Nuclear magnetic resonance (NMR) spectroscopy indicated a conversion of 92% from the bromohexyl groups in P-FL-BT-1 to vinylimidazolium bromide in P-FL-BT-2 (Figure 5.27).

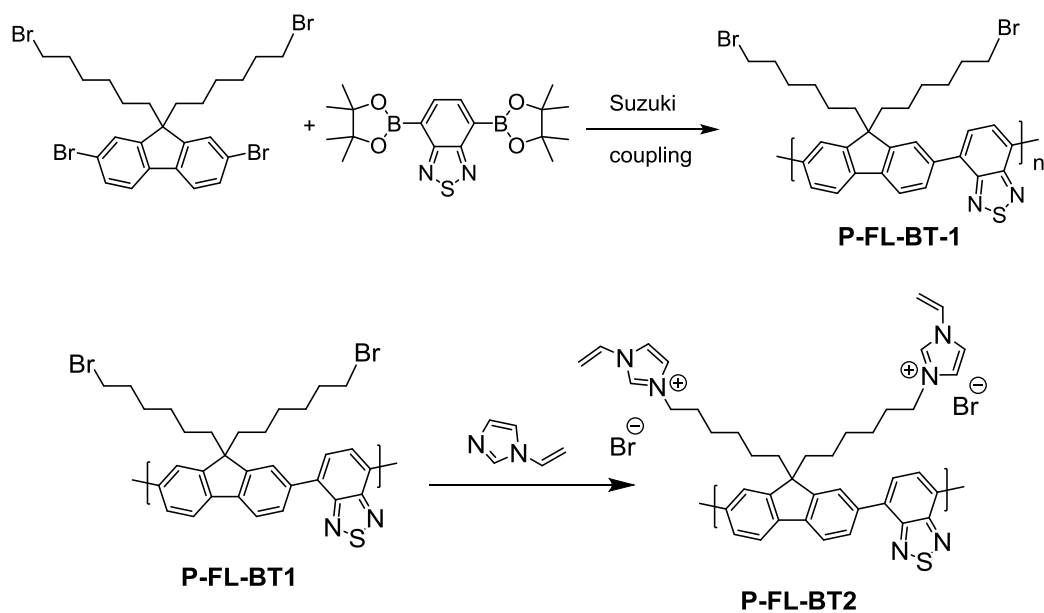


Figure 5.26: Synthetic route toward cross-linkable polyfluorenebenzothiadiazole (P-FL-BT2).

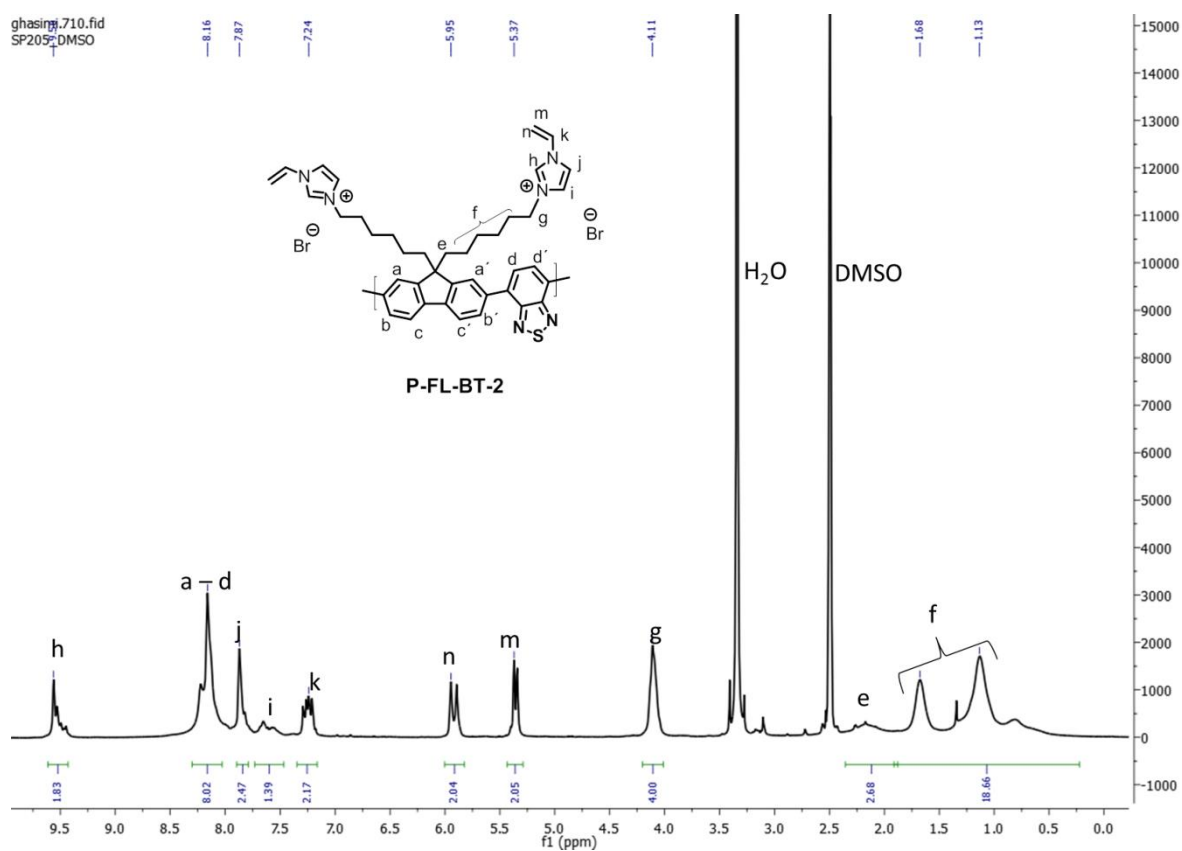


Figure 5.27: ¹H-NMR spectrum of P-FL-BT2.

Thermogravimetry analysis (TGA) showed comparable thermal behavior of P-FL-BT-1 and P-FL-BT-2 until about 230 °C (Figure 5.28).

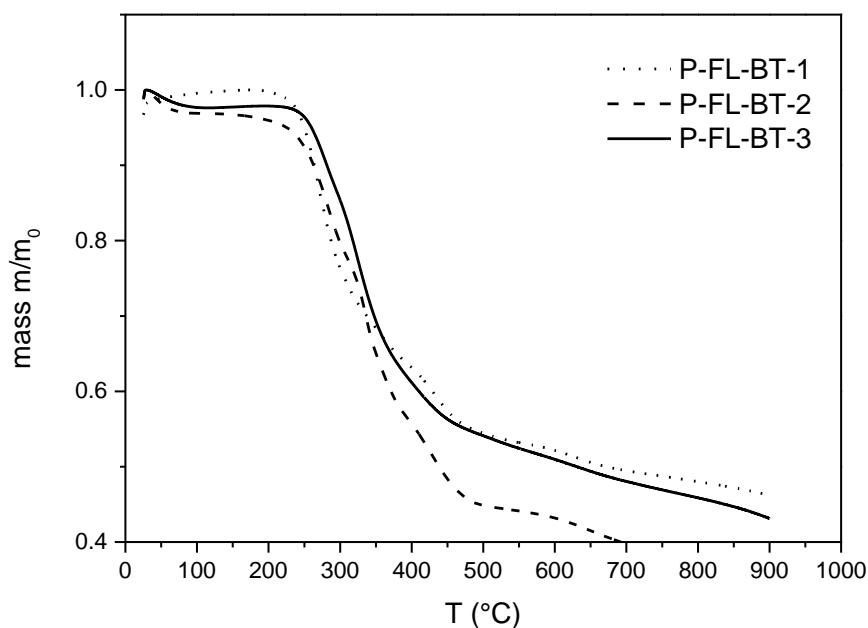


Figure 5.28: TGA analysis of the different polymers.

UV/vis absorption and fluorescence emission spectra showed a bathochromic shift of P-FL-BT-2 compared to P-FL-BT-1 (Figure 5.29).

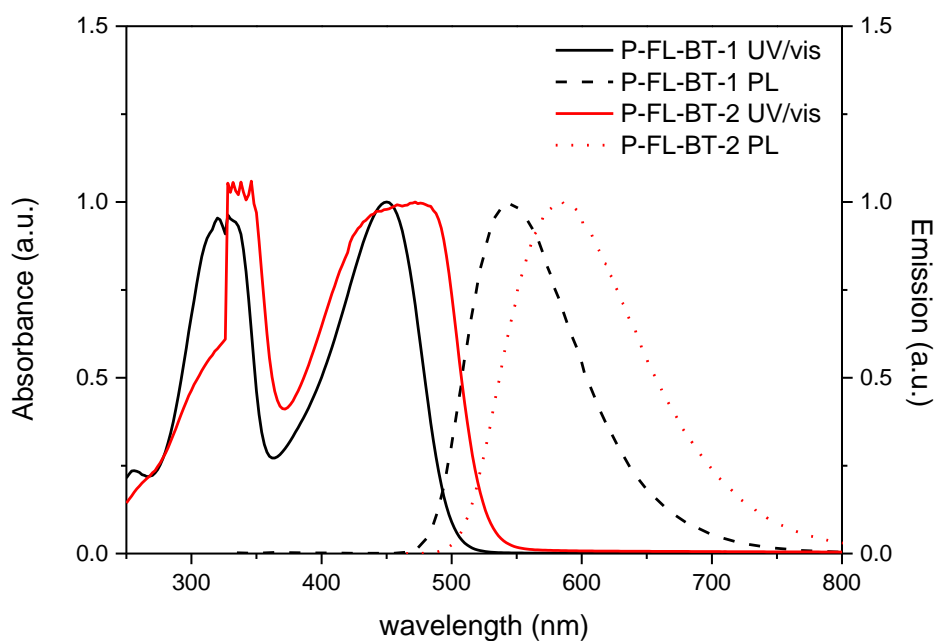


Figure 5.29: UV/vis absorption and emission spectra of P-FL-BT-1 and P-FL-BT-2.

A slightly increase of the band gap from 2.49 eV for P-FL-BT-1 to 2.37 eV for P-FL-BT-2 can be derived from the absorption edges (Table 5.3).

Table 5.3. Optical properties of P-FL-BT-1, P-FL-BT-2 and P-FL-BT-3.

Polymer	UV/vis λ_{\max} (nm)	Fluorescence λ_{\max} (nm)	Optical band gap (eV)
P-FL-BT-1	450	543	2.49
P-FL-BT-2	475	586	2.37
P-FL-BT-3	broad	600	2.11

5.2.3 Photocatalytic activity for self-initiated cross-linking and Characterization

It was previously shown that conjugated macromolecular systems could mediate the electron transfer under visible light irradiation and thus act as photosensitizer.^[136-140] Therefore, the conjugated structure of P-FL-BT-2 to our opinion should fulfill the requirement as a visible light-active photoinitiator. Additionally, given the fact that P-FL-BT-2 consists of hydrophilic imidazolium side chain and a hydrophobic polymer main chain, which creates an amphiphilic pattern, it could simultaneously act as a stabilizer for colloidal systems, a concept that has been proven previously for such IL-based polyelectrolytes.^[141-142] The critical micelle concentration (CMC) of P-FL-BT-2 was measured to be 0.90 mM (Figure 5.30).

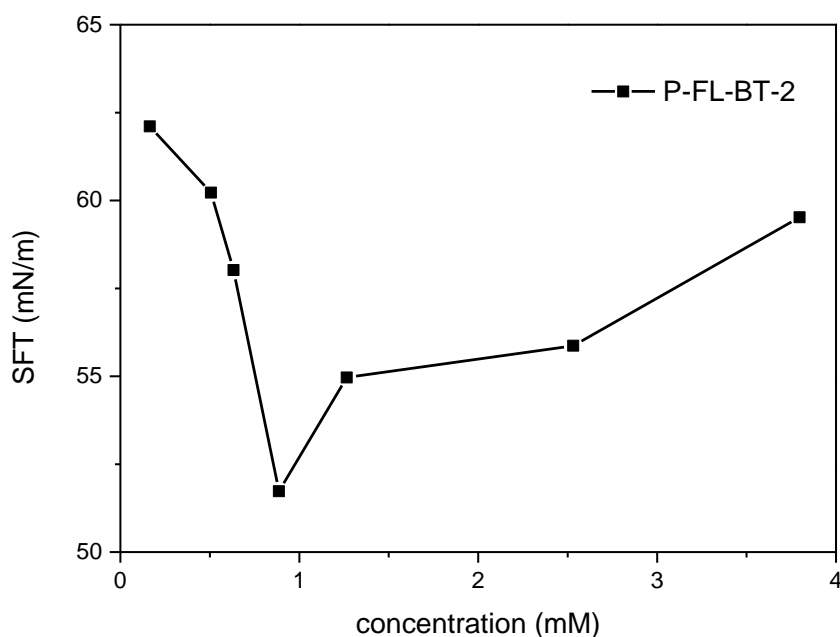


Figure 5.30: Critical micelle concentration measurement of P-FL-BT-2.

This value is similar to that of hexacetyltrimethylammonium bromide (CTAB, 0.92 mM), a widely used cationic surfactant in aqueous media. To investigate the double role of P-FL-BT-2 as visible light photoinitiator and stabilizer for colloidal systems, the following two experiments were performed. First, a dilute solution of P-FL-BT-2 in water (0.1 mg/ml) was irradiated under a white LED lamp without using any additional radical initiator, yielding a stable dispersion (Figure 5.31).

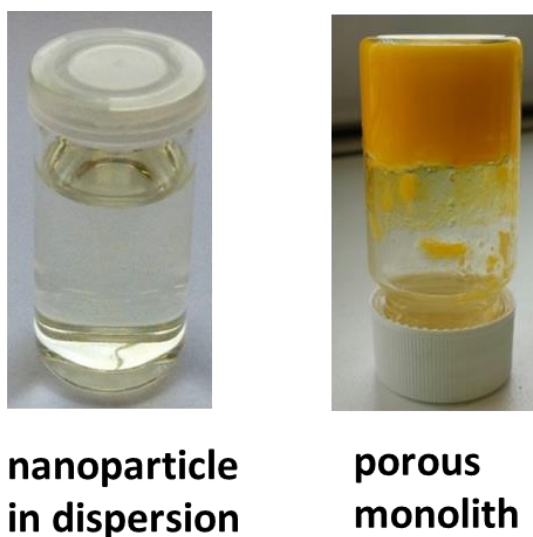


Figure 5.31: (a) Photographs of P-FL-BT-3 as nanoparticles in aqueous dispersion (0.10 mg/ml) and porous monolith (0.67 mg/ml).

Transmission electron microscopy (TEM) analysis showed particles of a diameter of 85 ± 10 nm, indicative of formation of nanoparticles of the cross-linked polymer P-FL-BT-3 (Figure 5.32).

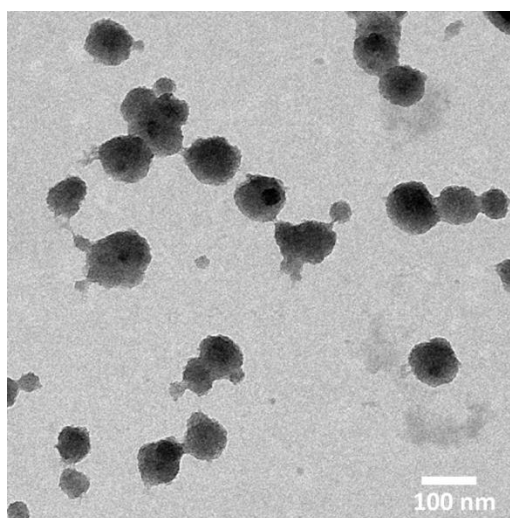


Figure 5.32: TEM image of P-FL-BT-3 as nanoparticles.

The dynamic light scattering (DLS) characterization gave a larger number average apparent diameter of ca. 141 nm (Figure 5.33).

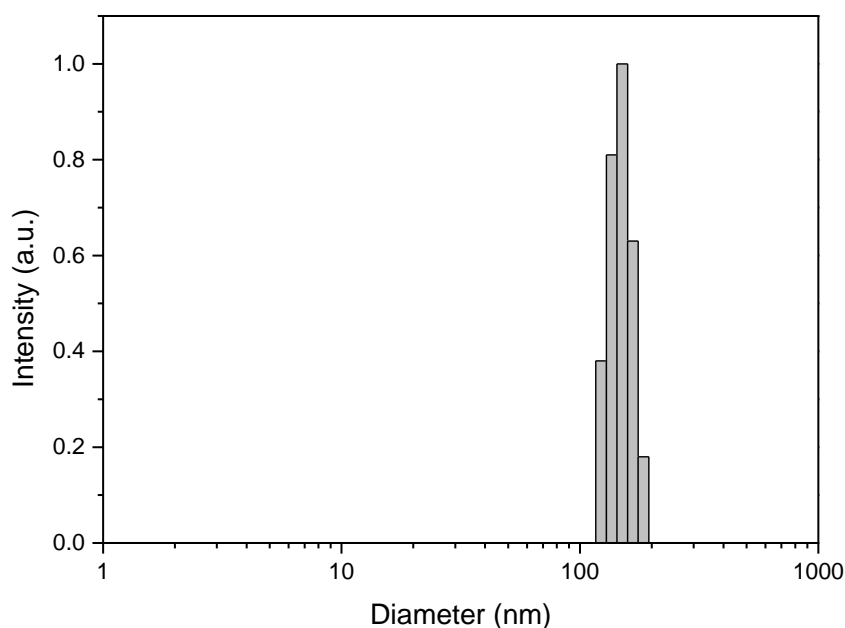


Figure 5.33: Dynamic light scattering measurement of P-FL-BT-3 as nanoparticles in water dispersion.

This can be explained by the fact that the nanoparticles in solution are in a swollen state with a hydration shell, which leads to a size expansion. The zeta-potential of the nanoparticle dispersion of +34.7 mV confirmed a stable colloidal system.

Further experimental details have been elucidated within a joint project with our collaboration partners Dr. Jiayin Yuan and Dr. Simon Prescher at the Max Planck Institute of Colloids and Interfaces in Golm, Germany. The following results in this work about the effects of anion exchange on dispersions have been taken from “Polyfluorene Polyelectrolyte Nanoparticles: Synthesis of Innovative Stabilizers for Heterophase Polymerization” published in *Macromol. Rapid Commun.* **2014**, 35, 1925–1930 with copyright (2016) from Wiley VCH (Weinheim). The anion exchange experiments were conducted by Dr. Simon Prescher.

In order to investigate the colloidal stability and colloidal behavior of CPE nanoparticles after anion exchange, nanoparticles based on P3Br have been synthesized. The cross-linkage to P3Br have have been achieved via radical polymerization of P2Br precursor (Figure 5.34).

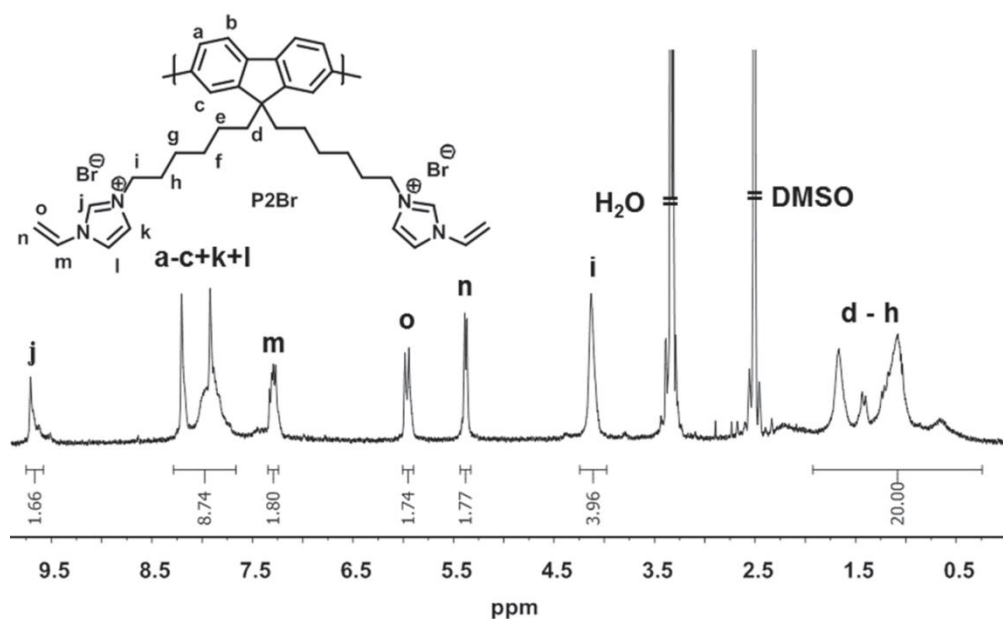


Figure 5.34: Proton NMR of P2Br.^[143]

In order to elucidate the effects of anion exchange on nanoparticles, P3Br nanoparticles were suspended in aqueous solution with BF_4^- , PF_6^- , and TFSI (Figure 5.35).^[143]

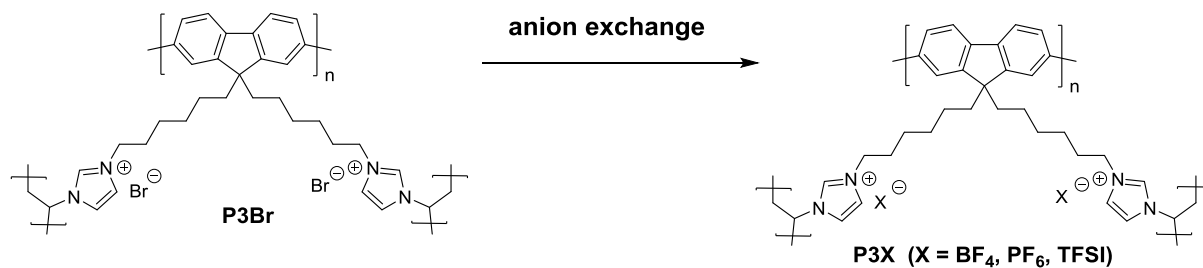


Figure 5.35: Anion exchange route of P3Br nanoparticles.

In Table 5.4 the dispersibility of charged P3Br nanoparticles in different media is described.

Table 5.4: Solubility of pristine P1, P3Br, and P3BF₄/PF₆/TFSI in different solvents; + = good, ± = medium, - = poor solubility.^{[36] [143]}

		Reichardt polarity scale ($E_T(30)$ [kcal/mol])				
		H ₂ O	THF	EtOAc	Acetone	DMF
Increased hydrophobicity ↓	Specimen					
	P3Br	+	-	+	+	+
	P3BF ₄	-	+	-	+	+
	P3PF ₆	-	-	-	+	+
	P3TFSI	-	+	-	+	+
	P1	-	+	-	-	±

According to the type of the counter anion, the hydrophilicity is increased with Br⁻ and decreased with PF₆⁻, BF₄⁻ and TFSI. With these hydrophobic anions the dispersability in acetone and DMF is significantly enhanced, while the formation of dispersions in water and ethylacetate are not possible. Due to amphiphilic properties of P3Br, stable dispersions are not only formed in water, but also in ethylacetate, acetone, and DMF. However, after the anion exchange with BF₄⁻ and TFSI the NPs become dispersible in THF, which was similar to the hydrophobic P1 polymer before the introduction of polar side groups. The tunable solution behavior makes it possible to process these NPs in different organic solvents. The variable dispersability indicates the property alternation of the nanoparticle surface, which can change the wetting behavior when applying these NPs as surface coatings. For example, P3Br dispersion formed a homogeneous film upon slow evaporation. By anion exchange, the contact angles measured from these films followed the hydrophobicity sequence Br⁻ (70°) < BF₄⁻ (89°) < PF₆⁻ (91°) < TFSI (94°).^[143]

Furthermore, the high interfacial activity of P-FL-BT-2 for a two phase emulsion system was demonstrated by the build-up of a porous polymer monolith by using the high internal phase emulsion polymerization technique (polyHIPE).^[144-146] Without any externally added surfactant, a stable water-in-oil emulsion formed by using a small amount of P-FL-BT-2 (4 mg in 5 ml H₂O/hexadecane (volume ratio 1:4)). Under white light irradiation, self-initiation and cross-linking took place and eventually resulted in a porous monolith (Figure 5.31), which is insoluble in common organic or aqueous solvents tested. The SEM images in a freeze-dried state showed a porous structure with interconnected pores inside the monolith (Figure 5.36).

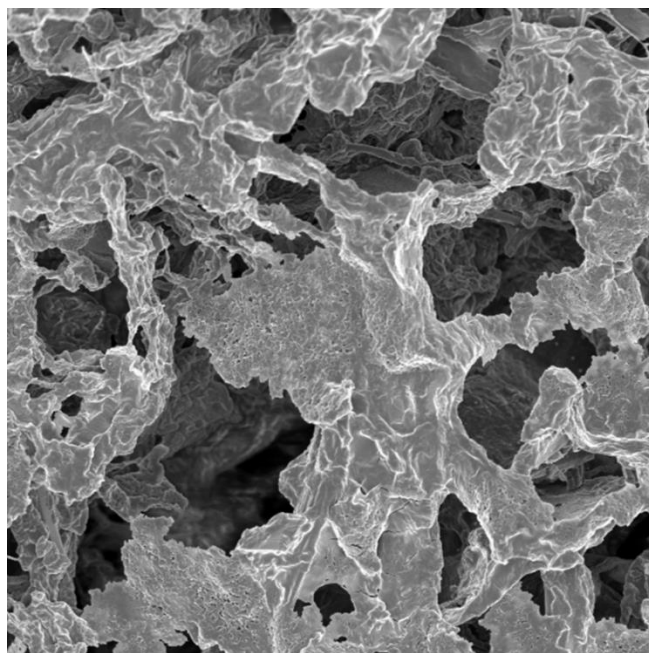


Figure 5.36: SEM image of a freeze-dried P-FL-BT-3 monolith.

In the confocal microscopy, water droplets of about 50 μm were observed inside the monolith in a wet state, indicating a large pore structure inside the polymer monolith (Figure 5.37).

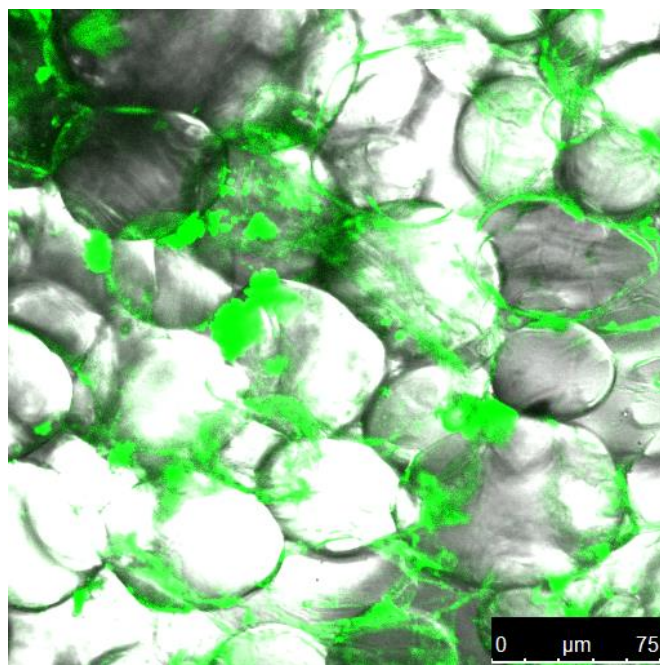


Figure 5.37: Confocal microscope image of P-FL-BT-3 monolith with its own fluorescence.

Solid-state ^{13}C CP-MAS NMR measurements showed the characteristic signals at ca. 113 and 120 ppm, which can be assigned to the carbons of the vinyl groups of P-FL-BT-2, disappeared after the light-induced cross-linking process and merged into the main aliphatic carbon signals between 20 and 60 ppm (Figure 5.38).

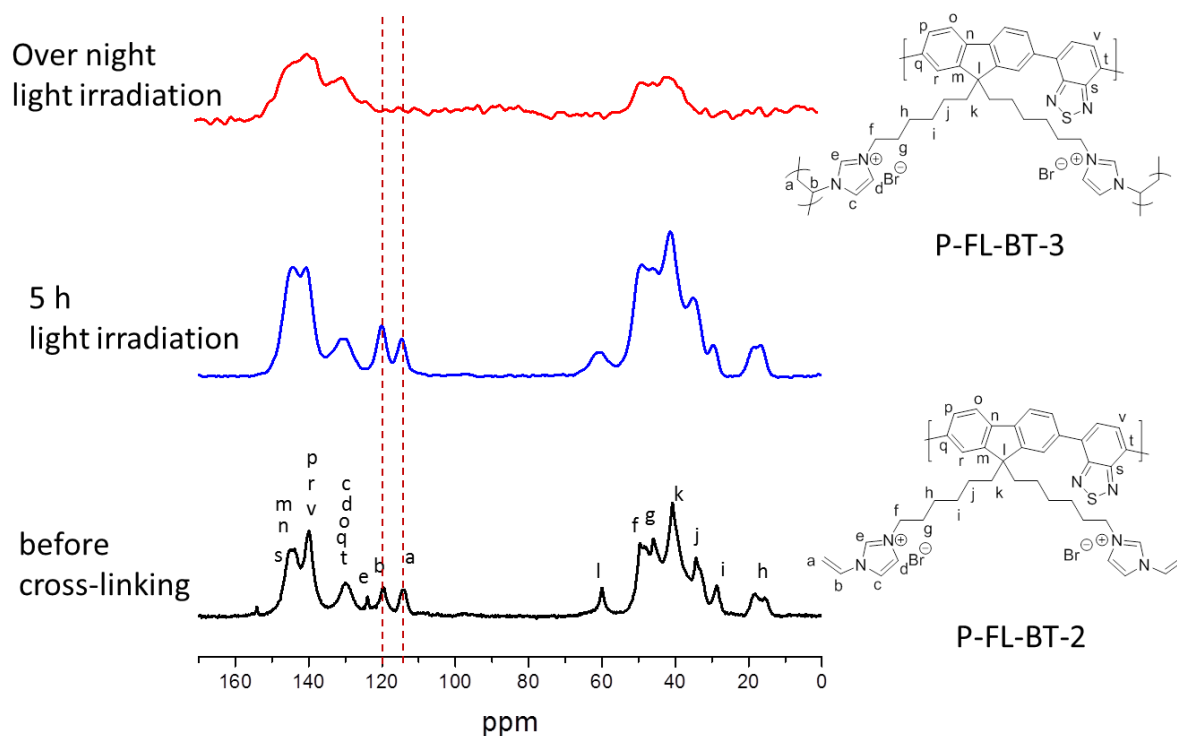


Figure 5.38: Solid-state ^{13}C CP MAS NMR spectra of P-FL-BT-2 before, during and after the light-induced cross-linking process. To note: the signals at ca. 113 and 120 ppm can be assigned to the carbons of the vinyl groups, which disappeared after the cross-linking and merged into the main aliphatic carbon signals between 20 and 60 ppm.

The UV/Vis diffuse reflectance spectrum (DRS) (Figure 5.39) of P-FL-BT-3 showed a slightly broader absorption band than P-FL-BT-1 and P-FL-BT-2 (Figure 5.40).

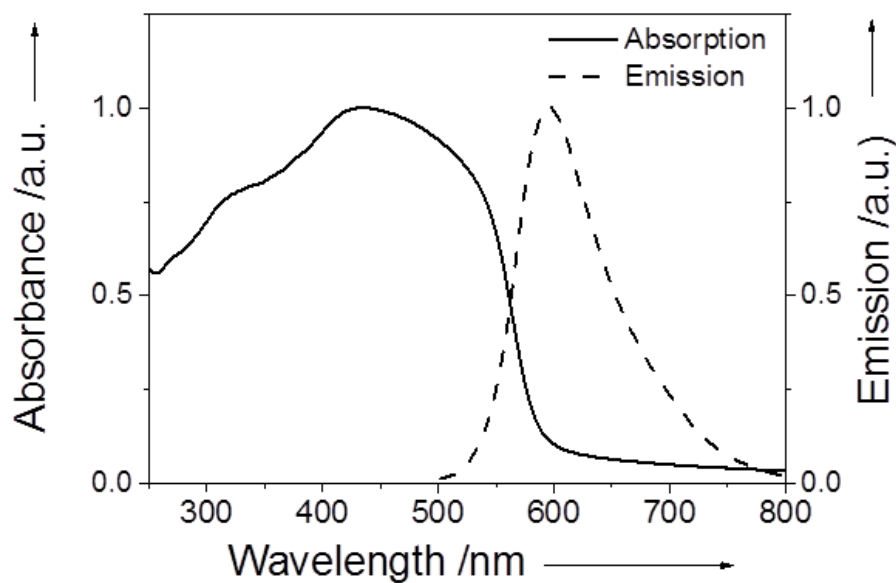


Figure 5.39: UV/Vis DRS and fluorescence emission spectra of monolithic P-FL-BT-3.

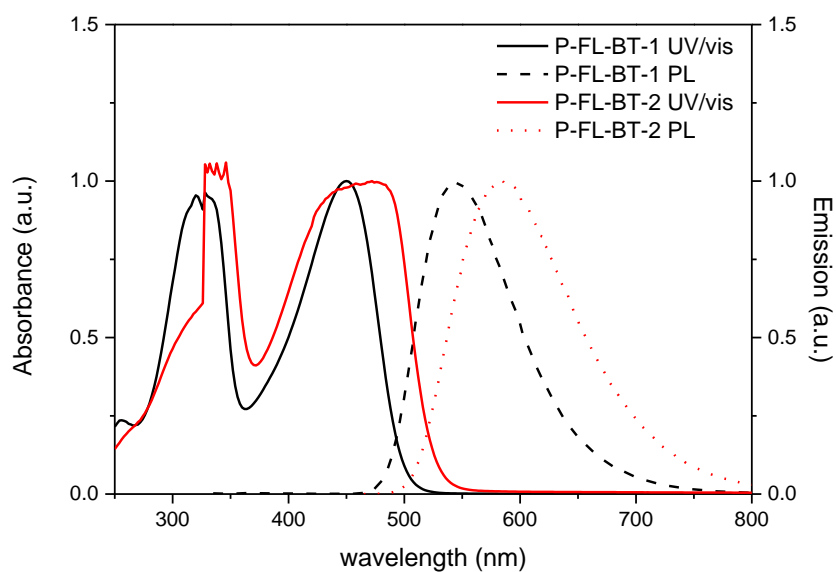


Figure 5.40: UV/vis absorption and emission spectra of P-FL-BT-1 and P-FL-BT-2.

A similar emission range with a maximum at 600 nm can be seen in comparison, i.e. in the visible light range. A band gap of ca. 2.11 eV can be derived from the absorption edge. This corresponds to the observed band gap of 2.07 eV measured by cyclic voltammetry (CV) (Figure 5.41).

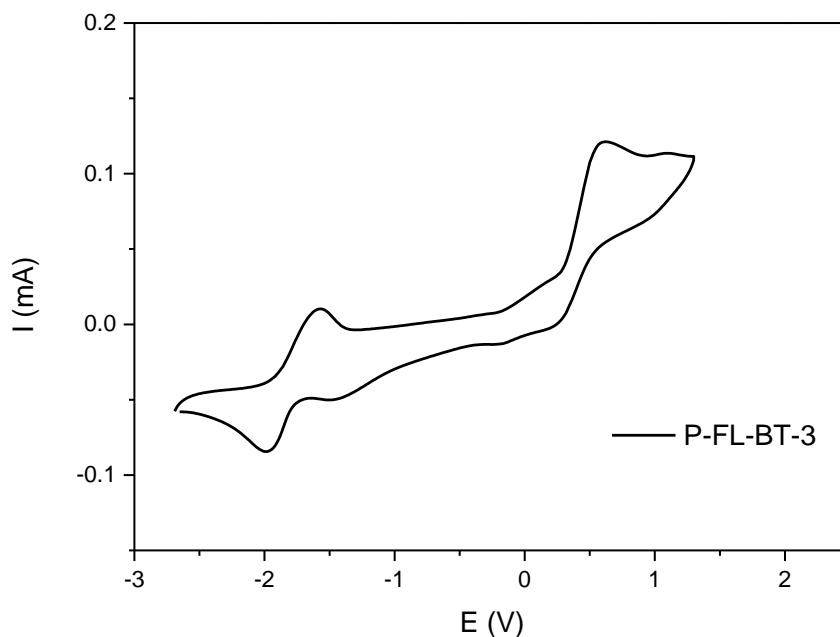


Figure 5.41: *Cyclic voltammetry of P-FL-BT-3 monolith.*

5.2.4 Photocatalytic Dye Degradation, Photoreduction of Cr(VI), Photopolymerization of Methyl Methacrylate (MMA)

Both aforementioned experiments demonstrated the ability of P-FL-BT-2 serving as visible light initiator for radical polymerization and simultaneously as stabilizer for emulsions. We suggest a modified initiation mechanism similar to the literature.^[147] Under visible light irradiation, the P-FL-BT-2 undergoes a transition to a long living triplet state, which subsequently reacts with the vinyl group of the imidazolium unit, forming an alkyl radical and a radical cation of P-FL-BT-2. The alkyl radical further attacks other vinyl groups and initiates the cross-linking process. The radical cation of P-FL-BT-2 likely catches a proton from the adjacent environment, most likely water, followed by a return to the ground state and completing of the catalytic cycle. To demonstrate the ability of the conjugated polymer backbone as visible light photoinitiator, a control experiment, i.e. the free radical polymerization of methyl methacrylate (MMA) using the hydrophobic polymer P-FL-BT-1 as photoinitiator was carried out. As expected, PMMA was obtained under the same light irradiation conditions without other initiators (Figure 5.42), proving the photoactivity of the conjugated backbone of the polymer.

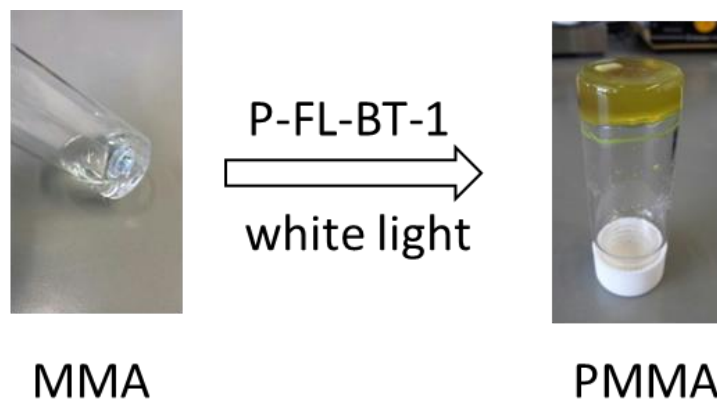


Figure 5.42: Visible light initiated free radical polymerization of MMA using P-FL-BT-1 as photoinitiator.

The feasibility of the monolithic P-FL-BT-3 as a promising heterogeneous photocatalyst in aqueous medium was tested. As organic dyes and heavy metals are well-known pollutants in industrial waste water, the photocatalytic degradation of rhodamine B and methylene blue as two model dyes, and photoreduction of aqueous Cr(VI) were carried out under visible light irradiation using the same white lamp. As displayed in Figure 5.43, the two organic dyes showed degradation rates of over 90% after irradiation of ca. 70 min. This is comparable to porous carbon nitride (C_3N_4), a state-of-art non-metal-based visible light photocatalyst, given the fact that the concentration of P-FL-BT-3 used here was about 10 times lower (0.1 mg/ml).^[148]

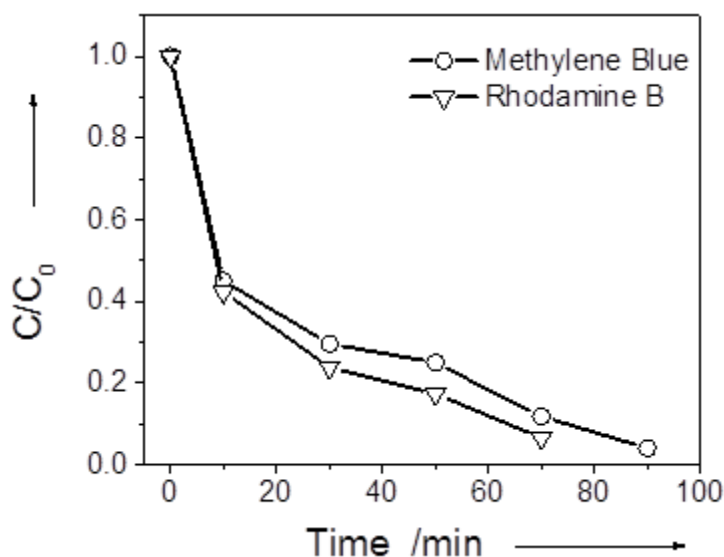


Figure 5.43: Photocatalytic degradation of rhodamine B and methylene blue.

Figure 5.44 displays the photocatalytic reduction of Cr(VI), with an almost quantitative conversion from the highly toxic Cr(VI) to much mild Cr(III)^[125] after 120 min. The efficiency of P-FL-BT-3 for Cr(VI) reduction was found to be also comparable to recently reported metal-based photocatalysts such as BiVO₄/Bi₂S₃^[149] or SnS₂/SnO₂^[150] under similar reaction conditions.

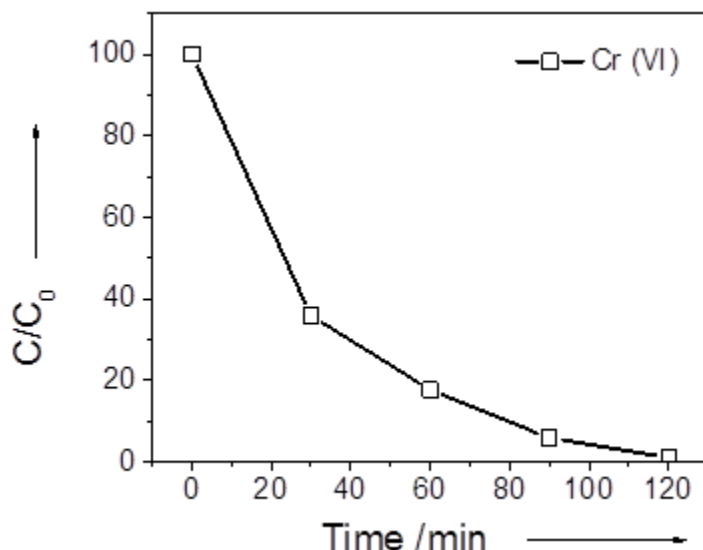


Figure 5.44: Photocatalytic reduction of Cr(VI) using P-FL-BT-3 in water under white light irradiation. C is the concentration of the organic dyes or Cr(VI), and C_0 is the initial concentration after reaching adsorption/desorption equilibrium in dark.

The photodegradation of the organic dyes in water is likely mediated by photochemically generated singlet oxygen, similar to a previous study.^[151] By absorption of light, P-FL-BT-3 as photosensitizer is excited to its singlet state (S) followed through subsequent intersystem crossing by population of a triplet state (T). The excited P-FL-BT-3 can transfer energy and spin to the ground state triplet oxygen, thus forming the excited singlet oxygen to attack the organic dyes.^[152-153] The potential required for the redox reaction from Cr(VI) to Cr(III) is 1.33 V (vs. NHE).^[126] P-FL-BT-3 has a band gap of 2.07 eV and the conduction band lies at -1.13 V (vs. NHE, Table 5.5) in the excited state, which is sufficient for the reduction of Cr(VI) to Cr(III).

Table 5.5: Electrochemical properties of P-FL-BT-3 monolith. (The HOMO/LUMO levels are calculated according to the equations: $E_{HOMO} = -(4.8 - E_{oxi-onset})$ eV and $E_{LUMO} = -(4.8 - E_{red-onset})$ eV^[154], ferrocene/ferrocenium redox-couple is used as reference).

$E_{Ox-Onset}$ [V]	$E_{red-Onset}$ [V]	HOMO [eV]	LUMO [eV]	Band gap [eV]
0.30	-1.77	-5.10	-3.03	2.07

We then studied the stability and reusability of the monolithic P-FL-BT-3 as heterogeneous photocatalyst by conducting the same photodegradation reaction of rhodamine B for 10 repeating cycles (Figure 5.45).

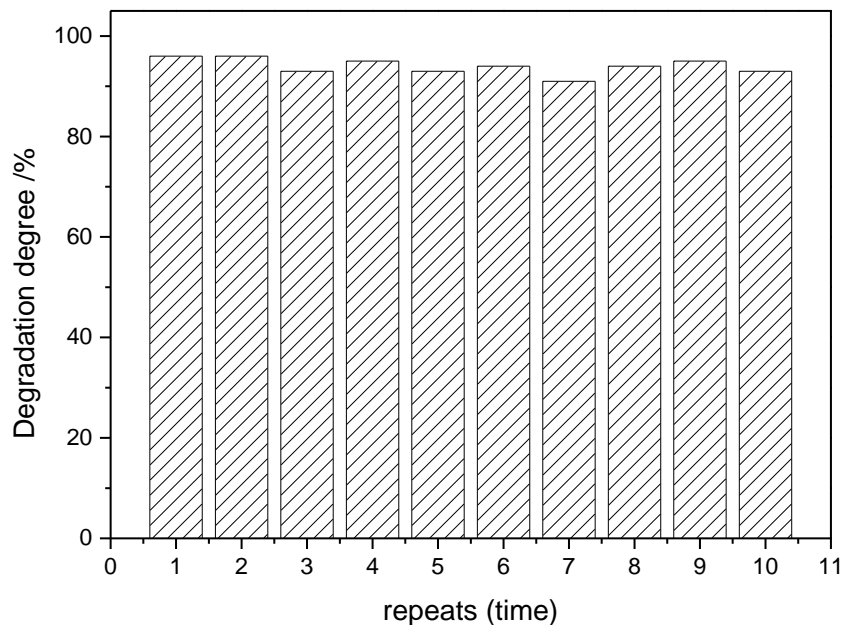


Figure 5.45: Repeating experiments of the photocatalytic degradation of Rhodamine B using P-FL-BT-3 in water under white light irradiation.

Rhodamine B was degraded almost quantitatively in each run, demonstrating that P-FL-BT-3 can be used as highly effective and stable water-compatible photocatalyst. It is worth to note that in the absence of P-FL-BT-3, these photoreactions did not occur at all under the same reaction conditions. A study with different scavengers^[155-157] showed that reactive species such as superoxide ($\cdot\text{O}_2^-$) played a crucial role during the photodegradation process of the organic dye. Other active species such as the photogenerated hole (h^+) or H_2O_2 only took a minor part to the catalytic process, while the effect of *singlet* oxygen ($^1\text{O}_2$) and hydroxy radical ($\cdot\text{OH}$) was minimal existent (Figure 5.46).

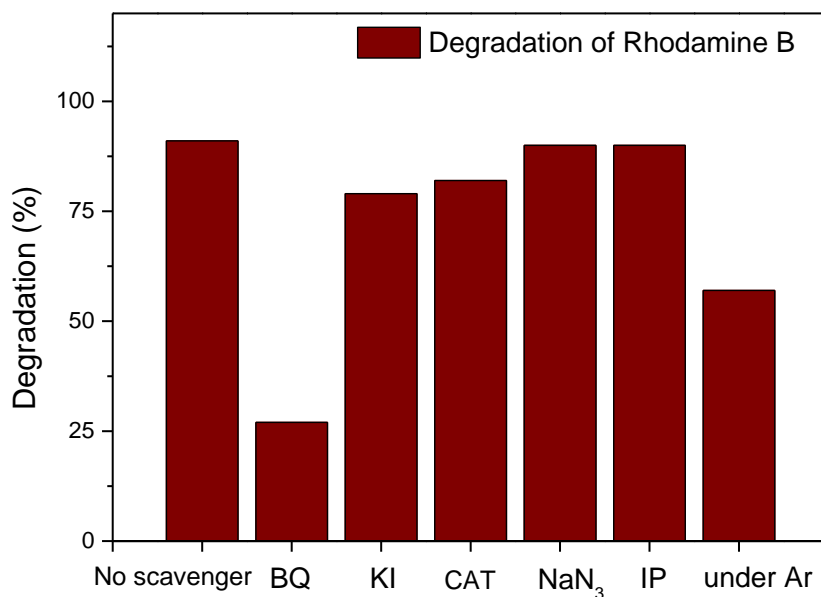


Figure 5.46: Effect of different scavengers, benzoquinone (BQ), potassium iodide (KI), catalase (CAT), sodium azide (NaN₃), isopropanol (IP) and the absence of oxygen (under argon (Ar)) on the degradation of rhodamine B over P-FL-BT-3 in water under 1 h of white light irradiation.

Note that the study on possible reactive species during the photodegradation of rhodamine B was conducted using different scavengers such as sodium azide (NaN₃) as ¹O₂ scavenger, benzoquinone (BQ) as [•]O₂⁻ scavenger, isopropanol (IP) as [•]OH scavenger, catalase (CAT) as H₂O₂ scavenger and potassium iodide (KI) as h⁺ scavenger. [155-157]

5.2.5 Conclusion

In summary, the presented design strategy enables the formation of hydrophilic cross-linked polymers from linear polyelectrolytes. The preceded hydrophilic modification of linear polymers and the incorporation into polymer networks enables materials with multiple properties. The formation of water-compatible heterogeneous polymers from linear polymers as multifunctional materials was investigated. The successful synthesis and application of a conjugated polyelectrolyte photocatalyst working under heterophase aqueous environment was demonstrated. The incorporation of the 1-alkyl-3-vinylimidazolium bromide ionic liquid species into the linear conjugated polymer backbone, a synthetically simple step, causes a multiple synergistic effects, here the water-solubility, self-photoinitiation ability, and interfacial activity. The obtained monolithic polymer can serve as efficient, recyclable, cost-effective heterogeneous photocatalyst under visible light in water, i.e. real daily life conditions to degrade organic dyes and reduce heavy metal ions such as Cr(VI) to Cr(III). We believe the design strategy and principle reported here can offer a very clean and side product-free, especially the surfactant-free synthetic pathway to obtain water-compatible photoactive polymers with desired morphology and a broader potential for other applications in aqueous medium under sustainable and environmentally friendly conditions.

5.3 Photocatalytic Stille-type coupling reactions using conjugated organic catalysts with visible light

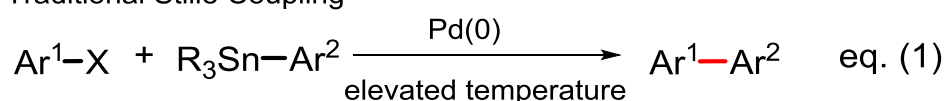
This section is based on results from the unpublished article “Photocatalytic Stille-type coupling reactions using conjugated organic catalysts with visible light”. The previous chapters dealt with the design of polymer-based heterogeneous photocatalysts and the aqueous applications. In this chapter, conjugated microporous polymers are applied to metal-free photocatalytic C-C coupling reactions. The main objective is to elucidate the photocatalytic reaction mechanism.

5.3.1 Introduction

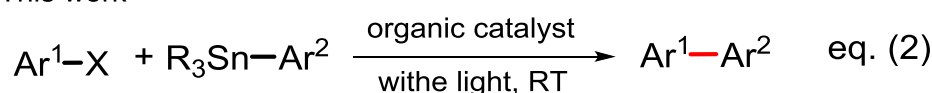
This section deals with the palladium-free photocatalytic Stille-type carbon-carbon coupling reaction of aryl-stannanes and aryl-iodides. Conjugated azulene-containing polymers were chosen as the visible light-active and pure organic photocatalyst. A broad range of different substrates were tested. The underlying photocatalytic reaction mechanisms were investigated in detail.

The Stille cross-coupling reaction is a highly versatile tool for carbon-carbon bond formations from aryl halides and aryl stannanes.^[158-160] The major requirement for the Stille coupling, however, is the necessary use of palladium complexes as catalysts (eq. 1). The search for a metal-free and pure organic alternative for the Pd-based catalyst still remains a challenge for the organic and materials chemists.

Traditional Stille Coupling



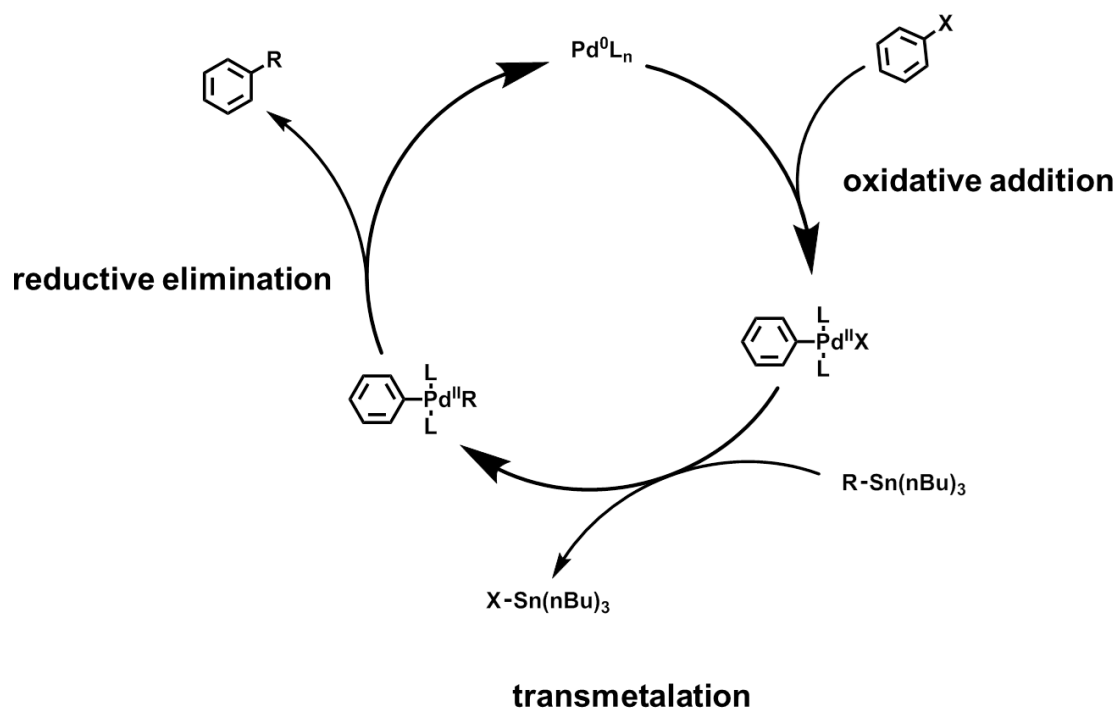
This work



Ar: aryl; X: halide; R: alkyl

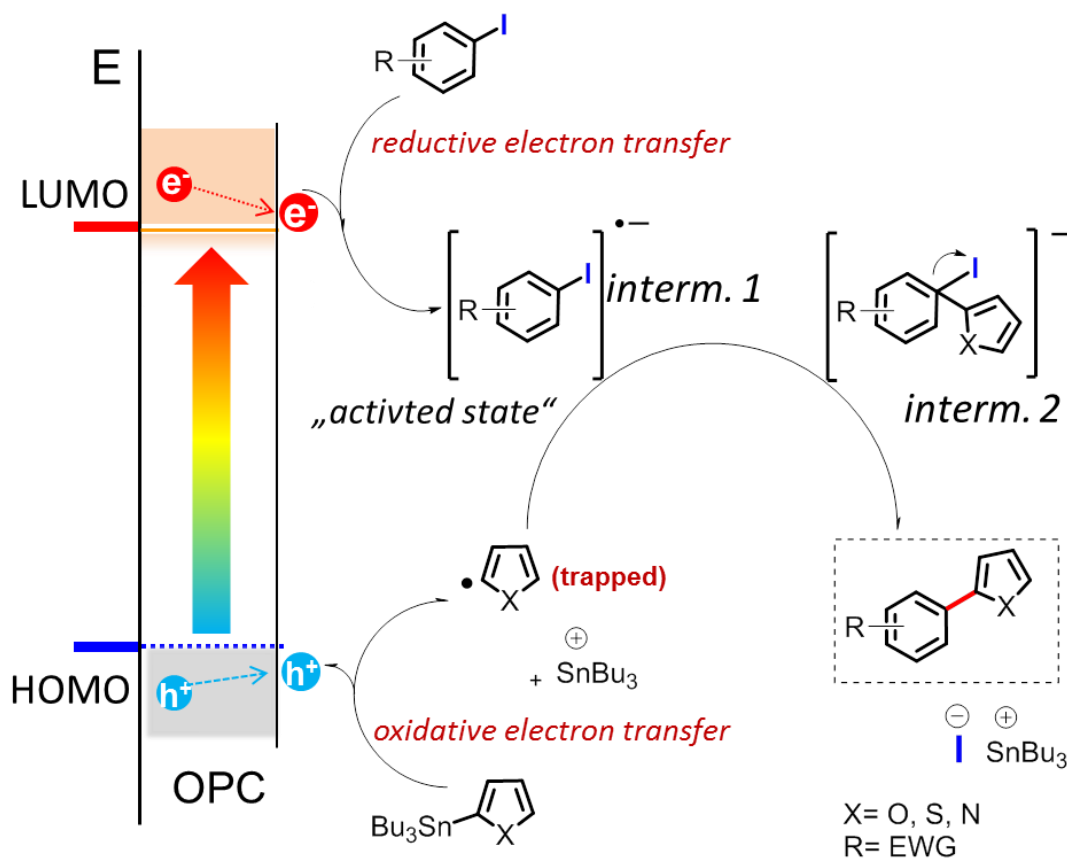
The reaction mechanism of the Stille coupling (Scheme 5.3) is characterized by distinct reaction steps. The oxidative addition of the aromatic halide to the Pd(II) complex, the rate determinant transmetalation between Pd(II) complex and the organotin compound and finally the reductive elimination where the coupling product is released and the Pd(0) is recovered for the next catalytic cycle.^[161-162] However, within the mechanistic key steps of the Stille

coupling, the oxidative addition of the aromatic halide to the palladium complex requires usually elevated temperatures in order to provide the activation enthalpy.^{[163] [164]}



Scheme 5.3: The palladium based catalytic cycle of the Stille coupling reaction.

Here, in this project a new photocatalytic Stille-type aromatic C-C bond formation pathway is presented (eq. 2) without the need of using palladium based catalysts or elevated temperatures. The reaction mechanism is driven by the coupling reaction of the photogenerated aryl radical, which was obtained via oxidative destannylation by the photogenerated hole of the organic photocatalyst, with the aryl halide, which was activated by the photogenerated electron. The proposed reaction mechanism is illustrated in Scheme 5.4. It was found that the reductive activation of the aryl halide by the photogenerated electron was mandatory for the successful C-C bond formation reaction. And both oxidation and reduction potentials of the corresponding aryl stannanes and iodides were crucial for the activation of the coupling reaction. Further studies using radical trapping agent and scavengers were conducted to reveal the mechanistic insight of the photocatalytic Stille-type coupling reaction.



Scheme 5.4: Proposed reaction mechanism of the palladium-free photocatalytic Stille-type coupling reaction using conjugated organic catalysts as photocatalyst (OPC: organic photocatalyst; interm.: intermediate; EWG: electron withdrawing group).

5.3.2 Synthesis and Characterization

In this study, conjugated azulene-containing polymers were chosen as the visible light-active and pure organic photocatalyst. The conjugated microporous polymer network P-Az-B was obtained via Suzuki cross-coupling reaction of 1,3-dibromoazulene with 1,3,5-phenyltriboronic acid tris(pinacol) ester with 1,3-dibromoazulene (Figure 5.47).

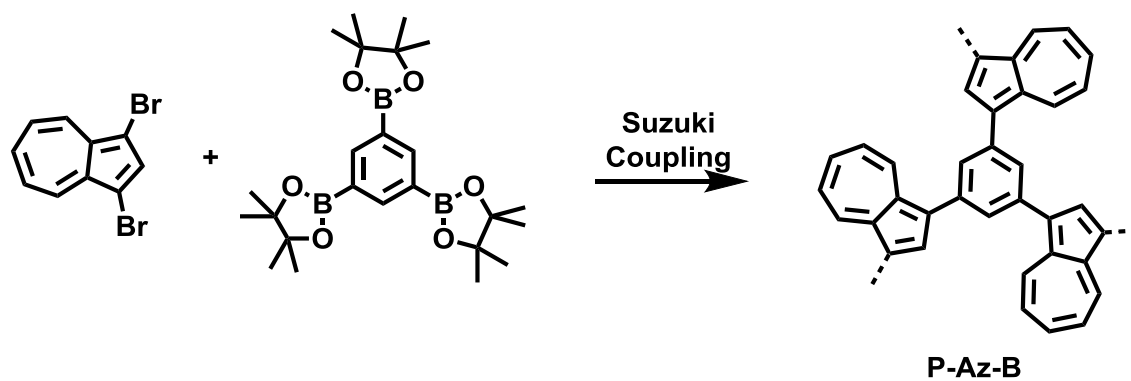


Figure 5.47: Synthesis of *P-Az-B* via Suzuki cross-coupling reaction.

To note, a modified synthetic route was employed. Here, the comonomer 1,3-dibromoazulene was added stepwise over three days into the reaction mixture, in order to obtain high porosity of the polymer. *P-Az-B* was insoluble in all common organic solvents tested and according to the thermogravimetric analysis highly stable (Figure 5.48).

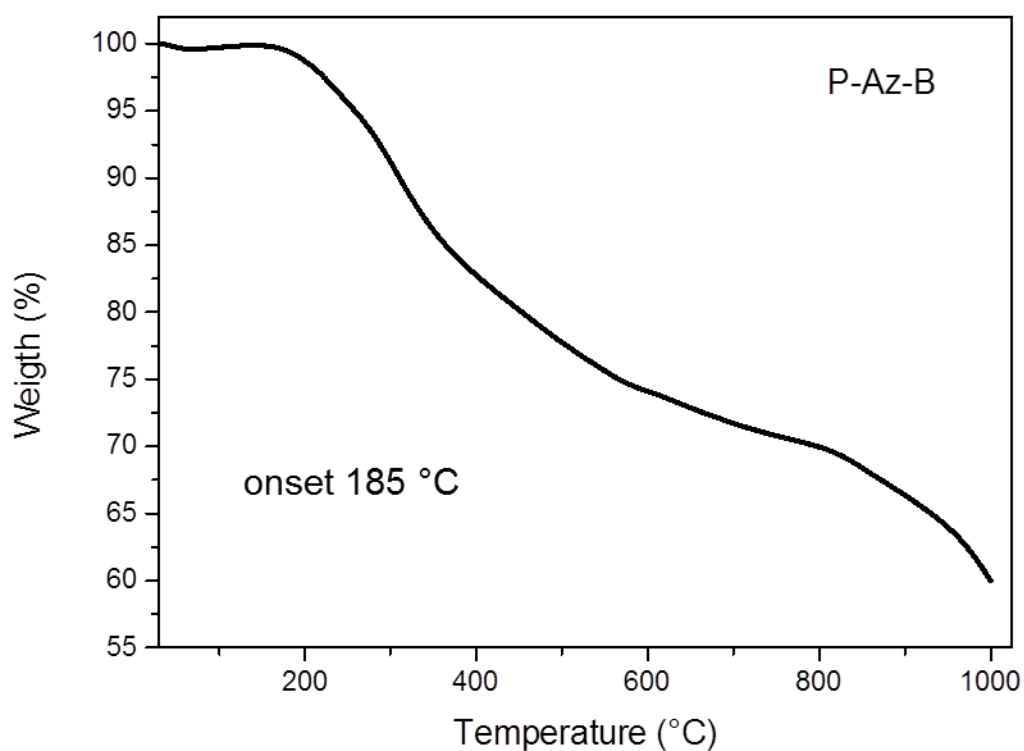


Figure 5.48: Thermogravimetric analysis of *P-Az-B* from 25 to 1000°C under nitrogen.

The SEM and TEM of P-Az-B showed a fused porous particle-like morphology (Figure 5.49).

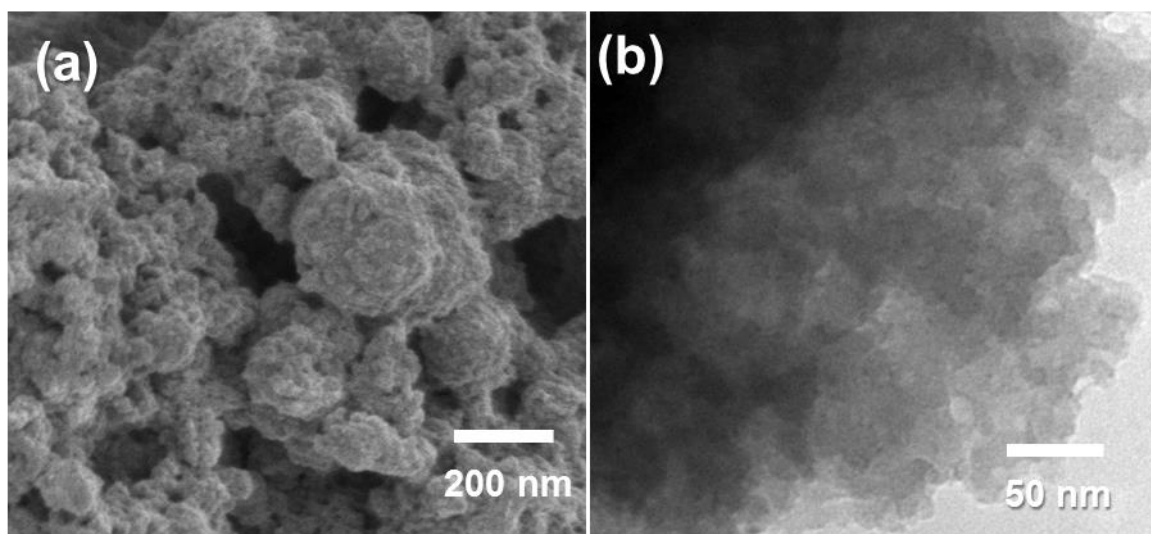


Figure 5.49: SEM (a) and TEM (b) images of P-Az-B.

The Brunauer-Emmett-Teller (BET) surface area of P-Az-B obtained via the modified stepwise-addition synthetic route was found to be 292 m²/g, achieving a significant increase of ca. 17-fold compared to the same polymer via bulk synthesis ($S_{\text{BET}} = 17 \text{ m}^2/\text{g}$, Table 5.6 and Figure 5.50a+c).

Table 5.6: Porosity data of P-Az-Bs which were obtained in different solvents and in comparison with the successive addition method of the monomer in DMF.

Solvent	S_{BET} (m ² /g)	Pore Size (nm)	Pore Volume (cm ³ /g)
THF	6	3.3	0.009
Dioxane	8	2.9	0.014
DMF	17	1.5	0.024
DMF (stepwise-addition of monomers)	292	1.5	0.28

According to increased surface areas, the averaged pore size analysis shows decreased values. Moreover, the overall pore size distribution shifted to lower pore widths when the stepwise-addition method was used (Figure 5.50b+d).

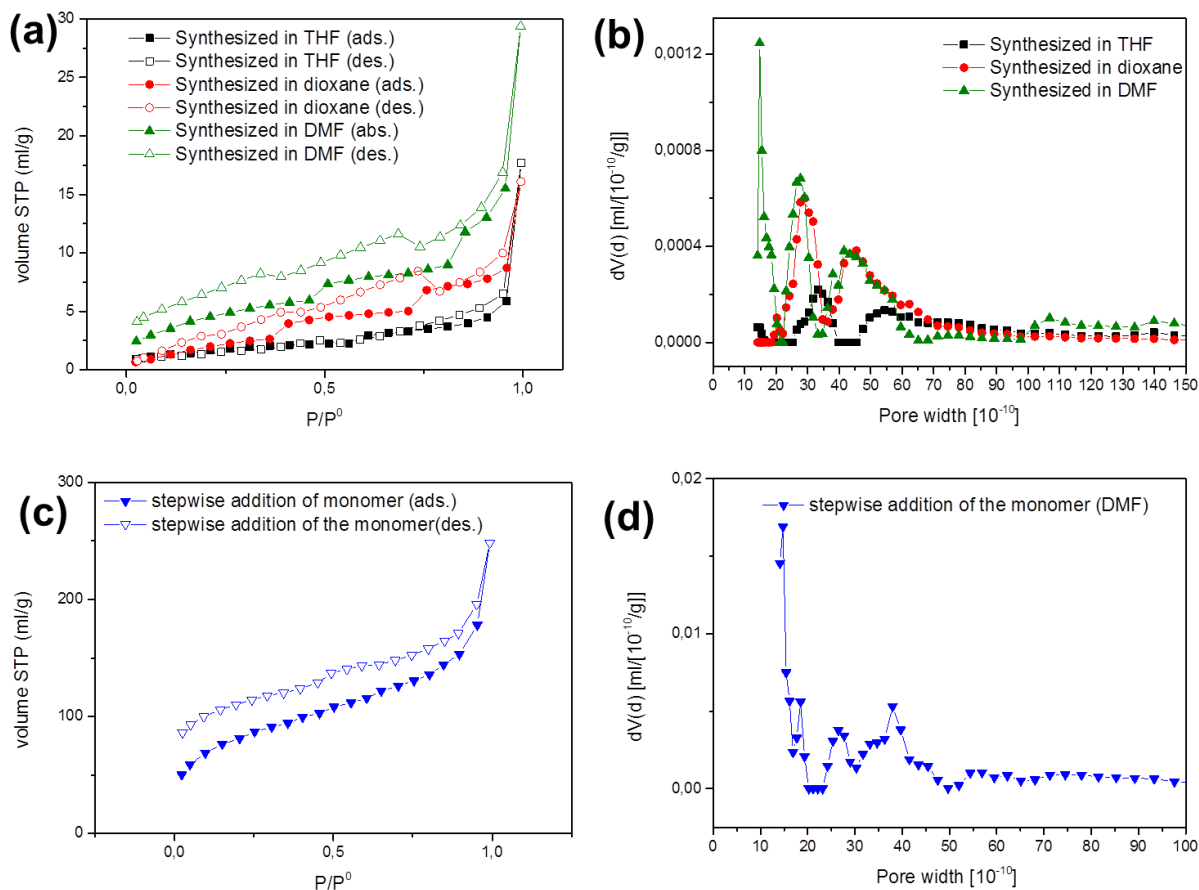


Figure 5.50: Gas sorption isotherms of the P-Az-B synthesized in (a) different solvents, (b) via stepwise addition of monomers during the polymerization, and (c) pore size distributions of P-Az-B synthesized in different solvents, and (d) via stepwise addition of monomers.

¹³C CP/MAS NMR spectroscopy (Figure 5.51) showed characteristic peaks at 123, 130, 136 and 137 ppm, which can be assigned to the 5- and 7-membered rings of the azulene unit. The peaks at 123 and 130 ppm were assigned to aromatic carbons of the phenyl units in the polymer backbone.

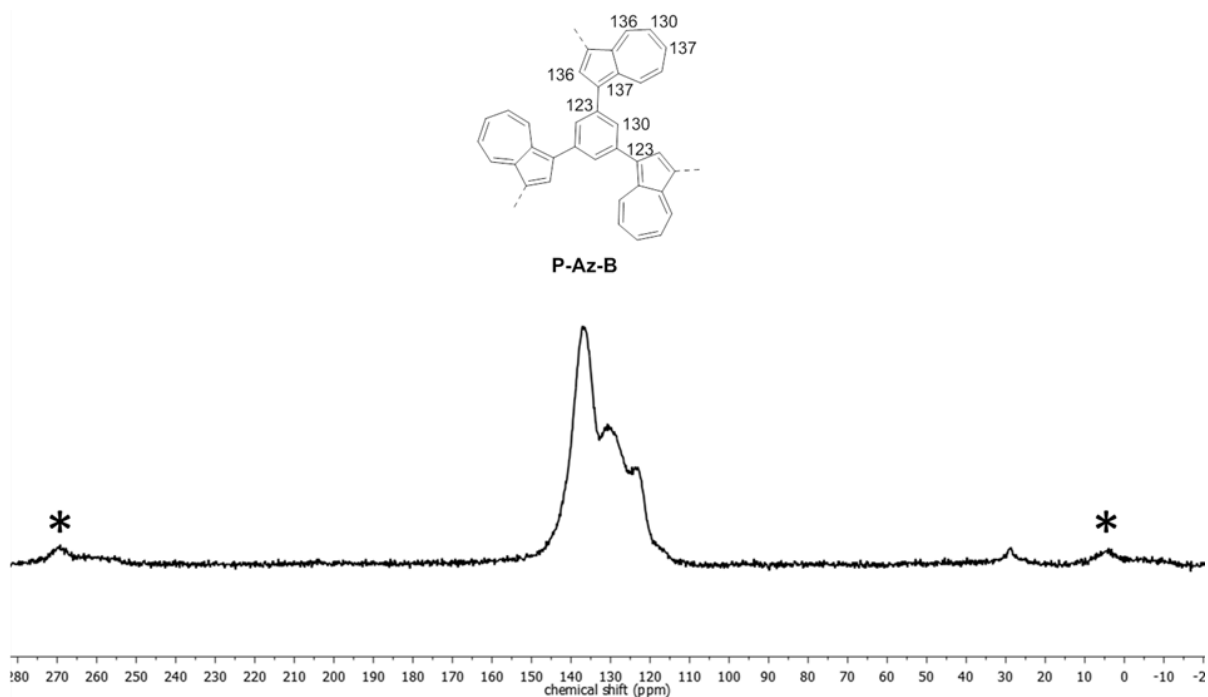


Figure 5.51: Solid state CP-MAS ^{13}C -NMR spectrum of P-Az-B at rotation frequency of 10 kHz (side bands*).

The FTIR spectrum of P-Az-B showed typical -C=C- stretching mode at ca. 1570 cm^{-1} of the azulene unit (Figure 5.52).^[165] The signals at around 1420 cm^{-1} indicate the skeleton vibration of the aromatic rings in the polymer, accompanied with the typical C-H stretching mode at 740 and 1090 cm^{-1} .

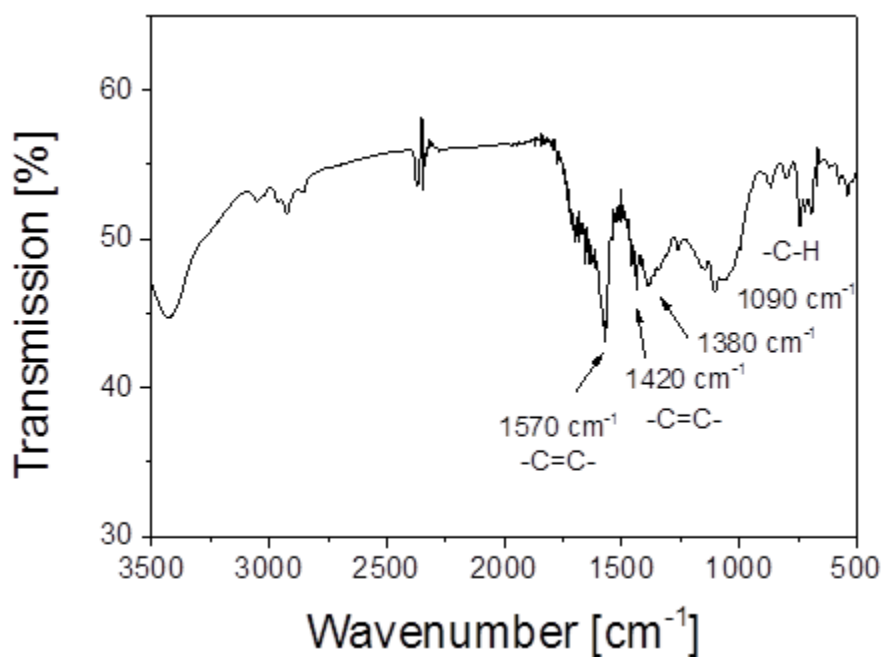


Figure 5.52: FT-IR spectrum of P-Az-B.

The UV-vis diffuse reflectance spectrum (DRS) revealed a broad absorption band of P-Az-B ranging from the visible into near-infrared region (<1200 nm), as displayed in Figure 5.53a. The corresponding Tauc-Plot of the UV-Vis DRS spectrum in Figure 5.53b revealed the optical band gap to be 2.03 eV, which is in good agreement with the electrochemical band gap 2.24 eV shown in Figure 5.54.

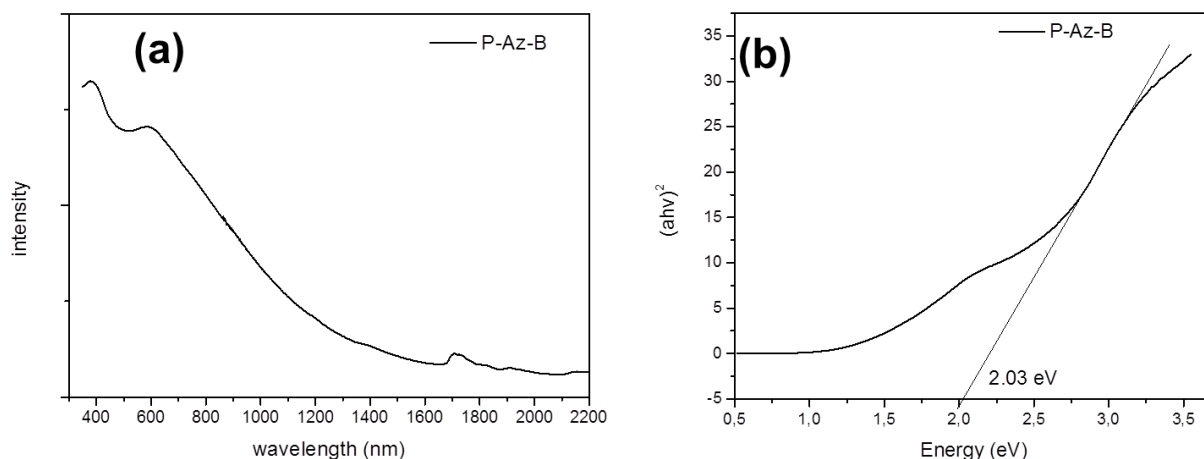


Figure 5.53: UV-Vis DRS spectrum (a) and additional Tauc-Plot (b) of P-Az-B.

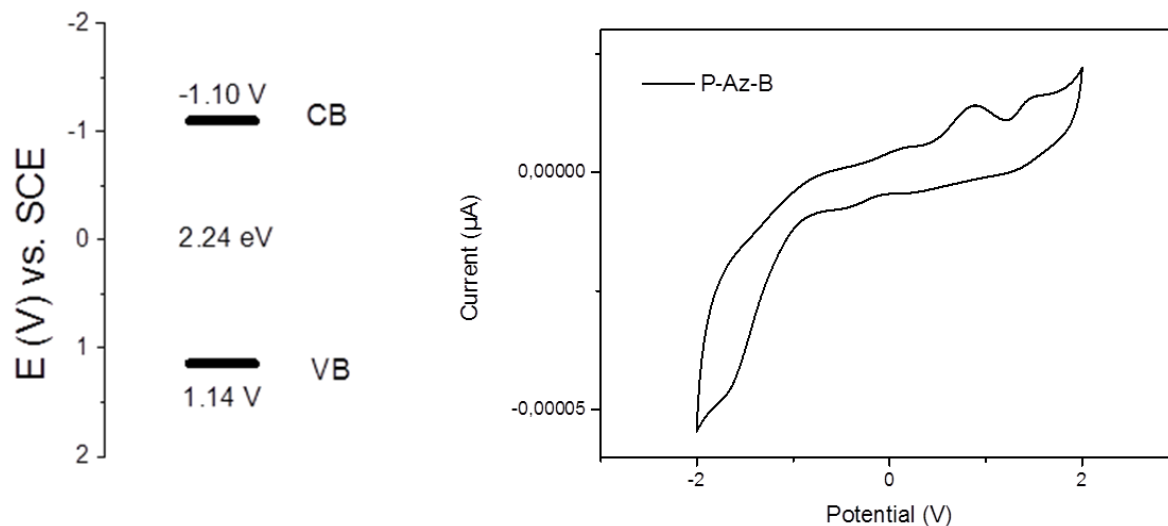


Figure 5.54: HOMO and LUMO band position (left) and the corresponding cyclic voltammogram (right) of P-Az-B.

For photocatalytic systems, the energy band positions represent their photo-generated redox potentials and are therefore the crucial parameters for the catalytic efficiency. To reveal the band structure of the polymer, cyclic voltammetry analysis was conducted (Figure 5.7).

Table 5.7: Electrochemical properties of P-Az-B and L-Az-B.

	HOMO [V vs. SCE]	LUMO [V vs. SCE]	Band [eV]	gap
P-Az-B	1.14	-1.10	2.24	
L-Az-B	1.52	-1.08	2.60	

The highest unoccupied molecular orbital (HOMO) and the lowest occupied molecular orbital (LUMO) of P-Az-B were determined to be +1.14 V and -1.10 V vs. saturated calomel electrode (SCE), respectively (Figure 5.54). These values are comparable with the redox potentials of well-established transition metal complex photocatalysts such as $[\text{Ru}(\text{bpy})_3]^{3+}$ (+1.29 V versus SCE) and $[\text{Ru}(\text{bpy})_3]^{2+}$ (-0.81 V vs. SCE).^[123] This might indicate a possible catalytic capability of P-Az-B for photoredox reactions.

Moreover, an efficient charge separation is a prerequisite for efficient photocatalytic reactions, which depends largely on molecular orbital distributions of HOMO and LUMO levels. Quantum mechanical calculations via density functional theory (DFT) of P-Az-B fragments (PhAz_3 and Ph_4Az_9) as shown in Figure 5.55, revealed significant spatial separation of ground state HOMO and excited state LUMO, whereas the azulene moieties acted as acceptors with increased probability for electron localizations in LUMO state.

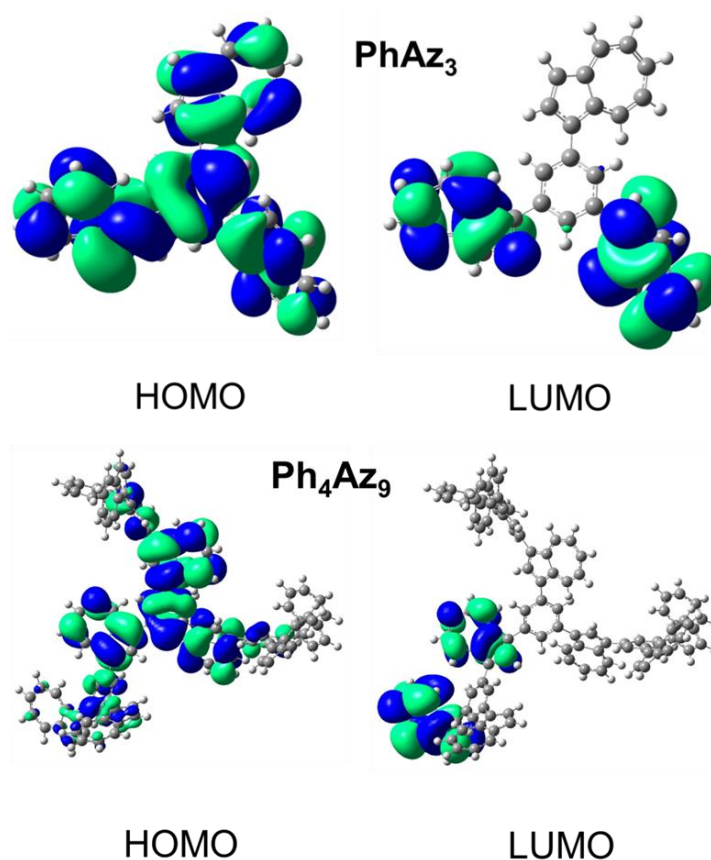


Figure 5.55: Molecular Orbital distribution of repeating fragments of P-Az-B (DFT, RB3LYP, 631G(d)).

In Table 5.8 the calculated HOMO/LUMO levels of PhAz₃ and Ph₄Az₉ are listed. It turned out that with increasing conjugated chain length the band gap was reduced.

Table 5.8: Molecular Orbital levels and the corresponding bandgaps of pre-optimized structures (DFT, RB3LYP, 631G(d))^[166] of fragments of P-Az-B.

	HOMO (V vs SCE)	LUMO (V vs SCE)	Bandgap (eV)
PhAz ₃	+0.76	-2.29	3.05
Ph ₄ Az ₉	+0.62	-2.27	2.89

5.3.3 Photocatalytic Applications and Investigation of Reaction Mechanism

As proposed in Scheme 5.3, the formation of the aryl radical via the oxidative electron transfer from the aryl stannane to the photogenerated hole of the organic photocatalyst is mandatory. We first examined the visible light-promoted destannylation reaction of various aryl tributylstannanes using P-Az-B as photocatalyst under the irradiation of a white LED lamp (0.25 W/m²). The results are listed in Table 5.9.

Table 5.9: Photocatalytic destannylation reaction of various aryl stannanes using P-Az-B as photocatalyst.^a

Ar-SnBu ₃ a	P-Az-B, white light THF, RT, 12h	Ar-H b	+ Ar-Ar c
Substrates:			
b1a: 26% 1b: N.D., 24h		2a: 12% 2b: 13%, 45h	3a: trace 3b: N.D., 24h
4a: 18% 4b: 75%, 40h		5a: 10% 5b: 83%, 40h	6a: 16% 6b: 69%, 45h
7a: trace 7b: N.D., 24h		8a: trace 8b: N.D., 24h	

^aReaction conditions: aryl tributylstannane (0.2 mmol), 5 mg P-Az-B, 5 ml THF, white LED (0.25 W/cm²), room temperature, 24 to 45 h. ^aYield determined via GCMS. ^bYield determined via HPLC.

It could be clearly determined that the aryl stannanes (e, f, and g) with oxidation potentials higher than the HOMO of P-Az-B (+1.14 V vs. SCE) could not be destannylated (Figure 5.56).

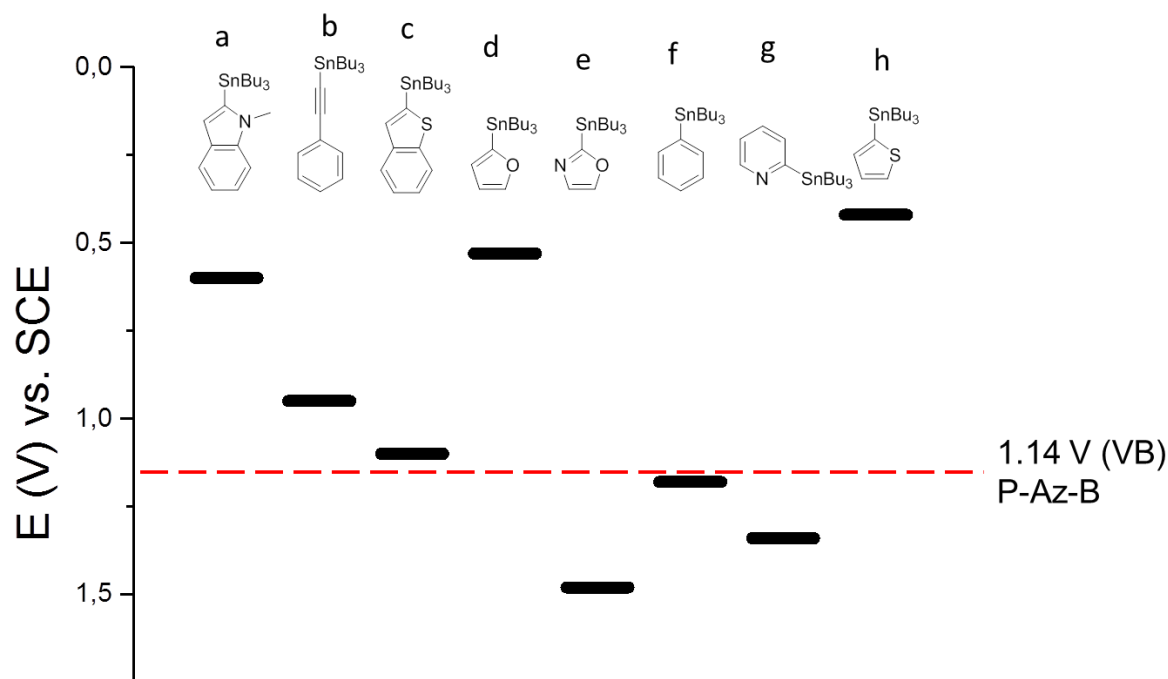


Figure 5.56: Oxidation potentials of the aryl stannanes compared to the HOMO level of P-Az-B, determined by cyclic voltammetry (vs. SCE).

Interestingly, the photo-destannylation of other aryl stannanes led not only to the protonated aromates, but also to their dimer, except furanyl (1a). It could be explained that thionyl (2a), indolyl (4a), benzothionyl (5a) and benzoethynyl (6a) could stabilize the radical aryl intermediate more efficiently and rather enhance the dimer formation (Figure 5.57).

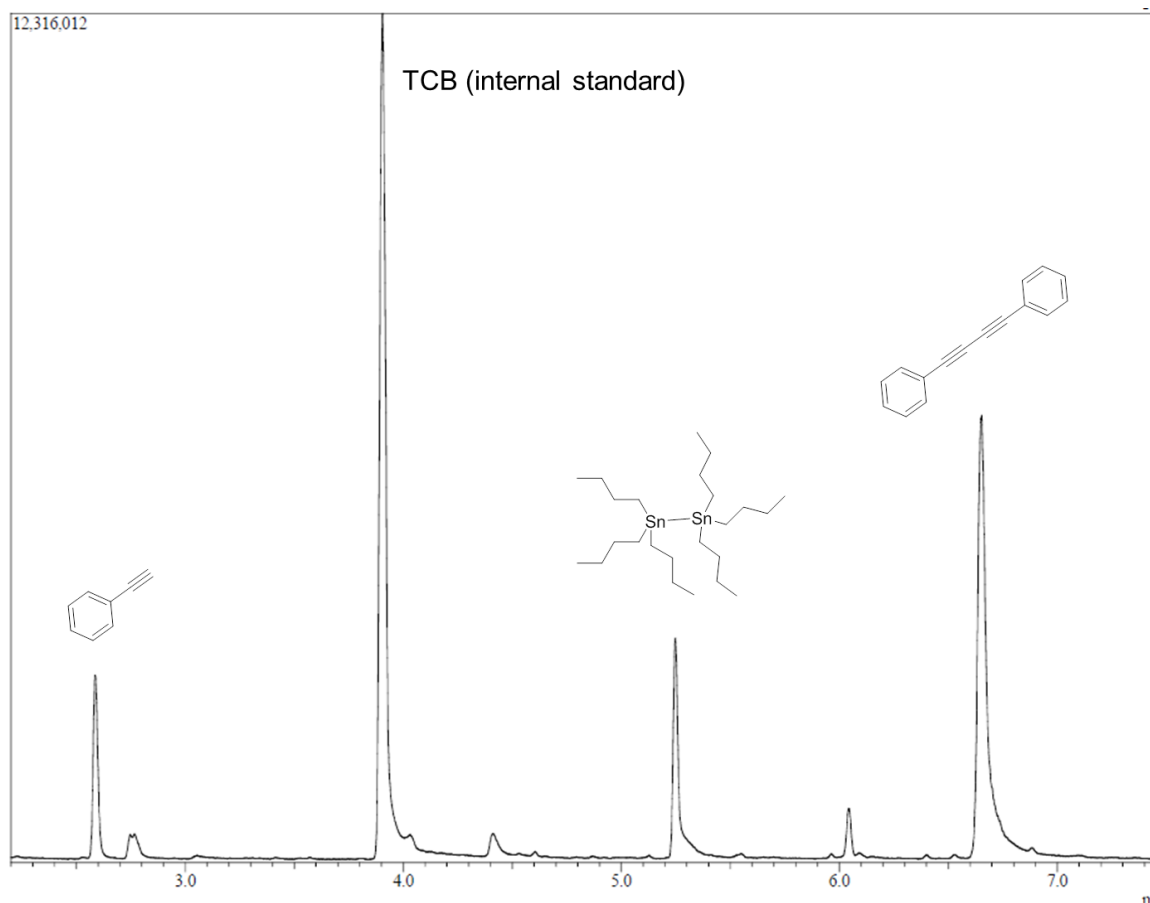


Figure 5.57: Photooxidation analysis of tributyl(phenylethynyl)tin by GC-MS after 45 h light irradiation.

The solvent (THF) could also act as a weak proton source during the photo-destannylation reaction. An additional radical trapping experiment via electron spin (EPR) resonance spectroscopy was conducted using furanyl stannane as model substrate (Figure 5.58). By adding *N-tert*-Butyl- α -phenylnitron (PBN) as radical trapping agent,^[167] a characteristic signal pattern of the stabilized radical could be clearly determined, demonstrating an aryl radical formation under the photocatalytic condition.

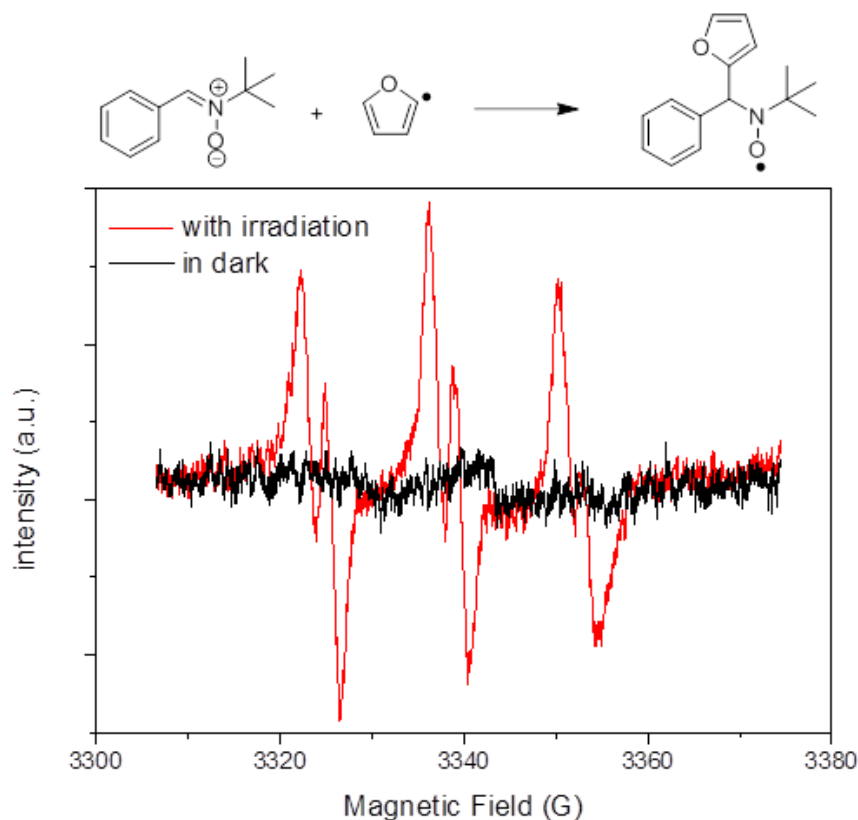
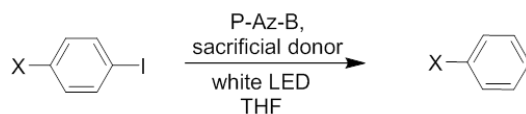


Figure 5.58: Photooxidation of 2-(tributylstannyl)furan and trapping of the resulting radical by *N*-tert-Butyl- α -phenylnitron (PBN).

Similar to the first half destannylation reaction as discussed before, we then conducted photo-dehalogenation of different aryl iodides. Significantly, none of the reactions led to the dehalogenated product (Table 5.10).

Table 5.10: Dehalogenation of aryl iodides using *P-Az-B* as photocatalyst.



Substituent X	Sacrificial donor	amount (mmol)	Conversion (%)
NO ₂	triethylamine	0.4	0
NO ₂	Hantzsch ester/triethylamine	0.2 / 0.4	0
NO ₂	diisopropylamine	0.4	0
CN	triethylamine	0.4	0
Carbonyl	triethylamine	0.4	0
Methoxy	triethylamine	0.4	0
H	triethylamine	0.4	0

This indicates that the photo-generated electrons from the LUMO level of P-Az-B (-1.18 V vs. SCE) was not sufficient enough for the complete dissociation of the C-I bond of the aryl iodides. An interesting observation could be made by determination of the reduction potential of aryl iodides via cyclic voltammetry (Figure 5.59).

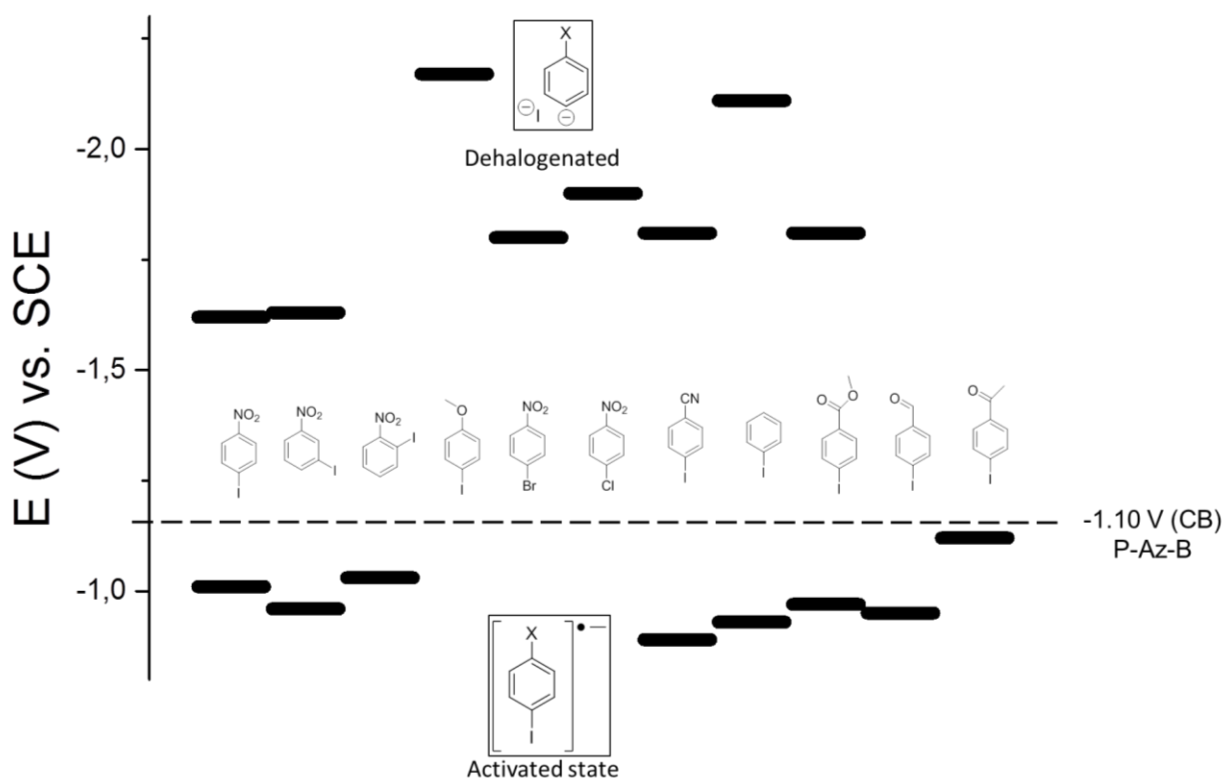


Figure 5.59: Reduction potential of aromatic halides compared to the LUMO of P-Az-B, determined by cyclic voltammetry (vs. SCE).

As illustrated in Figure 5.60, most aryl iodides exhibited two reduction potentials, as corresponding to the literature.^{[168] [169]} The second reduction potential rather corresponded to the dissociated state after a complete dehalogenation, which lay mostly higher than -1.6 V vs SCE. The first reduction potential represented the so-called activated state by forming an anionic radical. Especially the aryl iodides containing electron-withdrawing groups as such NO₂, CN, carbonyl or acetyl showed a lower first reduction potential than the LUMO of P-Az-B, indicating a possible formation of their anionic radical by receiving one photo-generated electron.

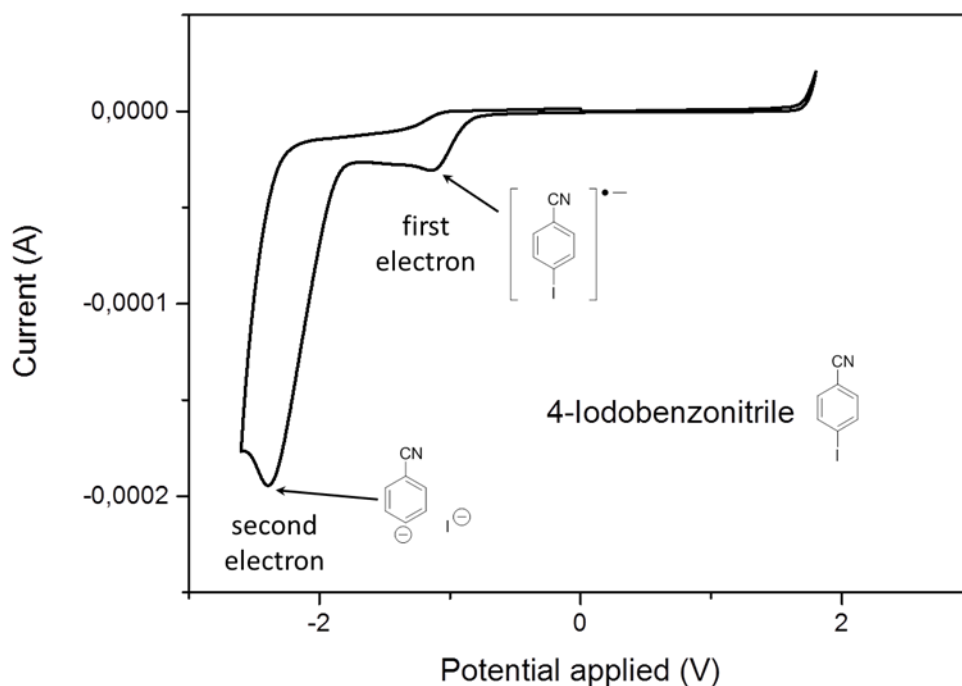
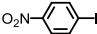
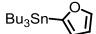

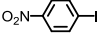
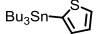

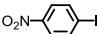
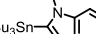
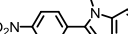
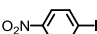
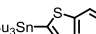
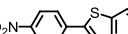
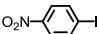
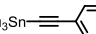
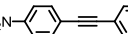
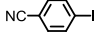
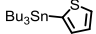
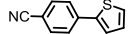
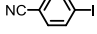
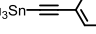
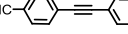
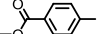
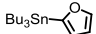
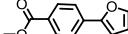
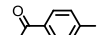
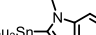
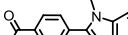
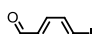
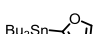
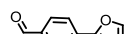
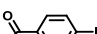
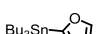
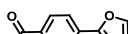

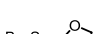
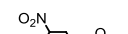
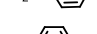

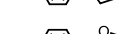
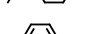

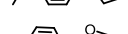
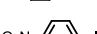
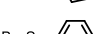
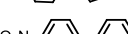
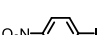
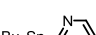
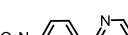
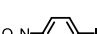
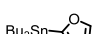

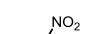

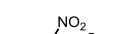
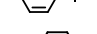

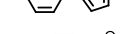
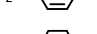




Figure 5.60: Cyclic voltammogram of 4-iodobenzonitril and the involved two electron reduction processes.

To complete the Stille-type reaction cycle, we then further examined the coupling reaction of various aryl iodides and stannanes. The substrates and products are listed in Table 5.11. It could be observed that only the Stille-type coupling of electron withdrawing group-substituted aryl iodides with activated energy lower than the LUMO of P-Az-B (-1.18 V vs. SCE) with aryl stannanes was successful (entries 1-12). Electron-donating group- or unsubstituted phenyl iodides did not lead to the formation of products (entries 13, 14). As expected, the employment of unreactive aryl stannanes with higher oxidation potentials, as shown in the aforementioned destannylation study, led to no desired coupling product (entries 15-17). A steric effect could be seen using 1-iodo-2-nitrobenzene, which could not be coupled with the aryl stannane (entry 18). The reaction of aryl bromide and chloride with aryl stannane did not lead to any product. This could be explained by the high stability of the carbon halogen bond of the anionic radical. A potential solution to lower the reduction energy of the aryl bromides or chlorides might be the introduction of more electron withdrawing substitutions on the aromatic ring.

Table 5.11: Scope of the photocatalytic Stille-type coupling reaction with various substrates using P-Az-B as photocatalyst.^a

Entry	Aryl halide	Stannane	Product	Yield ^b (%)
1				80
2				60
3				86
4				90
5				93
6				87
7				67
8				56
9				60
10				49
11				70
12				83
13				0
14				trace ^c
15				trace ^c
16				0
17				0
18				0
19				0
20				0

^aReaction conditions: halide (0.2 mmol), stannane (0.2 mmol), 5 mg P-Az-B, 4 ml THF, white LED (0.25 W/cm²), room temperature, 24 h. ^bIsolated yield via chromatography. ^cDetermined by GCMS.

The organic photocatalyst P-Az-B still contained a minimal palladium residue of ca. 7 ppm according to inductively coupled plasma atomic emission spectroscopy (ICP-AES). To eliminate the effect of the palladium residue inside the organic photocatalyst P-Az-B (7 ppm, ICP) during the Stille-type coupling reaction, we synthesized a linear oligomer (L-Az-B) based on azulene and phenyl units a soluble version of P-Az-B (< 1ppm). The synthesis of L-Az-B is shown in Figure 5.61.

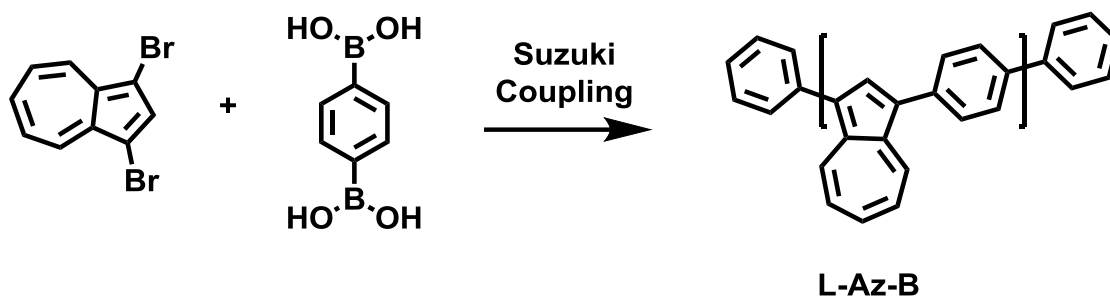


Figure 5.61: Synthesis of L-Az-B via Suzuki cross-coupling reaction.

In a homogeneous manner, the same photocatalytic coupling reactions using different substrates achieved similar conversion of the desired products (Table 5.12).

Table 5.12: Photocatalytic Stille-type coupling reaction with Examples using L-Az-B as photocatalyst.^a

Entry	Aryl halide	Stannane	Product	Yield ^b (%)
1				80
2				78
3				85

^aReaction conditions: halide (0.2 mmol), stannane (0.2 mmol), 3 mg L-Az-B, 4 ml THF, white LED (0.25 W/cm²), room temperature, 24 h. ^bIsolated yield via chromatography.

This demonstrated that the photocatalytic activity was derived from the conjugated polymer backbone structure rather than the minimal Pd residue.

To demonstrate the stability and reusability of the polymer-based heterogeneous photocatalyst P-Az-B, repeating experiments were conducted. P-Az-B could be used for five repeating cycles without significant change in its catalytic efficiency (Figure 5.61).

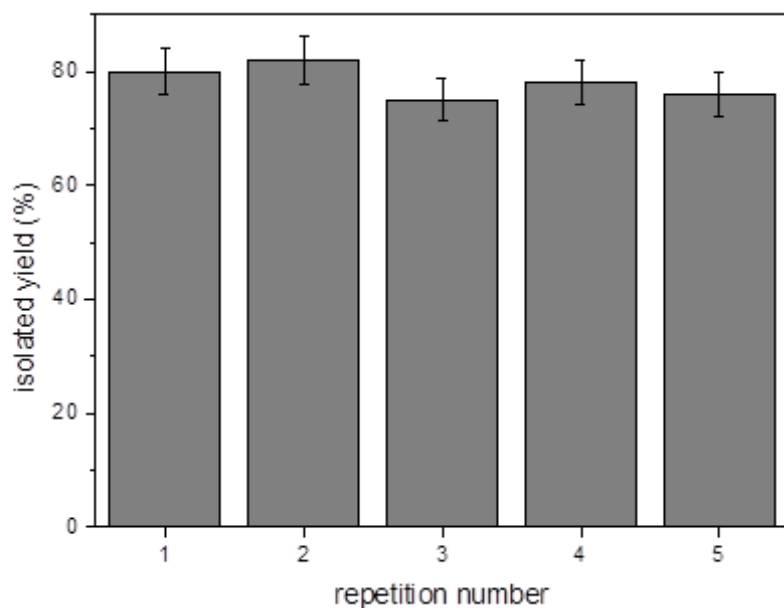


Figure 5.61: Repeating experiment of the photocatalytic Stille coupling of 4-iodonitrobenzene with 2-tri-*n*-butylstannylfuran by filtration and reusing the same P-Az-B photocatalyst after each repetition (isolated yields).

No clear change of the FTIR spectra of P-Az-B before and after the catalytic reaction was observed (Figure 5.62). The SEM images of P-Az-B in Figure 5.63 before (a) and after 5 cycles (b) of photocatalysis showed consistent unchanged surface morphologies.

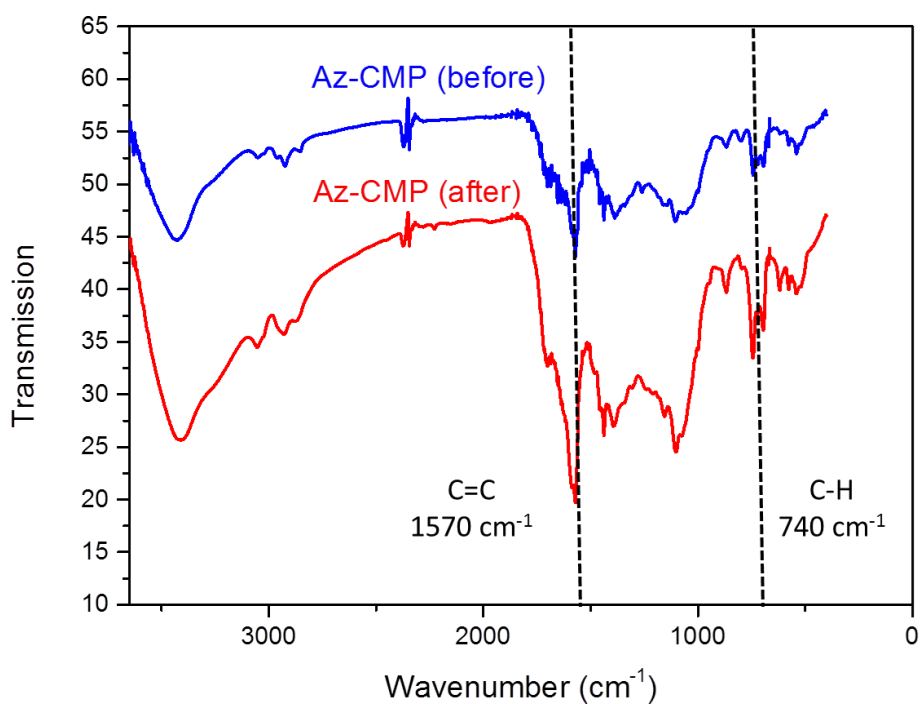


Figure 5.62: FT-IR spectra of P-Az-B before and after 5 cycles of photocatalysis.

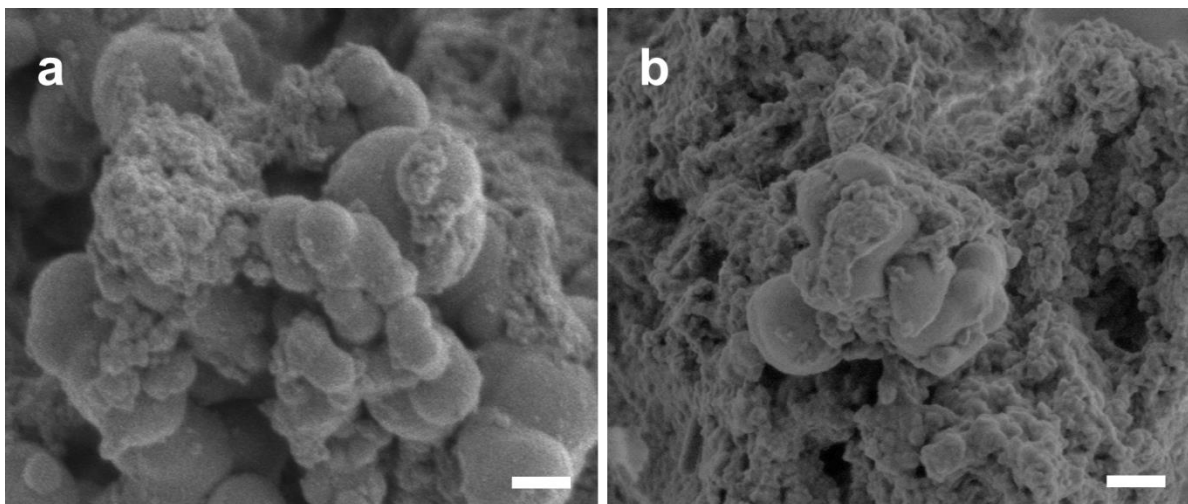


Figure 5.63: SEM image of porous P-Az-B before (a) photocatalytic cycles and after 5 subsequent cycles (b) (scale bar 200 nm).

Using a single wavelength blue LED lamp (460 nm, 0.26 W/cm²), the apparent quantum yield of P-Az-B could be calculated as 0.09%.

To further study the mechanistic insight of the photocatalytic Stille-type coupling reaction, we then performed time-resolved photoluminescence spectroscopy using L-Az-B as photocatalyst and furanyl stannane and iodobenzene as substrates to mimic the catalytic system. As shown in Figure 5.64, L-Az-B exhibited a fluorescence life time of ca. 1.94 ns. By adding furanyl stannane, the lifetime was quenched to 1.45 ns. Adding iodobenzene could decay the fluorescence lifetime of L-Az-B to ca. 0.96 ns. By adding both coupling partners, the fluorescence lifetime remained at 0.95 ns.

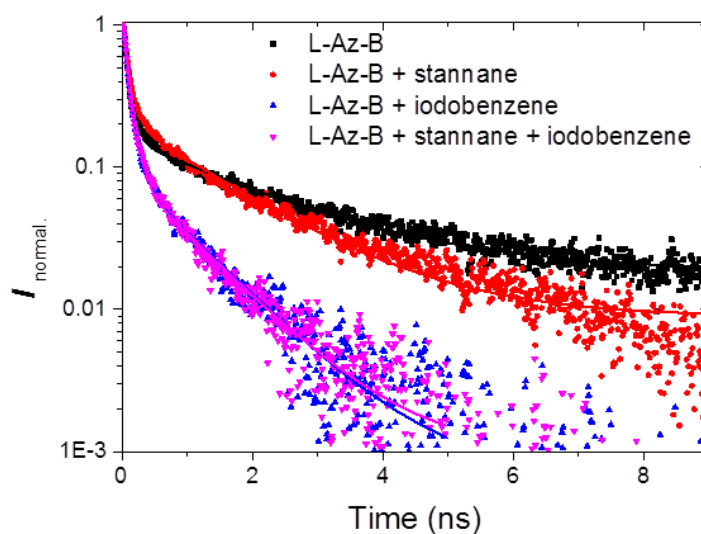


Figure 5.64: Photoluminescence lifetime quenching experiments with L-Az-B by aryl stannane and iodide.

This demonstrated a photo-induced electron transfer process from the photocatalyst onto the substrates and vice versa during the catalytic cycle. In order to understand the reductive quenching of iodonitrobenzene and the dehalogenation, a series of semi empiric thermodynamic calculations of favoured pathways were conducted. Figure 5.65 shows the relative Gibbs energies of different reduced intermediates. The results were consistent with the previously mentioned two step reductive dehalogenations of aromatic halides. Starting from iodonitrobenzene (407 kJ/mol), the first one electron transfer led to either the more favored iodonitrobenzene radical anion (156 kJ/mol) or to nitrobenzene radical (550 kJ/mol). After the second electron transfer step, full dehalogenation and the formation of nitrobenzene anion (368 kJ/mol) was simulated. However, the formation of cationic nitrobenzene intermediate was less probable. These results clearly indicated that the iodonitrobenzene radical anion pathway is the most favoured. The comparison of C-I bond length from 211 pm (experimental 214 pm) in neutral iodonitrobenzene to 220 pm in iodonitrobenzene radical anion led to conclusions about facilitated elimination of iodide.

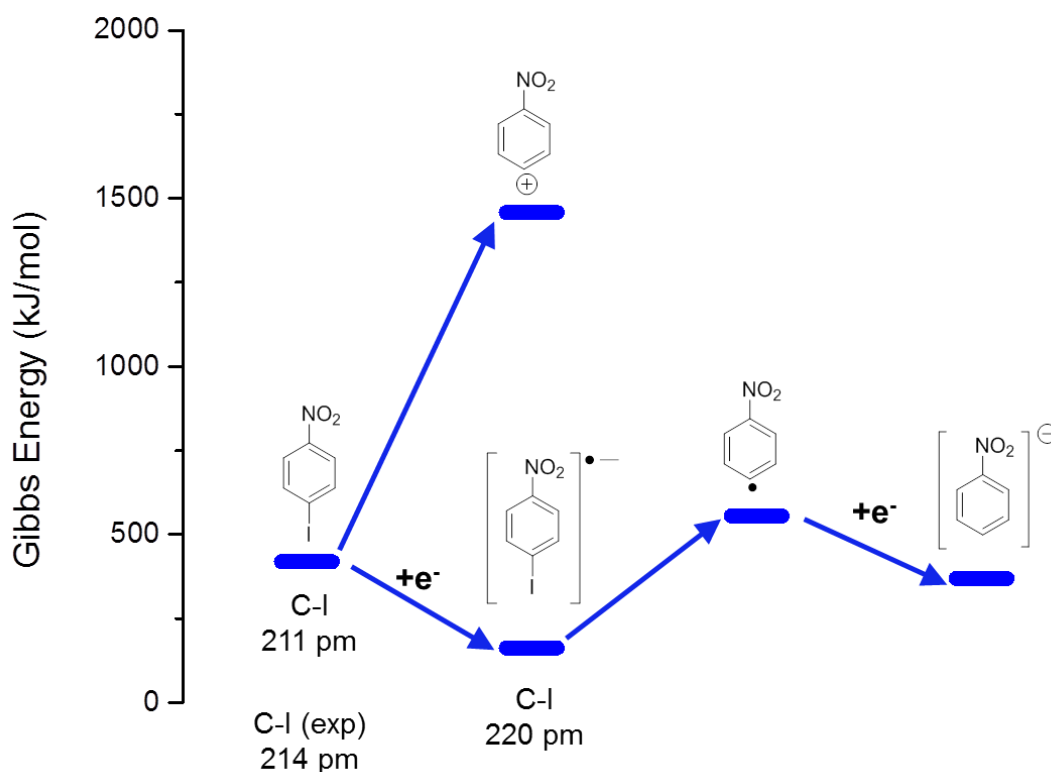


Figure 5.65: Semi-empiric calculation of relative thermodynamic Gibbs energies of aromatic dehalogenation, Method: Geometry optimization, Frequency Calculation, UPM6, Conditions: 1 atm, 298.15 K.

Based on the cyclic voltammetric redox potentials and excited state transition energy of L-Az-B and stannanes, free energies of photo-induced electron transfer processes in homogeneous solution were calculated. Table 5.13 shows the calculated Gibbs energies. It was found that most of the photooxidation processes of stannanes were favoured electron transfer steps (negative values). Owing to the higher HOMO level of L-Az-B, the

probabilities of the photooxidations of tributyl(phenyl)stannane and 2-(tributylstannyl)pyridine was slightly negative.

Table 5.13: Calculated free energies of photo-induced electron transfer processes from the aryl stannanes to L-Az-B according to the Gibbs equation: $\Delta G = E_{ox}(D/D^+) - E_{red}(A/A^-) - \Delta E_{00} + \Delta E_{Coulomb}$.

	$E_{red}(A/A^-)$ (kcal/mol)	E_{0-0} (kcal/mol)	Stannanes	$E_{ox}(D/D^+)$ (kcal/mol)	Free Energy (kcal/mol)
L-Az-B	-35.1	69	1-methyl-2-(tributylstannyl)-1H-indole	14	-20
			tributyl(phenylethynyl)stannane	22	-12
			benzo[b]thiophen-2-yltributylstannane	25	-9
			tributyl(furan-2-yl)stannane	12	-22
			2-(tributylstannyl)oxazole	34	0
			tributyl(phenyl)stannane	27	-7
			2-(tributylstannyl)pyridine	31	-3
			tributyl(thiophen-2-yl)stannane	10	-24

D: donor species; A: acceptor species, $E_{ox}(D/D^+)$: oxidation energy of the donor, $E_{red}(A/A^-)$: reduction energy of the acceptor, ΔE_{00} : excited singlet state energy, $\Delta E_{Coulomb}$: Coulombic potential energy, Negative values of the Gibbs energy indicate favored processes.^[170]

5.3.4 Conclusion

In summary, metal-free and reusable conjugated microporous polymers were successfully employed in organic bond formation reactions. The underlying photoredox processes gave new insights for understanding of photocatalytic reactions. A novel photocatalytic Stille-Type coupling reaction pathway for aromatic C-C bond formations using conjugated organic photocatalysts instead of palladium complexes was demonstrated. The reaction mechanism is driven between the coupling reaction of the aryl radical by oxidative destannylation of the aryl stannane, and the electron-activated aryl iodide. The driving force was the photogenerated electron/hole pair of the conjugated organic photocatalysts. Theoretical calculations confirmed that feasibility of the coupling reactions with specific substrates. The visible light-promoted Stille coupling reaction using pure organic photocatalysts offers a simple, sustainable and more economic synthetic pathway towards metal-free C-C bond formation, and can be applied for a broader range of coupling reactions. As a further perspective, we believe that non-toxic pseudohalides other than stannanes, if the oxidation

potential matches well with the photocatalysts, could also be chosen as a suitable coupling partner during the catalytic cycle.

6. Experimental Part

6.1 Materials and Instruments

Materials

All chemicals were purchased from commercial sources and were used without prior purification unless stated otherwise. Solvents were used in HPLC quality or extra dry. Water was used in Millipore quality (18.2 M Ω ·cm at 25 °C).

Azulen (99%, Alfa Aesar), 2,1,3-benzothiadiazole-4,7-bis(boronic acid pinacol ester) (98%, Combi Blocks), 1-bromo-4-nitrobenzene (99%, Sigma Aldrich), catalase from bovine liver (Aldrich), 1-chloro-4-nitrobenzene (99%, Aldrich), copper(II) chloride (99%, Sigma Aldrich), 2-dicyclohexylphosphino-2',4',6'-triisopropylbiphenyl (97%, Aldrich), 2,7-dibromo-9,9-bis(6-bromohexyl)fluorine (>98%, TCI), 1,5-diphenylcarbazine (DPC) (Aldrich), 4-iodoacetophenone (98%, Aldrich), 4-iodoanisole (98%, Aldrich), 4-iodobenzaldehyde (96%, Aldrich), iodobenzene (98%, Aldrich), 4-iodobenzonitrile (97%, Aldrich), 1-iodo-4-nitrobenzene (98%, Sigma Aldrich), 2-iodo-1-nitrobenzene (97%, Aldrich), 3-iodo-1-nitrobenzene (99%, Aldrich), iron(III) chloride hexahydrate (97%, Sigma Aldrich), 1-methylimidazole (99%, Alfa Aesar), N-bromosuccinimide (99%, Sigma Aldrich), N-tert-Butyl- α -phenylnitron (98%, Aldrich), methylene blue (high purity, Alfa Aesar), methyl-4-iodobenzoate (97%, Aldrich), methyl methacrylate (99%, Aldrich), N-methyl-2-(tributylstannyl)indole (97%, Aldrich), phenylacetylene (98%, Sigma Aldrich), potassium hexacyanoferrate(III) (99%, Sigma Aldrich), potassium iodide (99%, Sigma Aldrich), potassium chromate (> 99%, Sigma Aldrich), rhodamine B (97%, sigma Aldrich), sulfuric acid (95 %, analytical chemical grade, Fisher Chemical), tetrakis(triphenylphosphine)palladium(0) (99%, Aldrich), tributyl(phenylethynyl)tin (95%, Aldrich), 2-tributylstannylfuran (97%, Aldrich), 2-tributylstannylbenzo[b]thiophene (95%, Aldrich), 1,3,5-triethynylbenzene (98%, Alfa Aesar), tributylphenylstannane (97%, Aldrich), 2-(tributylstannyl)pyridine (85%, Aldrich), 2-(tri-n-butylstannyl)oxazole (97%, Aldrich), trifluoroacetic acid (99%, Acros Organics), 1-vinylimidazole (99%, Alfa Aesar),

Instruments

Gel permeation chromatography (GPC)

The measurements were performed on a PSS-SECcurity GPC/SEC system (Agilent Technologies 1260 Infinity). Equipped with a SDV (PSS) column (particle size 10 μm) and a UV (PSS 1260 VWD) and refractory index (PSS 1260 RID) detector. The average flow rate was 1 ml/min at 30 °C. The polystyrene standard was applied prior to analysis.

UV-Vis Diffuse Reflectance Spectroscopy (UV-Vis DRS)

The solid state UV-Vis remission spectra were performed on Perkin Elmer Lambda 900 UV-vis/NIR spectrometer equipped the integration sphere. The device was equipped with the PMT UV-Vis photomultiplier and the PbS NIR detector. The grinded solid samples were attached to transparent scotch tape and finally applied to the BaSO₄ coated holder of the sphere remission chamber.

UV-Vis Spectroscopy (UV-Vis)

The UV-Vis absorption spectra in solution were performed on a Perkin Elmer Lambda 25 spectrometer. In order to measure background spectra the 2 beam absorption arrangement was selected. Suprasil quartz cuvettes with 1 cm optical paths were used.

Fourier Transform Infrared Spectroscopy (FT-IR)

FT-IR measurements were performed with the Perkin Elmer Spectrum BX System. The samples were prepared by the KBr pellet method.

Fluorescence Spectroscopy

Solid state fluorescence measurements were performed on a J&M TIDAS fluorescence Spectrometer. Fluorescence measurements in liquid phase were taken from a TECAN Plate Reader Infinite M100.

Thermogravimetric Analysis (TGA)

The thermogravimetric measurements were performed on a Mettler-Toledo TGA851 by monitoring the temperature-dependent weight loss in the range from 25 to 1000 °C with 10 °C/min heating rate.

Electron Paramagnetic Resonance Spectroscopy (EPR)

The EPR measurements were performed on a Magnettech Miniscope MS200, equipped with a temperature controller TC HO2 and a microwave generator Model 3200 (XL Microwave). The measurements were conducted at a B_0 of 3350 Gauss and a sweep of maximum 150 G with a sweep time of 60 s. The adjusted X-band microwave frequency was 9.39 GHz. For the preparation of solid or liquid samples Hirschmann ringcaps® Duran® glass capillaries with sealing rubber were taken. For light induced radicals the samples were stored in the dark for several days prior to measurement.

Cyclic Voltammetry (CV)

The cyclic voltammograms were performed on a Metrohm Autolab PGSTAT204 potentiostat/galvanostat using tetrabutylammonium hexafluorophosphate (0.1 M) as electrolyte in anhydrous dichloromethane. The 3 electrode setup was used with platinum wire as counter electrode, glassy carbon as working electrode and Standard Calomel Electrode (SCE) as reference electrode. The measurements were conducted at a scan rate of 100 mV/s. The HOMO/LUMO levels were calculated according to the equations: $E_{\text{HOMO}} = - (4.4 + E_{\text{ox-onset}})$ eV and $E_{\text{LUMO}} = - (4.4 + E_{\text{red-onset}})$ eV. For conversion from Standard Calomel Electrode (SCE) to the Normal Hydrogen Electrode (NHE) potential, the equation: $E_{\text{NHE}} = E_{\text{SCE}} - 0.24$ V was used.^[127]

Surface Tension Measurement (Tensiometry)

The surface tensions and critical micelle formation concentration were measured with a dynamic contact angle measuring instrument and tensiometer DCAT 21 system (dataphysics) at room temperature in water.

Scanning Electron Microscopy (SEM)

Scanning electron microscopy images were recorded with a low voltage high resolution scanning electron microscope LEO Gemini 1530 from Zeiss equipped with a wolfram emitter. The acceleration voltage was kept according to the sample stability below 3 kV. The samples were attached to carbon tapes and sputtered with platinum (2.5 nm layer thickness).

Transmission electron microscopy (TEM)

Transmission electron microscopy images were recorded on a JEOL JEM 1400 with LaB₆ emitter at an acceleration voltage of 120 kV. For sample preparation the diluted sample dispersions were applied by dropping on carbon coated copper grids.

Quantum mechanical calculations

The quantum mechanical simulations of molecular properties were calculated by the Gaussian 09 program suite. Geometry optimizations of the molecule structures were calculated on the density functional theory level with the Becke, three-parameter, Lee-Yang-Parr (B3LYP) hybrid functional and the valence split basis 631G(d).^[166] The HOMO-LUMO levels were derived from these calculations. Thermodynamic data were calculated on the semi-empirical level PM6 by geometry optimization and subsequent vibrational analysis.

Nuclear Magnetic Resonance Spectroscopy (NMR)

The NMR spectra were measured with a Bruker Avance 300. The following resonance frequencies were used: ^1H (300 MHz) and ^{13}C (75 MHz). All chemical shifts were related trimethylsilan (TMS). The ^1H values were given according the following notation: s = singlet, d = doublet, t = triplet, q = quartet, m = multiplet. The ^{13}C measurements were performed by applying either the *attached proton testing* (ATP) or the *composite pulse decoupling* (CPD) methods. The ^{13}C spectra were assigned according the following description: quat = quaternary, tert = tertiary, sec = secondary, prim = primary. Solid-state NMR ^{13}C measurements were performed on a Bruker Avance 300. The magic angle spinning (MAS) setup with a spinning frequency of 10 kHz was applied. Cross polarization techniques with different polarization transfer durations between 1 and 3 ms were chosen. Adamantan and L-Alanin as external standards were used prior to measurement.

Surface Area and Porosity Measurements via Gas Sorption

The surface areas and pore size distributions of the porous polymers were measured by Quantachrome Autosorb 1. The samples were degassed for 24 h in vacuum at temperatures ranging from 80 to 120 °C. Pore size distributions and pore volumes were calculated by the *quenched solid density functional theory* (QSDFT, based on N_2 -carbon adsorption isotherms at 77K, and the slit-pore model) for disordered micro/mesoporous carbon materials with rough surfaces. The BET surface areas were based on P/P^0 data points from 0 to 0.25 and the *non-local density functional theory* (NLDFT) was applied as BET fitting model.

6.2 Water compatible conjugated microporous poly-azulene networks as visible light photocatalysts in aqueous medium

6.2.1 Synthesis of azulene CMP: P-Az-1

A 50 ml Schlenck tube was charged with a solution of 142 mg (0.5 mmol) 1,3-dibromoazulene, 117 mg 1,4-dibromobenzene (0.5), and 150 mg (1 mmol) 1,3,5-triethynylbenzene in 4 ml DMF/triethylamine (1:1) under inert gas atmosphere. 58 mg (0.05 mmol, 5 mol%) tetrakis(triphenylphosphine) palladium(0) and 30 mg CuI (0.05 mmol, 5 mol%) were added and the mixture was heated up to 80 °C for 24 h. The crude material was washed with water several times and extracted with MeOH and DCM in a Soxhlet apparatus. The obtained products were green solids with a yield of 76%.

6.2.2 Synthesis of azulene CMP: P-Az-2

A 50 ml Schlenck tube was charged with a solution of 284 mg (1 mmol) 1,3-dibromoazulene and 150 mg (1 mmol) 1,3,5-triethynylbenzene in 4 ml DMF/triethylamine (1:1) under inert gas atmosphere. 58 mg (0.05 mmol, 5 mol%) tetrakis(triphenylphosphine) palladium(0) and 30 mg CuI (0.05 mmol, 5 mol%) were added and the mixture was heated up to 80 °C for 24 h. The crude material was washed with water several times and extracted with MeOH and DCM in a soxhlet apparatus. The obtained products were green solids with a yield of 90%.

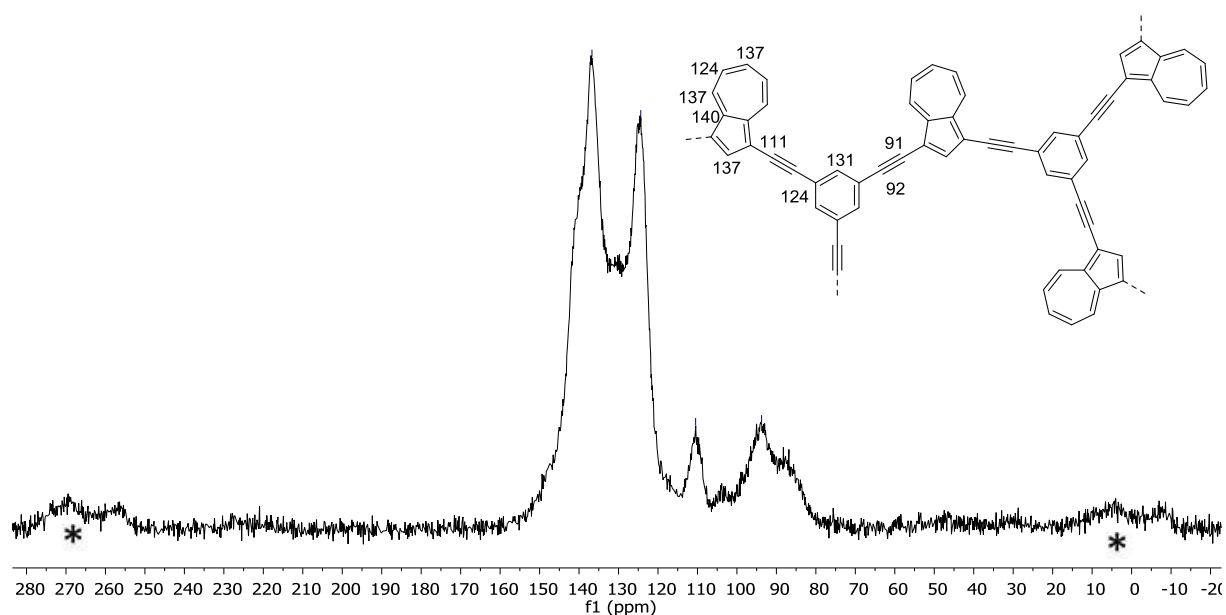
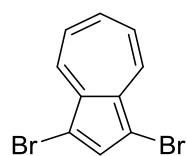


Figure 6.1: ¹³C-NMR CP-MAS solid state NMR spectrum of P-Az-2 (* sidebands).

6.2.3 Protonation of the poly-azulene networks

A sample of Az-CMP was mixed and covered with trifluoroacetic acid (TFA). The slurry was first dried at room temperature by a stream of air. Afterwards it was dried at 50 °C in a vacuum heating chamber for several hours. The remaining material was dark and brittle compared to the non-protonated material.

6.2.4 Synthesis of 1,3-dibromoazulene



According to the literature,^[171] 500 mg (3.9 mmol, 1 eq.) azulene was solved in 50 ml THF and cooled to 0 °C. 1.53 g (8.6 mmol, 2.2 eq.) of N-bromosuccinimide were solved in 30 ml THF and cooled to 0 °C. The cold NBS solution was added dropwise under exclusion of light over a time period of one hour. The mixture was allowed to warm up to room temperature and stirred for 24 h. The crude mixture was extracted by dichloromethane and washed several times with water. The combined organic phases were dried and concentrated. The final purification was accomplished by column chromatography (hexane). Dark green crystals were obtained. Yield: 963 mg (87%)

¹H NMR 8.32 (d, 2H), 7.81 (s, 1H), 7.68 (m, 1H), 7.28 (t, 2H) ppm.

¹³C NMR: (300 MHz, CDCl₃, 25 °C): δ = 140, 138.2, 136.7, 135.7, 124 ppm.

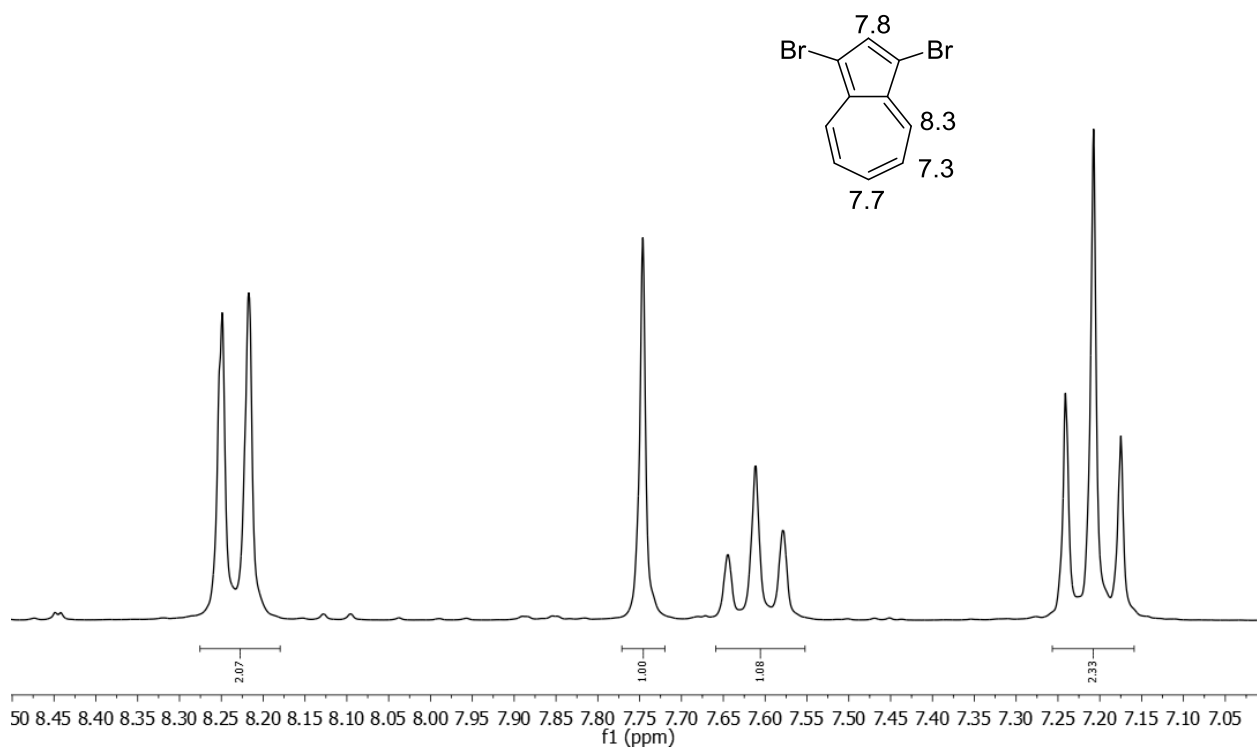


Figure 6.2: $^1\text{H-NMR}$ NMR spectrum of 1,3-dibromoazulene.

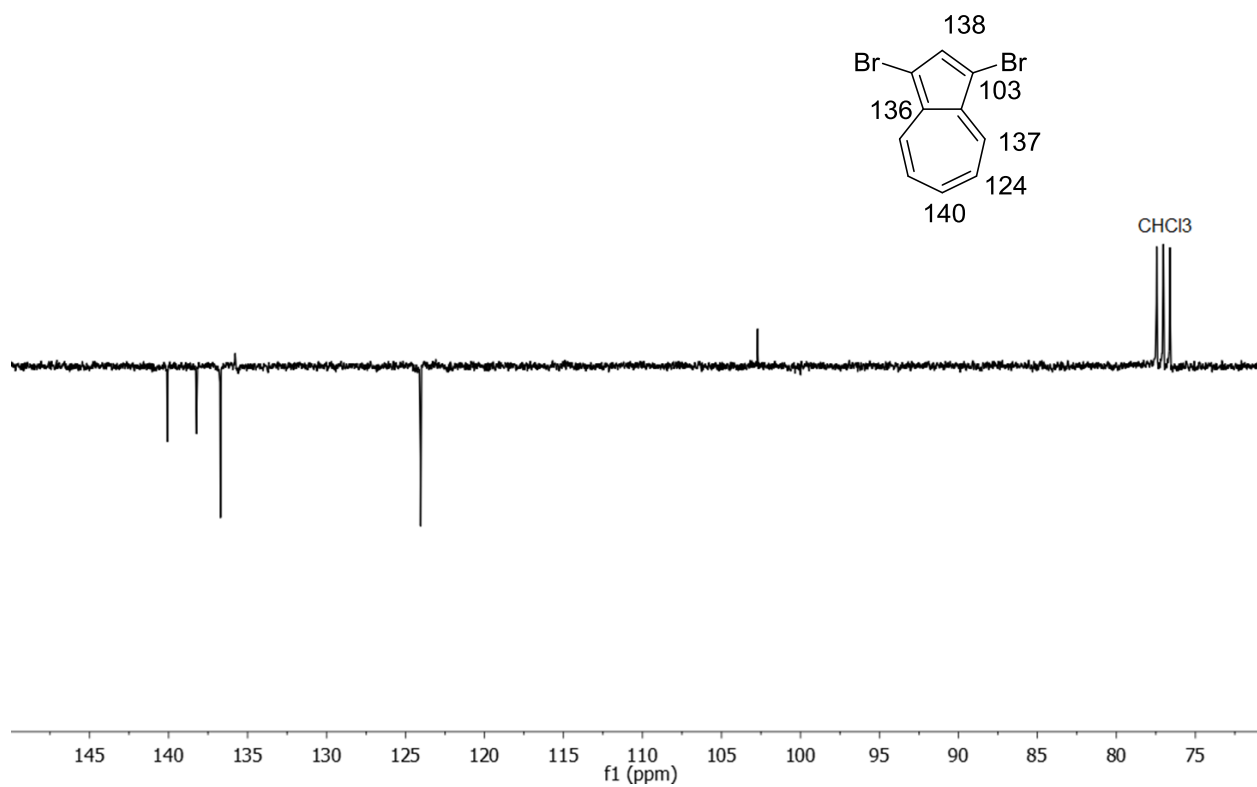
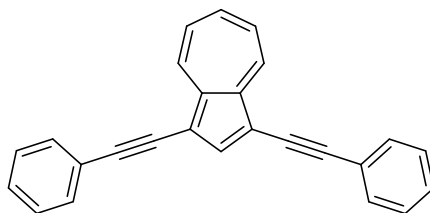


Figure 6.3: $^{13}\text{C-NMR}$ APT spectrum of 1,3-dibromoazulene.

6.2.5 Synthesis of 1,3-Bis(phenylethynyl)azulene (Az-Ph₂)



A 50 ml Schlenck tube was charged with a solution of 142 mg (0.5 mmol) 1,3-dibromoazulene, 112 mg Phenylacetylene (1.1 mmol) in 5 ml DMF/triethylamine (1:1) under inert gas atmosphere. 29 mg (0.025 mmol, 5 mol%) tetrakis(triphenylphosphine) palladium(0) and 20 mg CuI (0.10 mmol, 20 mol%) were added and the mixture was heated up to 80 °C for 48 h. The crude mixture was extracted by dichloromethane and washed several times with water. The combined organic phases were dried and concentrated. The final purification was accomplished by column chromatography (hexane). Dark green crystals were obtained.

Yield: 64 mg (40%)

¹H NMR (300 MHz, CDCl₃, 25 °C): 8.61 (d, 2H), 8.14 (s, 1H), 7.71 (m, 1H), 7.63 (m, 4H), 7.36 (m, 6H), 7.32 (m, 2H) ppm.

¹³C NMR: (75 MHz, CDCl₃, 25 °C): δ = 141.9, 141.5, 140.0, 137.1, 131.4, 128.4, 127.9, 125.6, 123.9, 110.6, 94.1, 84.9 ppm.

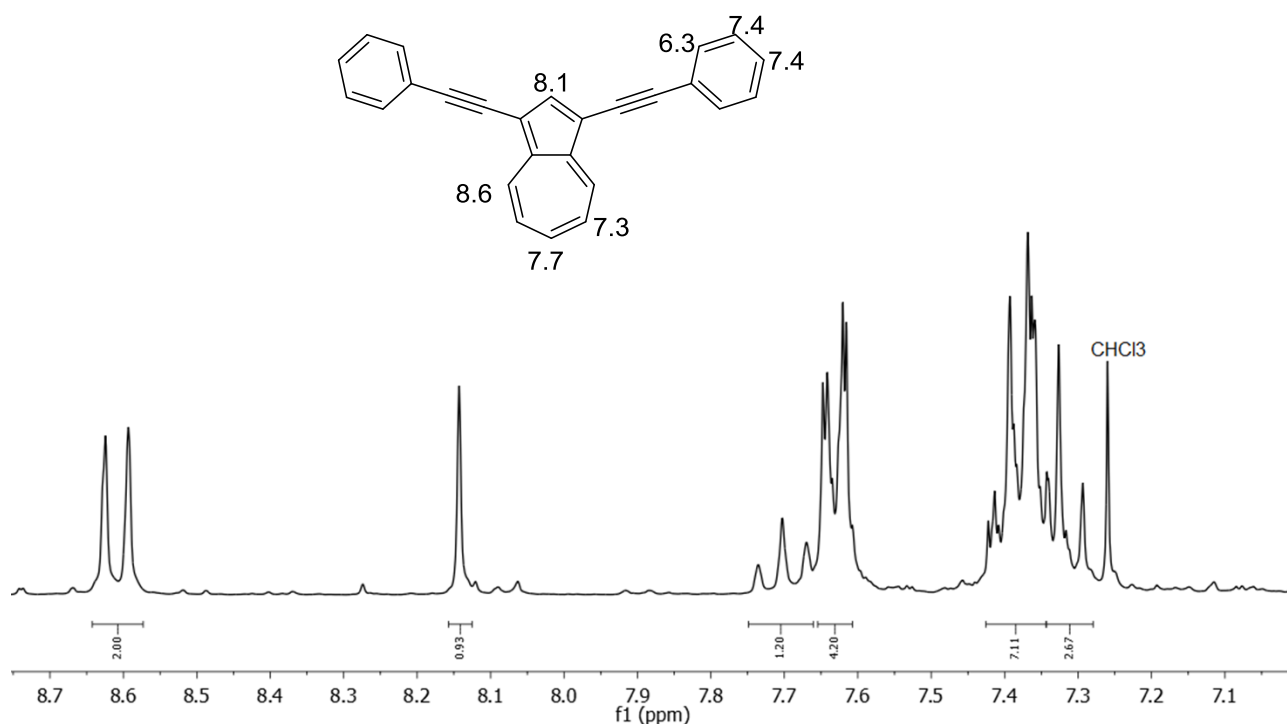


Figure 6.4: ¹H-NMR NMR spectrum of 1,3-bis(phenylethynyl)azulene (Az-Ph₂).

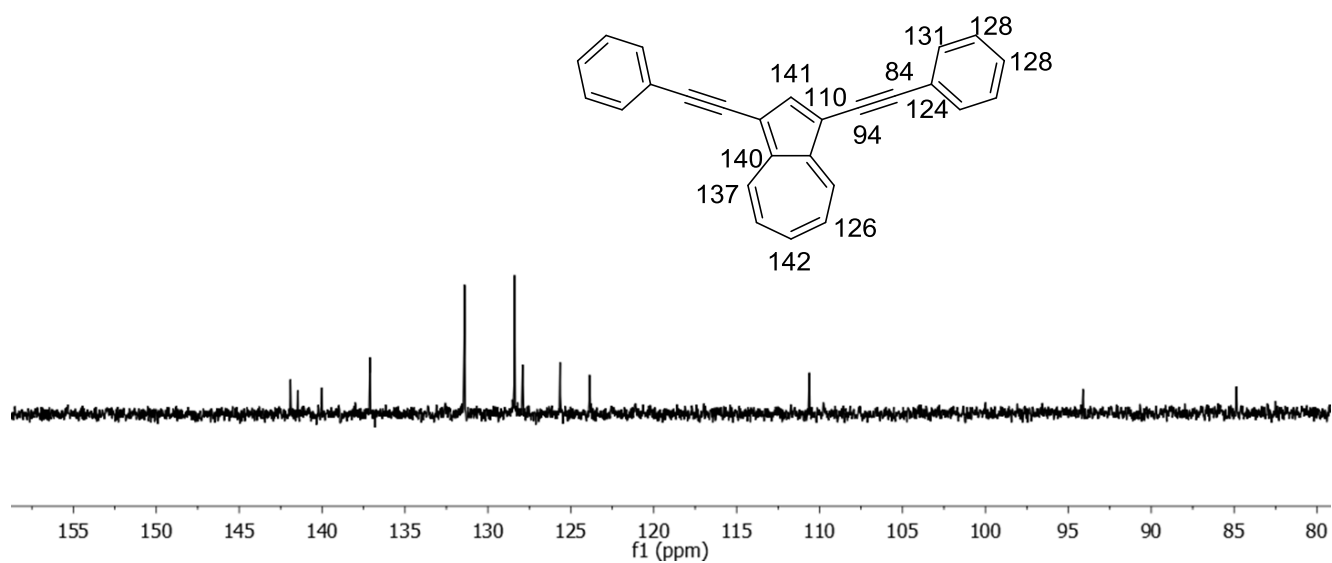


Figure 6.5: ¹³C-NMR CPD spectrum of 1,3-bis(phenylethynyl)azulene (Az-Ph₂).

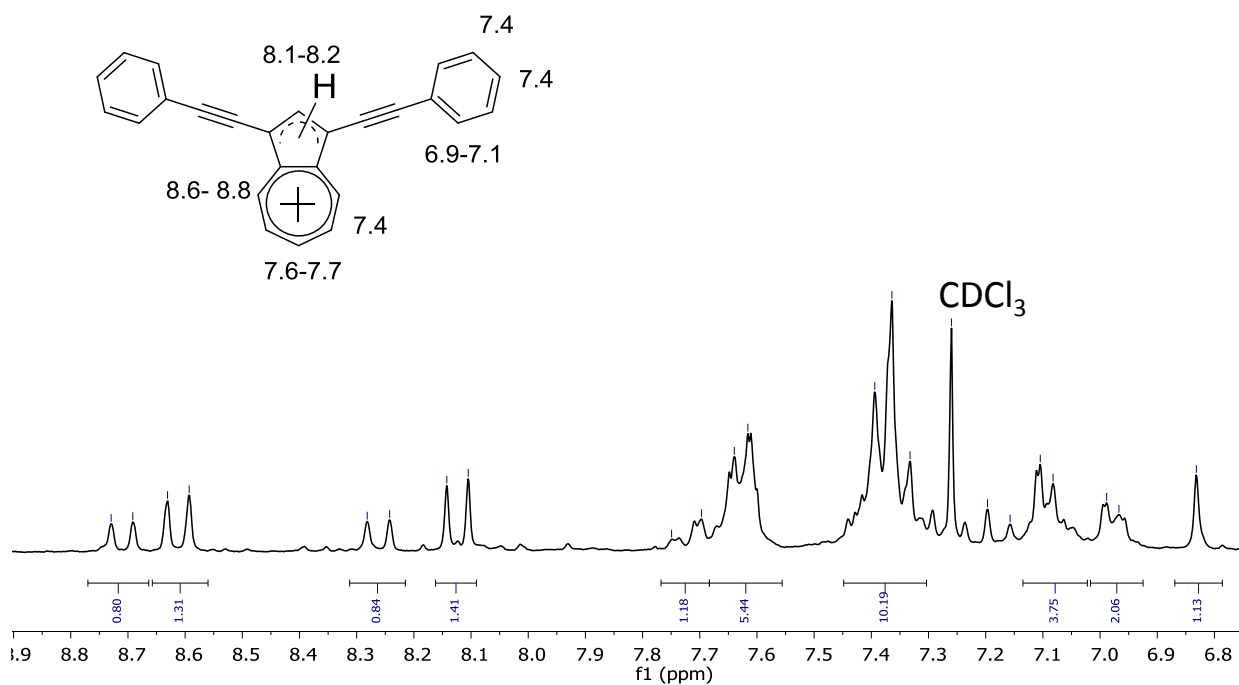


Figure 6.6: ¹H-NMR NMR spectrum of 1,3-bis(phenylethynyl)azulene (Az-Ph₂) after protonation with TFA.

6.2.6 Photocatalytic reduction of Cr(VI) to Cr(III) using poly-azulene networks

In a 25 ml vial, 3 mg protonated poly-azulene were added into 5 ml of Cr(VI) solution (K_2CrO_7 in H_2O , 25 mg/l). Under inert atmosphere, the mixture was stirred for 1 h in order to adjust an adsorption/desorption equilibrium. Light irradiation was conducted with a 23 W fluorescence energy saving light bulb (OSRAM). The Cr(III) concentration was determined at 540 nm by titration with a diphenylcarbazide (DPC) solution determined using the UV-vis spectroscopy.^[172] In detail, 100 μ l of solution after photocatalytic reduction of Cr(VI) was mixed with 0.9 ml of 0.2 M H_2SO_4 , followed by addition of 20 μ l of freshly prepared 0.25% (w/v) DPC in acetone. After stirring for about 1 min, it was allowed to stand for 15 min so as to ensure full color development. The developed purple color formed was then measured at 540 nm.

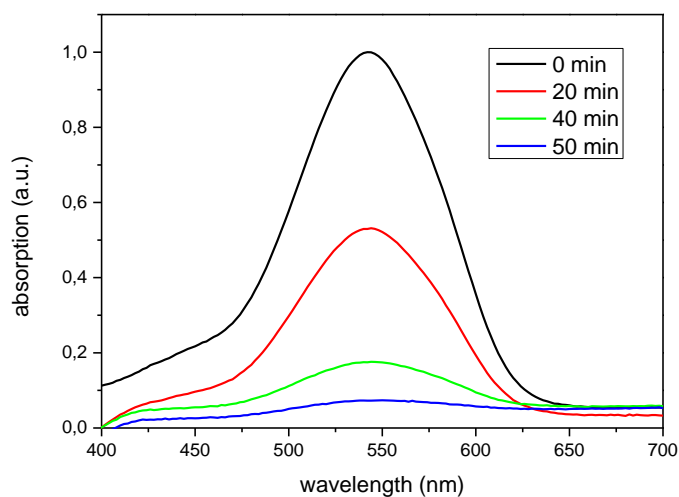


Figure 6.7: UV/vis absorption of DPC for determination of the photocatalytic reduction Cr^{VI} to Cr^{III} using P-Az-1 as photocatalyst in water under white light irradiation.

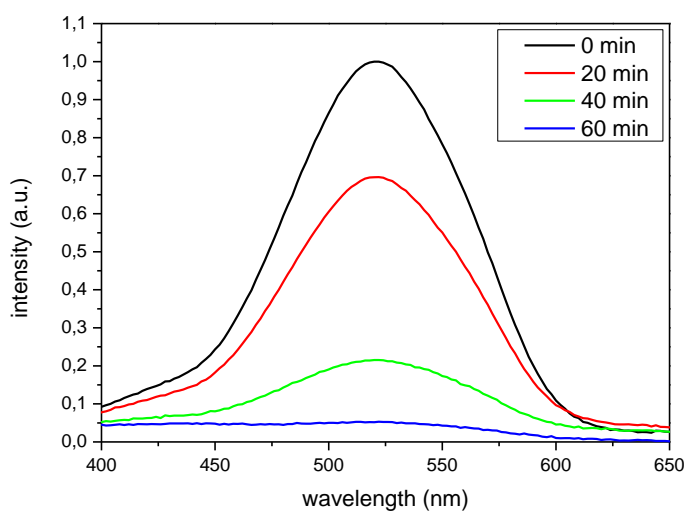


Figure 6.8: UV/vis absorption of DPC for determination of the photocatalytic reduction Cr^{VI} to Cr^{III} using P-Az-2 as photocatalyst in water under white light irradiation.

6.2.7 Photocatalytic reduction of Cr(VI) to Cr(III) using protonated Az-Ph₂

Similar to the procedure using the polymer, 3 mg protonated Az-Ph₂ were added into 5 ml of Cr(VI) solution (K₂CrO₇ in H₂O, 25 mg/l). Under inert atmosphere, the mixture was stirred for 1 h in order to adjust an adsorption/desorption equilibrium. Light irradiation was conducted with a 23 W fluorescence energy saving light bulb (OSRAM). The Cr(III) concentration was determined at 540 nm by titration with a diphenylcarbazide (DPC) solution determined using the UV-vis spectroscopy as described in the experimental part.

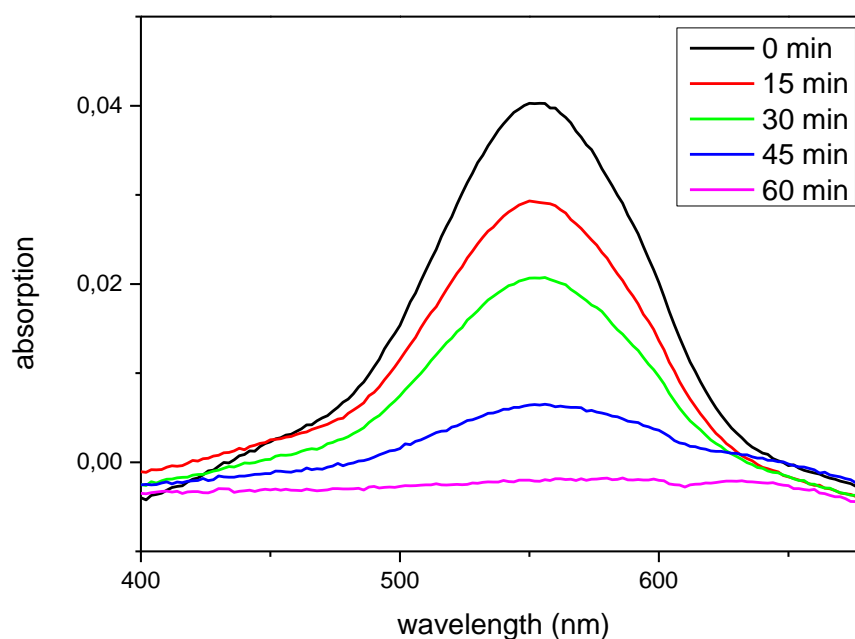


Figure 6.9: UV/vis absorption of DPC for determination of the photocatalytic reduction Cr(VI) to Cr(III) using Az-Ph₂ as homogeneous photocatalyst in water under white light irradiation.

6.2.8 Photoreduction of Cr(VI) to Cr(III) using poly-azulene networks and additional metal cations as co-catalysts in a cascade cycle

The co-catalysts FeCl_3 or CuCl_2 (1 equivalent with regard to Cr(VI)) were added to the reaction solution. The samples have been taken every 10 min in order to detect the amount of Cr(VI) in the solution. The photoreduction of Cr(VI) was conducted as mentioned above and by monitoring with the DPC method.

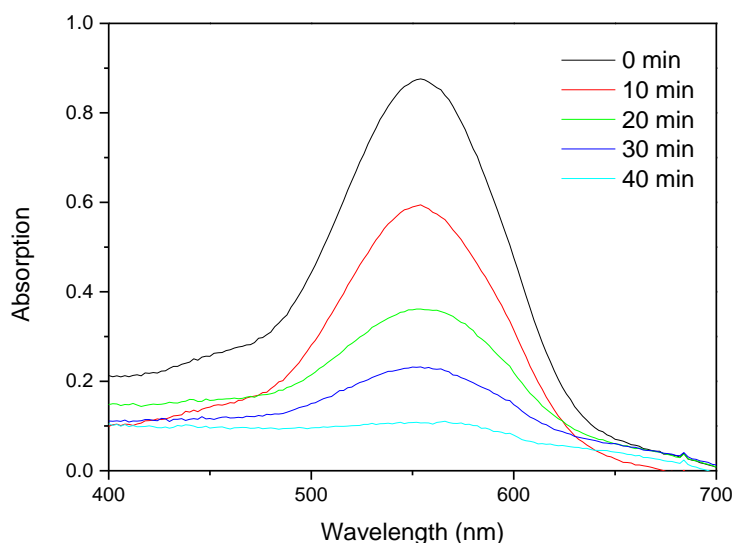


Figure 6.10: UV/vis absorption of DPC for determination of the photocatalytic reduction Cr(VI) to Cr(III) using *P-Az-1* photocatalyst and Fe(III)Cl_2 as cascade co-catalyst in water under white light irradiation.

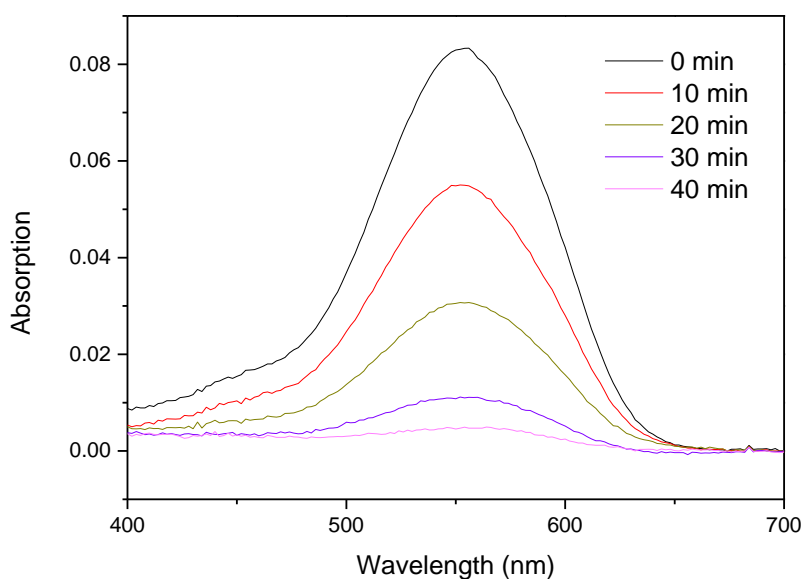


Figure 6.11: UV/vis absorption of DPC for determination of the photocatalytic reduction Cr(VI) to Cr(III) using *P-Az-1* photocatalyst and Cu(II)Cl_2 as cascade co-catalyst in water under white light irradiation.

6.2.9 Photoreduction of Cr(VI) to Cr(III) using poly-azulene networks and formic acid as extra electron donor

The reaction conditions were similar to that of only using P-Az-1h. Formic acid (0.36 mmol/ml) was added in excess. The samples have been taken every 10 min in order to detect the amount of Cr(VI) in the solution. And the photoreduction rate of Cr(VI) were conducted as mentioned above and by monitoring with the DPC method.

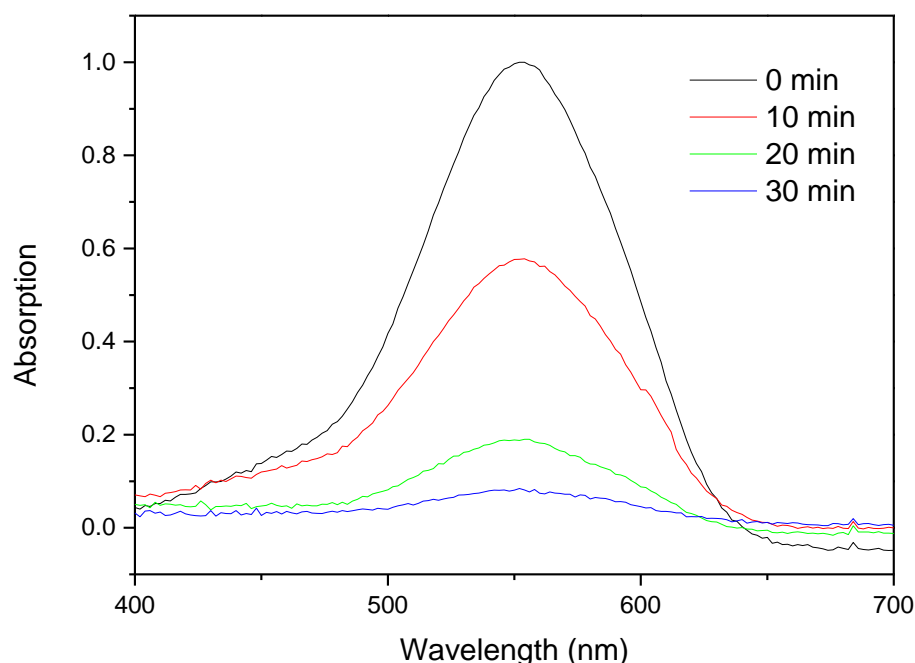


Figure 6.12: UV/vis absorption of DPC for determination of the photocatalytic reduction Cr(VI) to Cr(III) using P-Az-1 photocatalyst and formic acid as electron donor in water under white light irradiation.

6.2.10 Determination of Fe(II) in the cascade catalytic cycle

In a 10 ml Vial 2 mg Potassium ferricyanide ($K_3[Fe(CN)_6]$) was dissolved in 5 ml deionized water. After dispersing 5 mg of P-Az-1h the mixture was degassed and irradiation using the 23 W energy saving light bulb for 40 min. The presence of Fe(II) could be visualized by the change of color from yellow to blue (see Figure 5.22).

6.2.11 Repeating experiments

The repetition of the photoreduction and testing of the photocatalytic long-term performance was conducted by addition of 0.1 ml of a concentrated Cr(VI) solution (2.5 mg K_2CrO_7 in 2

ml H₂O) to the reaction vial. The progress of the photoreduction was monitored as mentioned above with the DPC method.

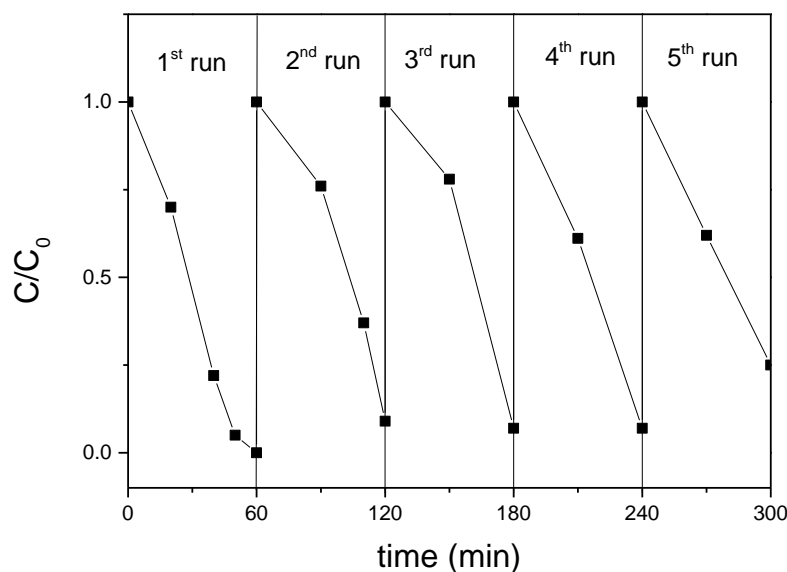


Figure 6.13: Repeating cycles of the photocatalytic reduction of Cr(VI) using P-Az-2h as catalyst. C is the initial concentration of Cr(VI), and C_0 is the initial concentration after research reaching adsorption/desorption equilibrium in dark.

6.2.12 Apparent Quantum Yield Measurements

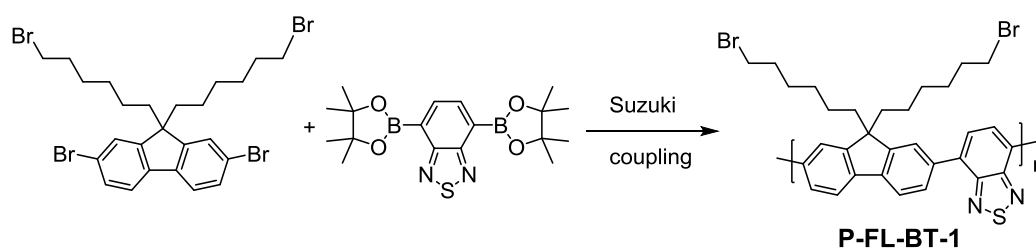
In order to determine the apparent quantum yield, the photoreduction of Cr(VI) to Cr(III) was conducted as mentioned before with a blue LED (460 nm, 0.26 W/cm²). The conversion was determined after 20 min by UV-Vis spectroscopy. The illumination area was 6.76 cm² and the LED intensity was measured by a Coherent Lab-Max energy meter. The apparent quantum yield was estimated by following equation:

$$\begin{aligned} \Phi(AQY) &= \frac{\text{moles of product evolved}}{\text{moles of incident photons}} \\ &= \frac{N_e}{N_p} \times 100\% = \frac{M \times N_A}{\frac{E_{total}}{E_{photon}}} \times 100\% \\ &= \frac{M \times N_A}{S \times P \times t} \times 100\% = \frac{M \times N_A \times \hbar \times c}{S \times P \times t \times \lambda} \times 100\% \\ &\quad \hbar \times \frac{c}{\lambda} \\ &= 0.09\% \end{aligned}$$

re, M is the amount of product molecules (mol), N_A is Avogadro constant ($6.022 \times 10^{23}/\text{mol}$), h is the Planck constant ($6.626 \times 10^{-34} \text{J}\cdot\text{s}$), c is the speed of light ($3 \times 10^8 \text{m/s}$), S is the irradiation area (cm^2), P is the intensity of irradiation light (W/cm^2), t is the photoreaction time (s), λ is the wavelength of the monochromatic light (m).

6.3 Heterophase photocatalyst from water-soluble conjugated polyelectrolytes: a self-initiation example under visible light

6.3.1 Synthesis of P-FL-BT-1



A 25 ml Schlenk tube was filled with 646 mg (1mmol, 1 eq.) 2,7-dibromo-9,9-bis(6-bromohexyl)fluorene and 388 mg (1 mmol, 1 eq.) 2,1,3-Benzothiadiazole-4,7-diboronic acid pinacolester and the mixture was dissolved in 6 ml THF. Additionally, 70 mg (0.06 mmol, 6 mol%) Tetrakis(triphenylphosphine)palladium (0), 28 mg (0.06 mmol, 6 mol%) XPHOS, and 2 ml of a potassium carbonate solution (967 mg in 2 ml H_2O) were added and the mixture was degassed for 20 min. The mixture was heated and left stirring at 80 °C for 18 h under argon atmosphere. After cooling down to room temperature the reaction mixture was poured into 100 ml of water and extracted three times by 100 ml of dichloromethane. The organic phase was filtrated by celite and dried over MgSO_4 . After removing the solvent the obtained material was extracted in a Soxhlet apparatus and washed with methanol for two days. Yield: 590 mg (95%). M_n : 15050 g/mol, M_w : 34095 g/mol, PDI: 2.27.

^1H NMR (300 MHz, CDCl_3 , 25 °C): δ 7.95 (8H), 3.24 (4H), 2.10 (4H), 1.66 (4H), 1.25 (8H), 0.88 (4H).

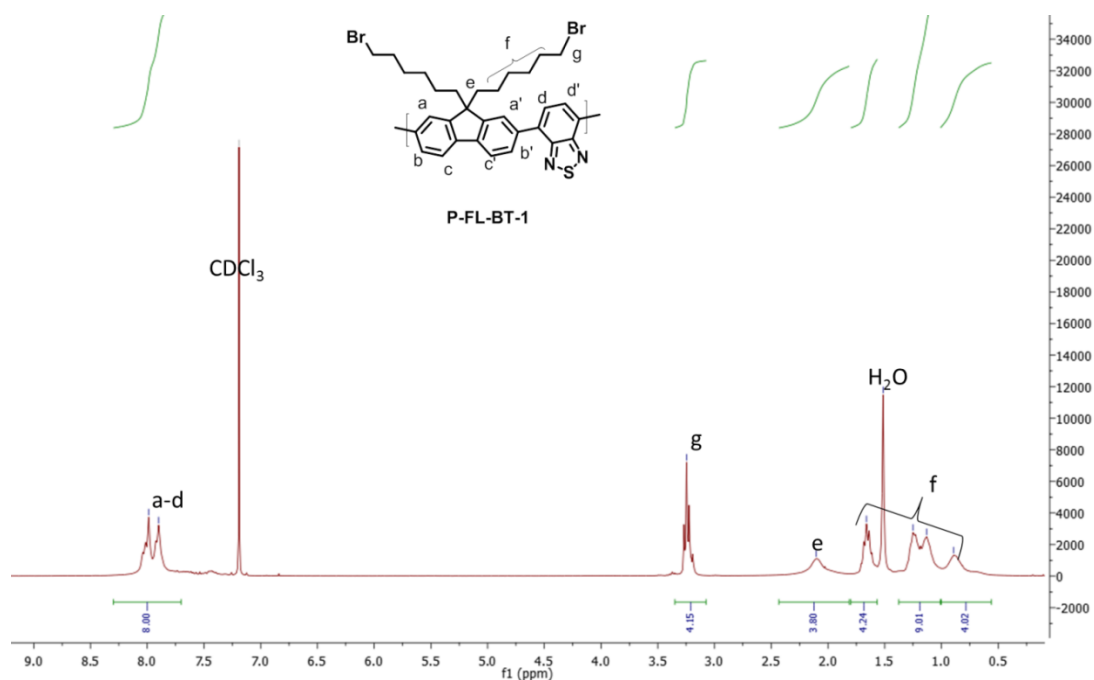
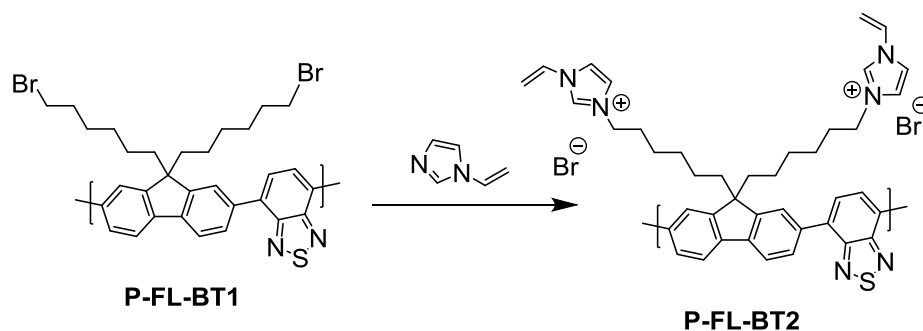


Figure 6.14: $^1\text{H-NMR}$ spectrum of *P-FL-BT-1*.

6.3.2 Synthesis of *P-FL-BT-2*



In a 25 ml Schlenk tube, 0.1 g (0.16 mmol) **P-FL-BT-1** was added to 2 ml THF and stirred until dissolved under argon atmosphere. Subsequently, 4 mL DMF, 5.0 g (52 mmol) 1-vinylimidazole, and 0.25 g (1.13 mmol) 2,6-di-tert-butyl-4-methylphenol were added under stirring. The reaction mixture was then stirred for 24 h at 60 °C, 80 °C and 100 °C respectively. The crude product was precipitated in THF and washed with THF several times. The product was stored at 4 °C for further use. Yield: 91 mg (88%). Functionalization: approximately 92%.

$^1\text{H-NMR}$ (400 MHz, DMSO-d_6 , 25 °C): δ (ppm) = 9.55 (bs, 2H), 8.24-7.60 (m, 12H), 7.25 (m, 2H), 5.95 (d, 2H), 5.38 (d, 2H), 4.12 (bs, 4H), 1.76-0.86 (m, 20H).

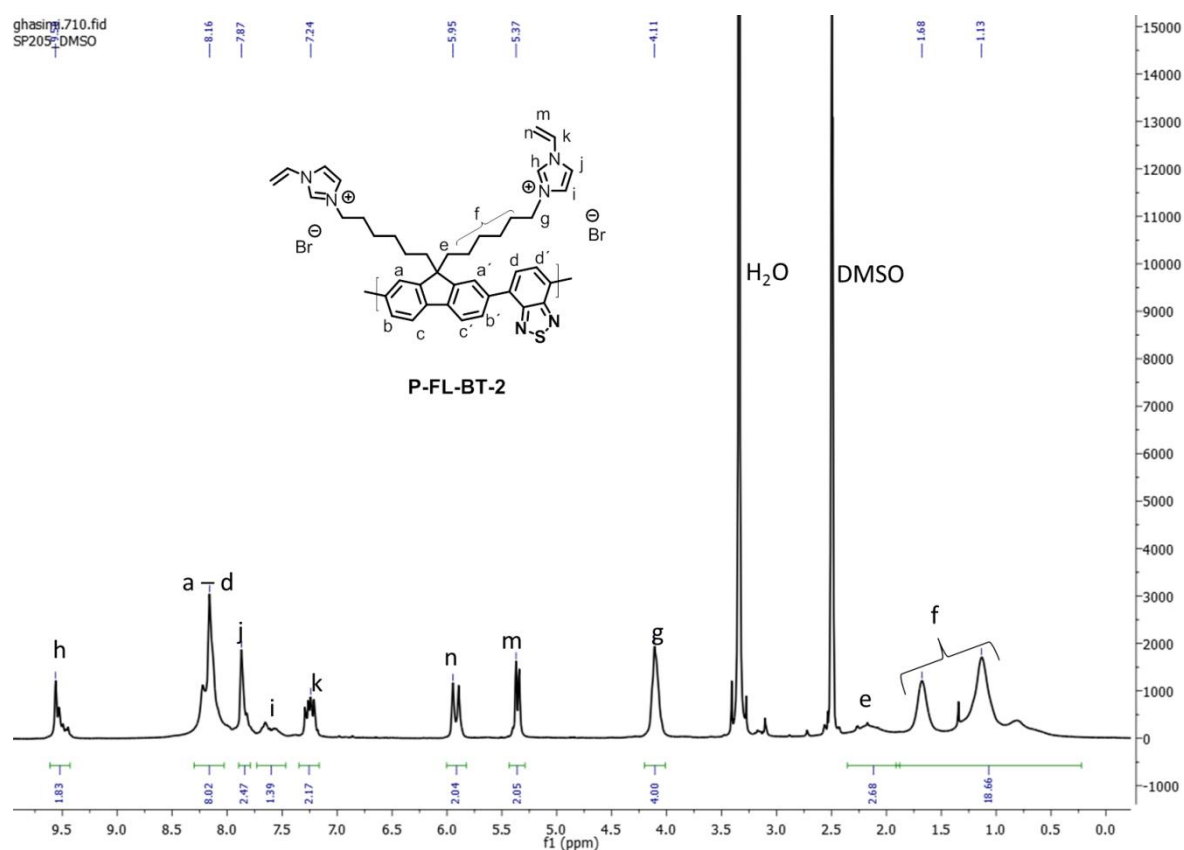


Figure 6.15: $^1\text{H-NMR}$ spectrum of P-FL-BT-2.

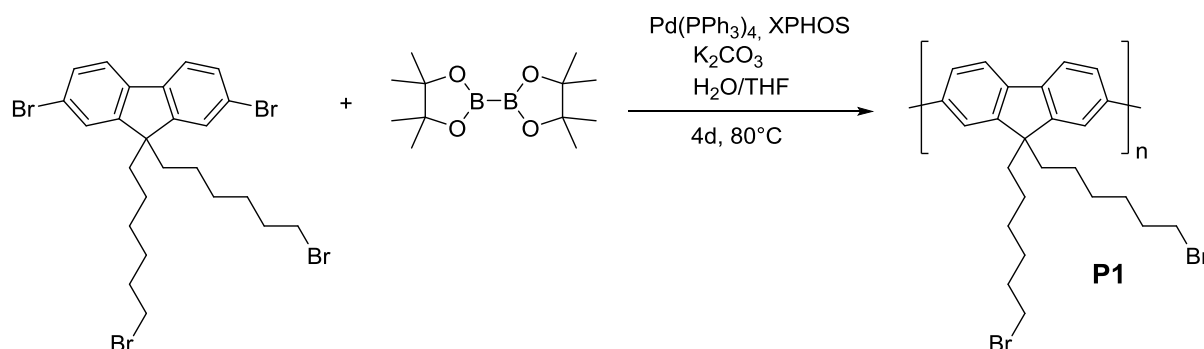
6.3.3 Synthesis of P-FL-BT-3 as nanoparticles

An aqueous solution of P-FL-BT-2 (0.1 mg/ml) were degassed for 5 min, under constant stirring the solution was irradiated with a white LED (1.2 W/cm², OSA Opto Lights) for 3 h, until the particle size became constant according to DLS measurement.

6.3.4 Synthesis of P-FL-BT-3 as porous monolith

The water in oil emulsion was made by slowly adding 4 mL of hexadecane to 1 ml of an aqueous solution of P-FL-BT-2 (4 mg/ml) under vigorous stirring using an Ultra Turrax IKA T18 mechanical stirrer at 14000 RPM. After 10 min, the homogeneous mixture became viscous and was exposed to visible light generated by a white LED lamp (1.2 W/cm², OSA Opto Lights) overnight. The resulted monolith was then rinsed a few times with methanol and placed on a shaker to remove the residual hexadecane overnight. Afterwards, the obtained polymer monolith underwent freeze-drying before further characterization studies were conducted.

6.3.5 Synthesis of poly(9,9-bis(6-bromohexyl)-fluorene) P1



A 25 ml Schlenck tube was filled with 1.5 g (2.3 mmol, 1 eq.) 2,7-dibromo-9,9-bis(6-bromohexyl)fluorene and 585 mg (2.3 mmol, 1 eq.) bis(pinacolato)diboron and the mixture was dissolved in 12 ml THF. Additionally, 160 mg (0.14 mmol, 6 mol%) Tetrakis(triphenyl)phosphinepalladium (0), 66 mg (0.14 mmol, 6 mol%) XPHOS, and 4 ml of a potassium carbonate solution (2.23 g in 4 ml H₂O) were added and the mixture was degassed for 20 min. The mixture was heated and left stirring at 80 °C for 4 d under argon atmosphere. After cooling down to room temperature the reaction mixture was poured into 100 ml of water and extracted three times by 100 ml of dichloromethane. The organic phase was filtrated by celite and dried over MgSO₄. The product was concentrated in a rotatory evaporator and precipitated in methanol. In order to remove oligomeric fractions the obtained product was Soxhlet extracted with methanol. Overall the yield for the polymer was 1.05 g (94%).^[143]

Mn: 4680 g/mol, PDI: 2.2

¹H-NMR (400.1 MHz, CDCl₃): δ (ppm) = 7.83 (d, 2H), 7.66 (m, 4H), 3.31 (t, 4H), 2.16 (m, 2H), 1.71 (m, 6H), 1.24 (m, 10H), 1.09-0.84 (m, 2H).

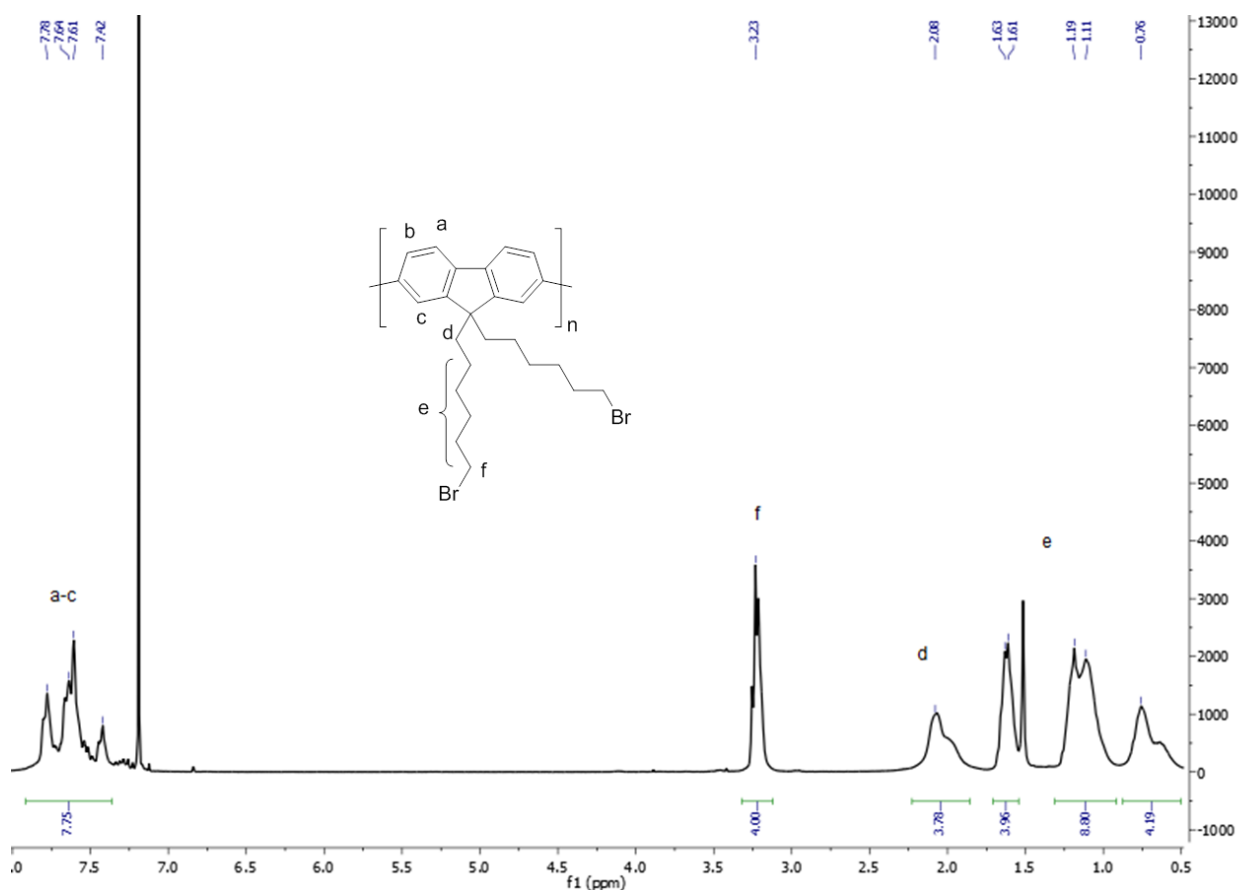


Figure 6.16: $^1\text{H-NMR}$ spectrum of P1.

6.3.6 Synthesis of P2Br

In a 50 ml schlenk tube under argon atmosphere 0.5 g (1 mmol) poly(9,9-bis(6-bromohexyl)-fluorene) (P1) was added to 10 ml THF and stirred until dissolved. Subsequently, 20 mL DMF, 25 g (0.26 mol) 1-vinylimidazole, and 1.25 g (5.67 mmol) 2,6-di-tert-butyl-4-methylphenol were added under viragoes stirring to the solution. The reaction mixture was stirred 24 h at 60 °C, 80 °C and 100 °C respectively. The crude product was precipitated in THF and washed with THF several times. The product was stored in THF at 7 °C for further use. Overall the yield for the polymer was 358 mg (71 %).

$^1\text{H-NMR}$ (400 MHz, DMSO- d_6 , 25 °C): δ (ppm) = 9.71 (bs, 2H), 8.21 (s, 2H), 7.92 (m, 6H), 7.29 (m, 2H), 5.94 (d, 2H), 5.39 (d, 2H), 4.13 (bs, 4H), 1.92-0.29 (m, 20H).

Functionalization: 90%. This value is calculated by comparing the integration area of peak o with peak i (see Figure 5.34).^[143]

6.3.7 Synthesis of P3Br

In a 50 ml schlenk flask under argon atmosphere 300 mg (0.48 mmol) of P2Br, 30 mg (0.1 mmol) 2,2'-azobis[2-methyl-N-(2-hydroxyethyl)propionamide], and 35 ml deionized water were mixed. 3 freeze-pump-thaw cycles were applied in order to remove oxygen. The reaction mixture was stirred at 85 °C for 24 h. The crude product was washed with deionized water several times. The yield of P3Br was 288 mg (96%).^[143]

6.3.8 Synthesis of P3X (X = BF₄, PF₆ or TFSI)

Ion exchange was performed by using two solutions: 1) 50 mg (0.08 mmol) of P3Br dispersed in 20 ml deionized water, and 2) 1.05 eq. of sodium tetrafluoroborate, potassium hexafluorophosphate or lithium bis(trifluoromethanesulfonyl)imide in 10 ml deionized water. 2) is then added dropwise to 1) under vigorous stirring. The precipitate was washed with deionized water to remove residual salt.^[143]

6.3.9 Synthesis of PMMA using P-FL-BT-1 as photoinitiator

In a glass vial, a mixture of MMA (2 ml, 9.39 mmol), P-FL-BT-1 (3 mg) and Et₃N (2 ml) were added. The mixture was purged with N₂ for 5 min and the vial was sealed from air. The mixture was then irradiated with a white LED lamp (1.2 W/cm², OSA Opto Lights) overnight. After the irradiation, the mixture was dissolved in THF and reprecipitated in methanol. The polymer is collected by filtration and dried under vacuum at 40 °C overnight. Gel permeation chromatography (GPC) was measured using PMMA as standard by determination of UV/vis absorption at 254 nm to separate the product and P-FL-BT-1. *M_n*: 35338 Da, *M_w*: 87775 Da, PDI: 2.48.

6.3.10 Photodegradation of rhodamine B and methylene blue

About ¼ of the porous monolith of P-FL-BT-3 (ca. 1 mg) was placed into a 20 ml vial containing the organic dye solution (10 ml, 10 mg/ml). The vial was kept 1 cm away from the white LED lamp under stirring under air. UV/vis samples were taken periodically to track the degradation rates of the dyes.

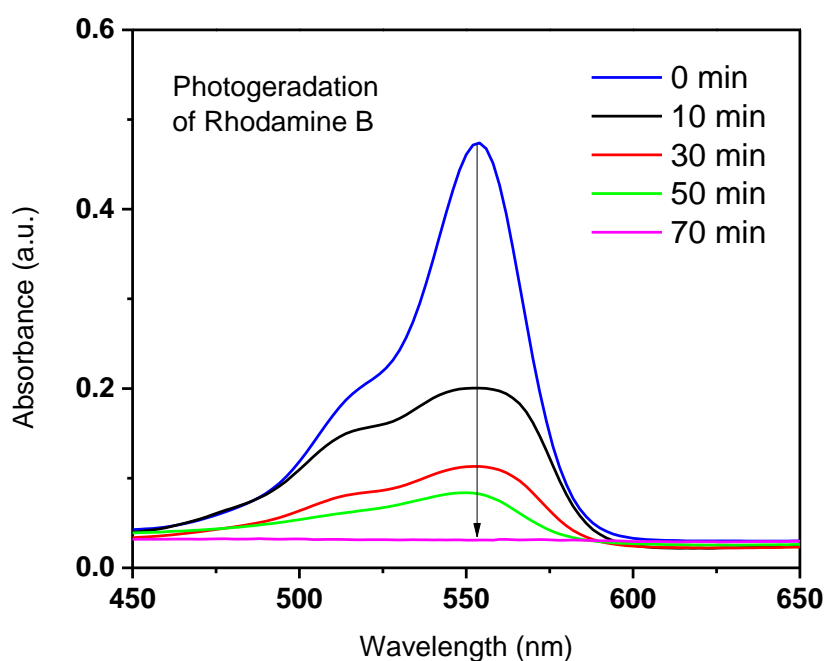


Figure 6.17: Photocatalytic degradation of Rhodamine B using P-FL-BT-3 in water under white light irradiation.

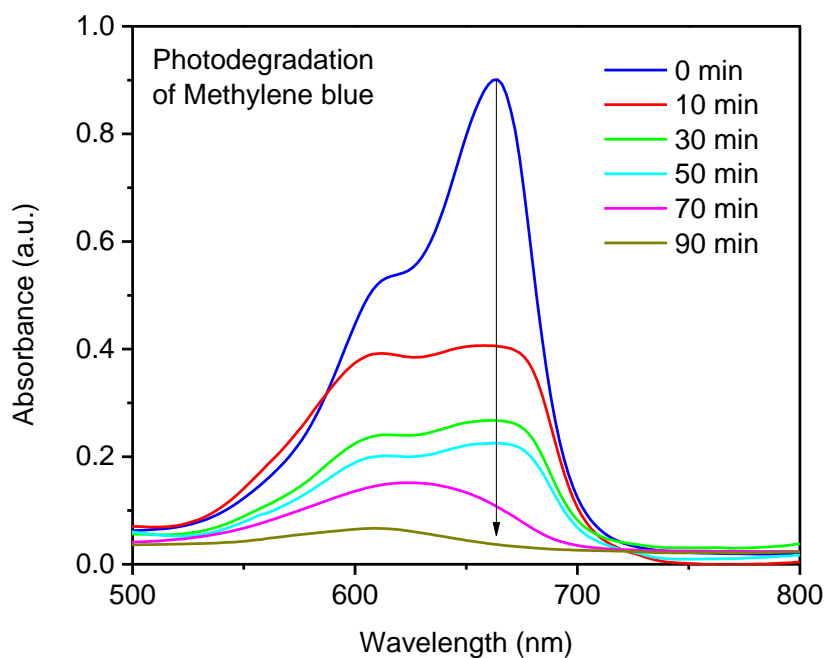


Figure 6.18: Photocatalytic degradation of Methylene blue using P-FL-BT-3 in water under white light irradiation.

For the repeating experiments, the same procedure was repeated 10 times.

6.3.11 Photoreduction of Cr(VI) to Cr(III)

In a 10 ml vial, 1/2 of the porous monolith of P-FL-BT-3 (ca. 1 mg) was placed into 5 ml of Cr(VI) solution (25 mg/l). Under inert atmosphere, the mixture was irradiated with a white LED and stirred constantly. The Cr(VI) concentration was determined at 540 nm by titration with a diphenylcarbazide (DPC) solution determined using the UV-vis spectroscopy. In detail, 1 mL of solution after photocatalytic reduction of Cr(VI) was mixed with 9 ml of 0.2 M H₂SO₄, followed by addition of 0.2 mL of freshly prepared 0.25% (w/v) DPC in acetone. After stirring for about 1 min, it was allowed to stand for 15 min so as to ensure full color development. The developed purple color formed was then measured at 540 nm.

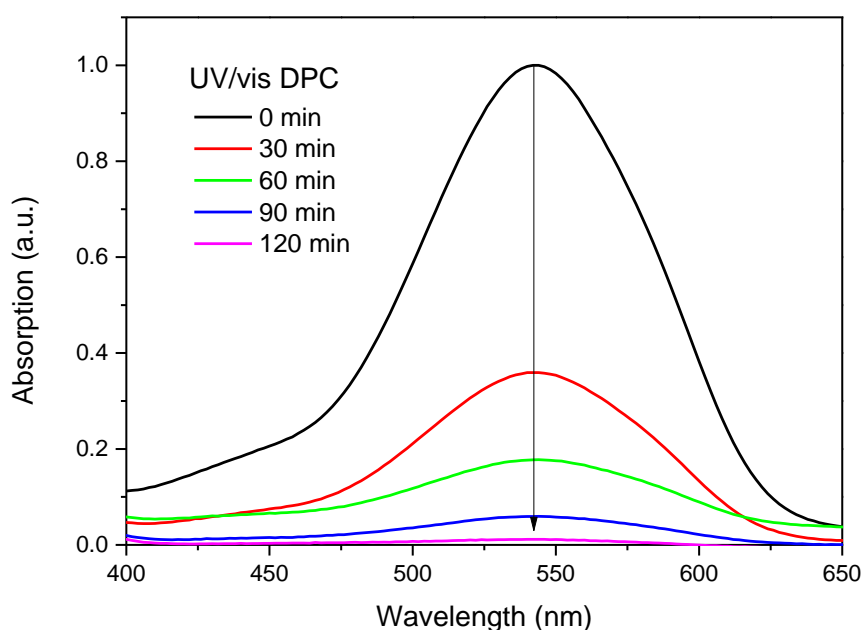


Figure 6.19: UV/vis absorption of DPC for determination of the photocatalytic reduction Cr^{VI} to Cr^{III} using P-FL-BT-3 as photocatalyst in water under white light irradiation.

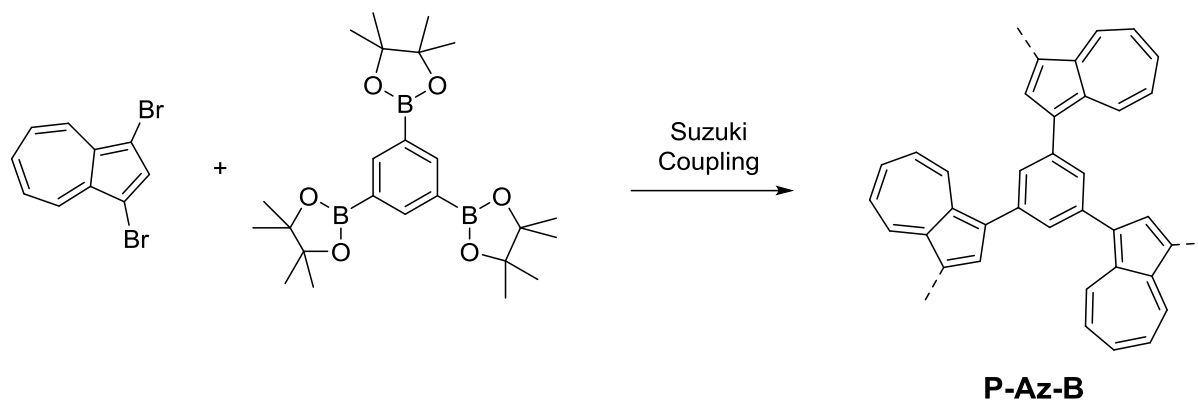
6.3.12 Scavenger study of rhodamine B degradation using P-FL-BT-3 as photocatalyst

1 mg of P-FL-BT-3 was dispersed in 5 ml of rhodamine B solution (10 mg/ml) in a 10 ml glass vial in air. To the reaction mixture different scavengers (ca. 0.5 mmol) were added and irradiated using a white LED under constant stirring for 1 h. Reaction conditions with different scavengers: 1,4-benzoquinone (BQ) (54 mg), sodium azide (NaN₃) (33 mg), isopropanol (IP) (30 mg), potassium iodide (KI) (83 mg) and catalase (CAT) (7.5 mg, 2000 -

4000 U/mg). The degradation degree of rhodamine B was analyzed by UV-vis spectroscopy and the results are displayed in Figure 5.46.

6.4 Photocatalytic Stille-type coupling reactions using conjugated organic catalysts with visible light

6.4.1 Synthesis of P-Az-B



A 25 ml Schlenk tube was filled under argon with 210 mg phenylboronic acid (0.46 mmol, 1 eq), 67 mg 1,3-dibromoazulene (0.23 mmol, 0.5 eq), 32 mg Pd(PPh₃)₄ (6 mol%). After dissolving the mixture in 6 ml DMF, 2 ml of aqueous potassium carbonate (4.45 mg, 3.22 mmol, 7 eq) was added. The reaction mixture was heated at 90 °C under continuous stirring. After 24 hours additional 67 mg 1,3-dibromoazulene (0.23 mmol, 0.5 eq) was added to the reaction mixture. After another 24 h, the last step was repeated and again 67 mg 1,3-dibromoazulene (0.23 mmol, 0.5 eq) was added to the reaction mixture, while keeping the reaction for 24 h at 90°C. Finally the reaction mixture was refluxed at 145 °C for further 24 h. Each addition step was accompanied with a change of color from pale green, dark blue, to black. After cooling down to room temperature, the reaction mixture was filtered, washed several times with brine, water, and several times with dichloromethane and THF. The black powder was extracted by Soxhlet extraction (MeOH, DCM) for 2 d. Yield: 108 mg (52 %).

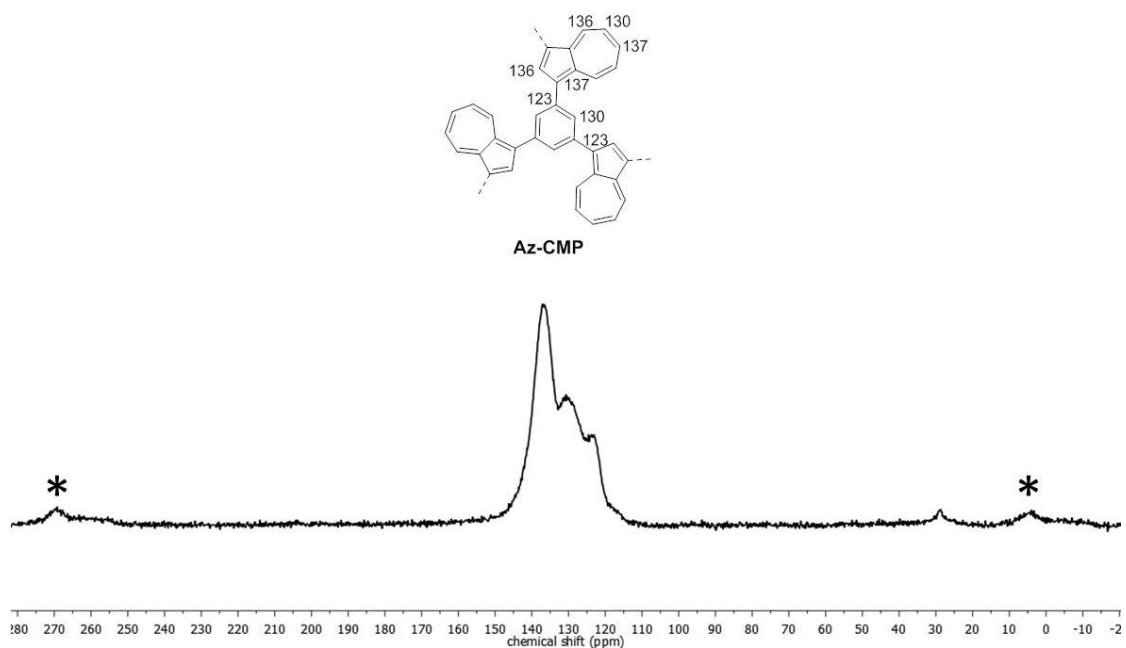
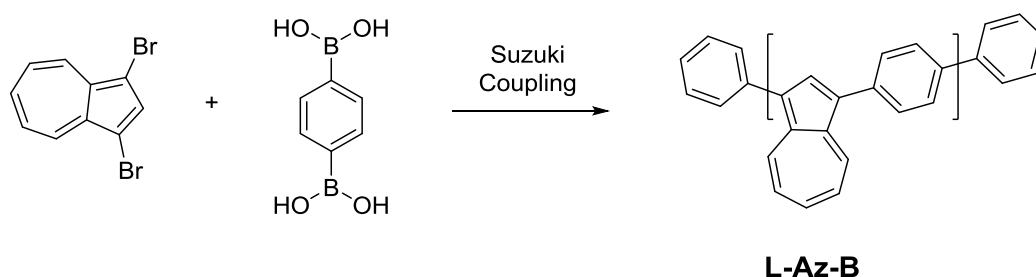


Figure 6.20: Solid state CP-MAS ^{13}C -NMR spectrum of *P*-Az-B at rotation frequency of 10 kHz (side bands*).

6.4.2 Synthesis of L-Az-B



A 25 ml Schlenk tube was filled under argon with 142 mg 1,3-dibromoazulene (0.5 mmol, 1 eq), 83 mg phenylboronic acid (0.5 mmol, 1 eq), 35 mg $\text{Pd}(\text{PPh}_3)_4$ (6 mol%). After dissolving the mixture in 4 ml THF, 2.3 ml of aqueous potassium carbonate (484 mg, 3.5 mmol, 7 eq) was added. The reaction mixture was left at reflux temperature while it was stirring about 48 h. Additional 61 mg phenylboronic acid (0.5 mmol) were added as endcapping agent. The mixture was again refluxed for 6 h before cooling down to room temperature. The reaction mixture was washed with brine and water, and extracted three times with 100 ml of dichloromethane. The organic phase was filtered over celite to remove traces of precipitations of the catalysts. After drying over MgSO_4 the solvent was removed under reduced pressure. The crude product was purified with column chromatography. The final product was precipitated in cold methanol. 83 mg (82%) of dark green powder was obtained.

M_w : 1023 g/mol, PDI: 1.27

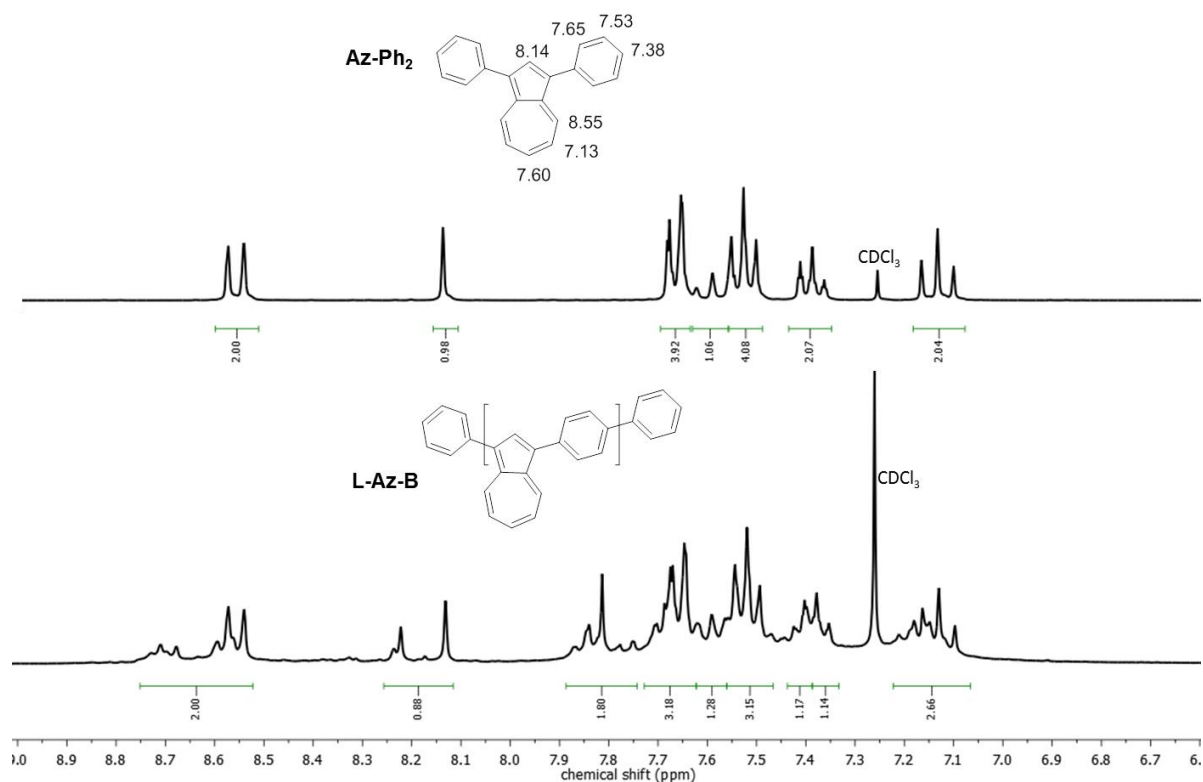
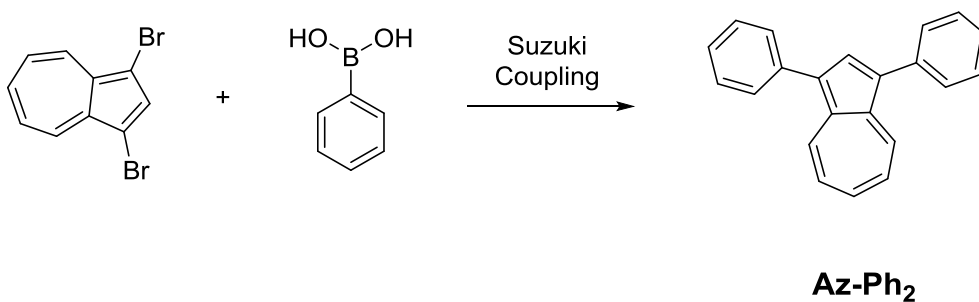


Figure 6.21: $^1\text{H-NMR}$ spectrum of **Az-Ph₂** and **L-Az-B**.

6.4.3 Synthesis of 1,3-bis(phenyl)azulene (**Az-Ph₂**)

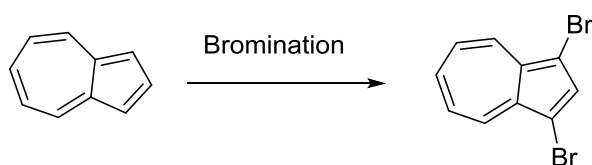


A 25 ml Schlenk tube was filled under argon with 100 mg 1,3-dibromoazulene (0.35 mmol, 1 eq), 86 mg phenylboronic acid (0.70 mmol, 2 eq), 25 mg $\text{Pd(PPh}_3)_4$ (6 mol%). After dissolving the mixture in 4 ml THF, 1.5 ml of aqueous potassium carbonate (341 mg, 2.47 mmol, 7 eq) was added. The reaction mixture was left at reflux temperature while it was stirring about 24 h. After cooling down to room temperature, the reaction mixture was washed with brine and water, and extracted three times with 100 ml of dichloromethane. The

organic phase was filtered over Celite® to remove the catalyst residue. After drying over MgSO₄, the solvent was removed under reduced pressure. The crude product was purified with column chromatography with hexane as eluent. 36 mg (37%) of dark blue solid was obtained.

¹H NMR (300 MHz, CDCl₃, 25 °C): δ (ppm) = 8.45 (d, 2H), 8.04 (s, 1H), 7.55 (m, 4H), 7.50 (t, 1H), 7.43 (m, 4H), 7.28 (m, 2H), 7.03 (t, 2H)

6.4.4 Bromination of azulene



According to the procedure in 6.2.2.

6.4.5 Photocatalytic destannylation reaction of aryl stannanes using P-Az-B as photocatalyst

A 25 ml Schlenk tube was filled with 5 mg P-Az-B, 0.2 mmol aryl stannane in 5 ml THF. The reaction mixture was kept under stirring in air while it was irradiated with a white LED lamp (1.2 W/cm², OSA Opto Lights) for 24-45 hours. After the reaction was finished the catalyst was removed by filtration and the raw product was purified by column chromatography with hexane/ethylacetate (5:1 volume ratio) as eluent.

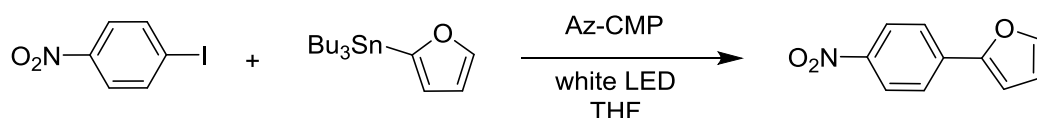
6.4.6 Radical trapping experiment with N-tert-butyl- α -phenylnitrone (PBN)

A 20 ml vial was filled under argon atmosphere with 5 mg P-Az-B, 65 μ l 2-(tributylstannyl)furan, 0.05 M PBN, and 4 ml anhydrous THF. The mixture was irradiated under stirring with a white LED lamp. Samples were taken at different times and measured by EPR. In order to exclude other interactions of radical species with PBN, a control experiment was conducted with P-Az-B and PBN in THF.

6.4.7 General procedure for the photocatalytic Stille-type coupling of aromatic iodides with stannanes

A 25 ml Schlenk tube was filled under argon atmosphere with 5 mg of P-Az-B, 0.2 mmol of ArI, and 0.2 mmol of the corresponding tri-n-butylstannane. Additional 4 ml dry THF was added and the mixture was irradiated with a white LED lamp (1.2 W/cm², OSA Opto Lights) while it was stirring for 24 h. After the reaction was finished the catalyst was recovered by filtration and the raw product was purified by column chromatography with hexane/ethylacetate (5:1 volume ratio) as eluent.

6.4.8 Repeating experiments of the photocatalytic Stille-type coupling of 4-iodonitrobenzene with 2-(tributylstannyl)furan

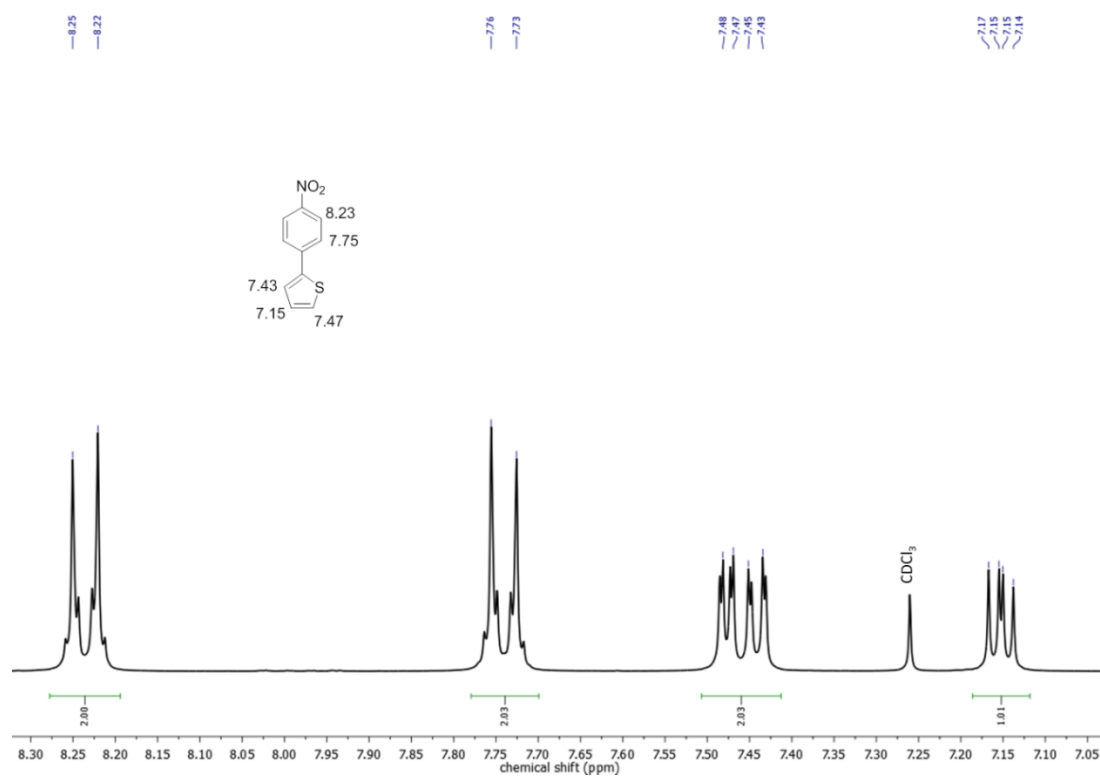
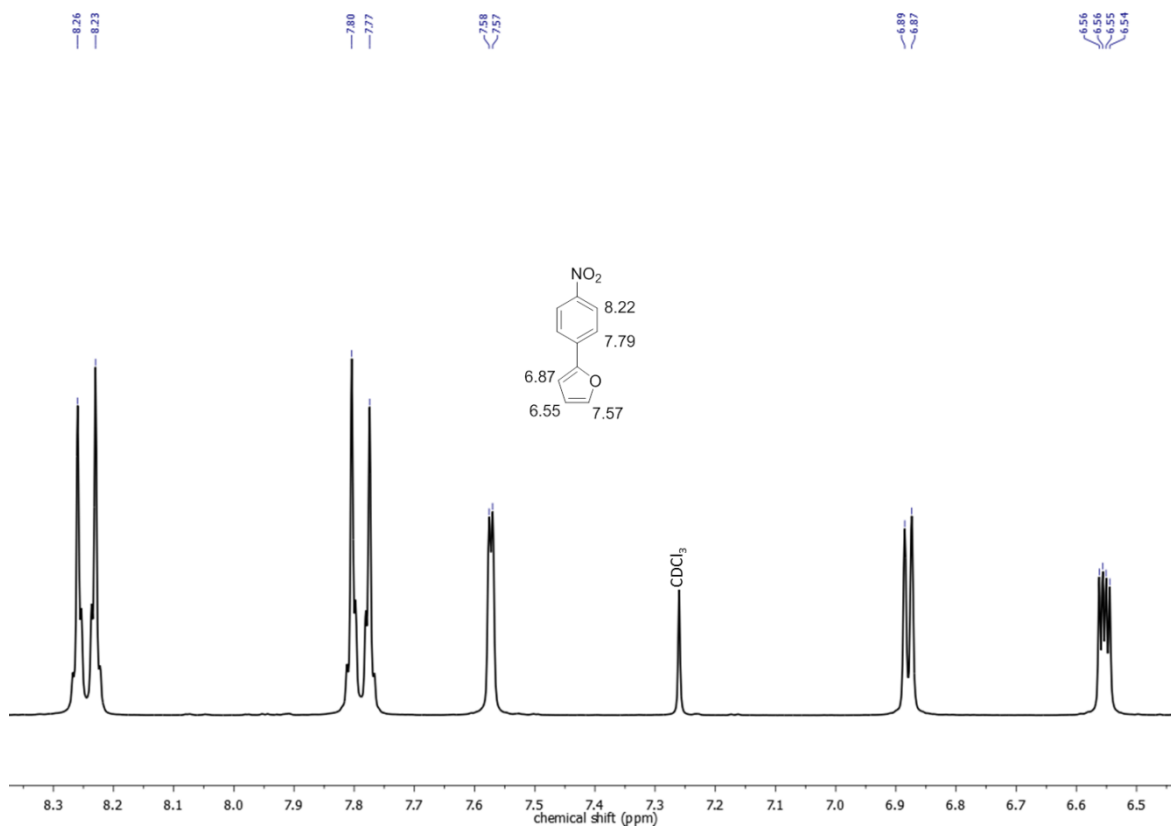


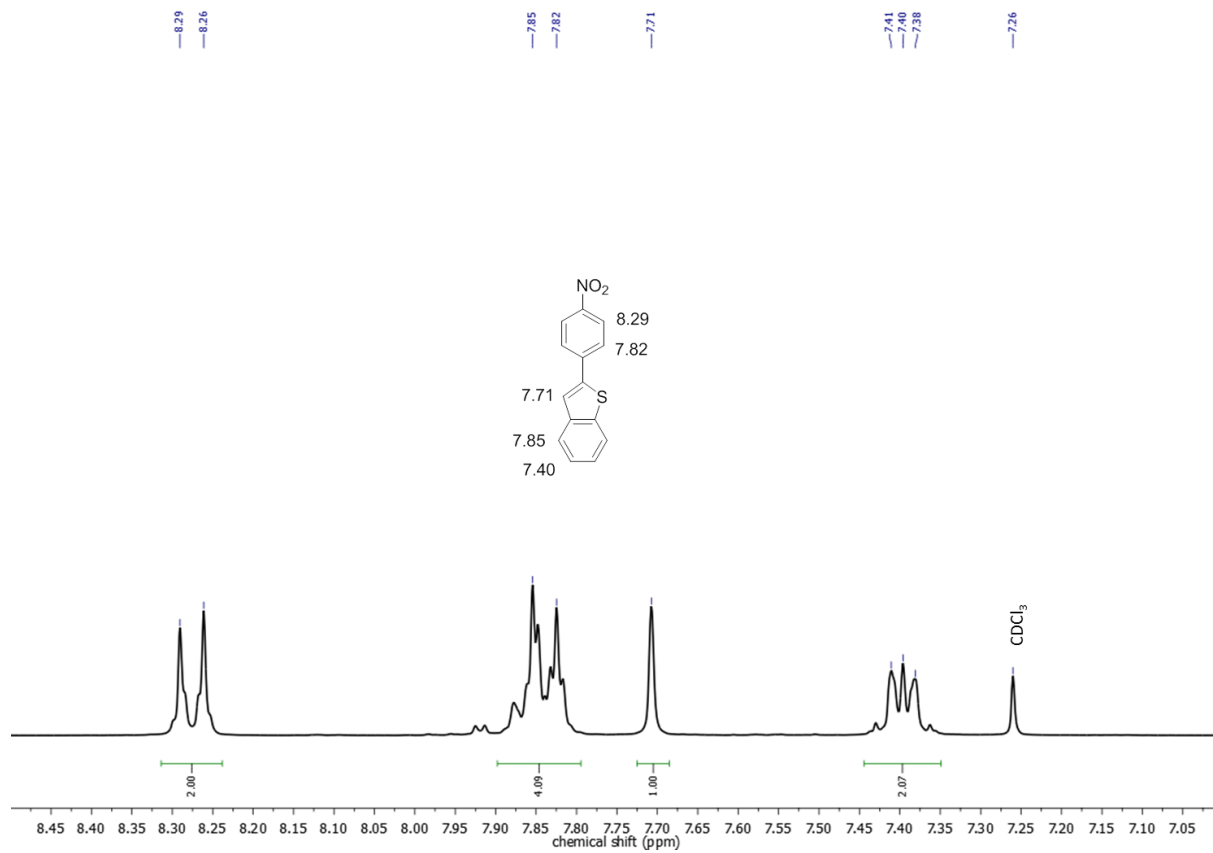
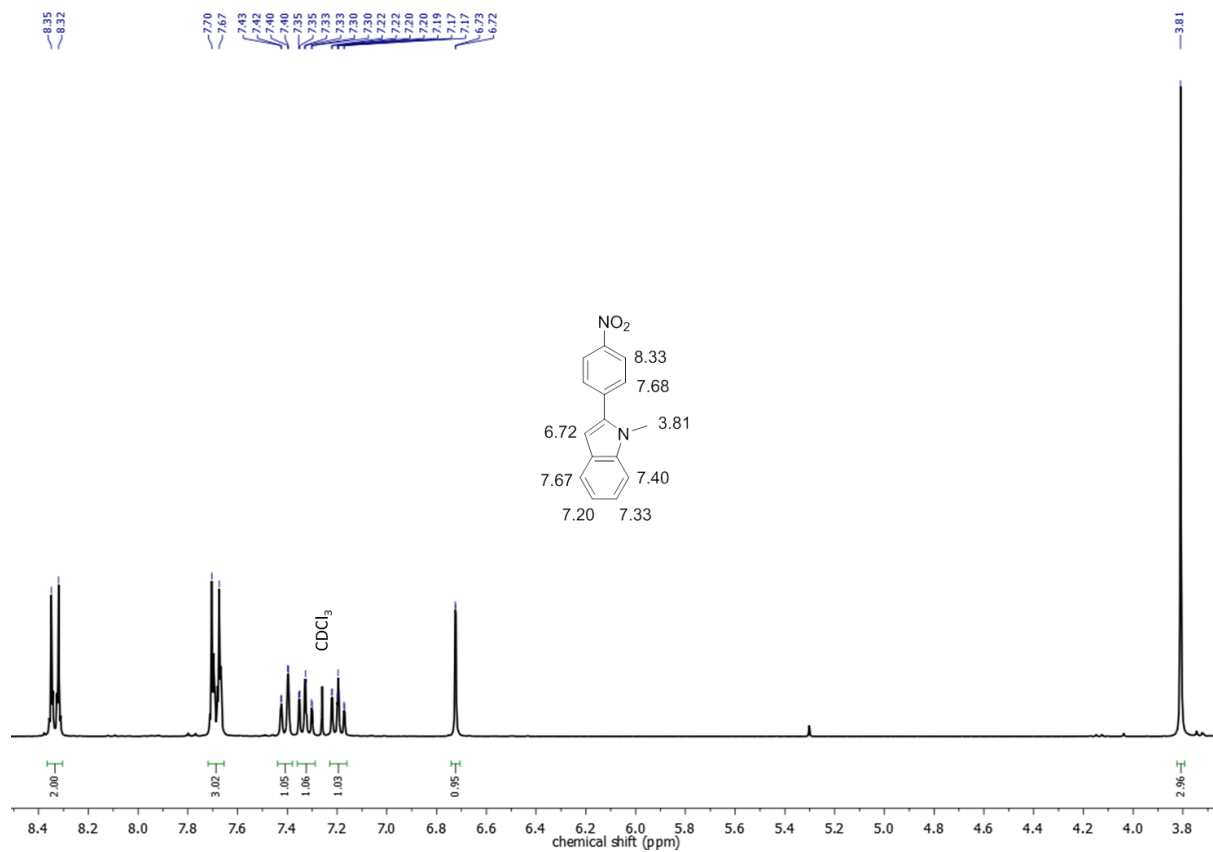
A 25 ml Schlenk tube was filled under argon atmosphere with 20 mg of P-Az-B, 0.2 mmol of 4-iodonitrobenzene, and 0.2 mmol of 2-(tributylstannyl)furan. Additional 4 ml dry THF was added and the mixture was irradiated with a white LED lamp (1.2 W/cm², OSA Opto Lights) while it was stirring for 24 h. After the reaction was finished the catalyst was recovered by membrane filtration and the raw product was purified by column chromatography with hexane/ethylacetate (5:1 volume ratio) as eluent. The same batch of P-Az-B was reused in 5 consecutive runs by the above mentioned procedure.

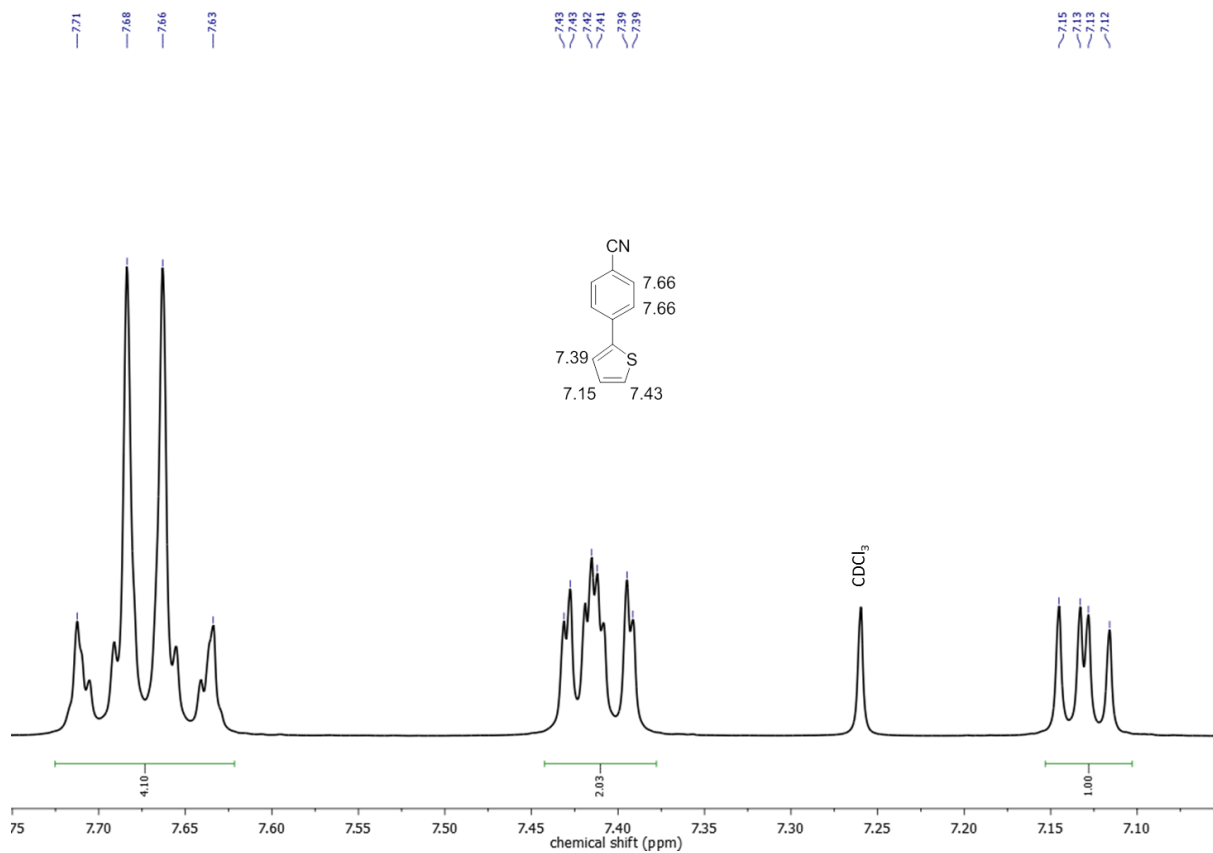
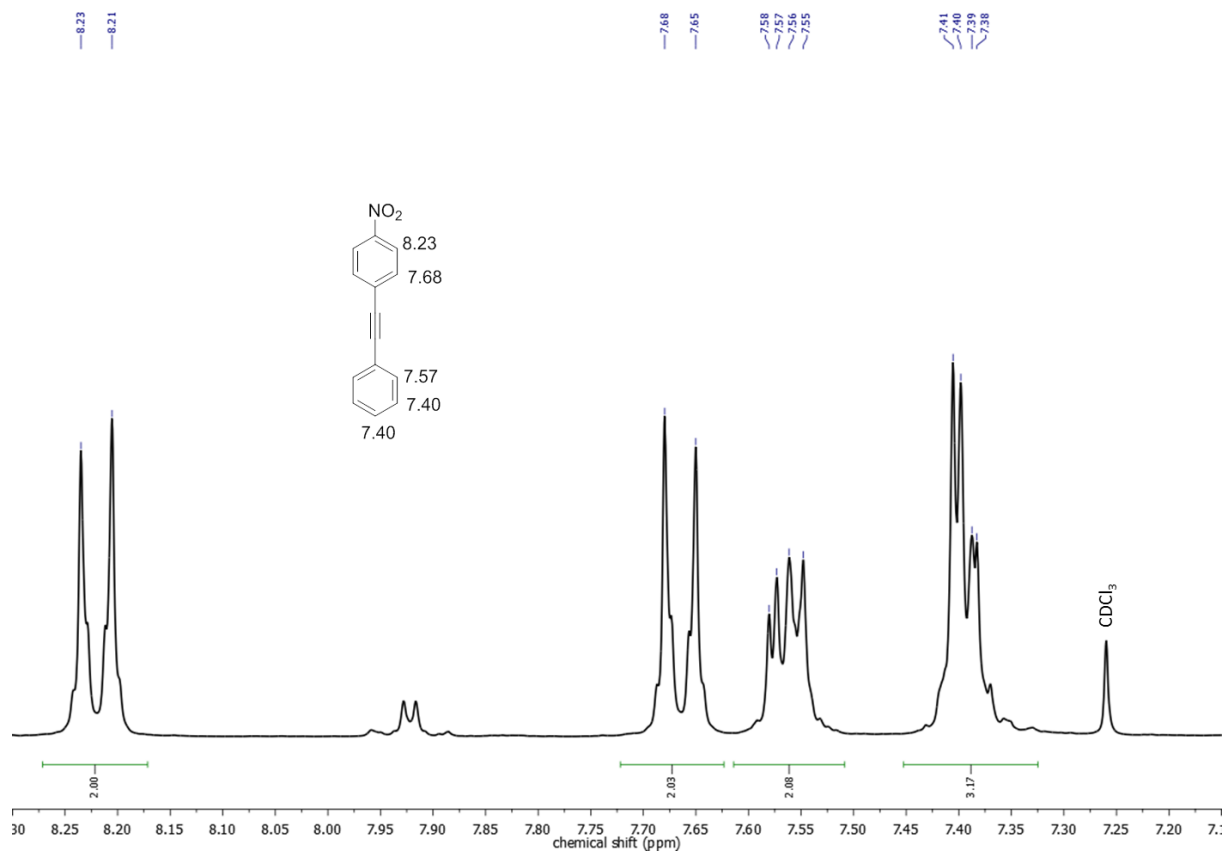
6.4.9 Apparent Quantum Yield Measurements

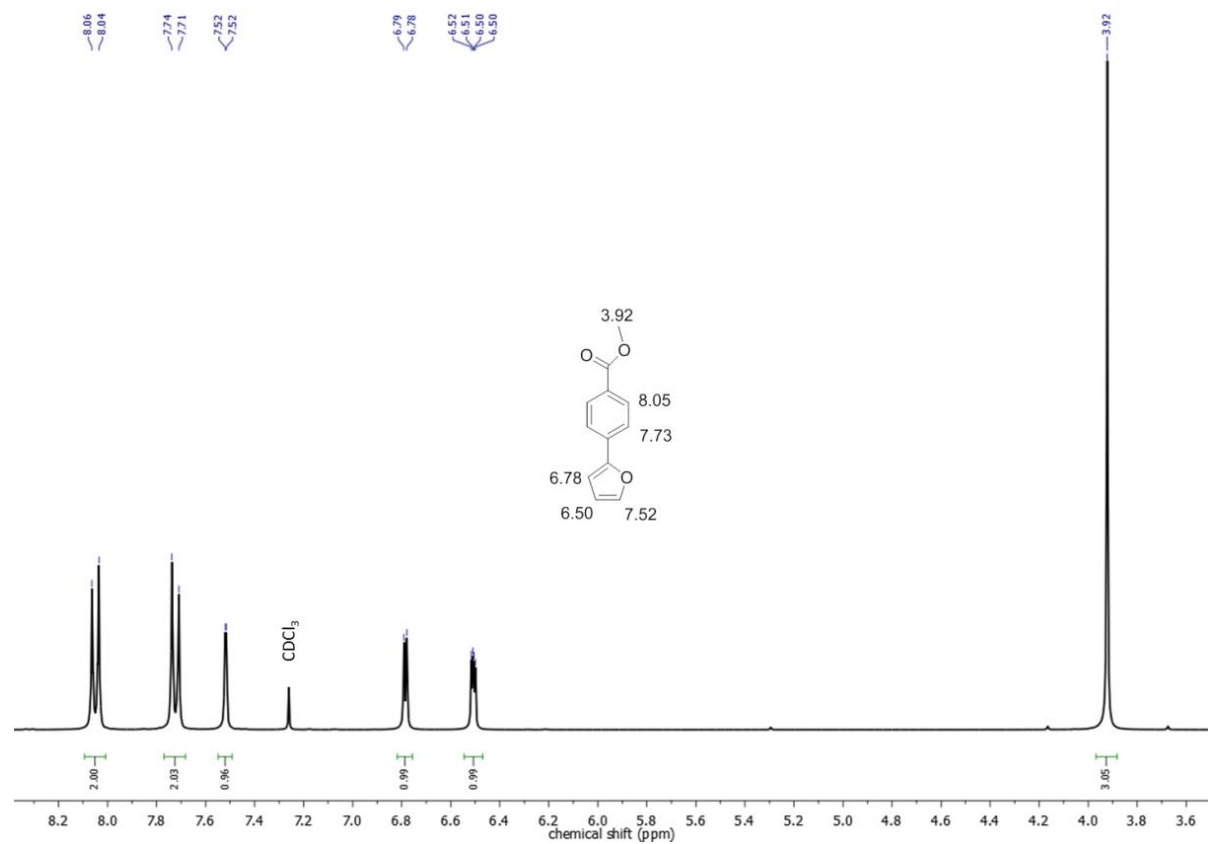
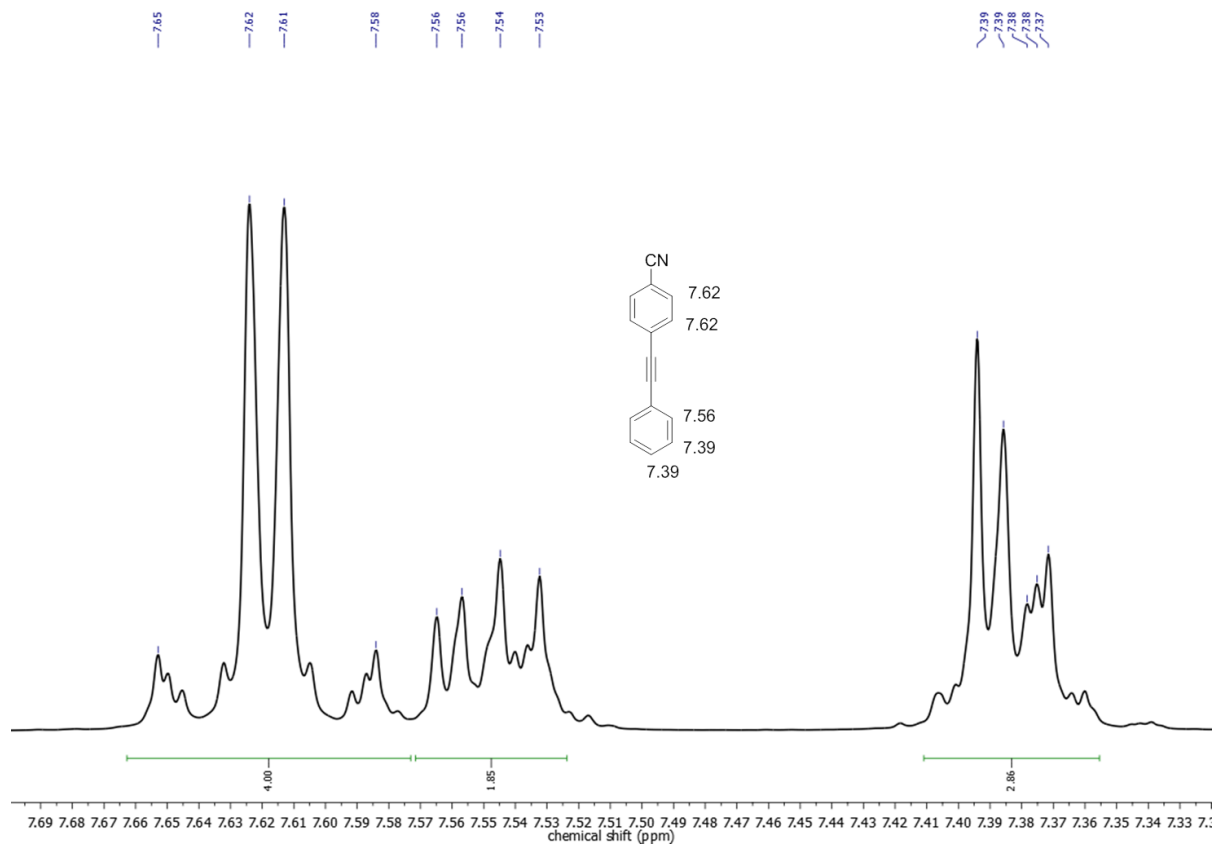
The apparent quantum yield was determined according the procedure described in 6.2.12. In order to determine the apparent quantum yield, the photocatalytic Stille coupling was conducted by irradiating 5 mg P-Az-B, 50 mg (0.2 mmol) 4-iodonitrobenzen, and 63 μ l (0.2 mmol) 2-(tributylstannyl)furan with a blue LED (460 nm, 0.26 W/cm²). The conversion was determined after 1 h by column chromatography.

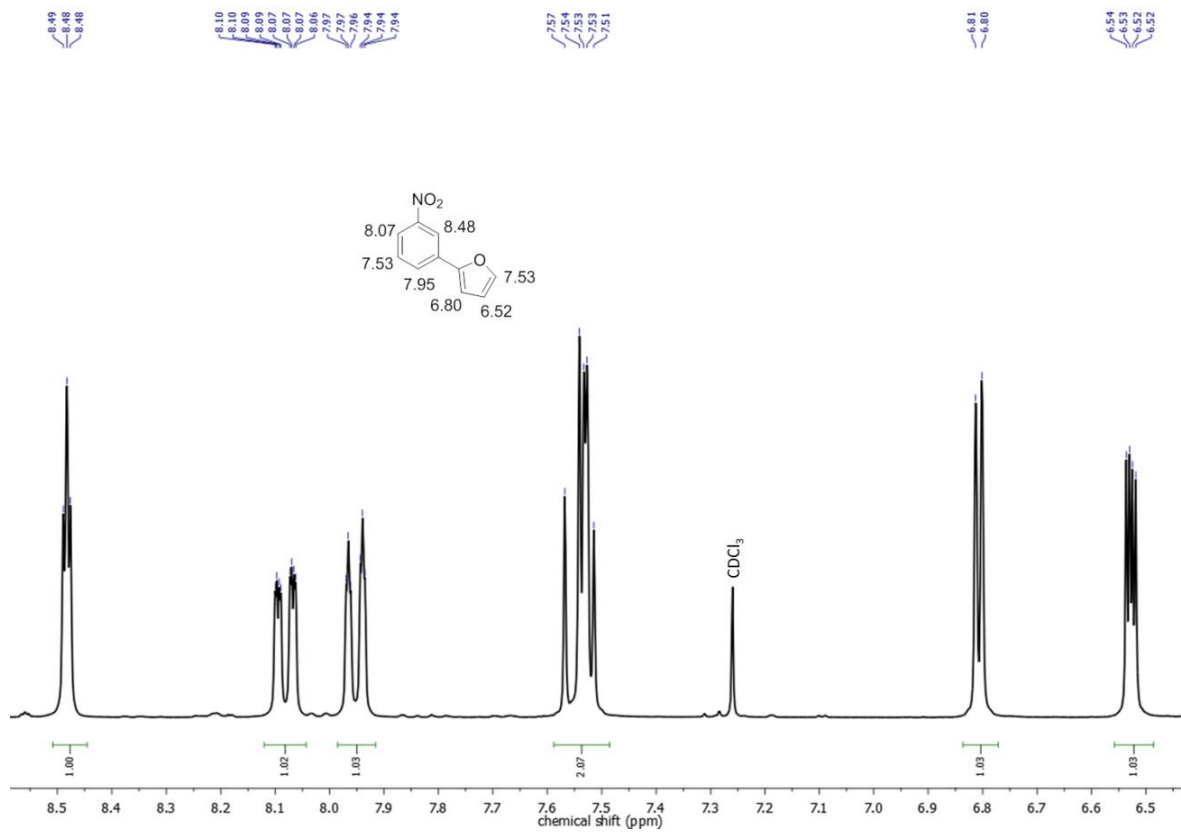
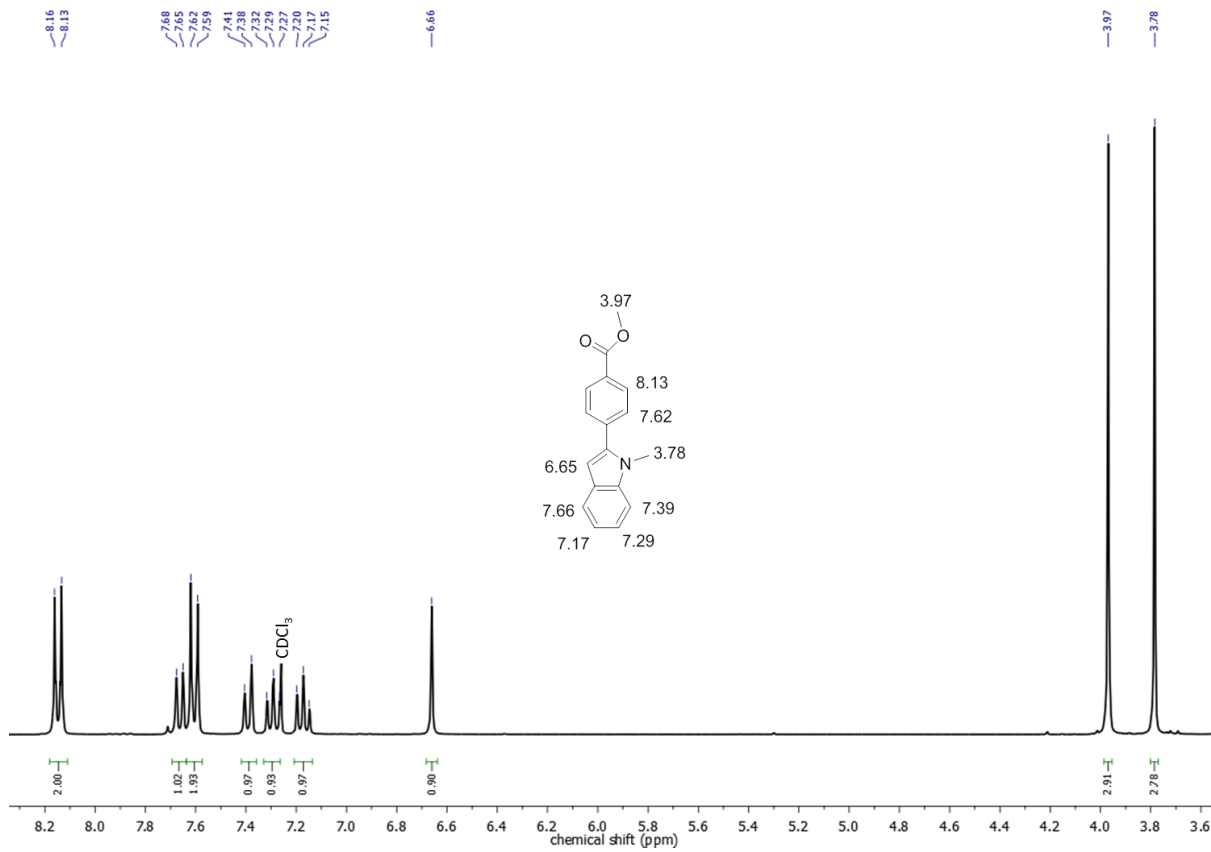
6.4.10 $^1\text{H-NMR}$ spectra of coupling products

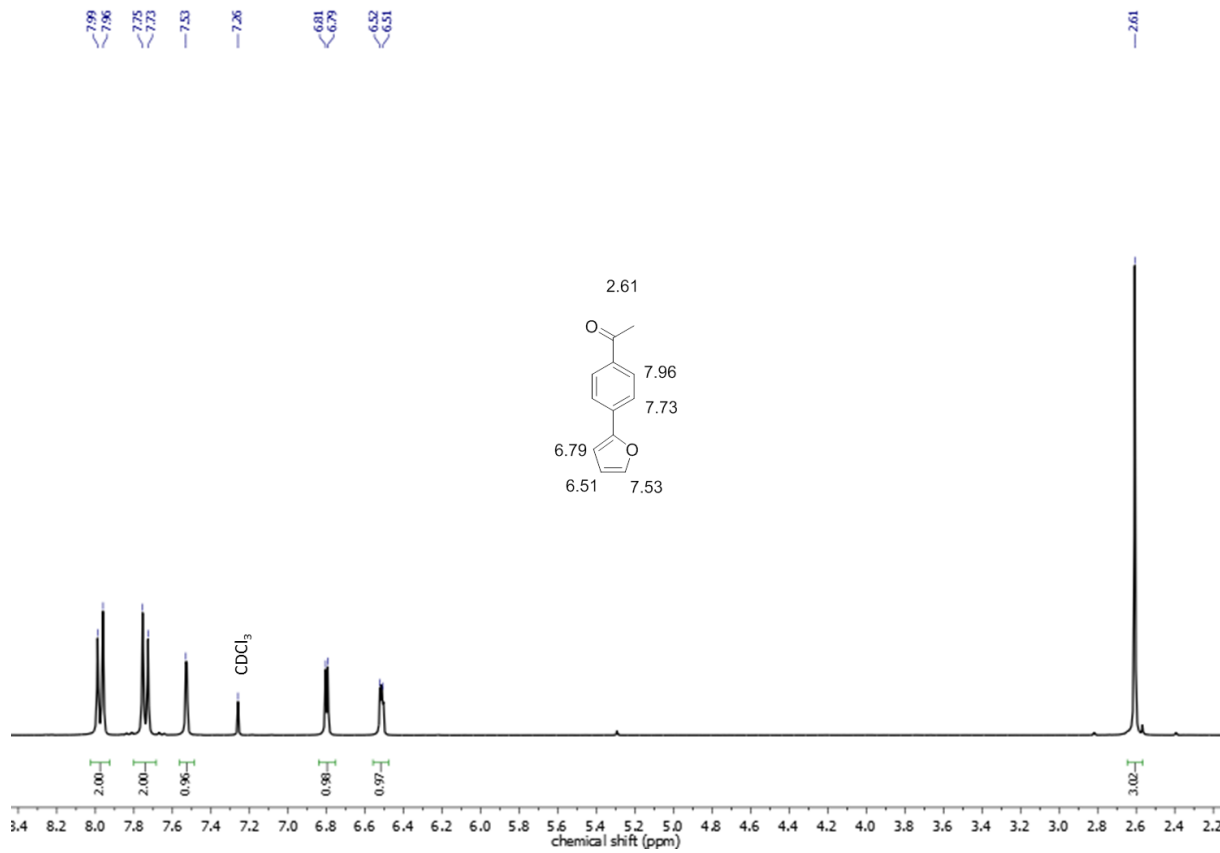
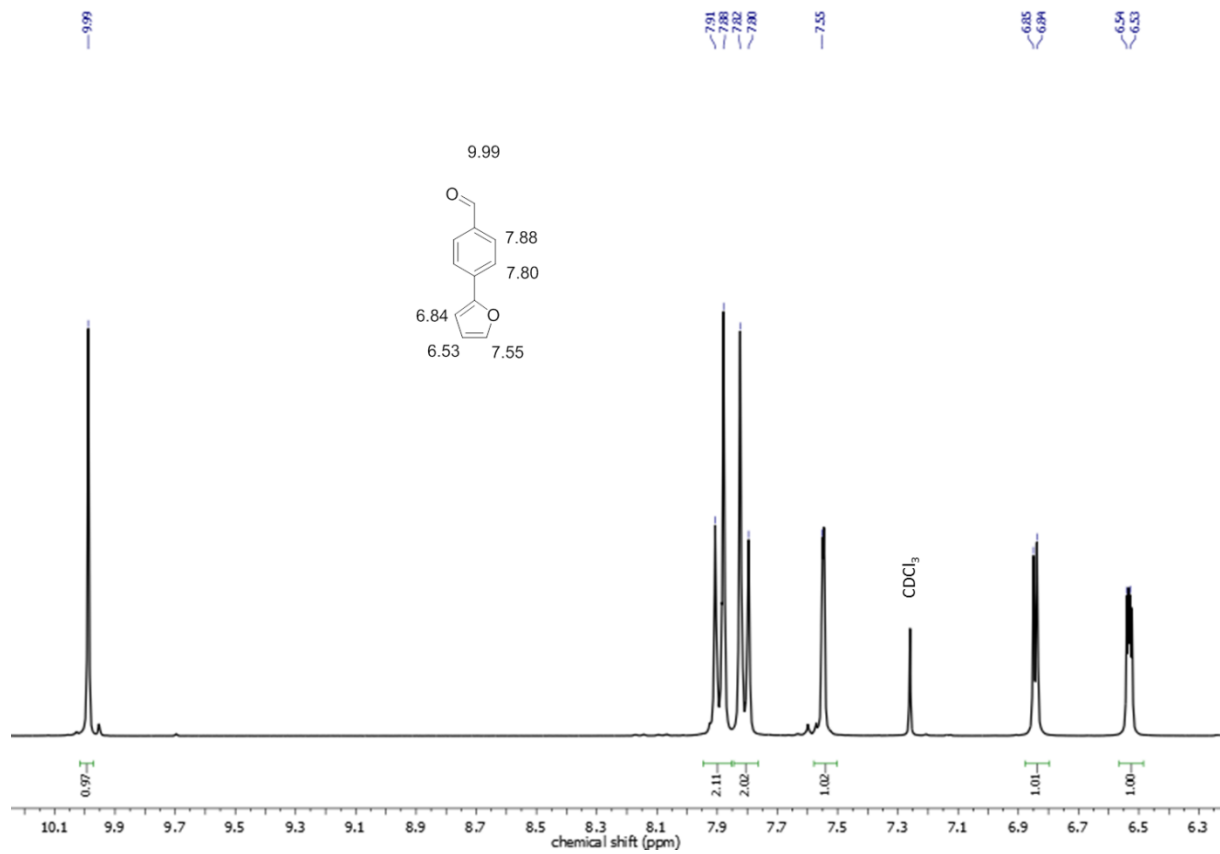




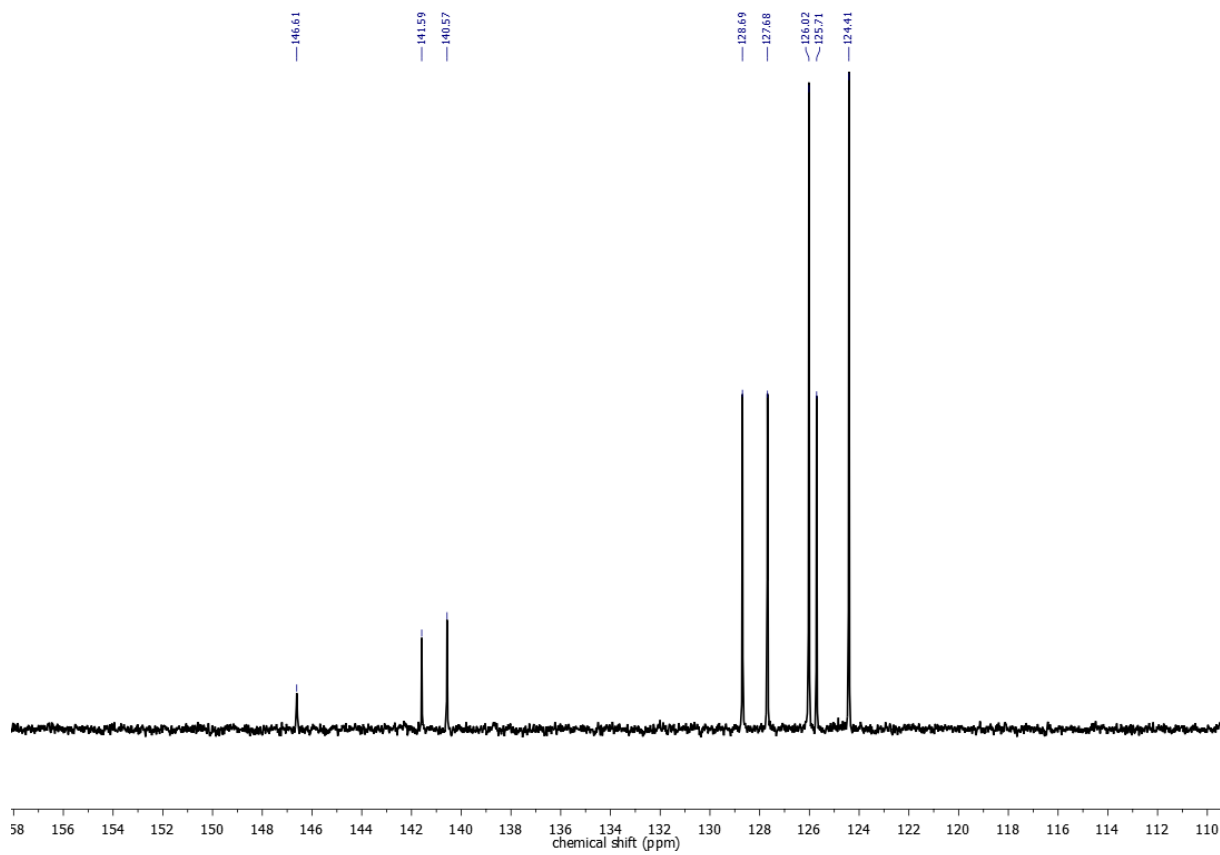
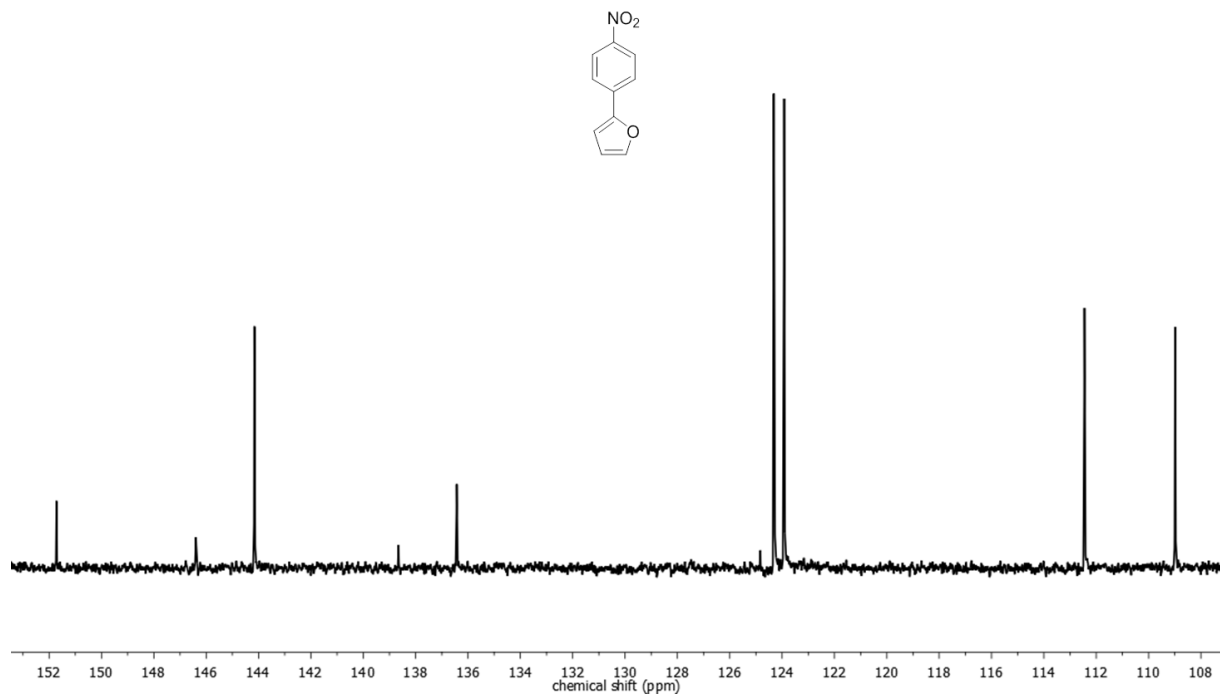


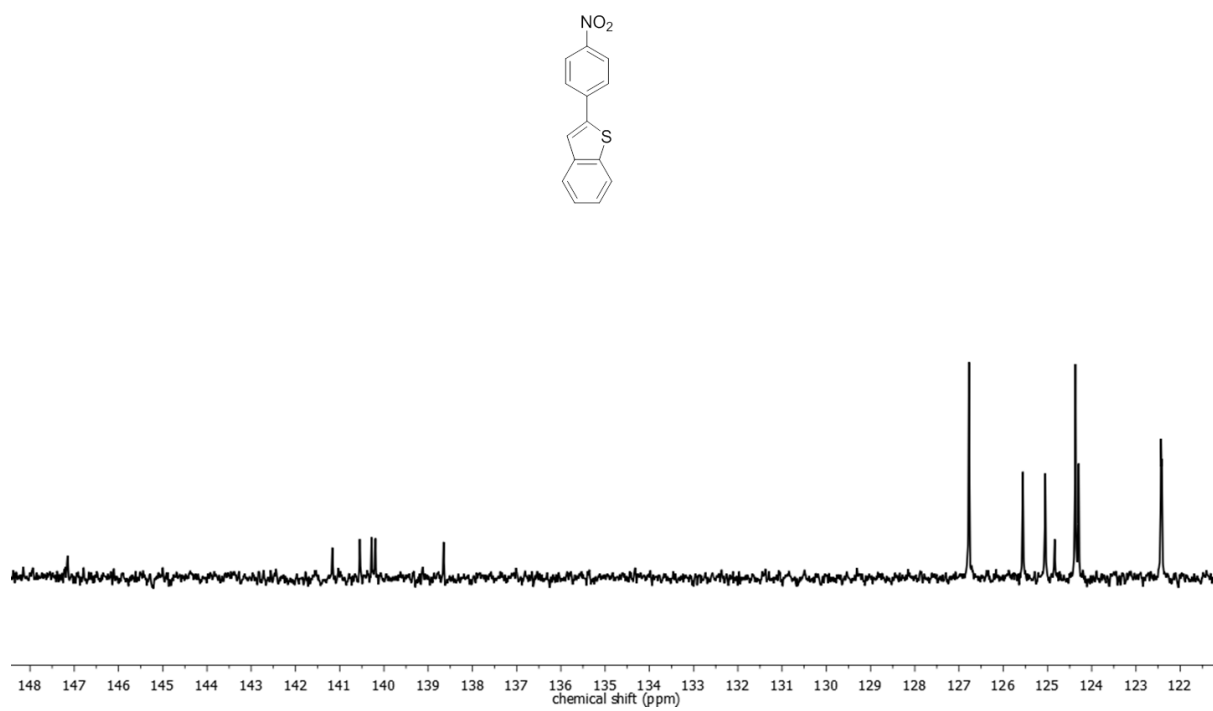
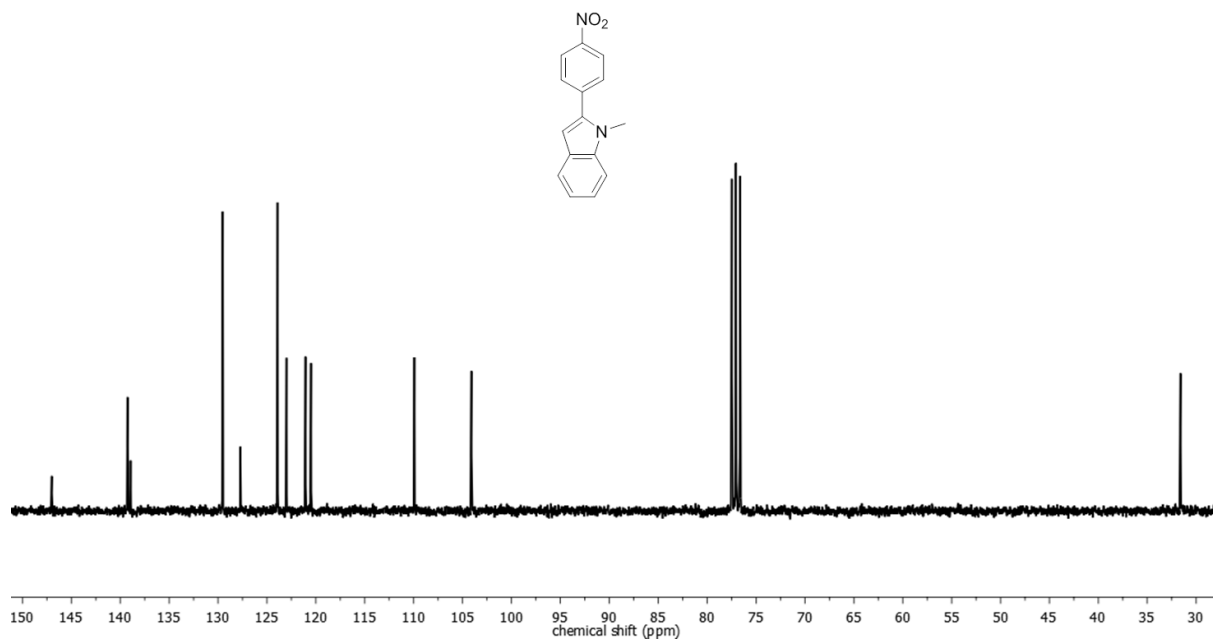


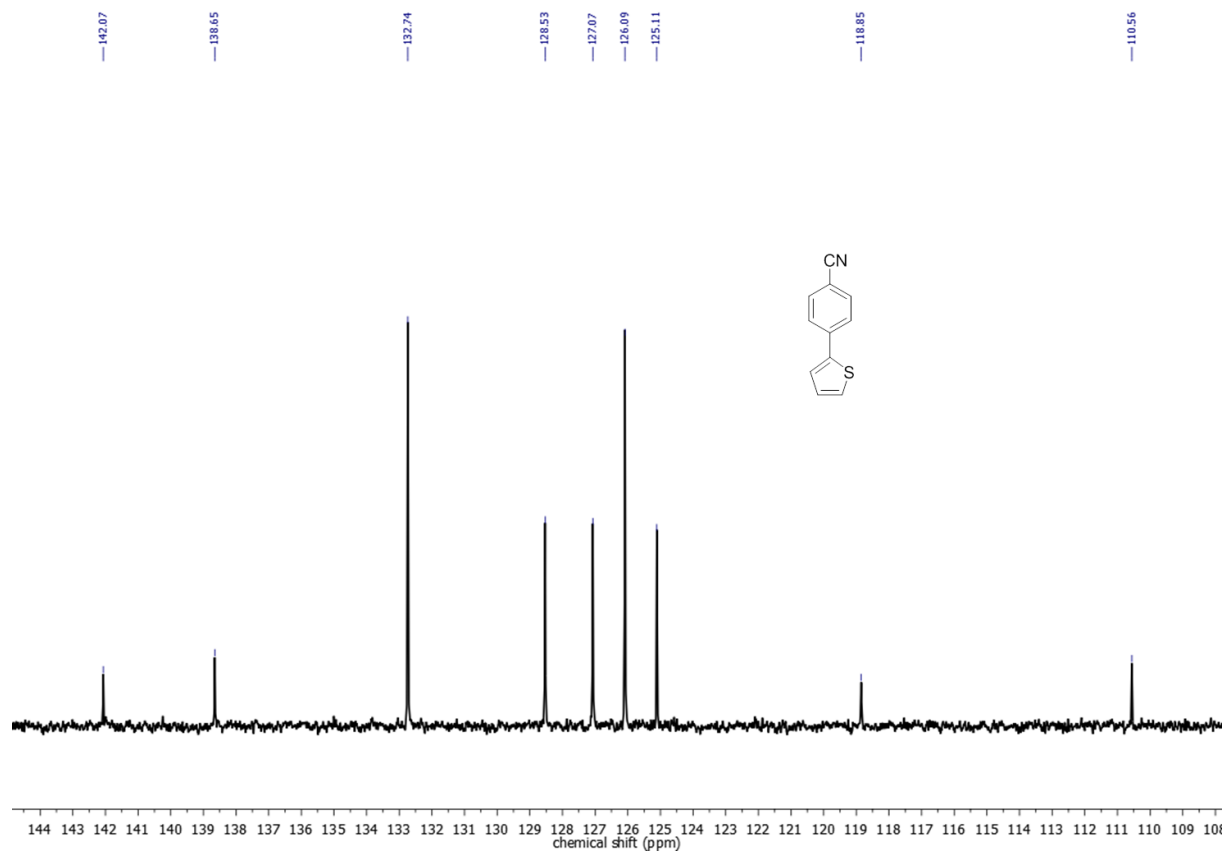
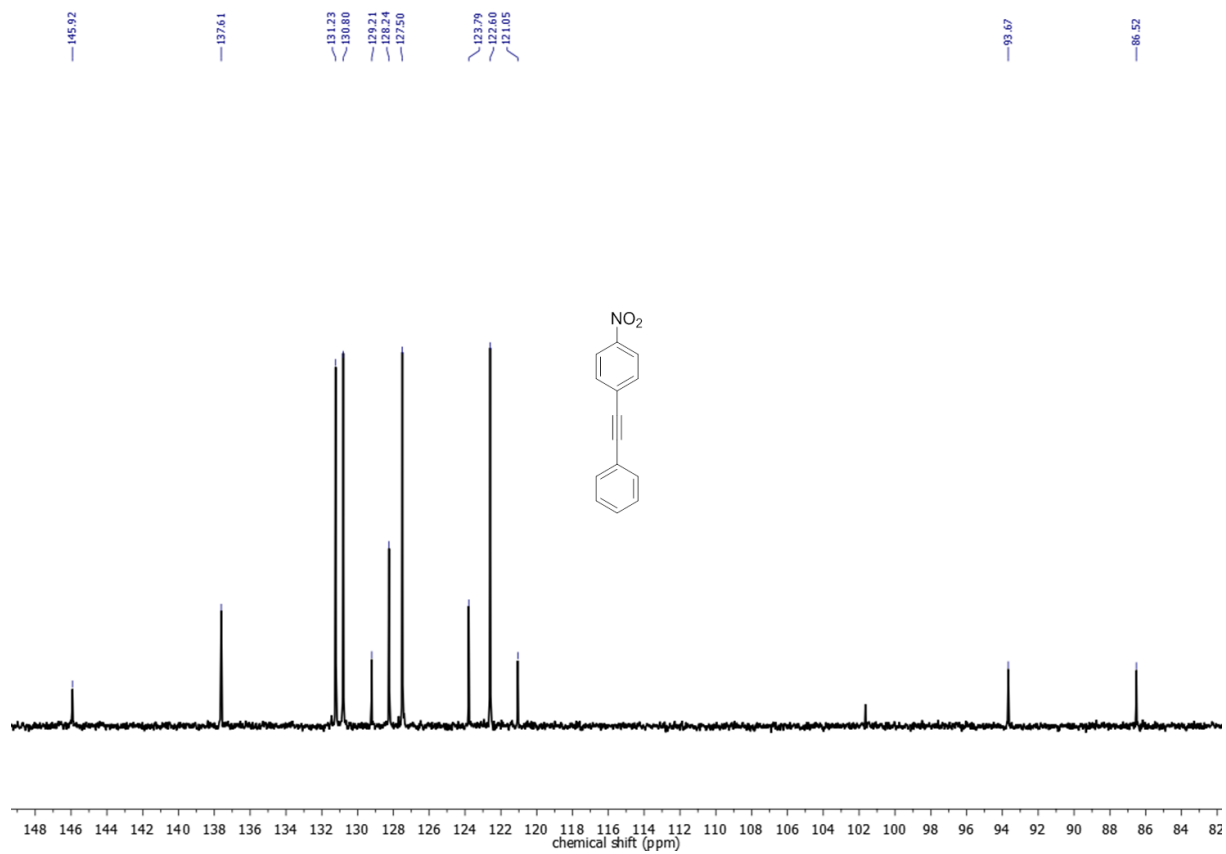


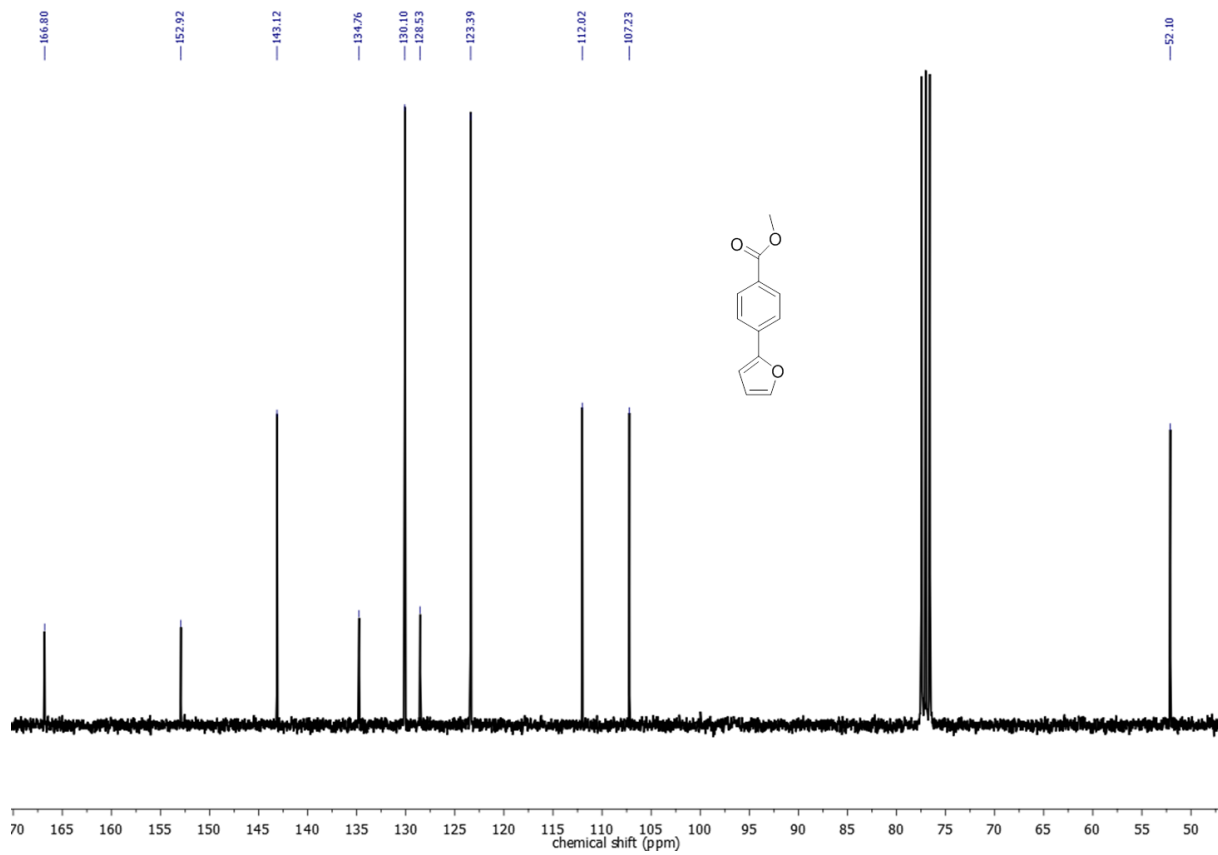
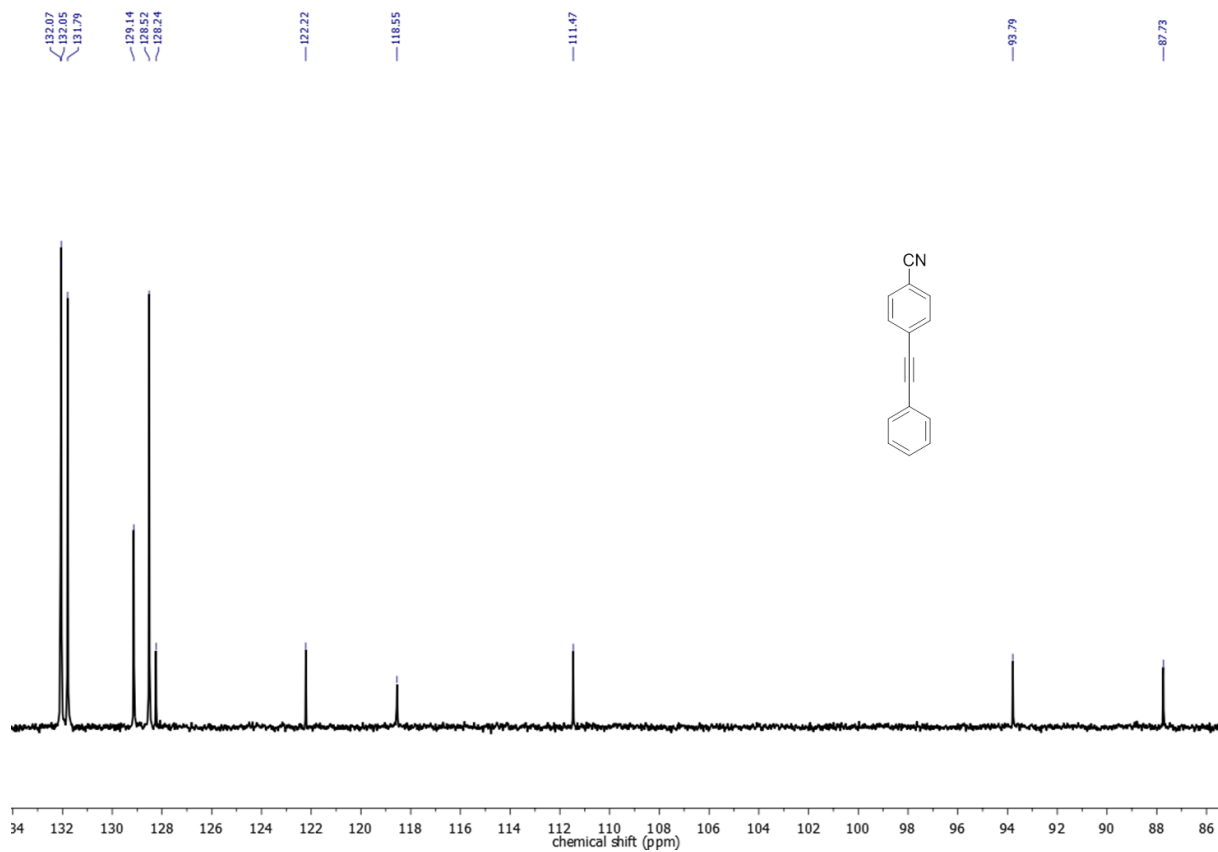


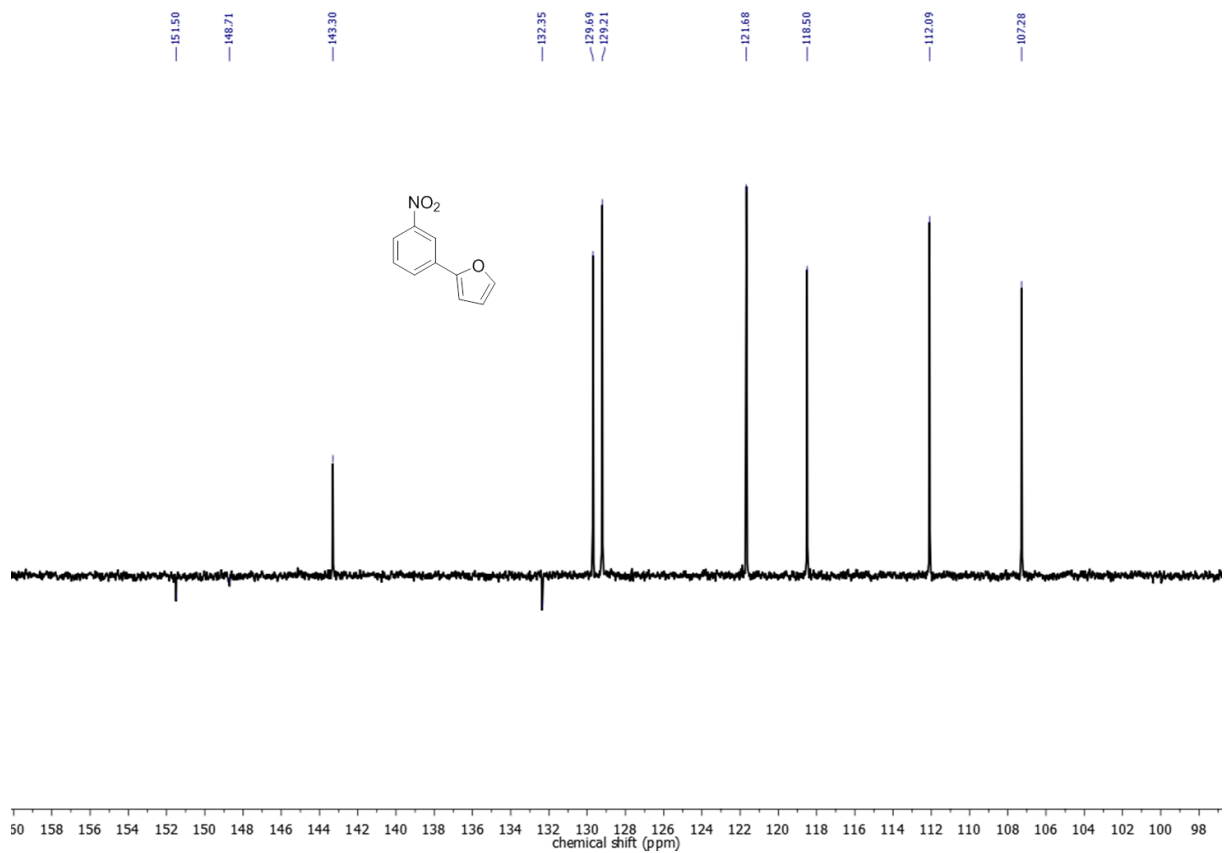
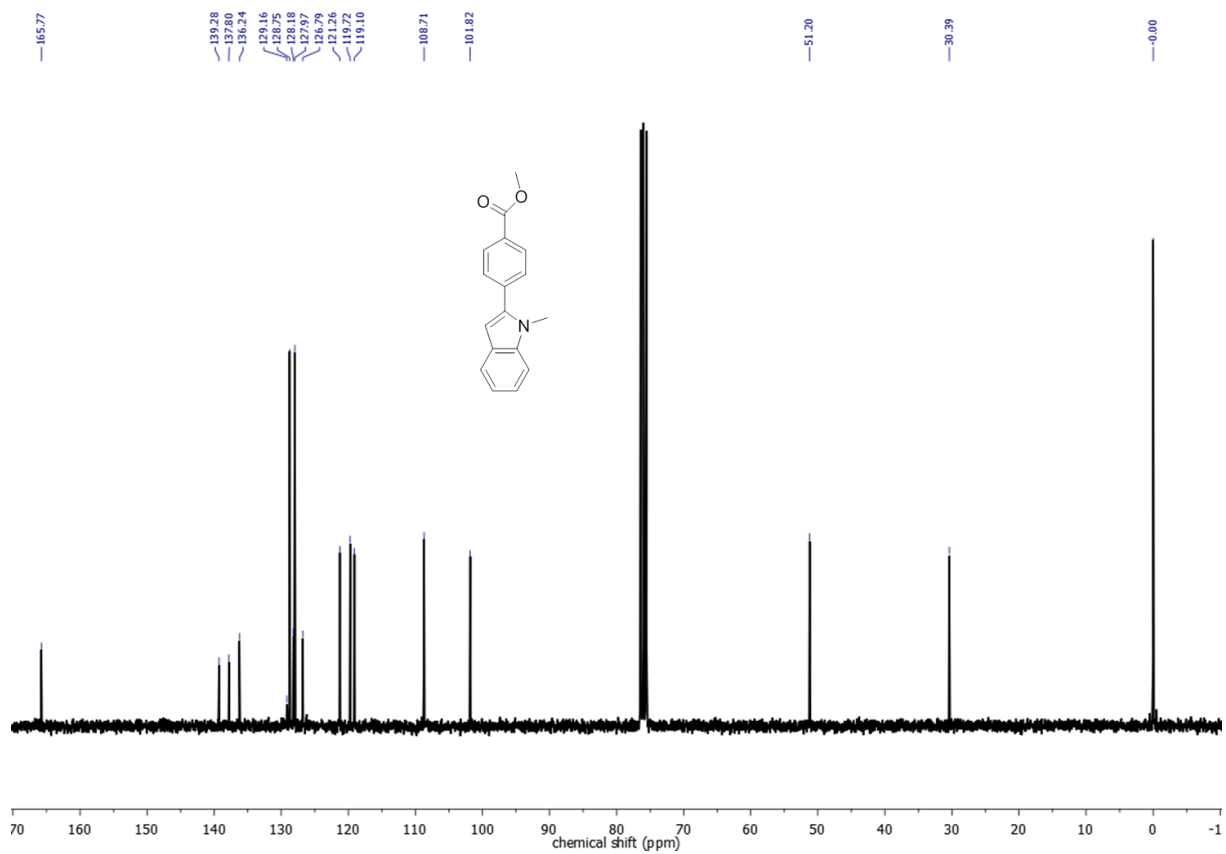
6.4.11 ^{13}C -NMR spectra of coupling products

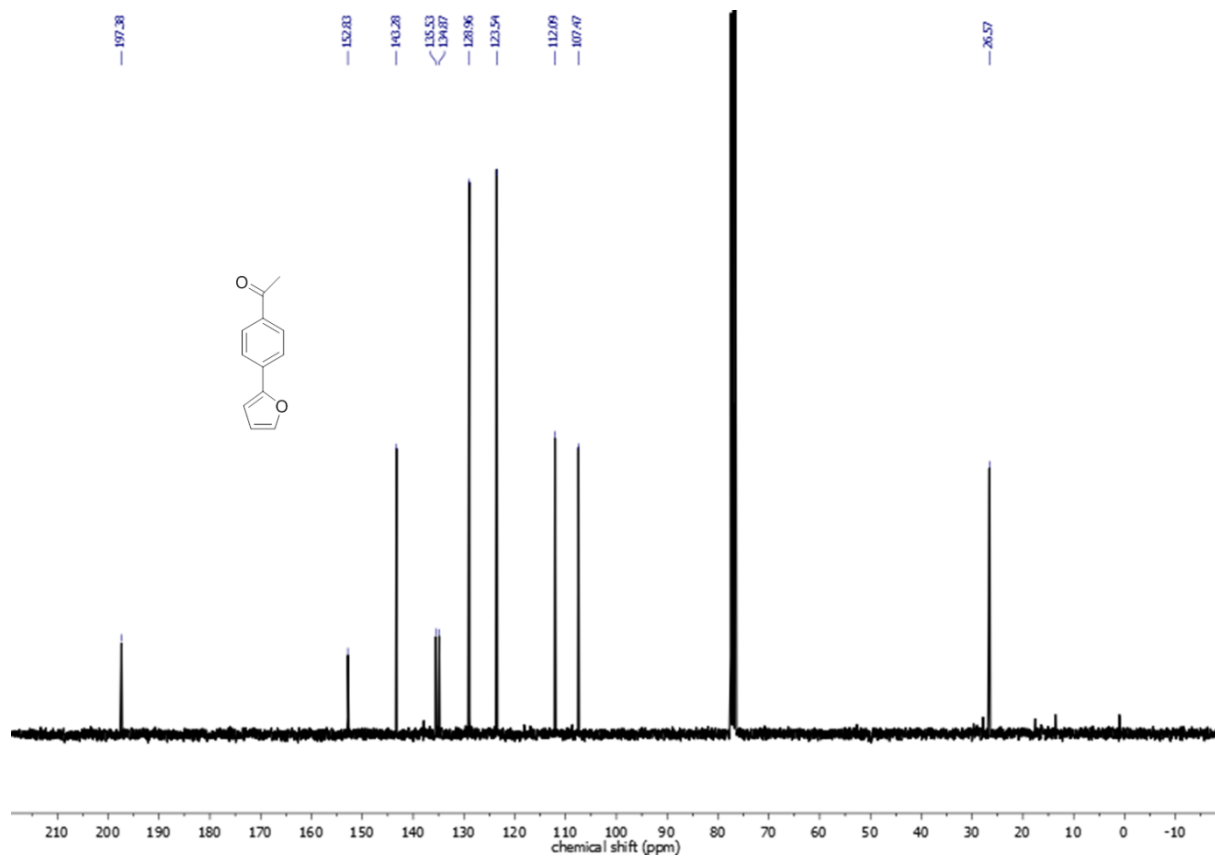
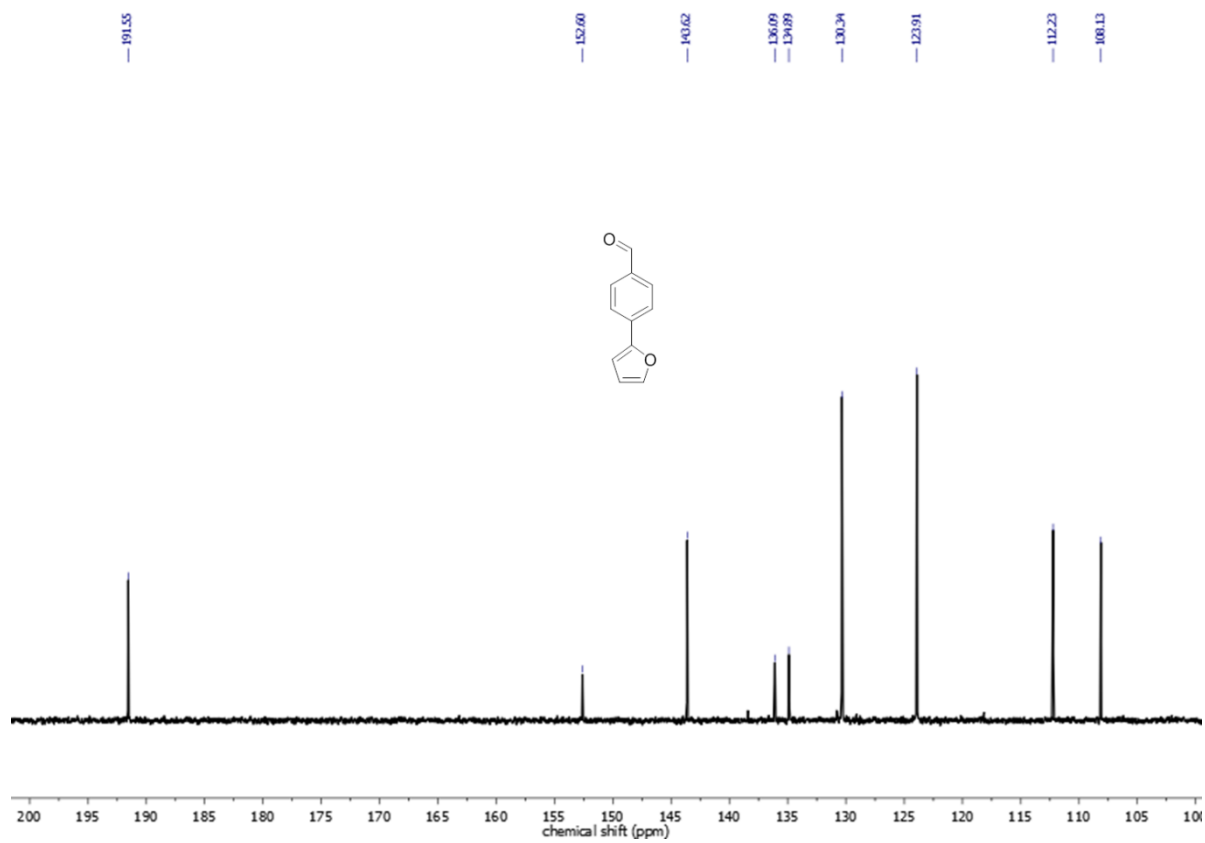












7. Overall Conclusion and Outlook

In this thesis, two different aspects of porous conjugated polymers as visible-light-active and heterogeneous photocatalysts have been discussed: 1.) Synthesis strategies for control of hydrophilicity 2.) Metal-free photoredox mediated reaction design as replacement for traditional transition metal-catalyzed carbon-carbon bond formation reactions.

The main strategies of water-compatible conjugated porous polymers were demonstrated by the following examples:

1.) Stimuli-responsive bifunctional azulene monomers have been incorporated via copolymerization with trifunctional co-monomers into hydrophobic conjugated microporous polymers (CMPs) as pristine materials. To control the hydrophilicity a simple protonation method of azulene units was conducted, leading to the formation of the cationic tropyllium unit and therefore hydrophilic polymer networks. The photocatalytic performance of hydrophilic polymers was demonstrated via model reactions such as photoreduction of toxic heavy metal ions in water, or cascade photoredox reactions using Fe(III) or Cu(II) as electron mediating agents.

2.) A second design strategy for hydrophilic, highly porous conjugated polymers, was demonstrated in formation of cross-linked conjugated polyelectrolytes (CPEs). The CPEs consisted of a photoactive, electron donor and acceptor containing poly-fluorene-benzothiadiazole main chain, and ionic vinylimidazolium side groups. This structural construction led to amphiphilic nature of the polymers, showing a surfactant-like property with critical micelle concentration (CMC) of ca. 0.90 mM. This value is similar to that of hexacetyltrimethylammonium bromide (CTAB, 0.92 mM), a widely used cationic surfactant in aqueous media. Given the photoactive and conjugated main chain, the designed polymer could act successfully as a photosensitizer for the visible light-initiated cross-linking reaction of the vinyl groups, leading to a so-called “self-initiated” cross-linking reaction of the polymer under visible light irradiation in its water solution, which caused the formation of polymer nanoparticles, or in a water in oil emulsion system, which led to the formation of highly porous polymer monoliths. The performance of the highly porous polymer monolith as heterogeneous photocatalyst in water was demonstrated via the photodegradation of organic dyes, the photoreduction of heavy metal ions, and the radical photopolymerization of methyl methacrylate.

The development of metal-free photoredox mediated reaction design as replacement for traditional transition metal-catalyzed carbon-carbon bond formation reactions was introduced as the following:

3.) Azulene-based conjugated microporous polymers have been used as homogeneous and heterogeneous photocatalysts in Stille-type C-C coupling reactions. To understand the photocatalytic C-C reaction mechanism of aromatic stannanes and iodides, two different reaction steps, i.e. the photooxidative destannylation and photoreductive activation of aromatic iodides have been studied independently. It was found that the photogenerated

electron/hole pairs provided the driving force for the Stille-type C-C coupling reaction. The results of the reaction mechanistic investigation were confirmed via analysis of redox potentials, radical trapping experiments, photoluminescence quenching experiments, and calculation of thermodynamic values of photoreductive and photooxidative processes. The photocatalytic performance of the azulene photocatalysts were demonstrated by a series of aromatic stannanes and iodides with different substitution groups. It was shown that suitable substrate molecules for the photocatalytic Stille-type coupling were electron deficient aromatic iodides and electron rich aromatic stannanes.

It is also worth to mention that the repeating experiments of the novel photocatalysts showed a high stability of the porous polymers without significant loss of photocatalytic efficiency.

The here presented design strategy could be seen as a general materials platform for design of novel pure organic, metal-free and heterogeneous photocatalysts based on conjugated porous polymers. The application field should be limited on chemical transformation reactions, but also could be extended in a wider range towards biological or biomedical use of these novel materials in aqueous media.

8. List of Abbreviations

APT	attached proton testing
AQY	apparent quantum yield
BET	Brunnauer-Emmet-Teller
CB	conduction band
CMC	critical micelle concentration
CMP	conjugated microporous polymers
COF	covalent organic framework
CPD	composite pulse decoupling
CPE	conjugated polyelectrolyte
CP-MAS	cross polarization magic angle spinning
CTAB	hexacetyltrimethylammonium bromide
CV	cyclic voltammetry
DCM	dichloromethane
DLS	dynamic light scattering
DMF	dimethylformamide
DPC	diphenylcarbazide
DRS	diffuse reflectance spectroscopy
e^-	free electron
E_g	band gap energy
$E_{0,0}$	excitation energy for the S_0 - S_1 transition
$\Delta E_{coloumbic}$	energy of coloumbic interaction
E_{hom}	activation barrier for homogeneous reactions
E_{het}	activation barrier for heterogeneous reactions
E_{ox}^o	standard electrode potential for oxidation
$E_{oxi-onset}$	oxidation onset level
EPR	Electron Paramagnetic Resonance Spectroscopy
E_{red}^o	standard electrode potential for reduction
$E_{red-onset}$	reduction onset level

EtOAc	ethylacetate
FRET	fluorescence resonance energy transfer
FT-IR	fourier transform infrared spectroscopy
G_{ET}	gibbs energy for photoinduced electron transfer
GHz	gigahertz
GPC	Gel permeation chromatography
h^+	photogenerated hole
h	planck constant
HCP	hyper cross-linked polymers
HIPE	high internal phase emulsion
HOMO	highest occupied molecular orbitals
HPLC	high-performance liquid chromatography
LUMO	lowest unoccupied molecular orbital
MAS	magic angle spinning
MeOH	methanol
MHz	megahertz
MLCT	metal to ligand charge-transfer
MMA	methyl methacrylate
MOF	metal organic framework
ν	frequency
NHE	normal hydrogen electrode
NMR	nuclear magnetic resonance
NP	nanoparticle
PBS-PFP	poly(1,4-phenylene-[9,9-bis(4-phenoxybutylsulfonate)]fluorene-2,7-diyl)
PE	polyelectrolyte
PFP-	
NMe ₂ EtBr	poly[(9,9-dihexyl-2,7-fluorene)-alt-co-(2,5-bis{3-[(N,N-dimethyl)-N-ethylammonium]-1-oxapropyl}-1,4-phenylene)] dibromide
PMMA	poly(methyl methacrylate)
ppm	parts per million

PPP-NEt ₃	poly(para-phenylene)triethylamine iodide
PPP-OPSO ₃	poly[2,5-bis(3-sulfonatopropoxy)-1,4-phenylene-alt-1,4-phenylene] sodium salt
PTHS	Poly(6-(thiophen-3-yl)hexane-1-sulfonate)
PTMIm	2,5-poly(thiophene-3-(1-methylimidazolium-3-ethyloxy))bromide
PTPANa	2,5-poly(thiophene-3-sodium propionate)
RPM	rounds per minute
SCE	standard calomel electrode
SEM	scanning electron microscopy
SFT	surface tension
TEM	transmission electron microscopy
TGA	thermal gravimetric analysis
THF	tetrahydrofuran
TMS	trimethylsilane
UV	ultraviolet
V	volt
VB	valence band
Vis	visible
WCPP	water-compatible conjugated porous polymers
XPHOS	2-dicyclohexylphosphino-2',4',6'-triisopropylbiphenyl

9. Literature

- [1] F. J. Sáez-Martínez, J. Mondéjar-Jiménez, J. A. Mondéjar-Jiménez, *Journal of Cleaner Production*, **2015**, 86, 471-473.
- [2] EEA, in *State of Environment Reports (SOER 2015); Energy*, European Environment Agency, **2015**.
- [3] EEA, in *State of Environment Reports (SOER 2015), Increasing environmental pollution*, European Environment Agency, **2015**.
- [4] F. Krausmann, S. Gingrich, N. Eisenmenger, K.-H. Erb, H. Haberl, M. Fischer-Kowalski, *Ecological Economics*, **2009**, 68, 2696-2705.
- [5] EEA, in *State of Environment Reports (SOER 2015), Resource efficiency and the low-carbon economy*, European Environment Agency, **2015**.
- [6] I. A. R. A. Sheldon, U. Hanefeld, *Green Chemistry and Catalysis*, Wiley-VCH, Weinheim, **2007**.
- [7] Y. Li, Z.-Y. Fu, B.-L. Su, *Advanced Functional Materials*, **2012**, 22, 4634-4667.
- [8] G. Ciamician, *Science*, **1912**, 36, 385-394.
- [9] A. Albini, M. Fagnoni, *ChemSusChem*, **2008**, 1, 63-66.
- [10] M. Neumann, S. Fuldner, B. König, K. Zeitler, *Angewandte Chemie International Edition*, **2011**, 50, 951-954.
- [11] D. M. Schultz, T. P. Yoon, *Science*, **2014**, 343.
- [12] T. P. Yoon, M. A. Ischay, J. Du, *Nat Chem*, **2010**, 2, 527-532.
- [13] P. Niu, L.-C. Yin, Y.-Q. Yang, G. Liu, H.-M. Cheng, *Advanced Materials*, **2014**, 26, 8046-8052.
- [14] S. Yang, Y. Gong, J. Zhang, L. Zhan, L. Ma, Z. Fang, R. Vajtai, X. Wang, P. M. Ajayan, *Advanced Materials*, **2013**, 25, 2452-2456.
- [15] J.-X. Jiang, F. Su, A. Trewin, C. D. Wood, N. L. Campbell, H. Niu, C. Dickinson, A. Y. Ganin, M. J. Rosseinsky, Y. Z. Khimiyak, A. I. Cooper, *Angewandte Chemie*, **2007**, 119, 8728-8732.
- [16] Z. J. Wang, K. Garth, S. Ghasimi, K. Landfester, K. A. I. Zhang, *ChemSusChem*, **2015**, 8, 3459-3464.

- [17] Z. J. Wang, S. Ghasimi, K. Landfester, K. A. I. Zhang, *Journal of Materials Chemistry A*, **2014**, *2*, 18720-18724.
- [18] Z. J. Wang, S. Ghasimi, K. Landfester, K. A. I. Zhang, *Chemical Communications*, **2014**, *50*, 8177-8180.
- [19] Z. J. Wang, S. Ghasimi, K. Landfester, K. A. I. Zhang, *Advanced Materials*, **2015**, *27*, 6265-6270.
- [20] R. Li, Z. J. Wang, L. Wang, B. C. Ma, S. Ghasimi, H. Lu, K. Landfester, K. A. I. Zhang, *ACS Catalysis*, **2016**, *6*, 1113-1121.
- [21] K. Takimiya, I. Osaka, M. Nakano, *Chemistry of Materials*, **2014**, *26*, 587-593.
- [22] T. Lei, J.-Y. Wang, J. Pei, *Chemistry of Materials*, **2014**, *26*, 594-603.
- [23] Y. L. Can Li, *Bridging Heterogeneous and Homogeneous Catalysis*, Wiley-VCH, Weinheim, **2014**.
- [24] P. N. A. Behr, *Applied Homogeneous Catalysis*, Wiley-VCH, Weinheim, **2012**.
- [25] J. W. N. I. Chorkendorff, *Concepts of Modern Catalysis and Kinetics*, Wiley-VCH, Weinheim, **2005**.
- [26] E. M. McCash, *Surface Chemistry*, Oxford University Press, New York, **2004**.
- [27] H. D. Roth, *Angewandte Chemie International Edition in English*, **1989**, *28*, 1193-1207.
- [28] M. P. Thekaekara, *Solar Energy*, **1976**, *18*, 309-325.
- [29] A. W. A. D. McNaught, in *International Union of Pure and Applied Chemistry (IUPAC) Gold Book*, Blackwell Science, Oxford UK, **2006**.
- [30] J. W. Tucker, C. R. J. Stephenson, *The Journal of Organic Chemistry*, **2012**, *77*, 1617-1622.
- [31] N. J. Turro, *Modern Molecular Photochemistry*, University Science Books, Sausalito, **1991**.
- [32] S. O. Poelma, G. L. Burnett, E. H. Discekici, K. M. Mattson, N. J. Treat, Y. Luo, Z. M. Hudson, S. L. Shankel, P. G. Clark, J. W. Kramer, C. J. Hawker, J. Read de Alaniz, *The Journal of Organic Chemistry*, **2016**, *81*, 7155-7160.
- [33] M. H. Shaw, J. Twilton, D. W. C. MacMillan, *The Journal of Organic Chemistry*, **2016**, *81*, 6898-6926.
- [34] C. D. McTiernan, S. P. Pitre, J. C. Scaiano, *ACS Catalysis*, **2014**, *4*, 4034-4039.
- [35] K. Miyazawa, Y. Yasu, T. Koike, M. Akita, *Chemical Communications*, **2013**, *49*, 7249-7251.

- [36] C. Reichardt, *Chemical Reviews*, **1994**, *94*, 2319-2358.
- [37] F. Schüth, *Chemie Ingenieur Technik*, **2010**, *82*, 769-777.
- [38] O. K. Farha, I. Eryazici, N. C. Jeong, B. G. Hauser, C. E. Wilmer, A. A. Sarjeant, R. Q. Snurr, S. T. Nguyen, A. Ö. Yazaydin, J. T. Hupp, *Journal of the American Chemical Society*, **2012**, *134*, 15016-15021.
- [39] W. J. T. J. M. Thomas, *Principles and Practise of Heterogeneous Catalysis*, VCH, Weinheim, **1997**.
- [40] Q. Liu, Z. Tang, M. Wu, Z. Zhou, *Polymer International*, **2014**, *63*, 381-392.
- [41] L. Sun, Z. Liang, J. Yu, R. Xu, *Polymer Chemistry*, **2013**, *4*, 1932-1938.
- [42] J. R. Holst, E. Stöckel, D. J. Adams, A. I. Cooper, *Macromolecules*, **2010**, *43*, 8531-8538.
- [43] Y. Liao, J. Weber, C. F. J. Faul, *Chemical Communications*, **2014**, *50*, 8002-8005.
- [44] Y. Wei, W. Chen, X. Zhao, S. Ding, S. Han, L. Chen, *Polymer Chemistry*, **2016**, *7*, 3983-3988.
- [45] J. Schmidt, J. Weber, J. D. Epping, M. Antonietti, A. Thomas, *Advanced Materials*, **2009**, *21*, 702-705.
- [46] A. Palma-Cando, G. Brunklaus, U. Scherf, *Macromolecules*, **2015**, *48*, 6816-6824.
- [47] J.-X. Jiang, F. Su, A. Trewin, C. D. Wood, H. Niu, J. T. A. Jones, Y. Z. Khimyak, A. I. Cooper, *Journal of the American Chemical Society*, **2008**, *130*, 7710-7720.
- [48] E. Stockel, X. Wu, A. Trewin, C. D. Wood, R. Clowes, N. L. Campbell, J. T. A. Jones, Y. Z. Khimyak, D. J. Adams, A. I. Cooper, *Chemical Communications*, **2009**, 212-214.
- [49] R. Dawson, A. Laybourn, Y. Z. Khimyak, D. J. Adams, A. I. Cooper, *Macromolecules*, **2010**, *43*, 8524-8530.
- [50] R. S. Sprick, J.-X. Jiang, B. Bonillo, S. Ren, T. Ratvijitvech, P. Guiglion, M. A. Zwijnenburg, D. J. Adams, A. I. Cooper, *Journal of the American Chemical Society*, **2015**, *137*, 3265-3270.
- [51] B. Bonillo, R. S. Sprick, A. I. Cooper, *Chemistry of Materials*, **2016**, *28*, 3469-3480.
- [52] Y. Xu, A. Nagai, D. Jiang, *Chemical Communications*, **2013**, *49*, 1591-1593.
- [53] H. W. Langmi, J. Ren, B. North, M. Mathe, D. Bessarabov, *Electrochimica Acta*, **2014**, *128*, 368-392.
- [54] J.-X. Jiang, F. Su, H. Niu, C. D. Wood, N. L. Campbell, Y. Z. Khimyak, A. I. Cooper, *Chemical Communications*, **2008**, 486-488.

- [55] S. Yuan, B. Dorney, D. White, S. Kirklin, P. Zapol, L. Yu, D.-J. Liu, *Chemical Communications*, **2010**, 46, 4547-4549.
- [56] A. Li, R.-F. Lu, Y. Wang, X. Wang, K.-L. Han, W.-Q. Deng, *Angewandte Chemie International Edition*, **2010**, 49, 3330-3333.
- [57] S. Qiao, Z. Du, R. Yang, *Journal of Materials Chemistry A*, **2014**, 2, 1877-1885.
- [58] Q. Chen, M. Luo, P. Hammershøj, D. Zhou, Y. Han, B. W. Laursen, C.-G. Yan, B.-H. Han, *Journal of the American Chemical Society*, **2012**, 134, 6084-6087.
- [59] P. Makowski, J. Weber, A. Thomas, F. Goettmann, *Catalysis Communications*, **2008**, 10, 243-247.
- [60] J.-X. Jiang, C. Wang, A. Laybourn, T. Hasell, R. Clowes, Y. Z. Khimyak, J. Xiao, S. J. Higgins, D. J. Adams, A. I. Cooper, *Angewandte Chemie International Edition*, **2011**, 50, 1072-1075.
- [61] L. Chen, Y. Yang, D. Jiang, *Journal of the American Chemical Society*, **2010**, 132, 9138-9143.
- [62] K. Zhang, D. Kopetzki, P. H. Seeberger, M. Antonietti, F. Vilela, *Angewandte Chemie International Edition*, **2013**, 52, 1432-1436.
- [63] J.-X. Jiang, Y. Li, X. Wu, J. Xiao, D. J. Adams, A. I. Cooper, *Macromolecules*, **2013**, 46, 8779-8783.
- [64] R. R. Haikal, X. Wang, Y. S. Hassan, M. R. Parida, B. Murali, O. F. Mohammed, P. J. Pellechia, M. Fontecave, M. H. Alkordi, *ACS Applied Materials & Interfaces*, **2016**, 8, 19994-20002.
- [65] Z. Xiao, Y. Zhou, X. Xin, Q. Zhang, L. Zhang, R. Wang, D. Sun, *Macromolecular Chemistry and Physics*, **2016**, 217, 599-604.
- [66] M. G. Schwab, M. Hamburger, X. Feng, J. Shu, H. W. Spiess, X. Wang, M. Antonietti, K. Mullen, *Chemical Communications*, **2010**, 46, 8932-8934.
- [67] J. Luo, X. Zhang, J. Zhang, *ACS Catalysis*, **2015**, 5, 2250-2254.
- [68] N. Kang, J. H. Park, K. C. Ko, J. Chun, E. Kim, H.-W. Shin, S. M. Lee, H. J. Kim, T. K. Ahn, J. Y. Lee, S. U. Son, *Angewandte Chemie*, **2013**, 125, 6348-6352.
- [69] S. Dadashi-Silab, H. Bildirir, R. Dawson, A. Thomas, Y. Yagci, *Macromolecules*, **2014**, 47, 4607-4614.
- [70] L. Li, Z. Cai, *Polymer Chemistry*, **2016**.
- [71] M. Liras, M. Iglesias, F. Sánchez, *Macromolecules*, **2016**, 49, 1666-1673.
- [72] A. Li, H.-X. Sun, D.-Z. Tan, W.-J. Fan, S.-H. Wen, X.-J. Qing, G.-X. Li, S.-Y. Li, W.-Q. Deng, *Energy & Environmental Science*, **2011**, 4, 2062-2065.

- [73] R.-X. Yang, T.-T. Wang, W.-Q. Deng, *Scientific Reports*, **2015**, *5*, 10155.
- [74] P. Zhang, Z. Weng, J. Guo, C. Wang, *Chemistry of Materials*, **2011**, *23*, 5243-5249.
- [75] B. C. Ma, S. Ghasimi, K. Landfester, F. Vilela, K. A. I. Zhang, *Journal of Materials Chemistry A*, **2015**, *3*, 16064-16071.
- [76] R. Dawson, A. Laybourn, R. Clowes, Y. Z. Khimyak, D. J. Adams, A. I. Cooper, *Macromolecules*, **2009**, *42*, 8809-8816.
- [77] H. Urakami, K. Zhang, F. Vilela, *Chemical Communications*, **2013**, *49*, 2353-2355.
- [78] F. L. Shu Wang, *Functionalized Conjugated Polyelectrolytes, Design and Biomedical Applications*, Springer, Heidelberg, **2013**.
- [79] G. C. B. Bin Liu, *Conjugated Polyelectrolytes*, Wiley-VCH, Weinheim, **2013**.
- [80] Y.-J. Cheng, S.-H. Yang, C.-S. Hsu, *Chemical Reviews*, **2009**, *109*, 5868-5923.
- [81] H.-A. Ho, M. Boissinot, M. G. Bergeron, G. Corbeil, K. Doré, D. Boudreau, M. Leclerc, *Angewandte Chemie International Edition*, **2002**, *41*, 1548-1551.
- [82] J. C. Brendel, M. M. Schmidt, G. Hagen, R. Moos, M. Thelakkat, *Chemistry of Materials*, **2014**, *26*, 1992-1998.
- [83] A. D. Child, J. R. Reynolds, *Macromolecules*, **1994**, *27*, 1975-1977.
- [84] R. D. McCullough, P. C. Ewbank, R. S. Loewe, *Journal of the American Chemical Society*, **1997**, *119*, 633-634.
- [85] B. Liu, W.-L. Yu, Y.-H. Lai, W. Huang, *Chemical Communications*, **2000**, 551-552.
- [86] M. Wittmann, *Chemical Communications*, **1998**, 623-624.
- [87] U. Scherf, S. Adamczyk, A. Gutacker, N. Koenen, *Macromolecular Rapid Communications*, **2009**, *30*, 1059-1065.
- [88] H. D. Burrows, S. M. Fonseca, C. L. Silva, A. A. C. C. Pais, M. J. Tapia, S. Pradhan, U. Scherf, *Physical Chemistry Chemical Physics*, **2008**, *10*, 4420-4428.
- [89] M. Tokuda, H. Minami, *Journal of Colloid and Interface Science*, **2013**, *398*, 120-125.
- [90] J. Texter, *Macromolecular Rapid Communications*, **2012**, *33*, 1996-2014.
- [91] T. Alfrey, H. Morawetz, E. B. Fitzgerald, R. M. Fuoss, *Journal of the American Chemical Society*, **1950**, *72*, 1864-1864.
- [92] M. Li, G. Zhang, S. Xu, C. Zhao, M. Han, L. Zhang, H. Jiang, Z. Liu, H. Na, *Journal of Power Sources*, **2014**, *255*, 101-107.
- [93] M. A. J. Mazumder, F. Shen, N. A. D. Burke, M. A. Potter, H. D. H. Stöver, *Biomacromolecules*, **2008**, *9*, 2292-2300.

- [94] A. H. Sun, Y. Li, L. Huang, P. Cui, *Journal of Materials Science*, **2009**, *44*, 4112-4116.
- [95] A. M. Lehaf, M. D. Moussallem, J. B. Schlenoff, *Langmuir*, **2011**, *27*, 4756-4763.
- [96] R. Guterman, E. R. Gillies, P. J. Ragogna, *Langmuir*, **2015**, *31*, 5181-5189.
- [97] X. Sui, M. A. Hempenius, G. J. Vancso, *Journal of the American Chemical Society*, **2012**, *134*, 4023-4025.
- [98] X. Zhu, D. Jańczewski, S. S. C. Lee, S. L.-M. Teo, G. J. Vancso, *ACS Applied Materials & Interfaces*, **2013**, *5*, 5961-5968.
- [99] F. Yan, J. Texter, *Chemical Communications*, **2006**, 2696-2698.
- [100] X. Hu, J. Huang, W. Zhang, M. Li, C. Tao, G. Li, *Advanced Materials*, **2008**, *20*, 4074-4078.
- [101] A. R. K. Yoshihito Osada, *Polymer Gels and Networks*, Marcel Dekker, Inc., New York, **2002**.
- [102] F. Yan, J. Texter, *Angewandte Chemie International Edition*, **2007**, *46*, 2440-2443.
- [103] M. Zambianchi, F. D. Maria, A. Cazzato, G. Gigli, M. Piacenza, F. D. Sala, G. Barbarella, *Journal of the American Chemical Society*, **2009**, *131*, 10892-10900.
- [104] K. Lee, J. Lee, E. J. Jeong, A. Kronk, K. S. J. Elenitoba-Johnson, M. S. Lim, J. Kim, *Advanced Materials*, **2012**, *24*, 2479-2484.
- [105] C. Zhu, Q. Yang, L. Liu, S. Wang, *Journal of Materials Chemistry*, **2011**, *21*, 7905-7912.
- [106] C. Zhu, Q. Yang, L. Liu, S. Wang, *Chemical Communications*, **2011**, *47*, 5524-5526.
- [107] L. An, Y. Tang, F. Feng, F. He, S. Wang, *Journal of Materials Chemistry*, **2007**, *17*, 4147-4152.
- [108] P. Li, Y. F. Poon, W. Li, H.-Y. Zhu, S. H. Yeap, Y. Cao, X. Qi, C. Zhou, M. Lamrani, R. W. Beuerman, E.-T. Kang, Y. Mu, C. M. Li, M. W. Chang, S. S. Jan Leong, M. B. Chan-Park, *Nat Mater*, **2011**, *10*, 149-156.
- [109] L. Lu, F. H. Rininsland, S. K. Wittenburg, K. E. Achyuthan, D. W. McBranch, D. G. Whitten, *Langmuir*, **2005**, *21*, 10154-10159.
- [110] I. F. Dudley H. Williams, *Strukturaufklärung in der organischen Chemie*, 6. Auflage ed., Thieme Stuttgart, **1985**.
- [111] W. Schmidt, *Optische Spektroskopie*, 2. Auflage ed., Wiley-VCH, Weinheim, **2000**.
- [112] G. Kortüm, *Reflexionsspektroskopie*, Springer-Verlag, Berlin, **1969**.

- [113] G. J. E. Breitmaier, *Organische Chemie*, 5. Auflage ed., Thieme, Stuttgart, **2005**.
- [114] M. J. Duer, *Introduction to solid state NMR Spectroscopy*, Blackwell Publishing, Oxford, **2004**.
- [115] J. R. B. Schröder, *Physikalische Methoden in der Chemie*, VCH, Weinheim, **1985**.
- [116] D. K. Gosser, *Cyclic Voltammetry*, VCH Weinheim, **1994**.
- [117] K. S. W. Sing, *Pure and Applied Chemistry*, **1985**, 57.
- [118] H. Flegler, Klomparens, *Elektronenmikroskopie*, Spektrum akademischer Verlag, Heidelberg, **1995**.
- [119] K. H. Grellmann, E. Heilbronner, P. Seiler, A. Weller, *J. Am. Chem. Soc.*, **1968**, 90, 4238-4242.
- [120] E. Amir, R. J. Amir, L. M. Campos, C. J. Hawker, *J. Am. Chem. Soc.*, **2011**, 133, 10046-10049.
- [121] X. Wang, J. K.-P. Ng, P. Jia, T. Lin, C. M. Cho, J. Xu, X. Lu, C. He, *Macromolecules*, **2009**, 42, 5534-5544.
- [122] A. Mirlach, M. Feuerer, J. Daub, *Adv. Mater.*, **1993**, 5, 450-453.
- [123] J. M. R. Narayanam, C. R. J. Stephenson, *Chem Soc Rev*, **2011**, 40, 102-113.
- [124] D. G. Barceloux, D. Barceloux, *Clinical Toxicology*, **1999**, 37, 173-194.
- [125] Agency for Toxic Substances and Disease Registry (ATSDR). U.S. Department of Health and Human Services, Public Health Service., Atlanta, GA, **2012**.
- [126] W. M. Haynes, D. R. Lide, *CRC handbook of chemistry and physics*, 87th ed., CRC Press, Boca Raton, FL, **2006**.
- [127] C. M. Cardona, W. Li, A. E. Kaifer, D. Stockdale, G. C. Bazan, *Advanced Materials*, **2011**, 23, 2367-2371.
- [128] X. Wang, S. O. Pehkonen, A. K. Ray, *Ind. Eng. Chem. Res.*, **2004**, 43, 1665-1672.
- [129] D. England, N. Tambe, J. Texter, *ACS Macro Letters*, **2012**, 1, 310-314.
- [130] M. D. Green, T. E. Long, *Polymer Reviews*, **2009**, 49, 291-314.
- [131] J. Yuan, D. Mecerreyes, M. Antonietti, *Prog. Polym. Sci.*, **2013**, 38, 1009-1036.
- [132] P. Zare, A. Stojanovic, F. Herbst, J. Akbarzadeh, H. Peterlik, W. H. Binder, *Macromolecules*, **2012**, 45, 2074-2084.
- [133] X. Feng, X. Sui, M. A. Hempenius, G. J. Vancso, *J. Am. Chem. Soc.*, **2014**, 136, 7865-7868.

- [134] Y. Men, D. Kuzmicz, J. Yuan, *Current Opinion in Colloid & Interface Science*, **2014**, *19*, 76-83.
- [135] D. Wilms, J. Klos, A. F. M. Kilbinger, H. Löwe, H. Frey, *Organic Process Research & Development*, **2009**, *13*, 961-964.
- [136] M. C. DeRosa, R. J. Crutchley, *Coord. Chem. Rev.*, **2002**, *233-234*, 351-371.
- [137] E. Ji, T. S. Corbitt, A. Parthasarathy, K. S. Schanze, D. G. Whitten, *ACS Appl. Mater. Interfaces*, **2011**, *3*, 2820-2829.
- [138] S. Chemburu, T. S. Corbitt, L. K. Ista, E. Ji, J. Fulghum, G. P. Lopez, K. Ogawa, K. S. Schanze, D. G. Whitten, *Langmuir*, **2008**, *24*, 11053-11062.
- [139] Z. J. Wang, K. Landfester, K. A. I. Zhang, *Polym. Chem.*, **2014**, *5*, 3559-3562.
- [140] K. Zhang, Z. Vobecka, K. Tauer, M. Antonietti, F. Vilela, *Chem. Commun.*, **2013**, *49*, 11158-11160.
- [141] F. Yan, J. Texter, *Angew. Chem., Int. Ed.*, **2007**, *46*, 2440.
- [142] J. Y. Yuan, N. ten Brummelhuis, M. Junginger, Z. L. Xie, Y. Lu, A. Taubert, H. Schlaad, *Macromol. Rapid Commun.*, **2011**, *32*, 1157.
- [143] S. Prescher, S. Ghasimi, P. Höhne, K. Grygiel, K. Landfester, K. A. I. Zhang, J. Yuan, *Macromolecular Rapid Communications*, **2014**, *35*, 1925-1930.
- [144] M. S. Silverstein, N. R. Cameron, in *Encyclopedia of Polymer Science and Technology*, John Wiley & Sons, Inc., **2002**.
- [145] M. S. Silverstein, *Prog. Polym. Sci.*, **2014**, *39*, 199-234.
- [146] N. R. Cameron, *Polymer*, **2005**, *46*, 1439-1449.
- [147] B. Kiskan, J. S. Zhang, X. C. Wang, M. Antonietti, Y. Yagci, *Acs Macro Letters*, **2012**, *1*, 546-549.
- [148] M. Shalom, S. Inal, C. Fettkenhauer, D. Neher, M. Antonietti, *J. Am. Chem. Soc.*, **2013**, *135*, 7118-7121.
- [149] X. H. Gao, H. B. Bin Wu, L. X. Zheng, Y. J. Zhong, Y. Hu, X. W. Lou, *Angew. Chem. Int. Ed.*, **2014**, *53*, 5917-5921.
- [150] Y. C. Zhang, L. Yao, G. Zhang, D. D. Dionysiou, J. Li, X. Du, *Appl. Catal. B-Environ.*, **2014**, *144*, 730-738.
- [151] K. Zhang, D. Kopetzki, P. H. Seeberger, M. Antonietti, F. Vilela, *Angew. Chem. Int. Ed.*, **2013**, *52*, 1432-1436.
- [152] C. Schweitzer, R. Schmidt, *Chem. Rev.*, **2003**, *103*, 1685-1758.

- [153] M. C. DeRosa, R. J. Crutchley, *Coord. Chem. Rev.*, **2002**, 233–234, 351-371.
- [154] J. L. Bredas, R. Silbey, D. S. Boudreux, R. R. Chance, *J. Am. Chem. Soc.*, **1983**, 105, 6555.
- [155] L.-S. Zhang, K.-H. Wong, H.-Y. Yip, C. Hu, J. C. Yu, C.-Y. Chan, P.-K. Wong, *Environ. Sci. Technol.*, **2010**, 44, 1392-1398.
- [156] N. Zhang, S. Liu, X. Fu, Y.-J. Xu, *J. Phys. Chem. C*, **2011**, 115, 9136-9145.
- [157] H. Li, Y. Liu, X. Gao, C. Fu, X. Wang, *ChemSusChem*, **2015**, 8, 1189-1196.
- [158] D. Milstein, J. K. Stille, *J. Am. Chem. Soc.*, **1978**, 100, 3636-3638.
- [159] J. K. Stille, *Angew. Chem. Int. Ed.*, **1986**, 25, 508-524.
- [160] D. R. Rutherford, J. K. Stille, C. M. Elliott, V. R. Reichert, *Macromolecules*, **1992**, 25, 2294.
- [161] V. Farina, *Pure and Applied Chemistry*, **1996**, 68, 6.
- [162] D. Milstein, J. K. Stille, *Journal of the American Chemical Society*, **1979**, 101, 4981-4991.
- [163] K. Vikse, T. Naka, J. S. McIndoe, M. Besora, F. Maseras, *ChemCatChem*, **2013**, 5, 3604-3609.
- [164] C. Amatore, F. Pfluger, *Organometallics*, **1990**, 9, 2276-2282.
- [165] S. Ghasimi, K. Landfester, K. A. I. Zhang, *ChemCatChem*, **2016**, 8, 694-698.
- [166] M. J. Frisch, G. W. Trucks, H. B. Schlegel, G. E. Scuseria, M. A. Robb, J. R. Cheeseman, G. Scalmani, V. Barone, B. Mennucci, G. A. Petersson, H. Nakatsuji, M. Caricato, X. Li, H. P. Hratchian, A. F. Izmaylov, J. Bloino, G. Zheng, J. L. Sonnenberg, M. Hada, M. Ehara, K. Toyota, R. Fukuda, J. Hasegawa, M. Ishida, T. Nakajima, Y. Honda, O. Kitao, H. Nakai, T. Vreven, J. A. Montgomery Jr., J. E. Peralta, F. Ogliaro, M. J. Bearpark, J. Heyd, E. N. Brothers, K. N. Kudin, V. N. Staroverov, R. Kobayashi, J. Normand, K. Raghavachari, A. P. Rendell, J. C. Burant, S. S. Iyengar, J. Tomasi, M. Cossi, N. Rega, N. J. Millam, M. Klene, J. E. Knox, J. B. Cross, V. Bakken, C. Adamo, J. Jaramillo, R. Gomperts, R. E. Stratmann, O. Yazyev, A. J. Austin, R. Cammi, C. Pomelli, J. W. Ochterski, R. L. Martin, K. Morokuma, V. G. Zakrzewski, G. A. Voth, P. Salvador, J. J. Dannenberg, S. Dapprich, A. D. Daniels, Ö. Farkas, J. B. Foresman, J. V. Ortiz, J. Cioslowski, D. J. Fox, Gaussian, Inc., Wallingford, CT, USA, **2009**.
- [167] M.-A. Tehfe, J. Lalevée, S. Telitel, E. Contal, F. Dumur, D. Gigmès, D. Bertin, M. Nechab, B. Graff, F. Morlet-Savary, J.-P. Fouassier, *Macromolecules*, **2012**, 45, 4454-4460.
- [168] D. E. Bartak, K. J. Houser, B. C. Rudy, M. D. Hawley, *Journal of the American Chemical Society*, **1972**, 94, 7526-7530.

- [169] T. Kitagawa, T. P. Layloff, R. N. Adams, *Analytical Chemistry*, **1963**, *35*, 1086-1087.
- [170] A. D. McNaught, Wilkinson, A., in *International Union of Pure and Applied Chemistry (IUPAC) Gold Book*, 2nd ed., Blackwell Science, Oxford UK.
- [171] F. Brouwer, J. Alma, H. Valkenier, T. P. Voortman, J. Hillebrand, R. C. Chiechi, J. C. Hummelen, *Journal of Materials Chemistry*, **2011**, *21*, 1582-1592.
- [172] W. Yang, L. Zhang, Y. Hu, Y. Zhong, H. B. Wu, X. W. Lou, *Angewandte Chemie International Edition*, **2012**, *51*, 11501-11504.

10. Scientific Contributions

Publications

- 1.) Saman Ghasimi, Simon Bretschneider, Wei Huang, Katharina Landfester, Kai A. I. Zhang: Photocatalytic Stille-type coupling reactions using conjugated organic catalysts with visible light, **2016**, (submitted).
- 2.) Saman Ghasimi, Katharina Landfester, Kai A. I. Zhang: Water Compatible Conjugated Microporous Polyazulene Networks as Visible-Light Photocatalysts in Aqueous Medium, *ChemCatChem*, **2016**, 8, 694 – 698.
- 3.) Saman Ghasimi, Simon Prescher, Zi Jun Wang, Katharina Landfester, Jiayin Yuan, Kai A. I. Zhang: Heterophase Photocatalysts from Water-Soluble Conjugated Polyelectrolytes: An Example of Self-Initiation under Visible Light, *Angewandte Chemie International Edition*, **2015**, 54, 14549 –14553.
- 4.) Saman Ghasimi, Simon Prescher, Zi Jun Wang, Katharina Landfester, Jiayin Yuan, Kai A. I. Zhang: Heterophasen-Photokatalysatoren aus wasserlöslichen Polyelektrolyten: ein Beispiel für die Selbstinitiierung unter sichtbarem Licht, *Angewandte Chemie*, **2015**, 127, 14757 – 14761.
- 5.) Zi Jun Wang, Saman Ghasimi, Katharina Landfester, Kai A. I. Zhang: Bandgap Engineering of Conjugated Nanoporous Poly-benzobisthiadiazoles via Copolymerization for Enhanced Photocatalytic 1,2,3,4-Tetrahydroquinoline Synthesis under Visible Light, *Advanced Synthesis & Catalysis*, **2016**, 358, 2576 – 2582. **Contribution: Solid-state NMR.**
- 6.) Can Yang, Beatriz Chiyin Ma, Linzhu Zhang, Sen Lin, Saman Ghasimi, Katharina Landfester, Kai A. I. Zhang, Xinchun Wang: Molecular Engineering of Conjugated Polybenzothiadiazoles for Enhanced Hydrogen Production by Photosynthesis, *Angew. Chem. Int. Ed.*, **2016**, 55, 1 – 6. **Contribution: Solid-state NMR.**
- 7.) Wei Huang, Zi Jun Wang, Beatriz Chiyin Ma, Saman Ghasimi, Dominik Gehrig, Frédéric Laquai, Katharina Landfester, Kai A. I. Zhang: Hollow Nanoporous Covalent Triazine Frameworks via Acid Vapor-Assisted Solid Phase Synthesis for Enhanced Visible Light Photoactivity, *Journal of Materials Chemistry A*, **2016**, 4, 7555–7559. **Contribution: Solid-state NMR.**
- 8.) Run Li, Zi Jun Wang, Lei Wang, Beatriz Chiyin Ma, Saman Ghasimi, Hao Lu, Katharina Landfester, Kai A. I. Zhang: Photocatalytic Selective Bromination of Electron-Rich Aromatic Compounds Using Microporous Organic Polymers with Visible Light, *ACS Catalysis*, **2016**, 6, 1113–1121. **Contribution: Solid-state NMR, synthesis method development: stepwise addition of monomers.**

9.) Beatriz Chiyin Ma, Saman Ghasimi, Katharina Landfester, Kai A. I. Zhang: Enhanced Visible Light Promoted Antibacterial Efficiency of Conjugated Microporous Polymer Nanoparticles via Molecular Doping, *Journal of Materials Chemistry B*, **2016**, 4, 5112-5118. **Contribution: Solid-state NMR.**

10.) Zi Jun Wang, Saman Ghasimi, Katharina Landfester, Kai A. I. Zhang: Molecular Structural Design of Conjugated Microporous Poly(Benzooxadiazole) Networks for Enhanced Photocatalytic Activity with Visible Light, *Advanced Materials*, **2015**, 27, 6265–6270. **Contribution: Solid-state NMR, EPR.**

11.) Zi Jun Wang, Kim Garth, Saman Ghasimi, Katharina Landfester, Kai A I Zhang: Conjugated Microporous Poly(Benzochalcogenadiazole)s for Photocatalytic Oxidative Coupling of Amines under Visible Light, *ChemSusChem*, **2015**, 8, 3459 – 3464. **Contribution: Solid-state NMR, EPR.**

12.) Beatriz Chiyin Ma, Saman Ghasimi, Katharina Landfester, Filipe Vilela, Kai A. I. Zhang: Conjugated Microporous Polymer Nanoparticles with enhanced dispersibility and water compatibility for photocatalytic applications, *Journal of Materials Chemistry A*, **2015**, 3, 16064–16071. **Contribution: Solid-state NMR.**

13.) Zi Jun Wang, Saman Ghasimi, Katharina Landfester, Kai A. I. Zhang: Photocatalytic Suzuki Coupling Reaction Using Conjugated Microporous Polymer with Immobilized Palladium Nanoparticles under Visible Light, *Chemistry of Materials*, **2015**, 27, 1921–1924. **Contribution: Solid-state NMR, EPR.**

14.) Simon Prescher, Saman Ghasimi, Patrick Höhne, Konrad Grygiel, Katharina Landfester, Kai A. I. Zhang, Jiayin Yuan: Polyfluorene Polyelectrolyte Nanoparticles: Synthesis of Innovative Stabilizers for Heterophase Polymerization, *Macromolecular Rapid Communications*, **2014**, 35, 1925–1930. **Contribution: Polymer synthesis.**

15.) Zi Jun Wang, Saman Ghasimi, Katharina Landfester, Kai A. I. Zhang: A conjugated porous poly-benzobisthiadiazole network for visible light-driven photoredox reaction, *Journal of Materials Chemistry A*, **2014**, 2, 18720–18724. **Contribution: Polymer synthesis, Solid-state NMR, EPR.**

16.) Zi Jun Wang, Saman Ghasimi, Katharina Landfester, Kai A I Zhang: Highly porous conjugated polymers for selective oxidation of organic sulfides under visible light, *Chemical Communications*, **2014**, 50, 8177-8180. **Contribution: Solid-state NMR, Quantum mechanics calculations (DFT).**

Conferences

1.) Poster presentation: “Heterophase Photocatalysts from Water-Soluble Conjugated Polyelectrolytes: An Example of Self-Initiation under Visible Light” (Saman Ghasimi, Simon Prescher, Zi Jun Wang, Katharina Landfester, Jiayin Yuan, Kai A. I. Zhang), European Polymer Federation (EPF) Congress, Dresden, 21.-26.6 2015, awarded best poster in poster competition.